

**Characterization and therapeutic exploitation of molecular  
vulnerabilities in genetically defined lung cancer**

Inaugural-Dissertation

zur

Erlangung des Doktorgrades

der Mathematisch-Naturwissenschaftlichen Fakultät

der Universität zu Köln

vorgelegt von

Marcel A. Dammert

aus

Bruchsal

Veröffentlichung: Köln, 2022

Berichterstatter: Prof. Dr. Martin L. Sos

(Gutachter) Prof. Dr. Ana J. García Sáez

Tag der mündlichen Prüfung: 01.12.2021

# Contents

<b>Summary</b>	2
<b>Zusammenfassung</b>	4
<b>Introduction</b>	6
Differential applicability of targeted therapy in lung cancer	6
Tyrosine kinase inhibitors in <i>EGFR</i> -mutant and <i>RET</i> -rearranged NSCLC	7
MYC family members define therapeutic vulnerabilities in small cell lung cancer	10
Targeting deregulated transcription in NUT carcinoma	13
Aims of this work	14
<b>Publications</b>	15
Overcoming <i>EGFR</i> <sup>G724S</sup> -mediated osimertinib resistance through unique binding characteristics of second-generation <i>EGFR</i> inhibitors	15
Drugging the catalytically inactive state of <i>RET</i> kinase in <i>RET</i> -rearranged tumors	29
MYC paralog-dependent apoptotic priming orchestrates a spectrum of vulnerabilities in small cell lung cancer	42
Systematic kinase inhibitor profiling identifies CDK9 as a synthetic lethal target in NUT midline carcinoma	54
<b>Discussion</b>	69
Overcoming <i>EGFR</i> <sup>G724S</sup> -mediated osimertinib resistance through unique binding characteristics of second-generation <i>EGFR</i> inhibitors	69
Drugging the catalytically inactive state of <i>RET</i> kinase in <i>RET</i> -rearranged tumors	70
MYC paralog-dependent apoptotic priming orchestrates a spectrum of vulnerabilities in small cell lung cancer	71
Systematic kinase inhibitor profiling identifies CDK9 as a synthetic lethal target in NUT midline carcinoma	72
Concluding remarks	74
<b>References</b>	76
<b>Erklärung zur Dissertation</b>	83

## Summary

Lung cancer is one of the most common cancer types and responsible for the largest number of cancer-related deaths worldwide. Typically, lung cancer arises in individuals with heavy smoking background and only rarely in never-smokers. Various cells of origin within the lung give rise to distinct, molecularly heterogeneous lung cancer subtypes with the two major subtypes non-small cell lung cancer (NSCLC) and small cell lung cancer (SCLC). Targeted therapy options also vary significantly between the specific subtypes and while oncogene-driven lung adenocarcinoma (LUAD) is already successfully treated with targeted drugs, no targeted therapies are available in SCLC.

LUAD is often driven genetic alterations such as point mutations and rearrangements in genes of receptor tyrosine kinases (RTKs) like *EGFR* leading to aberrant activation of receptor tyrosine kinase signaling and oncogenic transformation. Mutation-selective small molecule RTK inhibitors have been developed to specifically kill oncogene-addicted cancer cells. Introduction of third generation EGFR inhibitor osimertinib substantially increased survival of *EGFR*-mutant LUAD patients but on-target resistance mutations such as EGFR G724S limit osimertinib efficacy leading to tumor relapse. Remarkably, we observed that second-generation EGFR inhibitor afatinib displayed selective activity against EGFR G724S in cell line and animal models. In contrast to osimertinib, afatinib still binds to EGFR G724S and reduces cellular viability, EGFR signaling, transformation and *in vivo* growth of EGFR G724S cells, therefore providing a possible treatment strategy for patients that relapse after osimertinib treatment due to EGFR G724S.

Oncogenic gene fusions involving *RET* also lead to cellular transformation and LUAD tumorigenesis. Previously, multi-kinase inhibitors were used to treat *RET*-rearranged cancers with limited success due to lack of RET-specificity and RET gatekeeper mutations impeding inhibitor binding. We identified AD80, a type II kinase inhibitor that binds RET in the DFG-out conformation. AD80 displayed selective activity against common RET fusions KIFB-RET and CCDC6-RET and retained activity against RET V804M gatekeeper mutation. AD80 efficiently reduced RET- and downstream signaling as well as RET-associated gene expression. AD80 also displayed *in vivo* efficacy in CCDC6-RET patient-derived xenograft (PDX) models, demonstrating the potential of type II inhibitors as targeted therapy against RET-rearranged LUAD.

In contrast to NSCLC, SCLC is defined by inactivation of tumor suppressors *TP53* and *RB1* and lacks targetable oncogenic drivers. Frequent activation of MYC transcription

factor family members (*MYC*, *MYCL*, and *MYCN*) further accelerate tumor growth and aggressiveness. We found that activation of individual MYC family members entails differential molecular vulnerabilities. *MYC* overexpression is associated with high levels of DNA damage, repression of *BCL2* expression and high apoptotic priming, leading to higher sensitivity towards Aurora kinase and MCL1 inhibition whereas high *MYCL/MYCN* expression is associated with resistance against these perturbations. Our study highlights that MYC status can be predictive for therapy response and might be used for molecularly-guided, patient stratification for future targeted therapy regimens in SCLC.

A rare but very aggressive lung cancer type, NUT carcinoma is driven by BRD4-NUT fusion protein leading to large-scale epigenetic reprogramming and deregulated transcription of genes driving tumorigenesis. Using high-throughput viability screening, we identified that NUT carcinoma cells are preferentially sensitive against CDK9 inhibition. We observed, that CDK9 inhibition increases RNA Polymerase II pausing possibly reverting BRD4-NUT-mediated, transcriptional activation of pro-tumor genes warranting further investigation of CDK9 inhibition in NUT carcinoma.

## Zusammenfassung

Lungenkrebs ist einer der häufigsten Krebsarten und verzeichnet pro Jahr die weltweit meisten Krebs-assoziierten Todesfälle. Lungenkrebs tritt typischerweise als Folge von langjährigem Rauchen auf und nur sehr selten in Nichtraucherern. Die verschiedenen, molekular unterschiedlichen Subtypen von Lungenkrebs entstehen aus bestimmten Vorläuferzellen in der Lunge und man unterscheidet hauptsächlich zwischen dem nichtkleinzelligen Bronchialkarzinom (non-small cell lung cancer, NSCLC) und dem kleinzelligen Bronchialkarzinom (small cell lung cancer, SCLC). Aufgrund der großen Heterogenität dieser Subtypen ergibt sich die unterschiedliche Anwendbarkeit zielgerichteter Tumortherapie, welche bisher nur in Patienten mit Adenokarzinom (lung adenocarcinoma, LUAD) erfolgreich eingesetzt werden kann.

LUAD wird häufig durch aktivierende Punktmutationen oder genomische Rearrangements in Rezeptor-Tyrosinkinase (RTK) Genen wie z.B. *EGFR* verursacht. Dies führt zu deregulierter Aktivierung des RTK Signalwegs und onkogener Transformation. Selektive, kleinmolekulare Inhibitoren wurden entwickelt um zielgerichtet solche Onkogen-aktivierte Krebszellen zu töten. Die Einführung des Drittgenerations *EGFR* Inhibitors Osimertinib hat das Überleben von Patienten mit *EGFR*-mutierten Adenokarzinom wesentlich verlängert, jedoch entwickeln manche Patienten Osimertinib-resistente Mutationen in *EGFR* wie z.B. *EGFR* G724S, welche zur Tumorprogression führen. Wir haben herausgefunden, dass, im Gegensatz zu Osimertinib, der Zweitgenerations *EGFR* Inhibitor Afatinib an *EGFR* G724S binden kann und spezifisch den *EGFR* Signalweg inhibiert und somit das Wachstum und Überleben von *EGFR* G724S-mutierten Zellen reduziert. Somit wäre der Einsatz von Afatinib eine mögliche Therapieoption für Patienten mit *EGFR* G724S Mutation.

Onkogene Genfusionen in *RET* fungieren ebenfalls als starke, transformierende Treiber im Adenokarzinom. Zunächst wurden *RET*-rearrangierte Tumore mit Multi-Kinaseinhibitoren behandelt, welche aber aufgrund von fehlender Spezifität gegenüber *RET* und aufkommenden *RET* Resistenzmutationen nur begrenzt wirksam sind. Wir haben beobachtet, dass der type II Kinaseinhibitor AD80 an *RET* in der DFG-out Konformation bindet und *RET* inhibiert. Dies führt zu verminderter Aktivität des *RET* Signalwegs in Zellen mit KIF5B-*RET* und CCDC6-*RET* Fusionen und zudem in Zellen mit *RET* V804M Gatekeeper Mutation. Weiterhin verringert AD80 das Wachstum von CCDC6-*RET* Tumoren in Xenograft Modellen, was das Potenzial von type II

Kinaseinhibitoren als mögliche, zielgerichtete Therapie von *RET*-aktivierten Adenokarzinomen unterstreicht.

Im Gegensatz zu NSCLC ist SCLC durch die Inaktivierung der Tumorsuppressorgene *TP53* und *RB1* gekennzeichnet und es existieren keine therapeutisch adressierbaren, onkogene Treibermutationen. In SCLC sind häufig die verschiedenen Mitglieder der MYC Transkriptionsfaktorfamilie (*MYC*, *MYCL* und *MYCN*) aktiviert was zu beschleunigtem und aggressiverem Wachstum führt. Wir haben herausgefunden, dass je nachdem welcher MYC Transkriptionsfaktor aktiviert ist, sich unterschiedliche Sensitivitäten der Tumorzellen ergeben. *MYC* Überexpression führt zu erhöhtem DNA Schaden, Repression der *BCL2* Expression und verstärktem Apoptotic Priming. Dies korreliert mit erhöhter Sensitivität gegenüber Aurora Kinase- und MCL1 Inhibition. Hohe *MYCL*/*MYCN* Level hingegen vermitteln Resistenz gegen diese Therapie. Somit kann der MYC-Status des Tumors als prädiktiver Marker für das Ansprechen auf bestimmte Therapien fungieren.

Das NUT Karzinom ist eine sehr seltene und aggressive Art von Lungenkrebs und wird durch das onkogene Fusionsprotein BRD4-NUT initiiert. BRD4-NUT führt zu einer genomweiten, epigenetischen Reprogrammierung welche zur Induktion von wachstumsfördernden Genen führt. Mittels Hochdurchsatz-Viabilitätsscreening haben wir herausgefunden, dass CDK9 Inhibition effektiv und präferenziell gegen NUT Karzinom Zellen wirkt. Die Inhibition von CDK9 erhöht die Retention von RNA Polymerase II am Genpromotor und verhindert so potenziell die Transkription von Tumor-fördernden Genen. Diese Ergebnisse rechtfertigen die weitere Untersuchung von CDK9 Inhibition im NUT Karzinom.

# Introduction

## Differential applicability of targeted therapy in lung cancer

Lung cancer is the second most prevalent cancer type worldwide with 2.1 million new cases in 2020 and the leading cause for cancer-related deaths with approximately 1.8 million mortalities in 2020 (Sung et al., 2021). The relative 5-year survival rate of all lung cancer cases is 21.7% but varies significantly depending on particular lung cancer subtypes (National Cancer Institute, NCI). By far the highest risk factor for lung cancer is extensive, multi-year tobacco smoking accounting for approximately 80% of all lung cancer cases (Schabath and Cote, 2019). However, up to 20% of total lung cancer cases arise in never smokers with associated risk factors including exposure to secondhand smoke, inhalable carcinogens like asbestos, radon gas, high levels of air pollution, but also genetic predispositions and history of respiratory and immune-compromising diseases (Schabath and Cote, 2019; Sung et al., 2021). Based on histology, lung cancer is divided into two major subtypes: non-small cell lung cancer (NSCLC) accounting for 85%, and small cell lung cancer (SCLC) accounting for 15% of all lung cancer cases, respectively (Schabath and Cote, 2019). Recently new classification criteria for NSCLC were proposed, classifying NSCLC into squamous (30% of NSCLC cases) and non-squamous NSCLC (70% of NSCLC cases). Lung adenocarcinoma (LUAD) is the predominant NSCLC subtype comprising 90% of non-squamous NSCLC (Gridelli et al., 2015, Figure 1).

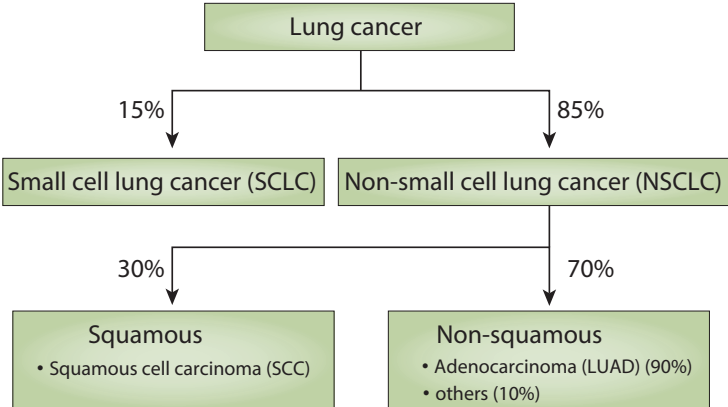


Figure 1: **Classification of lung cancer.** Lung cancer is categorized into small cell lung cancer (SCLC) and non-small cell lung cancer (NSCLC). SCLC make up 15% whereas NSCLC make up 85% of total lung cancer cases. NSCLC is further sub-divided in squamous and non-squamous NSCLC. Lung adenocarcinoma (LUAD) is the most prevalent NSCLC subtype (Gridelli et al., 2015, modified).

Lung cancer is mainly treated using surgery, radiation therapy, chemotherapy, targeted therapy, and recently immunotherapy. However, large molecular differences among lung cancer subtypes impact suitable therapy options. LUAD treatment practice dramatically changed in recent years from pleiotropic, cytotoxic chemotherapy towards targeted therapy directed against specific genomic alterations whereas standard of care in squamous cell carcinoma and SCLC is still largely comprised of chemotherapy.

### Tyrosine kinase inhibitors in *EGFR*-mutant and *RET*-rearranged NSCLC

LUAD tumorigenesis is often driven by aberrant activation of receptor tyrosine kinase (RTK) signaling, mostly caused by activating genomic alterations like mutations or rearrangements in RTK genes directly or genes of downstream signaling pathways (Blume-Jensen and Hunter, 2001). Receptor tyrosine kinases (RTKs) are a large superfamily of transmembrane receptor proteins that relay extracellular stimuli like mitogenic or proliferative cues into the cell by triggering several intracellular signaling cascades leading to regulatory and transcriptional responses. RTKs are activated through binding of ligands to the RTK extracellular domain inducing dimerization of the RTK, which activates the intracellular tyrosine kinase domain of the RTK leading to auto-phosphorylation of intracellular tyrosine residues using ATP as a substrate. These phospho-tyrosine residues are bound by adaptor proteins, which initiate signaling cascades through sequential phosphorylation culminating in the activation of transcription factors. Activation of diverse RTKs mainly converges on activation of four signaling cascades: RAS-MAPK (mitogen-activated protein kinase) pathway, phosphatidylinositol 3-kinase (PI3K)-AKT pathway, phospholipase c- $\gamma$  (PLC $\gamma$ ) pathway, and JAK-STAT pathway (Casaletto and McClatchey, 2012, Figure 2).

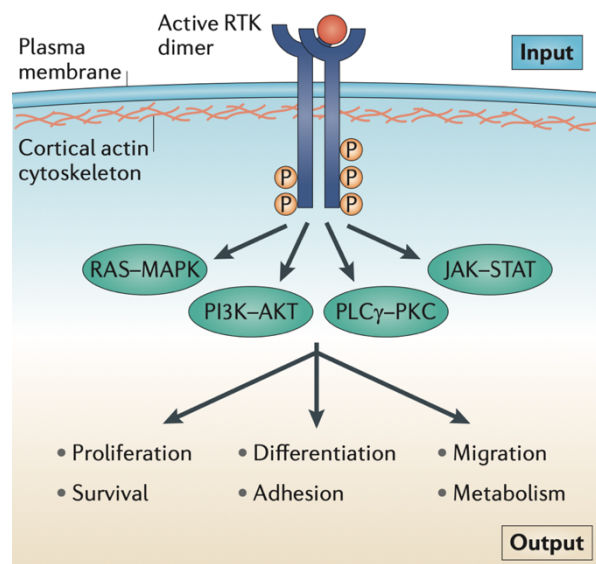


Figure 2: **Schematic representation of RTK-mediated signal transduction cascade.** RTK activation is induced by ligand binding to the extracellular domain and subsequent autophosphorylation of tyrosine residues in the intracellular domain. The phosphorylation sites are recognized by adaptor proteins that mediate the activation of several signaling pathways (RAS-MAPK, PI3K-AKT, PLC $\gamma$ , JAK-STAT) through sequential phosphorylation leading to increased proliferation, survival, differentiation, adhesion, migration, and metabolism (Casaletto and McClatchey, 2012).

Activation of these signaling cascades is associated with increased cell growth, proliferation, cell cycle progression, and inhibition of apoptosis and thus, aberrant activation of these pathways leads to oncogenic transformation and cancer development (Lemmon and Schlessinger, 2010). Deregulated, oncogenic RTK activity is caused by specific genomic alterations in RTK genes. In LUAD, commonly found alterations of RTK genes include activating mutations, in-frame deletions or more complex intragenic insertions of epidermal growth factor receptor (*EGFR*), amplifications and intragenic insertions in *ERBB2* (*HER2*), *ALK* rearrangements, gene fusion events in *ROS1*, *RET*, *NTRK*, or *NRG1* creating oncogenic-fusion proteins, or exon skipping variants of *MET*. In addition, activating mutations in downstream effectors like *KRAS* and *BRAF* also lead to increased PI3K-AKT and/or MEK-ERK pathway activation and oncogenic signaling (Herbst et al., 2018). Activating *EGFR* mutations are detected in approximately 30% of LUAD patients and the majority of these mutations are located in the tyrosine kinase domain and mainly consist of in-frame deletions in exon 19 (del19) and a point-mutation (L858R) in exon 21 (Collisson et al., 2014; Jordan et al., 2017; Skoulidis and Heymach, 2019). Building on the paradigm of oncogene addiction, i.e. cancer cells become dependent on one particular driver gene for their survival despite multiple co-occurring genomic lesions, small-molecule tyrosine kinase inhibitors (TKIs) were developed to specifically target oncogenic kinase signaling thereby killing the oncogene-addicted cancer cells (Weinstein and Joe, 2008). Multiple generations of TKIs have been sequentially developed to target EGFR: erlotinib and gefitinib (first generation), dacomitinib and afatinib (second generation), and osimertinib (third generation). All these TKIs bind to the ATP-pocket of the EGFR tyrosine kinase domain inhibiting autophosphorylation and activation of EGFR and subsequent downstream signaling (Da Cunha Santos et al., 2011). Clinically, EGFR inhibitors dramatically improved response rate and progression-free survival in *EGFR*-mutant patients compared to standard chemotherapy demonstrating the superiority of targeted therapy directed against oncogenic drivers (Mok et al., 2009; Sequist et al., 2013; Soria et al., 2018). Another

key aspect is the improved quality of life exhibited due to reduced organismal toxicity of specific inhibitors of the mutated kinase in cancer cells compared cytotoxic chemotherapy affecting all dividing cells. Currently, 3<sup>rd</sup> generation EGFR inhibitor osimertinib is used as first line, standard of care treatment in *EGFR*-mutated lung cancer (Ramalingam et al., 2020) due to better clinical performance and suppression of resistance mutations against 1<sup>st</sup> and 2<sup>nd</sup> generation inhibitors like the EGFR T790M gatekeeper mutation. Despite these clinical advancements, nearly all patients relapse through acquired resistance against EGFR inhibitors and several on- and off-target resistance mechanisms have been described in response to osimertinib. The most prevalent on-target resistance mutations EGFR C797S, G724S, L718Q, and S768I all impede osimertinib-mediated inhibition of EGFR leading to reactivation of oncogenic EGFR signaling (Passaro et al., 2021; Tumbrink et al., 2021, Figure 3).

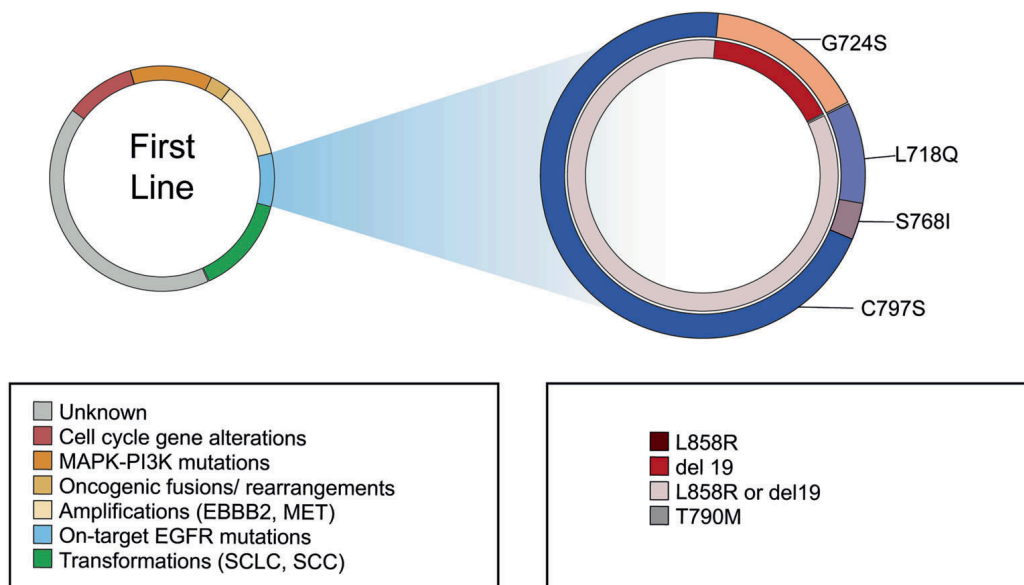


Figure 3: **Resistance mechanisms in response osimertinib in *EGFR*-mutant lung cancer.** Frequency of known resistance mechanisms against first-line osimertinib treatment of *EGFR*-mutant lung cancer patients is displayed. On-target EGFR mutations include C797S, G724S, L718Q, and S768I point mutations. Off-target resistance mechanisms include alterations in cell cycle genes, MAPK-PI3K pathway mutations, oncogenic fusion/rearrangement events, amplification of secondary oncogenes like *ERBB2*(*HER2*) or *MET*, and SCLC/SCC transformation (Tumbrink et al., 2021, modified).

Therefore, one of the main efforts of ongoing research in EGFR-targeted therapy is to combat the various resistance mechanisms against osimertinib.

Similar to *EGFR*, oncogenic alterations of the RTK rearranged during transfection (*RET*) proto-oncogene are also potent drivers of tumorigenesis, albeit with a lower prevalence – detected in about 2% of LUAD patients (Collisson et al., 2014;

Jordan et al., 2017; Skoulidis and Heymach, 2019). While activating point mutations in of RET such as RET M918T, C634R/Y/W, A883F, or C630R are common in thyroid tumors, *RET* rearrangements that create oncogenic gene fusions of *RET* and genes such as kinesin family member 5B (*KIF5B*) or coiled-coil domain containing 6 (*CCDC6*) are commonly found in lung cancer patients (Subbiah et al., 2020). The resulting fusion-proteins KIF5B-RET and CCDC6-RET display constitutively active tyrosine kinase activity leading to increased downstream signaling via RAS/MAPK, PI3K/AKT, JAK/STAT, PKA, and PKC pathways, which leads to oncogenic transformation and proliferation (Thein et al., 2021). Clinical treatment strategies targeting *RET*-rearranged NSCLC originally relied on non-specific, multi-kinase inhibitors (MKIs) like vandetanib and cabozantinib before recent approval of *RET*-specific inhibitors selpercatinib and pralsetinib (Thein et al., 2021). Similar to the clinical reality of EGFR TKIs however, *RET* MKI and *RET*-specific TKI-treated patients relapse carrying on-target, gatekeeper (*RET* V804M/L) or non-gatekeeper (*RET* G810C/S/R, Y806C/N, or V738A) mutations or off-target oncogenic alterations (Thein et al., 2021).

Thus, despite substantial clinical improvements provided by biomarker-driven, targeted therapy in NSCLC, relapse through acquired resistance requires more potent treatment strategies leading to full cancer eradication to break the vicious circle of response-resistance-relapse.

### **MYC family members define therapeutic vulnerabilities in small cell lung cancer**

In sharp contrast to NSCLC, SCLC lacks directly targetable oncogenic drivers like RTKs. Moreover, RTKs are rarely mutated in SCLC, and, if mutated, do not function as oncogenic drivers of the tumor. Because of these premises, TKI-mediated targeted therapy is not applicable to SCLC. Standard of care treatment still relies on combination chemotherapy like cisplatin/etoposide, with the recent addition of immune checkpoint inhibitors to chemotherapy regimens (Iams et al., 2020). In contrast to NSCLC, SCLC is typically a neuroendocrine carcinoma, almost exclusively arising in heavy smokers and originating from pulmonary neuroendocrine cells (Rudin et al., 2021). However, recently non-neuroendocrine tuft cells were found to give rise to a rare non-neuroendocrine subtype of SCLC (Huang et al., 2018). Moreover, SCLC is a highly aggressive cancer with early metastatic spread. Approximately 250 000 new SCLC cases are diagnosed per year with 200 000 SCLC-related deaths (Sung et al., 2021) and an overall 5-year survival rate below 5% making SCLC the most deadly

form of lung cancer (Rudin et al., 2021). Initially SCLC displays high response rates of 60-90% depending on tumor stage at diagnosis to platinum-based chemotherapy (Demedts et al., 2010). However, almost all patients rapidly relapse with chemorefractory tumors. Extensive intratumoral heterogeneity is a major contributor to the rapid outgrowth of chemoresistant sub-clones in progressive SCLC tumors (Su et al., 2019). Genetically, SCLC is defined by near universal loss-of-function mutations in both tumor suppressor genes *TP53* and retinoblastoma-associated protein (*RB1*). Based on the expression of lineage-defining transcription factors, four SCLC subtypes were proposed: *ASCL1*<sup>high</sup> and *NEUROD1*<sup>high</sup> comprise the neuroendocrine subtypes SCLC-A and SCLC-N whereas *POU2F3*<sup>high</sup> and *YAP1*<sup>high</sup> SCLC comprise the non-neuroendocrine subtypes SCLC-P and SCLC-Y (Rudin et al., 2019, Figure 4).

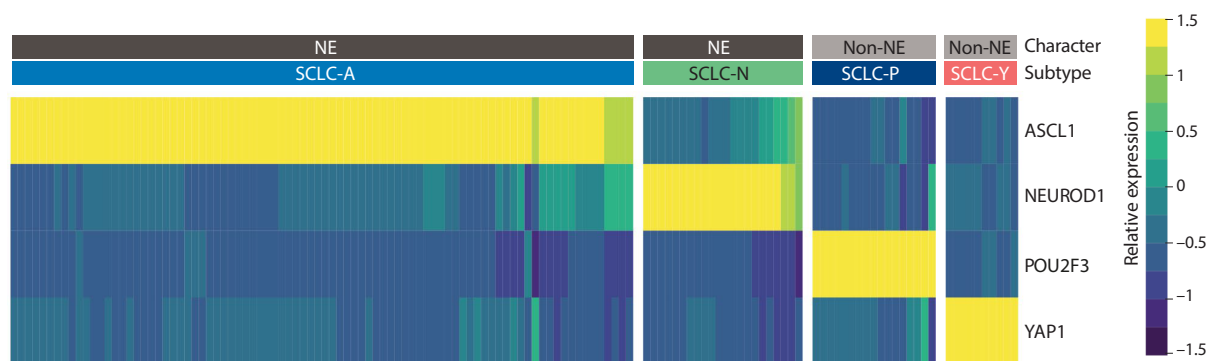


Figure 4: **Molecular subtypes of SCLC are defined by lineage transcription factor expression.** Heatmap showing relative expression of subtype-defining transcription factors in SCLC patients and patient-derived cell lines. SCLC is divided into neuroendocrine (NE) and non-neuroendocrine (Non-NE) subtypes. NE-SCLC is further subdivided into *ASCL1*<sup>high</sup> SCLC-A and *NEUROD1*<sup>high</sup> SCLC-N whereas *POU2F3*<sup>high</sup> SCLC-P and *YAP1*<sup>high</sup> SCLC-Y comprise Non-NE SCLC (Rudin et al., 2019, modified).

Another key genetic feature of SCLC are frequent amplifications and overexpression of MYC transcription factor family genes (*MYC*, *MYCL*, *MYCN*) (George et al., 2015; Peifer et al., 2012; Rudin et al., 2012). Notably, high *MYC* expression is more frequently observed in SCLC-N/P/Y than SCLC-A tumors, whereas high *MYCL* or *MYCN* expression is more prevalent in SCLC-A tumors (Rudin et al., 2021; Wooten et al., 2019). All MYC family members are structurally homologous basic helix-loop-helix transcription factors that bind DNA at E-box motifs leading to transcriptional activation or transcriptional repression depending on MYC-interaction partners. The MYC/MAX complex is associated with transcriptional activation whereas the MYC/MIZ1 complex is associated with transcriptional repression (Kress et al., 2015). In general, aberrant activation of all MYC family members induces metabolic activity, cell growth, cell cycle

progression and proliferation leading to oncogenic transformation and tumorigenesis (Wolf and Eilers, 2020). In SCLC, MYC paralogs are activated by overexpression (*MYC*, *MYCL*), amplification (all MYC family members) or gene-fusion (only *MYCL*) (Ciampricotti et al., 2021; George et al., 2015). Notably, expression of MYC family members is mutually exclusive, i.e. only one particular MYC family member is activated in a specific tumor cell (Brägelmann et al., 2017a; Dammert et al., 2019; George et al., 2015). Studies of genetically engineered SCLC mouse models demonstrated that activation of all MYC family members leads to substantially increased SCLC tumorigenesis and aggressiveness (Grunblatt et al., 2020; Kim et al., 2016; Mollaoglu et al., 2017). Their roles as driving oncogenes would define MYC family members as ideal drug targets, but due to their structural composition, direct targeting of MYC family members has so far not been achieved. To circumvent this predicament, indirect targeting of MYC based on synthetic lethality represents a promising approach against MYC-driven cancers. Applied to MYC, synthetic lethality strategies target pathways, which are deregulated after oncogenic MYC activation and become essential for the survival of the cancer cell but of untransformed cells, e.g. high MYC levels lead to increased rRNA transcription to fuel protein synthesis for rapid cell growth and proliferation, which renders these cells dependent on components of rRNA and protein synthesis pathways. Thus targeting of these pathways could specifically inhibit/kill MYC-activated cancer cells without harming normal cells (Thng et al., 2021, Figure 5).

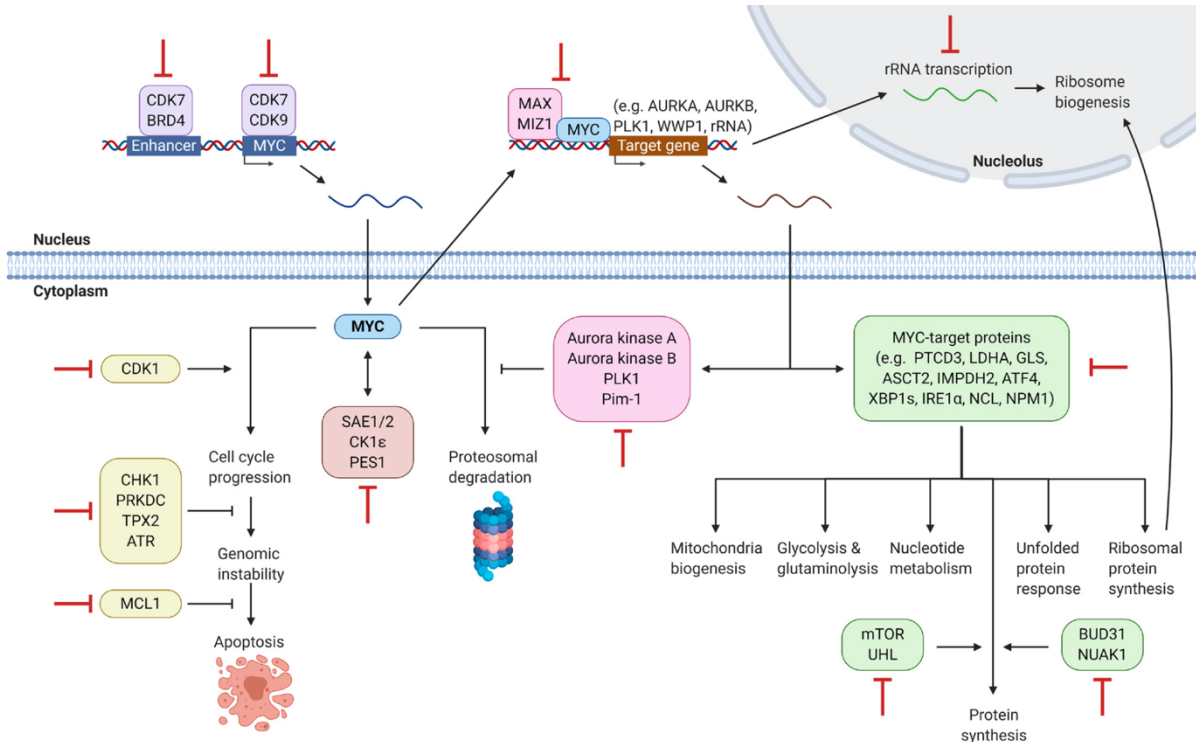


Figure 5: **Synthetic lethal vulnerabilities in MYC-driven cancer cells.** Several cellular pathways are deregulated upon MYC activation and contribute to malignant growth and thus represent potential targets for therapeutic intervention: transcription factors and chromatin modifiers regulating *MYC* expression (purple), MYC-activated cell cycle regulators (yellow), deregulated metabolic modulators (green), MYC-cofactors and interaction partners (pink), novel non-MYC-regulated synthetic lethal targets (brown) (Thng et al., 2021).

In SCLC, several synthetic lethal, MYC family member-associated vulnerabilities have been observed. High *MYC* expression leads to increased sensitivity towards Aurora kinase A (*AURKA*) inhibition (Mollaoglu et al., 2017; Sos et al., 2012), high *MYCL* expression leads to vulnerability against RNA polymerase I inhibition (Kim et al., 2016), and targeting de-ubiquitination enzyme *USP7* was observed as a *MYCN*-induced synthetic vulnerability (Grunblatt et al., 2020). Due to the pleiotropic influence of MYC family members regulating virtually all cellular processes either directly or indirectly, many more possible co-vulnerabilities are yet to be discovered. Furthermore, the detailed understanding of molecular differences and vulnerabilities induced by each MYC family member in SCLC could provide a basis for patient stratification for certain therapies depending on their MYC-status.

### **Targeting deregulated transcription in NUT carcinoma**

Only recently, nuclear protein in testis (*NUT*) carcinoma formerly *NUT* midline carcinoma was officially classified as neuroendocrine lung cancer type in the category of «Other and Unclassified carcinomas» (Travis et al., 2015). *NUT* carcinoma is an extremely rare and very aggressive cancer with a dismal median survival of only 6.7 months (French, 2018). *NUT* carcinoma is genetically defined by oncogenic fusion of the *NUT* gene to multiple fusion partners, mostly bromodomain and extraterminal domain-containing (BET) family genes *BRD4* and *BRD3*. The *BRD4*-*NUT* fusion protein combines the acetyl-histone-binding capability of *BRD4* with *NUT*-mediated binding of histone acetyl transferase (HAT) and transcriptional activator p300 (French, 2012). This dual function induces oncogenicity through the formation of aberrantly large euchromatic chromosomal domains marked by p300 occupancy and active histone marks driving the transcription of growth- and proliferation-related genes while precluding these activators from genomic regions of differentiation-associated genes leading to their repression (Alekseyenko et al., 2015). Pre-clinically, BET inhibitors like *JQ1* that competitively bind to the acetyl histone binding site within the bromodomain of the *BRD4* part of *BRD4*-*NUT* were highly effective against *NUT* carcinoma cells but

failed clinically due to limited efficacy and high toxicity (French, 2018). Similar to MYC in SCLC, direct targeting of deregulated transcription in NUT tumor driven by BRD4-NUT fusions proved unsuccessful and indirect, synthetic lethal vulnerabilities are explored.

In summary, the individual subtypes of lung cancer comprise a heterogeneous disease with profoundly different molecular and genetic characteristics that influence aggressiveness and therapeutic possibilities. Oncogene-driven NSCLC is amenable to molecularly stratified, targeted therapy using TKIs whereas SCLC lacks directly targetable alterations and personalized therapeutic options. This differential availability of targeted therapy is reflected in prognosis and survival rates, which dramatically improved in recent years for targeted therapy-treated NSCLC but remained nearly unchanged for SCLC (Gazdar et al., 2017; Gridelli et al., 2015).

### **Aims of this work**

The aims of this work are to address various aspects in the development, applicability and molecular characterization of targeted therapy strategies in different lung cancer subtypes with differential genetic characteristics.

First, the EGFR G724S mutation that confers resistance against clinically used, third generation EGFR inhibitor osimertinib is investigated in search for inhibitors that are active against EGFR G724S and possibly provide a treatment strategy for osimertinib-resistant tumors.

Second, the previously existent lack of specific inhibitors against RET tyrosine kinase in RET-rearranged LUAD motivated the investigation of type II kinase inhibitors in RET-rearranged cancer cells to possibly overcome the limitation of multi-kinase inhibitors.

Third, the molecular impact of the activation of each individual MYC family member in SCLC is characterized to decipher which specific molecular pathways and vulnerabilities are induced by the individual MYC family members and to evaluate possible therapeutic consequences following MYC family member activation.

Forth, high-throughput cell viability screening of an inhibitor library is conducted in a large number of lung cancer cell lines to find genetic features that determine inhibitor sensitivity.

## Publications

### **Overcoming EGFR<sup>G724S</sup>-mediated osimertinib resistance through unique binding characteristics of second-generation EGFR inhibitors**

Fassunke J, Müller F, Keul M, Michels S, **Dammert MA\***, Schmitt A, Plenker D, Lategahn J, Heydt C, Brägelmann J, Tumbrink HL, Alber Y, Klein S, Heimsoeth A, Dahmen I, Fischer RN, Scheffler M, Ihle MA, Priesner V, Scheel AH, Wagener S, Kron A, Frank K, Garbert K, Persigehl T, Püsken M, Haneder S, Schaaf B, Rodermann E, Engel-Riedel W, Felip E, Smit EF, Merkelbach-Bruse S, Reinhardt HC, Kast SM, Wolf J, Rauh D, Büttner R, Sos ML.

\* co-first author

Specific contributions:

- Generation and validation of Ba/F3 and NIH-3T3 cell lines bearing different *EGFR* mutations (EGFR del19, EGFR del19/G724S, EGFR G724S)
- Viability screening of *EGFR*-mutant cell lines against EGFR inhibitors
- Western blot analysis of *EGFR*-mutant cell lines upon EGFR inhibitor treatment
- Colony formation, soft-agar assays of *EGFR*-mutant cell lines upon EGFR inhibitor treatment
- Data analysis of xenograft experiments
- Manuscript editing

ARTICLE

DOI: 10.1038/s41467-018-07078-0

OPEN

# Overcoming $EGFR^{G724S}$ -mediated osimertinib resistance through unique binding characteristics of second-generation EGFR inhibitors

Jana Fassunke et al.<sup>#</sup>

The emergence of acquired resistance against targeted drugs remains a major clinical challenge in lung adenocarcinoma patients. In a subgroup of these patients we identified an association between selection of  $EGFR^{T790M}$ -negative but  $EGFR^{G724S}$ -positive subclones and osimertinib resistance. We demonstrate that  $EGFR^{G724S}$  limits the activity of third-generation EGFR inhibitors both in vitro and in vivo. Structural analyses and computational modeling indicate that  $EGFR^{G724S}$  mutations may induce a conformation of the glycine-rich loop, which is incompatible with the binding of third-generation TKIs. Systematic inhibitor screening and in-depth kinetic profiling validate these findings and show that second-generation EGFR inhibitors retain kinase affinity and overcome  $EGFR^{G724S}$ -mediated resistance. In the case of afatinib this profile translates into a robust reduction of colony formation and tumor growth of  $EGFR^{G724S}$ -driven cells. Our data provide a mechanistic basis for the osimertinib-induced selection of  $EGFR^{G724S}$ -mutant clones and a rationale to treat these patients with clinically approved second-generation EGFR inhibitors.

---

Correspondence and requests for materials should be addressed to J.W. (email: [juergen.wolf@uk-koeln.de](mailto:juergen.wolf@uk-koeln.de)) or to D.R. (email: [daniel.rauh@tu-dortmund.de](mailto:daniel.rauh@tu-dortmund.de)) or to R.Büt. (email: [reinhard.buettner@uk-koeln.de](mailto:reinhard.buettner@uk-koeln.de)) or to M.L.S. (email: [martin.sos@uni-koeln.de](mailto:martin.sos@uni-koeln.de)). <sup>#</sup>A full list of authors and their affiliations appears at the end of the paper.

The identification of *EGFR* mutations and the discovery of their exquisite sensitivity to epidermal growth factor receptor (EGFR) inhibitors dramatically changed the therapeutic routine for lung adenocarcinoma (LADC) patients<sup>1–3</sup>. Selective inhibition of EGFR with tyrosine kinase inhibitors (TKI), such as erlotinib or gefitinib, significantly prolongs the progression-free survival (PFS) up to 13.6 months in the first-line setting<sup>4–6</sup>. However, under therapeutic pressure resistant clones emerge in virtually all tumors and ultimately lead to progressive disease and failure of therapy<sup>7–9</sup>.

Third-generation EGFR inhibitors such as osimertinib have been designed to overcome acquired resistance induced by the *EGFR*<sup>T790M</sup> gatekeeper mutation<sup>10</sup>. Clinical results show that patients treated with osimertinib respond in up to 71% in the background of an acquired *EGFR*<sup>T790M</sup> mutation<sup>11,12</sup>. More recent data indicate that osimertinib treatment is even superior to single agent first-generation inhibitors such as erlotinib or gefitinib in terms of PFS and overall survival (OS) in the first-line setting<sup>13</sup>.

The recurrent acquisition of *EGFR*<sup>C797S</sup> mutations is currently thought to be the most frequent mechanism of resistance to osimertinib<sup>14–16</sup>. Alternative by-pass mechanisms involving *MET* amplification or activation of the MAPK pathway may also play a role in the development of resistance to third-generation EGFR inhibitors<sup>14,15,17</sup>. Here, we characterized the role of the acquired *EGFR*<sup>G724S</sup> mutation that was diagnosed in osimertinib-resistant lesions of four individual *EGFR*<sup>T790M</sup>-mutant LADC patients. We performed systematic biochemical, cellular, and structural analyses to determine the functional relevance of this mutation in the context of targeted EGFR inhibition.

## Results

**Acquisition of *EGFR*<sup>G724S</sup> is associated with cancer progression.** Within our LADC re-biopsy program we performed targeted sequencing of lesions that progressed under treatment with third-generation EGFR inhibitors. Interestingly, we identified two patients with no detectable *EGFR*<sup>G724S</sup> reads (P1, *EGFR*<sup>E746\_S752delinsV</sup>; P2, *EGFR*<sup>S752\_I759del</sup>) and two patients with low levels of *EGFR*<sup>G724S</sup> mutation (P3, *EGFR*<sup>E746\_T751delinsIP</sup>; P4, *EGFR*<sup>E746\_T751delinsIP</sup>) prior to start of third-generation EGFR inhibitor therapy (Fig. 1a–d; Supplementary Fig. 1A, Supplementary Table 1). Patient P1 (UICC stage IIIA, 59 years old, female) received osimertinib within the AURA trial (NCT01802632) after progression on erlotinib and the detection of an acquired *EGFR*<sup>T790M</sup> mutation (T1) (Fig. 1a). Osimertinib treatment resulted in a partial response (54% reduction based on RECIST 1.1) (Supplementary Fig. 1B, 1D). Even though progression occurred after 8.2 months with the growth of target lesions and a new *EGFR*<sup>T790M</sup>-negative and *EGFR*<sup>G724S</sup>-positive pleural effusion with a molecular fraction (MF, estimate of allelic fraction without calculating the purity and ploidy) of 6.3% (T2) (Supplementary Table 1C).

Patient P2 (UICC stage IV, 47 years old, female) received two consecutive lines of third-generation EGFR inhibitors upon progression to erlotinib and a combination of carboplatin/pemetrexed/bevacizumab. Treatment with the third-generation EGFR inhibitor EGF816 (CEGF816X2101; NCT02108964) was initiated after detection of *EGFR*<sup>T790M</sup> (Fig. 1c). EGF816 treatment resulted in a stable disease according to RECIST 1.1 for almost 6 months. At the time point of progression to EGF816 two pulmonary lesions were resected (T2). In one (EPII), the initially detected *EGFR*<sup>T790M</sup> mutation was lost and an *EGFR*<sup>G724S</sup> mutation was acquired with a MF of 71.1%. In the other sample (EPI), the *EGFR*<sup>T790M</sup> mutation (AF 39.3%) was still present and no *EGFR*<sup>G724S</sup> reads were detected (Fig. 1c,

Supplementary Table 1). Osimertinib treatment was initiated and resulted in a metabolic response of the liver metastases and the stabilization of other solid tumor lesions, including the remaining pulmonary lesions, as assessed by <sup>18</sup>F-FDG positron emission tomography (PET)-CT scans (Fig. 1d). However, a progressive malignant pleural effusion that contained *EGFR*<sup>G724S</sup>-mutant cells and no trace of the previously acquired *EGFR*<sup>T790M</sup> mutation was recorded after seven months of treatment (T3). In this example the MF of *EGFR*<sup>G724S</sup> exceeds the MF of our reference *EGFR*<sup>T790M</sup> reads but it is likely that the inherent noise of our PCR-based method overestimates the *EGFR*<sup>G724S</sup> reads and we assume similar levels of both mutants in this tumor<sup>18</sup>.

Two patients (P3, *EGFR*<sup>E746\_T751delinsIP</sup>; P4, *EGFR*<sup>E746\_T751delinsIP</sup>) were identified with a low MF of *EGFR*<sup>G724S</sup> before initiation of osimertinib treatment and persisting *EGFR*<sup>G724S</sup>-mutant reads at time of progression (Fig. 1a, Supplementary Table 1). Patient P3 (68 years old, UICC stage IV, female) showed a robust response to gefitinib and at time of progression after 32 months presented with a growing paravertebral *EGFR*<sup>T790M</sup>-positive lesion (MF of 6.9%, T1) as well as an *EGFR*<sup>G724S</sup> mutation (MF of 5.3%, T1; Supplementary Table 1). Treatment with osimertinib resulted in a good partial response according to RECIST 1.1 for a period of 6.8 months (Supplementary Fig. 1C). However, the lesion in which the *EGFR*<sup>G724S</sup> mutation was detected showed no significant decrease. A subsequent re-biopsy of the same paravertebral lesion showed a loss of *EGFR*<sup>T790M</sup> and the persistence of *EGFR*<sup>G724S</sup> (MF 49.6%, T2) (Fig. 1b).

The last patient (P4) (69 years old, UICC stage IV) with a known mutation was initially treated with erlotinib (Fig. 1a, Supplementary Fig. 1A, Supplementary Table 1). However, progression occurred after 36 months of treatment and a re-biopsy of a growing lesion revealed *EGFR*<sup>T790M</sup> as well as *EGFR*<sup>G724S</sup>-positive sequencing reads (T1). Treatment with osimertinib resulted in a PFS of 2.5 months (objective efficacy not determined by RECIST 1.1). Another re-biopsy of the growing lesion in the left lower lobe was collected revealing the loss of *EGFR*<sup>T790M</sup> and the outgrowth of a *EGFR*<sup>G724S</sup>-mutant subclone (AF 39.3%, T2) (Supplementary Table 1). Thus, although *EGFR*<sup>G724S</sup>-positive clones may be partially selected in tumors treated with first-generation EGFR inhibitors, a pronounced increase of *EGFR*<sup>G724S</sup>-positive sequencing reads is primarily associated with third-generation EGFR inhibitor treatment.

*EGFR*<sup>G724S</sup> mutations have been identified as very rare driver mutations and more recently, case reports have shown their potential role in acquired osimertinib resistance in LADC patients<sup>19–21</sup>. To assess the overall frequency of the acquired *EGFR*<sup>G724S</sup> mutation and other changes in EGFR, we revisited re-biopsy samples obtained from *EGFR*<sup>T790M</sup>-positive patients at time of progression under treatment with third-generation EGFR inhibitors. This cohort spans 30 patients; 22 of them received osimertinib (73.3%), four EGF816 (13.3%) and four rociletinib (13.3%). *EGFR*<sup>C797S</sup> was detected in three patients (10%), loss of *EGFR*<sup>T790M</sup> without no detectable *EGFR* acquired mutation was detected in 10 (33.3%) and loss of *EGFR*<sup>T790M</sup> and presence of *EGFR*<sup>G724S</sup> was seen in four patients (13.3%) (Fig. 1e). As this mutation seems to be less frequent in other cohorts, the actual prevalence across a broader panel of patients with acquired osimertinib resistance remains to be assessed<sup>14</sup>. Although only *EGFR*<sup>C797S</sup> mutations have a direct impact on the binding of third-generation EGFR inhibitors within the kinase, the mutual exclusivity between *EGFR*<sup>C797S</sup> and *EGFR*<sup>G724S</sup> indicates that the *EGFR*<sup>G724S</sup> mutations do not represent passenger events (Fig. 1f).

Overall, our data show that *EGFR*<sup>G724S</sup> mutations may emerge or persist in osimertinib-resistant clones that may evolve independently of acquired *EGFR*<sup>T790M</sup> mutations. The data further suggest a negative relation of the allelic frequencies of

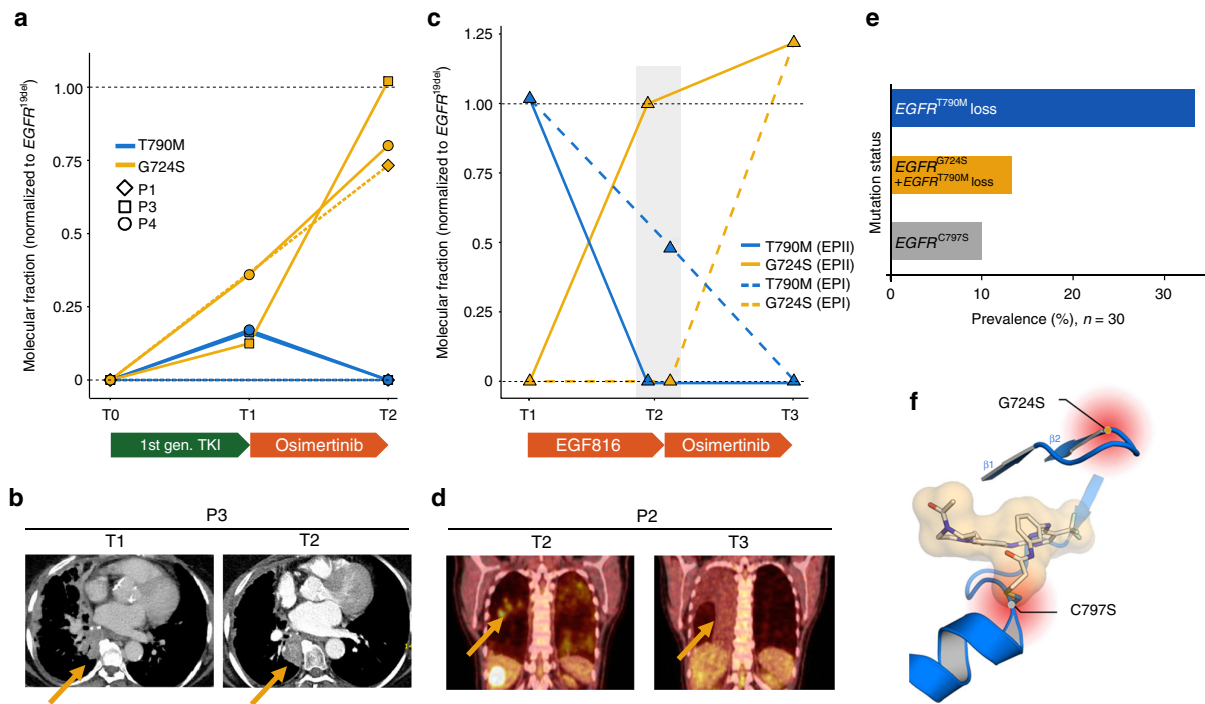


**Fig. 1** Insight into patient's examination results and prevalence of *EGFR* resistance mutations. **a** Graph showing the molecular fractions of *EGFR*<sup>T790M</sup> and *EGFR*<sup>G724S</sup> normalized to *EGFR*<sup>19del</sup> at first diagnosis (T0), prior to treatment with osimertinib (T1) and at progression to osimertinib (T2) in patients P1, P3, and P4. Treatment is indicated with bars below. All patients received a first-generation EGFR inhibitor (1st gen. TKI) prior to treatment with osimertinib. In P1, next-generation sequencing was not feasible at T1 and *EGFR* status was determined by Sanger sequencing (dotted lines). **b** The contrast-enhanced CT scans of patient P3 prior to treatment with osimertinib (T1) and at progression (T2) are exemplarily shown. The yellow arrows mark the spot of the biopsy collected in a growing lesion. **c** Prior to the start of osimertinib treatment (T2) two separate biopsies were collected (EPI, dotted line and EPII, solid line). Graph indicates the evolution of the molecular fractions of *EGFR*<sup>T790M</sup> and *EGFR*<sup>G724S</sup> in patient P2 prior to treatment with EGF816 (T1) and osimertinib (T2) and at progression to osimertinib (T3). **d** <sup>18</sup>F PET-CT scans shows P2 prior to treatment (T2) and at progression to treatment with osimertinib (T3). **e** Bar chart showing the frequencies of *EGFR* mutations (*EGFR*<sup>G724S</sup> and *EGFR*<sup>C797S</sup>) at progression to third-generation EGFR inhibition ( $n = 30$ ). **f** Positions of the osimertinib resistance mutations *EGFR*<sup>C797S</sup> and *EGFR*<sup>G724S</sup> within the binding site of the EGFR kinase domain are shown (PDB ID: 5UWD)

*EGFR*<sup>G724S</sup> and *EGFR*<sup>T790M</sup> under third-generation EGFR inhibition: increasing *EGFR*<sup>G724S</sup> frequencies were accompanied by decreasing *EGFR*<sup>T790M</sup> frequencies.

***EGFR*<sup>G724S</sup> mediates resistance to third-generation EGFR inhibitors.** To test the functional relevance of the identified *EGFR* mutation, we overexpressed different combinations of *EGFR*<sup>G724S</sup> and *EGFR*<sup>19del</sup> mutations in NIH-3T3 cells. Erlotinib as well as osimertinib treatment resulted in a major reduction of phospho-EGFR levels in *EGFR*<sup>19del</sup>-mutant cells already at concentrations of 0.3  $\mu$ M of osimertinib but not in cells that expressed *EGFR*<sup>G724S</sup> either alone or in combination with *EGFR*<sup>19del</sup> (Fig. 2a, b). We observed similar results with the third-generation EGFR inhibitor rociletinib, despite its lower potency against the *EGFR*<sup>19del</sup>-mutant (Supplementary Fig. 2A).

To validate our findings in an independent cellular model we generated Ba/F3 cells that overexpress *EGFR*<sup>19del</sup> or *EGFR*<sup>G724S</sup> alone and the combination of these mutations. The survival of these murine cells initially relies on IL-3 but can be switched to an oncogene such as mutant *EGFR*<sup>22,23</sup>. As expected the introduction of *EGFR*<sup>19del</sup> or *EGFR*<sup>G724S</sup> alone led to a transformation of Ba/F3 cells, but only *EGFR*<sup>19del</sup> showed high sensitivity to erlotinib and osimertinib (Fig. 2c, d, Supplementary Fig. 7A, B).

Based on these results and the increasing relevance of osimertinib in the front-line setting we focused on the resistance

phenotype against this third-generation EGFR inhibitor<sup>13</sup>. As in the patients we assume the *EGFR*<sup>G724S</sup> resistance mutations to occur in the background of *EGFR*<sup>19del</sup> we compared *EGFR*<sup>19del</sup> and *EGFR*<sup>+G724S</sup> sensitivity to third-generation EGFR inhibitors in vivo. To this end we employed murine xenograft models in which genetically modified NIH-3T3 cells were injected subcutaneously into nude mice (*NCR*<sup>nu/nu</sup>). Again, we observed efficient tumor formation for both double-mutant *EGFR*<sup>19del+G724S</sup> and single-mutant *EGFR*<sup>19del</sup> NIH-3T3 cells (Fig. 2e). Confirming our in vitro results osimertinib (5 mg/kg daily) treatment significantly slowed down tumor growth of *EGFR*<sup>19del</sup> NIH-3T3 cells compared with vehicle-treated tumors ( $p = 0.027$ ). Of note, osimertinib has a favorable pharmacokinetic profile and is known to halt tumor growth in EGFR-dependent patient-derived cell line xenografts at doses as low as 1 mg/kg daily<sup>10</sup>. However, we observed virtually no therapeutic effect for osimertinib (5 mg/kg daily) treated in double-mutant *EGFR*<sup>19del+G724S</sup> NIH-3T3 cells compared with vehicle-treated tumors (Fig. 2e, f). Since NIH-3T3 cells can partially form tumors in the absence of an oncogenic driver we did not observe any tumor shrinkage in our xenograft model, as one would expect for xenografts implanted with patient-derived cells<sup>24,25</sup>. As expected, we observed a significant induction of cleaved caspase-3-positive cells ( $p = 0.037$ ) (Fig. 2g, h) and a robust reduction of Ki67 positive cells only in *EGFR*<sup>19del</sup>-mutant but not in

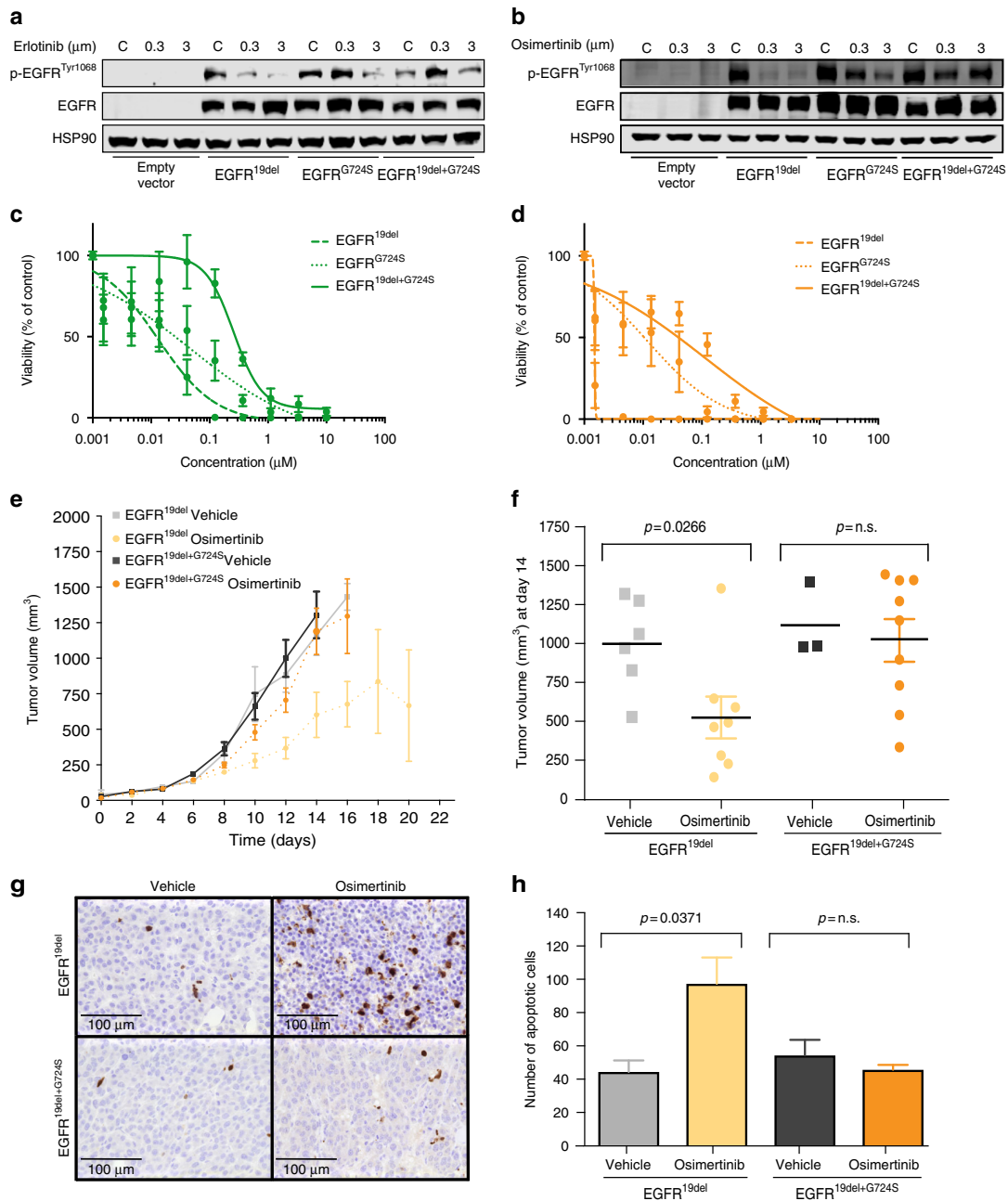


**Fig. 2** *EGFR*<sup>G724S</sup> mediates resistance to third-generation EGFR inhibitors in vitro and in vivo. **a** Immunoblotting results of NIH-3T3 cells (empty vector, *EGFR*<sup>19del</sup>, *EGFR*<sup>G724S</sup>, or *EGFR*<sup>19del+G724S</sup>) monitoring phospho-EGFR and total EGFR under erlotinib treatment (24 h). HSP90 was used as loading control. **b** Immunoblotting of NIH-3T3 cells under osimertinib treatment (24 h) is shown. Dose-response measurement of Ba/F3 cells expressing *EGFR*<sup>19del</sup>, *EGFR*<sup>G724S</sup>, or *EGFR*<sup>19del+G724S</sup> treated for 72 h with **c** erlotinib or **d** osimertinib. Experiments were performed at least three times. **e, f** Graphs show tumor volume of mice injected with NIH-3T3 *EGFR*<sup>19del</sup> and *EGFR*<sup>19del+G724S</sup> cells treated with osimertinib (5 mg/kg, i.p., once daily). **e** Tumor volumes (*EGFR*<sup>19del</sup> vehicle,  $n = 7$  mice; *EGFR*<sup>19del</sup> osimertinib,  $n = 8$  mice; *EGFR*<sup>19del+G724S</sup> vehicle,  $n = 7$  mice; *EGFR*<sup>19del+G724S</sup> osimertinib,  $n = 10$  mice) were assessed for 20 days by longitudinal caliper measurements every second day following treatment initiation. **f** Tumor volumes were quantified after 8 days of treatment. Volume changes in the osimertinib treatment cohort (dark gray and green) were compared with the vehicle-treated control group (light gray and green). Each dot represents a single tumor per mouse. Significance is calculated by two-tailed Student's  $t$  test, n.s.: non-significant. **g** Representative images of Cleaved Caspase-3 stainings. Tumors of mice bearing NIH-3T3 *EGFR*<sup>19del</sup> or *EGFR*<sup>19del+G724S</sup> cells were treated with vehicle solution HPMC (0, 5%) or osimertinib. Scale bar 100  $\mu\text{m}$ . **h** Quantification of Cleaved Caspase-3 staining. Number of apoptotic cells in the osimertinib-treated cohort (dark gray and green) was compared with the vehicle-treated control group (light gray and green)

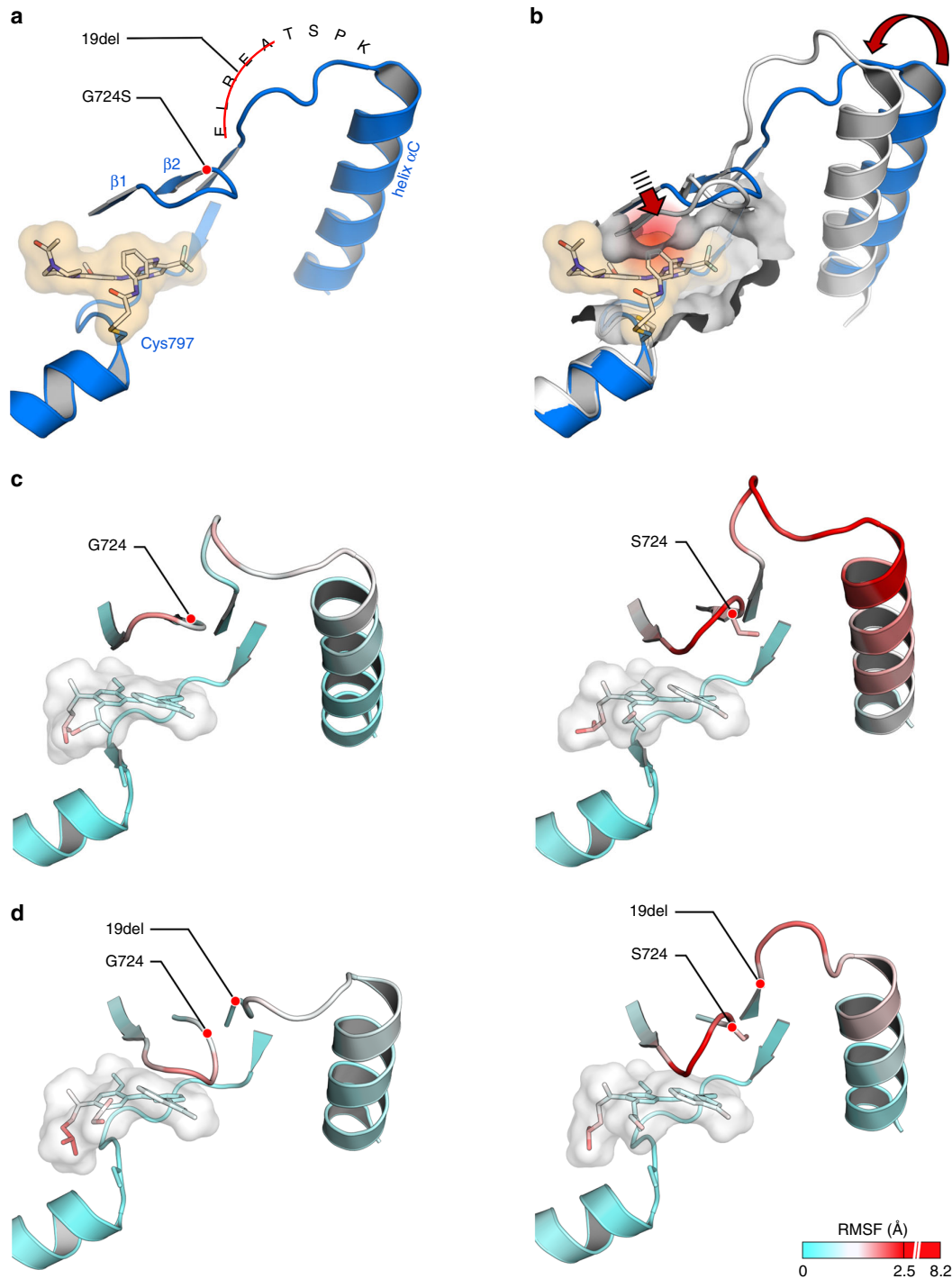


**Fig. 3** Structural analysis of EGFR<sup>19del+G724S</sup>. **a** Binding site of rociletinib bound EGFR (PDB ID: 5UWD). **b** Alignment of the rociletinib bound EGFR-binding site (blue, PDB ID: 5UWD) with exon 20-mutant EGFR (white, PDB ID: 4LRM) that reveals steric hindrance of third-generation TKIs with the glycine-rich loop and the adjacent sheet  $\beta 1$  upon a perturbed network between helix  $\alpha C$ , ELREA motif, and glycine-rich loop. **c** Comparison of MD simulations of osimertinib bound EGFR<sup>WT</sup> (left), EGFR<sup>G724S</sup> (right) (based on PDB ID: 4ZAU). **d** Comparison of MD simulations of osimertinib bound EGFR<sup>19del</sup> (left) or EGFR<sup>19del+G724S</sup> (right) (based on PDB ID: 4ZAU)

EGFR<sup>19del+G724S</sup>-mutant tumors that received osimertinib (Supplementary Fig. 2B–F).

These results clearly indicate that the EGFR<sup>G724S</sup> point mutation may confer resistance against third-generation EGFR inhibitors.

#### Structural impact of an altered glycine-rich loop conformation.

The glycine-rich loop is a crucial structural element for substrate and ligand binding. It is a highly conserved flexible element located in the N-lobe of the kinase domain and contains the canonical GxGxxG motif, where x may be any amino acid<sup>26,27</sup>.

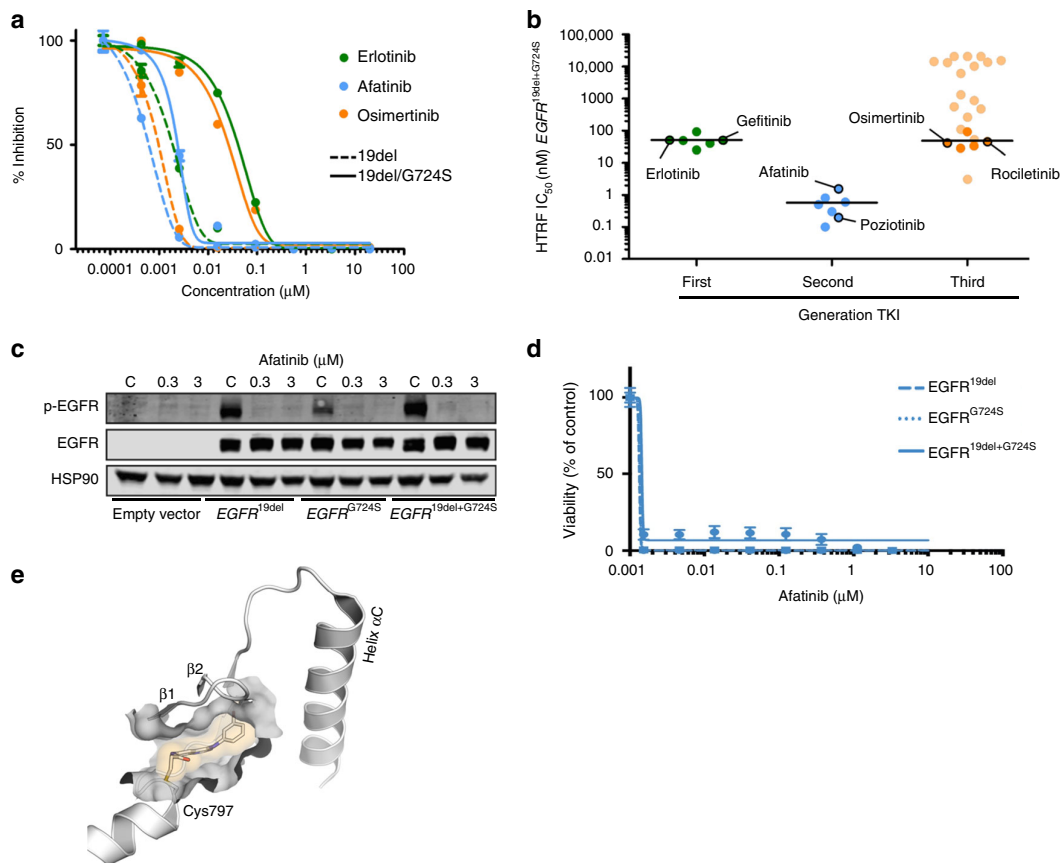


**Fig. 4** Biochemical profiling of EGFR<sup>G724S</sup>. **a** Homogeneous time-resolved fluorescence (HTRF) is used for IC<sub>50</sub>-determination for EGFR<sup>19del</sup> and EGFR<sup>19del+G724S</sup> with representative inhibitors. Representative dose-response curves of a single measurement in duplicates are shown. **b** Comparison of biochemical IC<sub>50</sub>-values with HTRF for the three generations of EGFR TKIs against EGFR<sup>19del+G724S</sup>. Values are the mean of three independent measurements in duplicates. **c** Immunoblotting results of NIH-3T3 cells (empty vector, EGFR<sup>19del</sup>, EGFR<sup>G724S</sup> or EGFR<sup>19del+G724S</sup>) showing phospho-EGFR and total EGFR under afatinib treatment (24 h). HSP90 was used as loading control ( $n = 3$ ). **d** Dose-response measurement of Ba/F3 cells expressing EGFR<sup>19del</sup>, EGFR<sup>G724S</sup>, or EGFR<sup>19del+G724S</sup> treated for 72 h with afatinib. Experiments were accomplished for at least three times. **e** Structure of exon 20 mutant EGFR, bound to 4-anilinoquinazoline based TKI PD168393, is shown

It does not come as a surprise that mutations in the glycine-rich loop can interfere with ligand binding and thus mediate resistance to kinase inhibitors as it was described previously for chronic myelogenous leukemia, where mutations in the glycine-rich loop in BCR-ABL cause resistance to imatinib<sup>28,29</sup>.

To assess the structural impact of the EGFR<sup>G724S</sup> mutation on the EGFR kinase we performed structural analysis based on a previously published co-crystal structure of rocicetinib bound to EGFR (PDB ID: 5UWD) (Fig. 3a)<sup>30</sup>. As described before the glycine-rich loop is an essential element for ligand binding and the glycine at position 724 is in direct contact with the adjacent ELREA motif that is subject to deletion mutations in affected patients. The ELREA sequence plays a crucial role in the alignment of the regulatory helix  $\alpha C$  that is a key element in the transition between the active and inactive kinase domain conformations<sup>30</sup>. It is therefore conceivable that the EGFR<sup>G724S</sup> mutation influences structure and dynamics of the binding site and thereby the affinity toward third-generation EGFR inhibitors. To illustrate the resistance mutation on the molecular level, we performed an alignment of a third-generation TKI bound to the EGFR-binding site (PDB ID: 5UWD) with a crystal structure of an exon 20-mutated form of EGFR (PDB ID: 4LRM). The experimental structure determination of the exon 20 mutant reveals a perturbed network of interactions within the regulatory

important helix  $\alpha C$ , the adjacent ELREA motif and the glycine-rich loop<sup>31,32</sup>, which we believe to be similar to the investigated G724S mutant. The alignment of these structures suggests that the glycine-rich loop can exist in a conformation that is incompatible with third-generation inhibitor binding (Fig. 3b). Therein, steric repulsion arises from the acrylamide-linker of rocicetinib or the methylindole moiety of osimertinib with the sheets  $\beta 1$  and  $\beta 2$  adjacent to the G-rich loop. Although the glycine-rich loop may undergo conformational changes upon ligand binding, the rearrangement might be hindered in the case of third-generation TKIs.

In line with these considerations, molecular dynamics (MD) simulation (based on PDB ID: 4ZAU)<sup>33</sup> revealed an altered ELREA motif in EGFR<sup>G724S</sup>, as compared with simulated wild-type protein when bound to osimertinib (Fig. 3c, Supplementary Fig. 3A left). Moreover, the introduction of serine to position 724 induces a high degree of dynamic flexibility in the network formed by helix  $\alpha C$ , ELREA motif, and glycine-rich loop, as represented by the determined root mean squared fluctuation (RMSF) values (Fig. 3c, Supplementary Fig. 3B; raw data are reported in the B-factor column of PDB structures for osimertinib bound to the EGFR variants studied in Supplementary Data 1–4). These enhanced fluctuations extend toward the methylindole residue of osimertinib. As pointed out in seminal work by

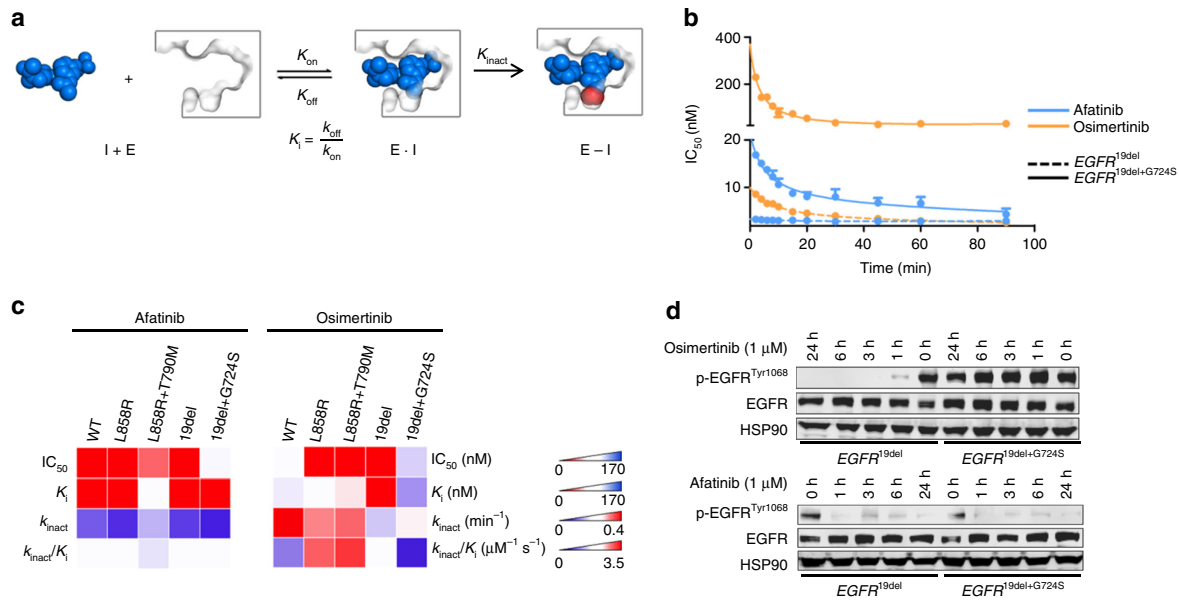


**Fig. 5** Kinetic evaluation of second- and third-generation EGFR TKIs against EGFR mutant proteins. **a** Schematic overview of two-step binding mechanism of covalent inhibitors to kinases with  $K_1$  (quotient of  $k_{\text{off}}$  and  $k_{\text{on}}$ ) describing the reversible binding affinity and  $k_{\text{inact}}$  describing the rate of inactivation. **b** Time-dependent  $\text{IC}_{50}$ -determination of afatinib and osimertinib on EGFR mutant proteins. Representative curves of single measurements in duplicates are shown. **c** Heatmap of biochemical  $\text{IC}_{50}$ -,  $K_1$ -, and  $k_{\text{inact}}$  determination of second- and third-generation EGFR TKIs against EGFR mutant proteins. Values are the mean of three independent measurements in duplicates. **d** Immunoblotting results of NIH-3T3 cells ( $\text{EGFR}^{19\text{del}}$  or  $\text{EGFR}^{19\text{del}+\text{G724S}}$ ) monitoring phospho-EGFR and total EGFR. Cells were treated for indicated times (0, 1, 3, 6, and 24 h) with osimertinib (1  $\mu\text{M}$ ) or afatinib (1  $\mu\text{M}$ ). HSP90 was used as loading control ( $n = 3$ )

Kuriyan, Shaw and co-workers<sup>34</sup>, substantial conformational impact of the exon 19 deletion on the helix  $\alpha\text{C}$  can be expected, whereas the structural and dynamical influence of additionally introducing the G724S mutation is unknown. Hence, we additionally simulated the corresponding  $\text{EGFR}^{19\text{del}}$  and  $\text{EGFR}^{19\text{del}+\text{G724S}}$  systems (Fig. 3d, Supplementary Fig. 3A right). Remarkably, despite the strain introduced by deleting the ELREA motif, increased flexibility particularly of the G-rich loop within the regulatory network is also evident for  $\text{EGFR}^{19\text{del}+\text{G724S}}$  relative to  $\text{EGFR}^{19\text{del}}$ . This finding is robust with respect to varying the starting structures of the simulations (Supplementary Fig. 3B). It appears that the mutant Ser724 side chain renders the regulatory network more flexible and induces altered conformations to the G-rich loop.

Based on these findings, a second line of argumentation could be valid: rather than steric repulsion, the increased flexibility might result in the loss of important interactions between third-generation inhibitors and the binding site that lead to the observed drug resistance. Taken together, we conclude that the  $\text{EGFR}^{\text{G724S}}$  mutation may provoke a conformation of the glycine-rich loop, which is incompatible with ligand binding and accounts for decreased binding efficiency as determined for third-generation EGFR inhibitors.

#### Altered EGFR inhibitor activity pattern through $\text{EGFR}^{\text{G724S}}$

We next addressed the question whether the  $\text{EGFR}^{\text{G724S}}$  mutation might directly interfere with the ability of third-generation EGFR inhibitors to bind to the EGFR kinase, as the mutation site is located in the glycine-rich loop, which is an important regulatory element (Supplementary Fig. 4A). Similar to our observations in NIH-3T3 cells, we detected a marked increase of  $\text{IC}_{50}$ -values in kinase assays using osimertinib against the double-mutant  $\text{EGFR}^{19\text{del}+\text{G724S}}$  as compared with the  $\text{EGFR}^{19\text{del}}$  single-mutant protein (100-fold) (Fig. 4a).

Having established the kinase assay platform, we next sought to test whether the  $\text{EGFR}^{\text{G724S}}$  mutation induces resistance against a specific class of EGFR inhibitors. Herein, we collected a library of more than 120 compounds, of which 90 compounds are proprietary and hence the results of 32 readily published compounds with a known anti-EGFR profile covering clinically relevant first-, second-, and third-generation EGFR inhibitors are discussed in the following (Fig. 4b, Supplementary Fig. 4B, Supplementary Table 2). We screened these inhibitors against both the single and the double-mutant EGFR kinase and observed two interesting patterns of inhibitor activity: (i) the introduction of the  $\text{EGFR}^{\text{G724S}}$  mutation in addition to the  $\text{EGFR}^{19\text{del}}$  mutation induces resistance against virtually all clinically used first- and third-generation inhibitors and (ii) all second-generation inhibitors including afatinib, poziotinib, and dacomitinib remained active against the  $\text{EGFR}^{19\text{del}+\text{G724S}}$  double-mutant kinase (Fig. 4b, Supplementary Table 2). Although, first- and second-generation inhibitors exhibit the same quinazoline scaffold, a remarkable difference in biochemical potency is evident. Alkylation of Cys797 is a distinct feature of second-generation TKIs that discriminates them from first-generation inhibitors. This finding indicates that a covalent bond formation to the target kinase is crucial to occupy the binding site efficiently. Interestingly, we also identified an aminoindazole-based inhibitor with low nanomolar activity against the double-mutant kinase that would not be classified as a second-generation EGFR inhibitor but indeed exhibits a different binding mode than osimertinib (Fig. 4b, Supplementary Table 2)<sup>35</sup>.

We next tested whether the biochemical activity of second-generation EGFR inhibitors in  $\text{EGFR}^{\text{G724S}}$ -mutant cells translates into a therapeutically relevant on-target activity in cellular models. We therefore assessed phospho-EGFR levels following afatinib exposure in NIH-3T3 cells expressing either the empty vector or vectors with  $\text{EGFR}^{19\text{del}}$ ,  $\text{EGFR}^{\text{G724S}}$  alone, or the

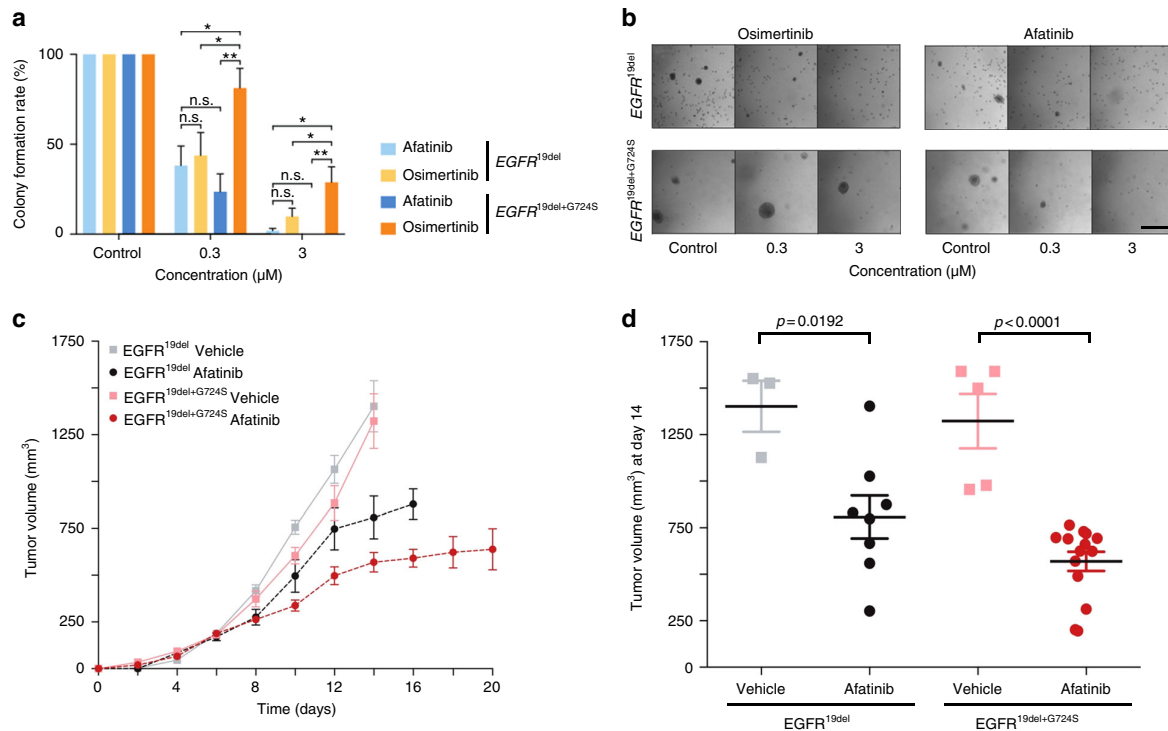


**Fig. 6** Sensitivity of  $EGFR^{G724S}$  to second-generation EGFR inhibitor in vitro and in vivo. **a** Relative mean colony number of NIH-3T3  $EGFR^{19del}$  cells compared with  $EGFR^{19del+G724S}$  cells was assessed in soft agar assays after 16 days under treatment. Cells were treated with osimertinib or afatinib. **b** Representative images of colonies under treatment are displayed in the lower panel. Scale bars, 50  $\mu\text{m}$  ( $n = 4$ ), n.s.: non-significant, \* =  $p < 0.05$ , \*\* =  $p < 0.01$ . **c, d** Graphs show tumor volume in mice injected with NIH-3T3  $EGFR^{19del}$  and  $EGFR^{19del+G724S}$  cells treated with afatinib (20 mg/kg, p.o., once daily). **c** Tumor volumes ( $EGFR^{19del}$  vehicle,  $n = 13$  mice;  $EGFR^{19del}$  osimertinib,  $n = 8$  mice;  $EGFR^{19del+G724S}$  vehicle,  $n = 11$  mice;  $EGFR^{19del+G724S}$  osimertinib,  $n = 14$  mice) were assessed for 20 days by longitudinal caliper measurements every second day following treatment initiation. **d** Tumor volumes were quantified after 8 days of treatment. Volume changes in the afatinib treatment cohort (dark gray and red) were compared with the vehicle-treated control group (light gray and light red). Each dot represents one tumor from a mouse. Significance is indicated by asterisk and calculated by two-tailed Student's  $t$  test

combination of both mutations  $EGFR^{19del+G724S}$  (Fig. 4c, Supplementary Fig. 7C). As expected, afatinib treatment led to a reduction of phospho-EGFR signaling that was independent of the presence of the  $EGFR^{G724S}$  mutation in the glycine-rich loop at concentrations between 10–100 nM (Fig. 4c, Supplementary Fig. 4C). We validated these findings in our Ba/F3 cell lines and found that  $EGFR^{G724S}$ -mutant cells largely retained sensitivity to afatinib at low nanomolar concentrations (Fig. 4d).

These results triggered us to revisit our previously analyzed crystal structure of exon 20-mutant  $EGFR$  (PDB ID: 4LRM) (Supplementary Fig. 5). In line with our biochemical data this structure shows that the binding of second-generation TKIs based on the 4-anilinoquinazoline scaffold (PD168393) to the altered binding site is well tolerated (Fig. 4e).

Thus, our data indicate that the  $EGFR^{G724S}$  mutation induces resistance toward third- and first-generation but retains sensitivity toward 4-aminoquinazoline based second-generation EGFR inhibitors.

#### **$EGFR^{G724S}$ reduces binding of third-generation EGFR TKI.**

Further in-depth kinetic evaluation including determination of kinetic parameters  $K_i$  and  $k_{inact}$  was conducted to more accurately define differences between second- and third-generation inhibitor binding. Binding of covalent inhibitors to a kinase is assumed to succeed in a two-step process: first the inhibitor binds to the kinase in a reversible fashion characterized by  $K_i$  and in a second

step the covalent bond is formed which can be specified with the rate of inactivation ( $k_{inact}$ ) (Fig. 5a)<sup>36,37</sup>.

In these experiments, we identified marked differences in the binding characteristics of second- and third-generation EGFR inhibitors to  $EGFR$ -mutants (Fig. 5b, c, Supplementary Table 3). For instance, the  $k_{inact}$  of osimertinib and rociletinib appears to be similar among the  $EGFR$ -mutants and the  $EGFR^{G724S}$  mutation does not negatively affect the covalent bond formation with Cys797. Our data further indicate that the  $EGFR^{G724S}$  mutation has a strong impact on the formation of the reversible protein-ligand complex in the context of these drugs which prove to bind in a less-affine manner indicated by increased  $K_i$ -values (osimertinib  $EGFR^{19del} < 1$  nM and  $EGFR^{19del+G724S}$  80 nM) (Fig. 5b, c). The second-generation EGFR inhibitor afatinib and the structurally related inhibitor poziotinib exhibit constant affinities and binding kinetics for  $EGFR^{WT}$ ,  $EGFR^{19del}$ , and  $EGFR^{19del+G724S}$  kinases (Fig. 5b, c). In addition, our data reveal that the loss of  $EGFR^{T790M}$ , as observed in all of the relapsed tumors that were enriched for  $EGFR^{G724S}$ -positive clones, further enhanced the loss of affinity of third-generation EGFR inhibitors. Third-generation inhibitors are designed to target a methionine gatekeeper residue in position 790, whereas second-generation inhibitors afatinib and poziotinib exhibit a more pronounced affinity toward threonine-carrying EGFR variants. Based on these findings we hypothesized that such a marked difference between afatinib and osimertinib in the engagement of the mutant kinase should be also detectable in cellular assays. We therefore tested

the ability of afatinib and osimertinib to inhibit phospho-EGFR over time (Fig. 5d, Supplementary Fig. 7D, E). In line with our biochemical data even at 1  $\mu$ M concentrations osimertinib was not able to reduce phospho-EGFR levels in NIH-3T3 cells expressing EGFR<sup>19del+G724S</sup>. In contrast to that, afatinib depleted phospho-EGFR levels in these cells as efficiently as in EGFR<sup>19del</sup> cells (Fig. 5d, Supplementary Fig. 7D, E).

Thus, our data suggest that in EGFR<sup>G724S</sup>-mutant kinase the reversible binding of second-generation EGFR inhibitors is superior to third-generation EGFR inhibitors and might therefore overcome EGFR<sup>G724S</sup>-driven resistance.

**EGFR<sup>G724S</sup> is sensitive to second-generation EGFR inhibitors.** A previous case report of a patient with acquired EGFR<sup>G724S</sup> mutation showed a remarkable response to the combination of osimertinib and afatinib<sup>21</sup>. To test whether the observed affinity to second-generation EGFR inhibitors translates into cellular activity we tested the ability of afatinib as single agent to outperform osimertinib activity in EGFR<sup>19del+G724S</sup>-driven cells. To this end, we plated NIH-3T3 cells that express either EGFR<sup>19del</sup> or EGFR<sup>19del+G724S</sup> in soft agar and treated the cells with increasing concentrations of both drugs over the time of 2 weeks. In line with our in vivo results osimertinib was only effective against the formation of EGFR<sup>19del</sup>-driven colonies at submicromolar concentrations but not against EGFR<sup>19del+G724S</sup>-mutant cells (Fig. 6a, b). However, afatinib largely prevented outgrowth of both EGFR<sup>19del</sup> and EGFR<sup>19del+G724S</sup>-driven colonies at submicromolar concentrations. Thus, the growth inhibition effect of afatinib compared with osimertinib was significantly higher ( $p = 0.01$ ) in EGFR<sup>19del+G724S</sup>-mutant cells (Fig. 6a, b).

To further evaluate the sensitivity of EGFR<sup>G724S</sup> either alone or in combination with EGFR<sup>19del</sup> to third-generation EGFR inhibitors in vivo we employed our murine xenograft models. Again, both single-mutant EGFR<sup>19del</sup> and double-mutant EGFR<sup>19del+G724S</sup> NIH-3T3 cells formed fast growing tumors in nude mice (Fig. 6c). As expected, afatinib (20 mg/kg daily) treatment significantly slowed down tumor growth of both single-mutant EGFR<sup>19del</sup> ( $p = 0.0192$ ) and double-mutant EGFR<sup>19del+G724S</sup> ( $p < 0.0001$ ) xenograft when compared with vehicle-treated tumors (Fig. 6d, Supplementary Fig. 6).

Overall, our results indicate that acquired EGFR<sup>G724S</sup> mutations robustly limit the activity of third-generation inhibitors, whereas sparing the second-generation EGFR inhibitors such as afatinib. Existing Food and Drug Administration (FDA)-approvals for some of these drugs may facilitate the translation of our results into clinical practice for genetically defined osimertinib-resistant lung cancer patients.

## Discussion

EGFR inhibitors represent a showcase for the therapeutic power of precision cancer medicine in genetically selected patients. Building on structural and functional insights, several lines of drug development efforts provided a rich source of clinically available drugs including second-generation EGFR inhibitors<sup>38–40</sup>. So far, these drugs played only a minor role for the targeted treatment of EGFR-mutant tumors as they largely failed to induce pronounced effects in patients that acquired a gatekeeper EGFR<sup>T790M</sup> mutation<sup>22,41,42</sup>. Although second-generation EGFR inhibitors bind irreversibly to EGFR these drugs lack the flexibility to circumvent a steric clash with the gatekeeper mutation<sup>22</sup>. Second-generation EGFR inhibitors are also very potent inhibitors of EGFR<sup>WT</sup> and therefore these drugs are likely to induce diarrhea or skin rash<sup>41</sup>. At the same time, afatinib is an FDA-approved drug for first-line treatment of

EGFR-mutant LADC with a known on-target resistance profile derived from preclinical models<sup>43,44</sup>.

Our clinical and functional characterization of the acquired EGFR<sup>G724S</sup> resistance mutation suggests a revision of the properties and clinical liabilities that are associated with second-generation EGFR inhibitors. This is becoming an even more relevant issue in the light of the encouraging results achieved with osimertinib in the front-line setting that might challenge the standard use of first-generation EGFR inhibitors in EGFR mutant patients<sup>13</sup>. First of all, the emergence of an EGFR<sup>G724S</sup> resistance mutation is associated with loss of EGFR<sup>T790M</sup>-positive subclones, and thus providing the right genetic context for the use of second-generation EGFR inhibitors. These observations are in line with previous reports on acquired osimertinib resistance that frequently report a loss of EGFR<sup>T790M</sup>-positive clones<sup>15,16</sup>. Although we cannot exclude the fact that additional signaling layers including FAK or SFK or co-occurring mutations that were not part of our panel may be involved in the observed resistance phenotype<sup>45–47</sup>, our genomic and functional data strongly support a dominant role of the acquired EGFR<sup>G724S</sup> mutation in the context of third-generation EGFR inhibitors. Thus, our findings might be relevant for a large group of patients receiving third-generation inhibitors. Interestingly, previous studies that characterized resistance patterns to third-generation EGFR inhibitors did not capture recurrent EGFR<sup>G724S</sup> mutations<sup>14,48</sup>. Although our limited sample size precludes broad conclusion on the real prevalence of this mutation it is conceivable that the size of the previous studies or a potential compound selection bias (osimertinib vs. rociletinib) may have underestimated the relevance of EGFR<sup>G724S</sup> mutations as a potential resistance mechanism. Our data indicate that EGFR<sup>G724S</sup> mutations seem to primarily affect the reversible first step of third-generation inhibitor binding within the ATP-binding pocket before irreversible attachment to Cys797 can occur. We conclude that the observed fluctuation of the glycine-rich loop plays a role in this phenotype, similar to other systems where anti-correlations between flexibility and ligand-binding affinity have been observed<sup>49,50</sup>. However, although the kinetics of third-generation EGFR inhibitor binding are perturbed dramatically, second-generation EGFR inhibitors are potent enough to establish such a reversible binding despite the EGFR<sup>G724S</sup> mutation. Thus, their liability in terms of an efficient engagement of EGFR<sup>WT</sup>, in the context of EGFR<sup>G724S</sup> resistance mutations turns into an asset.

Given the increasing number of patients receiving osimertinib our data are of high clinical relevance. Importantly, our study provides a molecular basis for the ability of EGFR<sup>G724S</sup> to induce resistance and suggest that second-generation EGFR inhibitors might overcome osimertinib resistance in these patients.

## Methods

**Experimental design.** The aim of this study was to examine the effects of the acquired EGFR<sup>G724S</sup> mutation that was observed in lung tumors that become resistant to osimertinib treatment. We conducted systematic cellular, in vivo, biochemical, and structural analyses to determine the functional relevance of this mutation in the context of first-, second-, and third-generation EGFR inhibition. To investigate the EGFR<sup>G724S</sup> mutation in combination with the different EGFR inhibitors we used the mouse fibroblast cell line NIH-3T3 and female nude mice. All experiments including immunoblotting, tumor volume measurement, soft agar assays, and biochemical assays were performed at least three times. For the biochemical analysis, we used activity-based assay for IC<sub>50</sub>-determination and kinetic characterization. Each reaction was performed in duplicate, and at least three independent determinations of each IC<sub>50</sub> were made. To characterize the acquired EGFR<sup>G724S</sup> resistance mutation on a molecular level we used structural modeling of EGFR kinase and validated our observations using computational modeling of publicly available co-crystal structures. For detailed information please see "Methods". The local animal protection committee and the local authorities approved all animal procedures. All patients consented into the analyses according to the local practice.

**Patients, efficacy assessments, and sample collection.** The four patients included into this analysis were treated with the third-generation EGFR inhibitor osimertinib within the AURA trial (NCT01802632), the compassionate use program or clinical routine upon progression to EGFR-targeted therapy (P1–P4). One patient, P2, also received treatment with the third-generation EGFR inhibitor EGF816 within the CEGF816X2101 phase I trial (NCT02108964). All patients consented to treatment according to the good clinical practice guideline and were treated according to the trial protocol and/or local practice. Patients received osimertinib at a dose of 80 mg qd and were treated until progression. Treatment doses were adapted if necessary in case of toxicity and adverse events. Tumor assessment was performed by computed tomography (CT) or <sup>18</sup>F-DG PET and magnetic resonance imaging according to the specifications given in the trial protocols and/or according to local standards. Efficacy was assessed using the response evaluation criteria for solid tumors, version 1.1 in patients P1 and P3 (RECIST 1.1)<sup>51</sup>. In patients P2 and P4 RECIST evaluation was not feasible. Response to osimertinib treatment was performed by <sup>18</sup>F-DG PET-CT in P2. In P4 baseline CT scan was older than 4 weeks, not fulfilling the requirements set up by RECIST 1.1. In patients where RECIST evaluation was not possible, progression was defined by the treating physician as growth of clinically significant lesions. Biopsy collection was performed through core needle biopsy, excisional biopsy, or cytology according to local standard procedures at time points T0 to T3. Samples at time points T1, T2, and T3 were collected in progressing tumor lesions. All tumor samples were fixed in formalin (4%) and embedded in paraffin (FFPE). To assess the frequency of *EGFR*<sup>G724S</sup> in the setting of acquired resistance to third-generation EGFR inhibitors, we analyzed FFPE tissue of patients from the Network Genomic Medicine and collaborating institutions. *EGFR*-mutant NSCLC patients who fulfilled the following criteria were included into the analysis: (1) sufficient tumor tissue for genomic characterization, (2) progressive disease while on treatment with a third-generation EGFR inhibitor. All patients consented into the analyses according to the local practice.

**Targeted next-generation sequencing.** Tumor tissue of patients was genomically characterized by massively parallel sequencing (MPS) and fluorescence in situ hybridization (FISH), if feasible. Until March 2015, MPS was carried out with an Ion AmpliSeq Custom DNA Panel (Thermo Fisher Scientific, Waltham, MA, USA) (Lun3 panel) and a MiSeq benchtop sequencer (Illumina, San Diego, USA). As from March 2015 MPS was carried out with a GeneRead DNAseq Custom Panel V2 (Qiagen, Hilden, Germany) consisting of 205 amplicons (Lun4 panel). Library preparation was performed according to the GeneRead DNAseq Gene Panel Handbook (Qiagen) as described earlier<sup>52</sup>.

**Cell viability.** In all, 5000 Ba/F3 cells/well were seeded in triplicates in a white-bottom 96-well plate in 90  $\mu$ l media/well. Compounds were prepared by serial dilution. Dimethyl sulphoxide was added to control wells in the highest dilution used in the assay. The cells were treated for 72 h with the compounds following determination of ATP content as surrogate for viability by CellTiter-Glo<sup>®</sup> assay (CTG) (Promega). CTG was incubated for at least 20 min on the cells without light. Luminescence was assessed on an Infinite 200 Pro microplate reader (Tecan). Data were analyzed and plotted in PRISM.

**Cell culture.** NIH-3T3 cells were cultured in Dulbecco's Modified Eagle's medium (DMEM) with 10% fetal bovine serum (FBS) (Thermo Fisher Scientific) and 1% penicillin–streptomycin (Thermo Fisher Scientific). Ba/F3 cells were cultured in Roswell Park Memorial Institute with 20% FBS and 1% penicillin–streptomycin (Thermo Fisher Scientific). The cells were incubated at 37 °C and 5% CO<sub>2</sub> in a humidified incubator. Cell lines expressing recombinant EGFR variants were generated by retroviral transduction. In brief, cDNA sequences encoding *EGFR*<sup>E746-S752del</sup>, *EGFR*<sup>G724S</sup>, or *EGFR*<sup>E746-S752del+G724S</sup> were cloned into a pBabe-puro vector and co-transfected with pCL-Eco helper plasmid into HEK 293T cells using TransIT-LT1 reagent (Mirus). After 48 h of transfection, retroviral particles were collected for infection of NIH-3T3 cells and Ba/F3 cells. After 24 h of infection, medium was replenished with growth medium containing puromycin (3  $\mu$ g/ml) to select for transduced cell clones. Cells were treated with first-, second-, and third-generation EGFR inhibitors (erlotinib, osimertinib, rociletinib (Selleckchem), and afatinib (LC Laboratories)) with different concentrations. Ba/F3 cells were a kind gift from Nikolaus von Bubnoff. NIH-3T3 cells were purchased from the “Deutsche Sammlung von Mikroorganismen und Zellkulturen (DSMZ) and the HEK 293T were purchased from the American Type Culture Collection (ATCC)<sup>®</sup>. All cell lines were authenticated with the STR method and were tested negative for mycoplasma contamination by qPCR analyses from GATC Biotech services.

**Soft agar assays.** On a layer of 1% bottom agar (Sigma-Aldrich) 10000 NIH-3T3 cells per well of a 12-well plate were suspended in DMEM (Thermo Fisher Scientific) containing 0.6% agar, 10% calf serum (PAA Laboratories), 0.5% sodium bicarbonate (PAN Biotech) and 1% sodium pyruvate (Thermo Fisher Scientific). After 16 days incubation pictures were taken with a Zeiss Axiovert 40 CFL microscope at  $\times$ 100 magnification and colony size was assessed with ImageJ (<http://rsbweb.nih.gov/ij/>).

**Immunoblotting.** For immunoblot analysis, cells were harvested and lysed in cold lysis buffer in the presence of protease and phosphatase inhibitors (Cell Signaling). Equal amounts (20  $\mu$ g) of protein were separated on 4–20% Novex Tris-Glycine gels (Invitrogen), blotted on polyvinylidene difluoride membranes and incubated with specific primary antibodies and fluorescently labeled secondary antibodies (IRDye, LI-COR). Proteins were detected with the Odyssey CLx imaging system (LI-COR). Protein levels were quantified with ImageStudio (LI-COR) and normalized to loading control. The following primary antibodies were used: total EGFR (Cell Signaling #2232, dilution 1:1000), HSP90 (Cell Signaling #4877, dilution 1:1000), p-EGFR Tyr1068 (Invitrogen #36-9700, dilution 1:1000). Anti-rabbit IgG (Cell Signaling #5151, 1:10000) was used as secondary antibody. Uncropped raw blots corresponding to data in Figs. 2a, 2b, 4c, and 5d can be found in the Supplementary Information.

**Xenograft models.** The local animal protection committee and the local authorities approved all animal procedures. Osimertinib (Cayman Chemical) was dissolved in 0.5% (Hydroxypropyl-) methylcellulose (Sigma-Aldrich) to a final concentration of 20 mg/ml. Osimertinib was administered daily up to 12 days at a dose of 5 mg/kg and afatinib at a dose of 20 mg/kg by oral gavage. NIH-3T3 *EGFR*<sup>19del</sup> and NIH-3T3 *EGFR*<sup>19del+G724S</sup> cells were resuspended in serum-free DMEM medium with 1% penicillin–streptomycin (Thermo Fisher Scientific) (at a concentration of  $2 \times 10^6$  cells in 100  $\mu$ l) and injected subcutaneously in both flanks of 8–12 weeks old female nude mice (RJ:NMRI-FOXN1 NU, Janvier Labs). Upon formation of palpable subcutaneous tumors (200–300 mm<sup>3</sup> tumor volume), mice were treated with vehicle solution (Hydroxypropyl-) methylcellulose (0.5%) or with osimertinib. Tumor size was monitored every second day by measurement of perpendicular diameters by an external caliper and calculated by use of the modified ellipsoid formula:  $V = 0.5 \times (\text{length} \times \text{width}^2)$ . Mice were killed and subcutaneous tumors were resected and fixed in 4% formalin for 24 h and embedded in paraffin. The harvested tumor samples were stained against the apoptotic-marker Cleaved Caspase-3, and the proliferation marker Ki67. For a quantification purpose, each marker was quantified using ten high-power-field ( $\times$ 400) pictures and the median was calculated for the given marker.

**Immunohistochemical staining.** Tissue samples were incubated in 4% formalin overnight and subsequently embedded in paraffin. For tissue analysis, 3–5  $\mu$ m sections were cut, de-paraffinized, and antigen retrieval was performed using either citrate at pH 6.0, or ethylenediaminetetraacetic acid (EDTA) at pH 9.0 for 20 min. Washing steps were performed using phosphate-buffered saline. Primary antibodies were purchased from Cell Signaling (Cleaved Caspase-3, #Asp175, dilution 1:100) and Cell Marque (Ki67, #SP6, dilution 1:100). Corresponding secondary antibody detection kits were used from Histofine<sup>®</sup> Simple stain and stained on an automated stainer (LabVision Autostainer 480S; Thermo Fisher).

**Computational modeling.** The structure 4ZAU deposited in the PDB was used as basic template for modeling the noncovalently bound EGFR–osimertinib complex. Missing residues were obtained from PDB entries 5CZH<sup>53</sup> for residues 748–755 (LREATSPKA/LREATSPKA), 863–865 (GAE/GAE), 873–874 (GG/GG), 985–991 (ERMHLP/ERMHLP), 1003–1007 (DEEDM/DEEDM) and from 3PP0<sup>54</sup> for residues 748–755 (LREATSPKA/LRENTSPKA), 863–865 (GAE/GAE), 874 (G/G), 991–1001 (SPTDSNFYRAL/PLDSTFYRSL). Terminal regions 693–697 and 1018–1022 were truncated, the mutation G724S and the still missing residue 1002 were introduced by Modeller 9.14<sup>55</sup>. For MD simulations, the proteins and ligand were treated by the ff14SB force field<sup>56</sup> and the GAFF model<sup>57</sup>, respectively, within AMBER 14<sup>58</sup>. The resulting simulation system for the wild type consisted of 24,358 TIP3P water molecules, seven sodium cations<sup>59</sup>, 5158 protein atoms, and 72 ligand atoms. The G724S system was composed of 25,651 TIP3P molecules, 7 sodium cations, 5162 protein atoms, and 72 ligand atoms. For both, *EGFR*<sup>WT</sup> and *EGFR*<sup>G724S</sup> mutation, the same simulation protocol was used, starting with a geometry optimization down to a final RMS gradient of 0.0001 kcal mol<sup>-1</sup> Å<sup>-1</sup> followed by 4 ns heating to 298.15 K in the canonical ensemble (Langevin thermostat) while applying harmonic restraints on protein Ca atoms. The resulting system was then simulated over 4 ns in the isothermal–isobaric ensemble (Berendsen barostat) at 1 bar pressure, also under der action of restraints. Finally, restraints except for fixed hydrogen bond distances were removed and the systems were run over 200 ns with a 2 fs time step using AMBER 16<sup>58</sup>. The stability of the simulations systems was checked by computing the structural root mean square deviations (RMSD) of Ca atoms from the respective initial snapshots of the production runs over time. (Supplementary Fig. 3C). The final 100 ns were used for clustering structures taken every 10 ps using the DBSCAN algorithm<sup>60</sup> in AMBER 16 with distance cutoffs 1.18 Å (*EGFR*<sup>WT</sup>) and 1.205 Å (*EGFR*<sup>G724S</sup>) and a minimum number of points to form a cluster set to 5. Final structures were obtained from centroids of the maximally populated clusters by geometry optimization in an implicit water environment (ALPB)<sup>61</sup>. RMSF fluctuations were computed over the final 100 ns and mapped onto the resulting structures (Supplementary Data 1–4) for further analysis. These structures were then modified by Modeller 9.14<sup>55</sup> to generate starting models for the simulation of *EGFR*<sup>19del</sup> and *EGFR*<sup>19del+G724S</sup> complexes by deleting residues 746 to 750 followed by system preparation steps as before, yielding 24271 water molecules, six sodium ions, 5075 protein- and 72

ligand atoms for *EGFR*<sup>19del</sup> and 26,866 water molecules, six sodium ions, 5079 protein- and 72 ligand atoms *EGFR*<sup>19del+G724S</sup>. Trajectories were generated and analyzed as before, using the last 75 ns (see RMSD plot Supplementary Fig. 3A) for clustering (DBSCAN cutoffs of 1.16 Å for *EGFR*<sup>19del</sup> and *EGFR*<sup>19del+G724S</sup>) and RMSF calculations. The simulations of the pure deletion and the double-mutant complexes were performed in order to check the independence of the system stability and fluctuation analysis of the initial conditions.

**Activity-based assay and kinetic characterization.** For biochemical assays *EGFR*<sup>WT</sup>, *EGFR*<sup>L858R</sup>, and *EGFR*<sup>L858R+T790M</sup> were purchased from Carna Bioscience (lot13CBS-0005K for *EGFR*<sup>WT</sup>; Carna, lot13CBS-0537B for *EGFR*<sup>L858R</sup>; and Carna, lot12CBS-0765B for *EGFR*<sup>L858R+T790M</sup>). However, *EGFR*<sup>19del</sup> and *EGFR*<sup>19del+G724S</sup> were expressed and purified as follows. First DNA-encoding residues comprising the juxtamembrane segment, the kinase domain and the C-terminal tail of human EGFR (UniProt entry P00533, residues 695–1210) were synthesized (GeneArt, Life Technologies). The construct was cloned into pLEX/Bac3 expression vector (MerkMillipore), using BamHI and Bsu36I restriction sites. Mutations were introduced by site-directed mutagenesis (QuikChange, Stratagene/Agilent Technologies). Transfection, virus generation, and amplification were carried out in *Spodoptera frugiperda* cell line S $\beta$  following the BacMAGIC protocol.

After three days of expression (27 °C, 110 rpm) the cells were harvested (3000 × g, 20 min), resuspended in buffer A (50 mM Tris, 500 mM NaCl, 10% glycerol, 1 mM dithiothreitol, pH 8) and homogenized by french press. The lysate was cleared by centrifugation at 40,000 × g for 1 h at 4 °C and loaded on a prepacked column (Glutathione HiCap from Qiagen). The elution was done with a gradient of buffer B (buffer A + 10 mM glutathione). For the final purification step the fractions containing the target protein were combined, concentrated and applied to a HiLoad 16/600 superdex 75 pg column (GE Healthcare) in buffer C (25 mM TRIS, 250 mM NaCl, 10% glycerol, pH 8). The purified protein was concentrated to 5 mg/mL and stored at –80 °C until further use. Protein identity was confirmed by ESI-MS analysis. IC<sub>50</sub>-determinations for EGFR and its mutants were performed with the HTRF KinEASE-TK assay from Cisbio according to the manufacturer's instructions. Briefly, the amount of EGFR in each reaction well was set to 0.60 ng of *EGFR*<sup>WT</sup> (0.67 nM), 0.10 ng of *EGFR*<sup>L858R</sup> (0.11 nM), 0.07 ng of *EGFR*<sup>L858R+T790M</sup> (0.08 nM), 1 ng of *EGFR*<sup>19del</sup> (1.1 nM) and 0.10 ng of *EGFR*<sup>19del+G724S</sup> (0.11 nM). An artificial substrate peptide (TK-substrate from Cisbio) was phosphorylated by EGFR. After completion of the reaction (reaction times: 25 min for WT, 15 min for *EGFR*<sup>L858R</sup>, 20 min for *EGFR*<sup>L858R+T790M</sup>, 15 min for *EGFR*<sup>19del</sup> and 25 min for *EGFR*<sup>19del+G724S</sup>), the reaction was stopped by addition of buffer containing EDTA as well as an antiphosphotyrosine antibody labeled with europium cryptate and streptavidin labeled with the fluorophore XL665. FRET between europium cryptate and XL665 was measured after an additional hour of incubation to quantify the phosphorylation of the substrate peptide. An EnVision multimode plate reader (PerkinElmer) was used to measure the fluorescence of the samples at 620 nm (Eu-labeled antibody) and 665 nm (XL665 labeled streptavidin) 50 μs after excitation at 320 nm. The quotient of both intensities for reactions made with eight different inhibitor concentrations was then analyzed using the Quattro Software Suite for IC<sub>50</sub>-determination. Each reaction was performed in duplicate, and at least three independent determinations of each IC<sub>50</sub> were made. For kinetic characterization ( $k_{inact}/K_i$ ), the inhibitors were incubated with *EGFR*-mutants over different periods of time (2–90 min), whereas durations of enzymatic and stop reactions were kept constant as stated above. A sixfold dilution series (eight data points per IC<sub>50</sub> curve) starting at 20 μM final compound concentrations was applied. Calculated IC<sub>50</sub>-values were plotted versus incubation time, and data were fit as described in the literature to determine  $k_{inact}$  and  $K_i$ <sup>37</sup>. MAb PT66-Eu cryptate (61T66KLB) stock solution was prepared according to manufactures instructions and diluted 1:1 with detection buffer for activity-based assay.

**MET and HER2 FISH analyses.** FISH was performed for determination of *MET* gene copy number using ZytoLight SPEC MET/CEN7 Dual Color Probe (ZytoVision). High-level amplification was defined in tumors with (a) *MET*/*CEN7* ratio ≥ 2.0 or (b) an average *MET* gene copy number per cell of ≥ 6.0, or (c) ≥ 10% of tumor cells containing ≥ 15 *MET* signals. Intermediate level of gene copy number gain being defined as (a) ≥ 50% of cells containing ≥ 5 *MET* signals and (b) criteria for high-level amplification are not fulfilled. Low level of gene copy number gain was defined as (a) ≥ 40% of tumor cells showing ≥ 4 *MET* signals and (b) criteria for high-level amplification or intermediate level of gene copy number gain are not fulfilled. All other tumors were classified as negative. For determination of *HER2* (*ERBB2*) status FISH was performed using a ZytoLight SPEC *ERBB2*/*CEN17* Dual Color Probe (ZytoVision). Amplification status was classified in analogy to the recommendations of the American Society of Oncology for *HER2* testing in breast cancer. Amplification of *HER2* was positive if (a) *ERBB2*/*CEN17* ratio ≥ 2.0 or (b) *HER2* GCN ≥ 6.0.

**Statistical analysis.** Statistical analysis was performed using GraphPad Prism 5 (GraphPad Software Inc). Data obtained from mice tumor analysis and in vitro assays were subjected to unpaired Student's *t* test. Data are plotted as means ±

standard error of the mean. Quantification of high-power-field analysis was calculated by Mann–Whitney *U* test.

## Data availability

The datasets generated during and/or analyzed during the current study are available from the corresponding author on reasonable request.

Received: 14 March 2018 Accepted: 12 September 2018

Published online: 07 November 2018

## References

- Lynch, T. J. et al. Activating mutations in the epidermal growth factor receptor underlying responsiveness of non-small-cell lung cancer to gefitinib. *N. Engl. J. Med.* **350**, 2129–2139 (2004).
- Paez, J. G. et al. EGFR mutations in lung cancer: correlation with clinical response to gefitinib therapy. *Science* **304**, 1497–1500 (2004).
- Pao, W. et al. EGF receptor gene mutations are common in lung cancers from “never smokers” and are associated with sensitivity of tumors to gefitinib and erlotinib. *Proc. Natl Acad. Sci. USA* **101**, 13306–13311 (2004).
- Clinical Lung Cancer Genome Project (CLCGP); Network Genomic Medicine (NGM). A genomics-based classification of human lung tumors. *Sci. Transl. Med.* **5**, 209ra153 (2013).
- Maemondo, M. et al. Gefitinib or chemotherapy for non-small-cell lung cancer with mutated EGFR. *N. Engl. J. Med.* **362**, 2380–2388 (2010).
- Rosell, R. et al. Screening for epidermal growth factor receptor mutations in lung cancer. *N. Engl. J. Med.* **361**, 958–967 (2009).
- Azam, M., Seeliger, M. A., Gray, N. S., Kuriyan, J. & Daley, G. Q. Activation of tyrosine kinases by mutation of the gatekeeper threonine. *Nat. Struct. Mol. Biol.* **15**, 1109–1118 (2008).
- Bean, J. et al. MET amplification occurs with or without T790M mutations in EGFR mutant lung tumors with acquired resistance to gefitinib or erlotinib. *Proc. Natl Acad. Sci. USA* **104**, 20932–20937 (2007).
- Yun, C. H. et al. The T790M mutation in EGFR kinase causes drug resistance by increasing the affinity for ATP. *Proc. Natl Acad. Sci. USA* **105**, 2070–2075 (2008).
- Cross, D. A. et al. AZD9291, an irreversible EGFR TKI, overcomes T790M-mediated resistance to EGFR inhibitors in lung cancer. *Cancer Discov.* **4**, 1046–1061 (2014).
- Janne, P. A. et al. AZD9291 in EGFR inhibitor-resistant non-small-cell lung cancer. *N. Engl. J. Med.* **372**, 1689–1699 (2015).
- Mok, T. S. et al. Osimertinib or platinum-pemetrexed in EGFR T790M-positive lung cancer. *N. Engl. J. Med.* **376**, 629–640 (2017).
- Soria, J. C. et al. Osimertinib in untreated EGFR-mutated advanced non-small-cell lung cancer. *N. Engl. J. Med.* **378**, 113–125 (2018).
- Chabon, J. J. et al. Circulating tumour DNA profiling reveals heterogeneity of EGFR inhibitor resistance mechanisms in lung cancer patients. *Nat. Commun.* **7**, 11815 (2016).
- Ortiz-Cuaran, S. et al. Heterogeneous mechanisms of primary and acquired resistance to third-generation EGFR inhibitors. *Clin. Cancer Res.* **22**, 4837–4847 (2016).
- Thress, K. S. et al. Acquired EGFR C797S mutation mediates resistance to AZD9291 in non-small cell lung cancer harboring EGFR T790M. *Nat. Med.* **21**, 560–562 (2015).
- Eberlein, C. A. et al. Acquired resistance to the mutant-selective EGFR inhibitor AZD9291 is associated with increased dependence on RAS signaling in preclinical models. *Cancer Res.* **75**, 2489–2500 (2015).
- Konig, K. et al. Implementation of amplicon parallel sequencing leads to improvement of diagnosis and therapy of lung cancer patients. *J. Thorac. Oncol.* **10**, 1049–1057 (2015).
- Cho, J. et al. Colon cancer-derived oncogenic EGFR G724S mutant identified by whole genome sequence analysis is dependent on asymmetric dimerization and sensitive to cetuximab. *Mol. Cancer* **13**, 141 (2014).
- Oztan, A. et al. Emergence of EGFR G724S mutation in EGFR-mutant lung adenocarcinoma post progression on osimertinib. *Lung Cancer* **111**, 84–87 (2017).
- Peled, N. et al. Subclonal therapy by EGFR TKIs guided by sequential plasma cell-free DNA in EGFR-mutated lung cancer. *J. Thorac. Oncol.* **12**, e81–e84 (2017).
- Sos, M. L. et al. Chemogenomic profiling provides insights into the limited activity of irreversible EGFR inhibitors in tumor cells expressing the T790M EGFR resistance mutation. *Cancer Res.* **70**, 868–874 (2010).
- Palacios, R. & Steinmetz, M. Il-3-dependent mouse clones that express B-220 surface antigen, contain Ig genes in germ-line configuration, and generate B lymphocytes in vivo. *Cell* **41**, 727–734 (1985).

24. Malchers, F. et al. Cell-autonomous and non-cell-autonomous mechanisms of transformation by amplified FGFR1 in lung cancer. *Cancer Discov.* **4**, 246–257 (2014).
25. Braunreiter, C. L., Hancock, J. D., Coffin, C. M., Boucher, K. M. & Lessnick, S. L. Expression of EWS-ETS fusions in NIH3T3 cells reveals significant differences to Ewing's sarcoma. *Cell Cycle* **5**, 2753–2759 (2006).
26. Hemmer, W., McGlone, M., Tsigelny, I. & Taylor, S. S. Role of the glycine triad in the ATP-binding site of cAMP-dependent protein kinase. *J. Biol. Chem.* **272**, 16946–16954 (1997).
27. Simard, J. R. et al. Fluorophore labeling of the glycine-rich loop as a method of identifying inhibitors that bind to active and inactive kinase conformations. *J. Am. Chem. Soc.* **132**, 4152–4160 (2010).
28. Shah, N. P. et al. Multiple BCR-ABL kinase domain mutations confer polyclonal resistance to the tyrosine kinase inhibitor imatinib (STI571) in chronic phase and blast crisis chronic myeloid leukemia. *Cancer Cell* **2**, 117–125 (2002).
29. Cowan-Jacob, S. W. et al. Structural biology contributions to the discovery of drugs to treat chronic myelogenous leukaemia. *Acta Crystallogr. D. Biol. Crystallogr.* **63**, 80–93 (2007).
30. Niessen, S. et al. Proteome-wide map of targets of T790M-EGFR-directed covalent inhibitors. *Cell Chem. Biol.* **24**, 1388–1400 e1387 (2017).
31. Yasuda, H. et al. Structural, biochemical, and clinical characterization of epidermal growth factor receptor (EGFR) exon 20 insertion mutations in lung cancer. *Sci. Transl. Med.* **5**, 216ra177 (2013).
32. Robichaux, J. P. et al. Mechanisms and clinical activity of an EGFR and HER2 exon 20-selective kinase inhibitor in non-small cell lung cancer. *Nat. Med.* **24**, 638–646 (2018).
33. Yosaatmadja, Y. et al. Binding mode of the breakthrough inhibitor AZD9291 to epidermal growth factor receptor revealed. *J. Struct. Biol.* **192**, 539–544 (2015).
34. Shan, Y. et al. Oncogenic mutations counteract intrinsic disorder in the EGFR kinase and promote receptor dimerization. *Cell* **149**, 860–870 (2012).
35. Tomassi, S. et al. Indazole-based covalent inhibitors to target drug-resistant epidermal growth factor receptor. *J. Med. Chem.* **60**, 2361–2372 (2017).
36. Singh, J., Petter, R. C., Baillie, T. A. & Whitty, A. The resurgence of covalent drugs. *Nat. Rev. Drug. Discov.* **10**, 307–317 (2011).
37. Krippendorff, B. F., Neuhaus, R., Lienau, P., Reichel, A. & Huisinga, W. Mechanism-based inhibition: deriving K(I) and k(inact) directly from time-dependent IC(50) values. *J. Biomol. Screen.* **14**, 913–923 (2009).
38. Arteaga, C. L. & Engelman, J. A. ERBB receptors: from oncogene discovery to basic science to mechanism-based cancer therapeutics. *Cancer Cell* **25**, 282–303 (2014).
39. Engel, J. et al. Insight into the inhibition of drug-resistant mutants of the receptor tyrosine kinase EGFR. *Angew. Chem. Int. Ed. Engl.* **55**, 10909–10912 (2016).
40. Heuckmann, J. M., Rauh, D. & Thomas, R. K. Epidermal growth factor receptor (EGFR) signaling and covalent EGFR inhibition in lung cancer. *J. Clin. Oncol.* **30**, 3417–3420 (2012).
41. Katakami, N. et al. LUX-Lung 4: a phase II trial of afatinib in patients with advanced non-small-cell lung cancer who progressed during prior treatment with erlotinib, gefitinib, or both. *J. Clin. Oncol.* **31**, 3335–3341 (2013).
42. Yu, H. A. et al. Phase 2 study of intermittent pulse dacomitinib in patients with advanced non-small cell lung cancers. *Lung Cancer* **112**, 195–199 (2017).
43. Park, K. et al. Afatinib versus gefitinib as first-line treatment of patients with EGFR mutation-positive non-small-cell lung cancer (LUX-Lung 7): a phase 2B, open-label, randomised controlled trial. *Lancet Oncol.* **17**, 577–589 (2016).
44. Kobayashi, Y. et al. Characterization of EGFR T790M, L792F, and C797S mutations as mechanisms of acquired resistance to afatinib in lung cancer. *Mol. Cancer Ther.* **16**, 357–364 (2017).
45. Blakely, C. M. et al. Evolution and clinical impact of co-occurring genetic alterations in advanced-stage EGFR-mutant lung cancers. *Nat. Genet.* **49**, 1693–1704 (2017).
46. Ichihara, E. et al. SFK/FAK signaling attenuates osimertinib efficacy in both drug-sensitive and drug-resistant models of EGFR-mutant lung cancer. *Cancer Res.* **77**, 2990–3000 (2017).
47. Shien, K. et al. JAK1/STAT3 activation through a proinflammatory cytokine pathway leads to resistance to molecularly targeted therapy in non-small cell lung cancer. *Mol. Cancer Ther.* **16**, 2234–2245 (2017).
48. Ramalingam, S. S. et al. Osimertinib as first-line treatment of EGFR mutation-positive advanced non-small-cell lung cancer. *J. Clin. Oncol.* **36**, 841–849 (2017).
49. Barouch-Bentov, R. et al. A conserved salt bridge in the G loop of multiple protein kinases is important for catalysis and for in vivo Lyn function. *Mol. Cell* **33**, 43–52 (2009).
50. Kannan, S. et al. Hydration effects on the efficacy of the epidermal growth factor receptor kinase inhibitor afatinib. *Sci. Rep.* **7**, 1540 (2017).
51. Eisenhauer, E. A. et al. New response evaluation criteria in solid tumours: revised RECIST guideline (version 1.1). *Eur. J. Cancer* **45**, 228–247 (2009).
52. Gultekin, S. E. et al. The landscape of genetic alterations in ameloblastomas relates to clinical features. *Virchows Arch.* **472**, 807–814 (2018).
53. Begley, M. J. et al. EGF-receptor specificity for phosphotyrosine-primed substrates provides signal integration with Src. *Nat. Struct. Mol. Biol.* **22**, 983–990 (2015).
54. Aertgeerts, K. et al. Structural analysis of the mechanism of inhibition and allosteric activation of the kinase domain of HER2 protein. *J. Biol. Chem.* **286**, 18756–18765 (2011).
55. Sali, A. & Blundell, T. L. Comparative protein modelling by satisfaction of spatial restraints. *J. Mol. Biol.* **234**, 779–815 (1993).
56. Maier, J. A. et al. ff14SB: improving the accuracy of protein side chain and backbone parameters from ff99SB. *J. Chem. Theory Comput.* **11**, 3696–3713 (2015).
57. Wang, J., Wolf, R. M., Caldwell, J. W., Kollman, P. A. & Case, D. A. Development and testing of a general amber force field. *J. Comput. Chem.* **25**, 1157–1174 (2004).
58. D. A. Case et al. AMBER 14/16. University of California, San Francisco (2014/2016).
59. Joung, I. S. & Cheatham, T. E. 3rd Determination of alkali and halide monovalent ion parameters for use in explicitly solvated biomolecular simulations. *J. Phys. Chem. B* **112**, 9020–9041 (2008).
60. Ester, M. K., H. Sander, J. & Xu, X. A density-based algorithm for discovering clusters in large spatial databases with noise. In *Proc. Second International Conference on Knowledge Discovery and Data Mining (KDD-96)*. 226–231 (AAAI Press, Portland, Oregon, 1996).
61. Sigalov, G., Fenley, A. & Onufriev, A. Analytical electrostatics for biomolecules: beyond the generalized Born approximation. *J. Chem. Phys.* **124**, 124902 (2006).

## Acknowledgements

We thank Alexandra Florin and Theresa Buhl for excellent technical support and members of the Sos lab for discussions. This work was supported by the Deutsche Forschungsgemeinschaft (KFO-286/FP2, RE 2246/2-1, RE 2246/7-1 to H.C.R., Cluster of Excellence RESOLV, EXC 1069, to S.M.K.), the Bundesministerium für Bildung und Forschung (e:Med 01ZX1303A to H.C.R., J.W., and R.B and 01ZX1406 to M.L.S.), the German federal state North Rhine Westphalia (NRW) as part of the EFRE initiative (grant LS-1-1-030a to H.C.R., R.B., J.W., S.M.-B., D.R., and M.L.S.), the Else Kröner-Fresenius Stiftung (EKFS-2014-A06 and 2016\_Kolleg.19, H.C.R., S.K.), the Deutsche Krebshilfe (111724, H.C.R.). Additional funding was provided by the Deutsche Krebshilfe as part of the Oncology Centers of Excellence funding program (to R.B., J.W., and G.H.). This work was also co-funded by the German Federal Ministry for Education and Research (NGFNPlus and e:Med) (Grant No. BMBF 01GS08104, 01ZX1303C), the Deutsche Forschungsgemeinschaft (DFG), the German federal state North Rhine-Westphalia (NRW) and the European Union (European Regional Development Fund: Investing In Your Future) (EFRE-800400), NEGECA (PerMed NRW), and EMODI (all for D.R.). Computer simulations were supported by the ITMC of TU Dortmund.

## Author contributions

Conception and design: J.F., F.M., M.K., S.M., M.A.D., S.M.-B., S.M.K., J.W., D.R., R.B., M.S.; acquisition of data (provided animals, cell culture experiments, acquired, and managed patients, etc.): J.F., F.M., M.K., S.M., M.A.D., A.S., J.L., C.H., H.L.T., Y.A., S.K., I.D., R.N.F., M.S., M.A.I., V.P., S.K., A.H.S., S.W., A.K., K.F., K.G., T.P., M.P., S.H., B.S., E.R., W.E.-R., E.F., E.F.S., S.M.-B., H.C.R.; biochemical profiling: M.K., J.L., D.R.; computational modeling: S.M.K., Y.A.; analysis and interpretation of data (e.g., statistical analysis, biostatistics, computational analysis): J.F., F.M., M.K., S.M., M.A.D., S.M.-B., S.M.K., J.W., D.R., R.B., M.L.S., D.P., A.H., J.B.; writing, review, and/or revision of the manuscript: J.F., F.M., M.K., S.M., M.A.D., D.P., A.H., J.L., M.S., M.A.I., S.K., R.N.F., S.M.K., M.L.S.

## Additional information

**Supplementary Information** accompanies this paper at <https://doi.org/10.1038/s41467-018-07078-0>.

**Competing interests:** J.F. and C.H. received speaking honoraria from AstraZeneca; R.N. F. received speaking honoraria from Bristol-Myers Squibb, MSD, Roche, Boehringer Ingelheim, consulting fees from Bristol-Myers Squibb, Roche and funding for scientific research from Bristol-Myers Squibb, MSD; M.S. received lecturer fees from AstraZeneca, lecturer, and consulting fees from Boehringer Ingelheim and consulting fees from Novartis; V.P. has received congress fees, travel fees, and accommodation from Novartis, Boehringer Ingelheim, Gilead, BMS; A.H.S. has participated in advisory boards for Bristol-Myers Squibb, Roche Pharma, and Merck Sharp & Dohme within the past 12 months; H.C.R. received consulting and lecture fees from Abbvie, Astra-Zeneca, Vertex and Merck, and received research funding from Gilead Pharmaceuticals; E.R. has received speaking honoraria from Celgene and received consulting fees from Novartis and BMS; E.F. has previously acted in a consulting or advisory role or speaker's bureau for: AstraZeneca, Boehringer Ingelheim, Bristol-Myers Squibb, Celgene, Eli Lilly, Guardanthealth, Merck Sharp & Dohme, Novartis, Pfizer, Roche, and Takeda; S.M.-B.

received speaking honoraria from AstraZeneca; J.W. received consulting and lecture fees from Abbvie, AstraZeneca, BMS, Boehringer Ingelheim, Chugai, Ignyta, Lilly, MSD, Novartis, Pfizer, Roche, and funding for scientific research from BMS, Johnson&Johnson, MSD, Novartis, Pfizer; D.R. received consultant and lecture fees from Astra-Zeneca, Merck-Serono, Takeda, Pfizer, Novartis, Boehringer Ingelheim, and Sanofi-Aventis; R.B. is an employee of Targos Molecular Pathology; M.L.S. received a commercial research grant from Novartis. The remaining authors declare no competing interests.

**Reprints and permission** information is available online at <http://npg.nature.com/reprintsandpermissions/>

**Publisher's note:** Springer Nature remains neutral with regard to jurisdictional claims in published maps and institutional affiliations.



**Open Access** This article is licensed under a Creative Commons Attribution 4.0 International License, which permits use, sharing, adaptation, distribution and reproduction in any medium or format, as long as you give appropriate credit to the original author(s) and the source, provide a link to the Creative Commons license, and indicate if changes were made. The images or other third party material in this article are included in the article's Creative Commons license, unless indicated otherwise in a credit line to the material. If material is not included in the article's Creative Commons license and your intended use is not permitted by statutory regulation or exceeds the permitted use, you will need to obtain permission directly from the copyright holder. To view a copy of this license, visit <http://creativecommons.org/licenses/by/4.0/>.

© The Author(s) 2018

Jana Fassunke<sup>1</sup>, Fabienne Müller<sup>2,3</sup>, Marina Keul<sup>4</sup>, Sebastian Michels<sup>5</sup>, Marcel A. Dammert<sup>2,3</sup>, Anna Schmitt<sup>6,7,8</sup>, Dennis Plenker<sup>2,3</sup>, Jonas Lategahn<sup>4</sup>, Carina Heydt<sup>1</sup>, Johannes Brägelmann<sup>2,3</sup>, Hannah L. Tumbrink<sup>2,3</sup>, Yannic Alber<sup>4</sup>, Sebastian Klein<sup>1,2,3,9</sup>, Alena Heimsoeth<sup>2,3</sup>, Ilona Dahmen<sup>3</sup>, Rieke N. Fischer<sup>5</sup>, Matthias Scheffler<sup>5</sup>, Michaela A. Ihle<sup>1</sup>, Vanessa Priesner<sup>5</sup>, Andreas H. Scheel<sup>1</sup>, Svenja Wagener<sup>1</sup>, Anna Kron<sup>5</sup>, Konrad Frank<sup>10</sup>, Katia Garbert<sup>2,3</sup>, Thorsten Persigehl<sup>11</sup>, Michael Püsken<sup>11</sup>, Stefan Haneder<sup>11</sup>, Bernhard Schaaf<sup>12</sup>, Ernst Rodermann<sup>13</sup>, Walburga Engel-Riedel<sup>14</sup>, Enriqueta Felip<sup>15</sup>, Egbert F. Smit<sup>16</sup>, Sabine Merkelbach-Bruse<sup>1</sup>, H. Christian Reinhardt<sup>6,7,8</sup>, Stefan M. Kast<sup>4</sup>, Jürgen Wolf<sup>5</sup>, Daniel Rauh<sup>4</sup>, Reinhard Büttner<sup>1,3,5</sup> & Martin L. Sos<sup>2,3,6</sup>

<sup>1</sup>Institute of Pathology, University Hospital of Cologne, Kerpener Str. 62, 50937 Cologne, Germany. <sup>2</sup>Molecular Pathology, Institute of Pathology, University Hospital of Cologne, Kerpener Str. 62, 50937 Cologne, Germany. <sup>3</sup>Department of Translational Genomics, Center of Integrated Oncology Cologne-Bonn, Medical Faculty, University of Cologne, Weyertal 115b, 50931 Cologne, Germany. <sup>4</sup>Faculty of Chemistry and Chemical Biology, TU Dortmund University, Otto-Hahn-Str. 4a, 44227 Dortmund, Germany. <sup>5</sup>Lung Cancer Group Cologne and Network Genomic Medicine (Lung Cancer), Department I of Internal Medicine, Center for Integrated Oncology Cologne-Bonn, University Hospital Cologne, Kerpener Str. 62, 50931 Cologne, Germany. <sup>6</sup>Center for Molecular Medicine Cologne, University of Cologne, Robert-Koch-Str. 21, 50931 Cologne, Germany. <sup>7</sup>Department I of Internal Medicine, University Hospital of Cologne, Weyertal 115b, 50931 Cologne, Germany. <sup>8</sup>Cologne Excellence Cluster on Cellular Stress Response in Aging-Associated Diseases, University of Cologne, Joseph Stelzmann Str. 26, 50931 Cologne, Germany. <sup>9</sup>Else Kröner Forschungskolleg Clonal Evolution in Cancer, University Hospital Cologne, Weyertal 115b, 50931 Cologne, Germany. <sup>10</sup>Section Pneumology, Clinic III of Internal Medicine, University Hospital of Cologne, Kerpener Str. 62, 50937 Cologne, Germany. <sup>11</sup>Institute of Diagnostic and Interventional Radiology, University Hospital of Cologne, Kerpener Str. 62, 50937 Cologne, Germany. <sup>12</sup>Hospital Dortmund gGmbH, Muensterstrasse 240, 44145 Dortmund, Germany. <sup>13</sup>Onkologie Rhein-Sieg, Schloßstraße 18, 53840 Troisdorf, Germany. <sup>14</sup>Department of Pneumology, Lung Hospital Cologne Merheim, City of Cologne Municipal Hospitals, Cologne, Germany. <sup>15</sup>Oncology Department, Vall d'Hebron University Hospital, Barcelona, Spain. <sup>16</sup>Thoracic Oncology Service, Netherlands Cancer Institute, Plesmanlaan 121, 1066 CX Amsterdam, The Netherlands. These authors contributed equally: Jana Fassunke, Fabienne Müller, Marina Keul, Sebastian Michels, Marcel A. Dammert, Anna Schmitt.

## **Drugging the catalytically inactive state of RET kinase in RET-rearranged tumors**

Plenker D, Riedel M, Brägelmann J, **Dammert MA**, Chauhan R, Knowles PP, Lorenz C, Keul M, Bührmann M, Pagel O, Tischler V, Scheel AH, Schütte D, Song Y, Stark J, Mrugalla F, Alber Y, Richters A, Engel J, Leenders F, Heuckmann JM, Wolf J, Dieblod J, Pal G, Peifer M, Aerts M, Gevaert K, Zahedi RP, Buettner R, Shokat KM, McDonald NQ, Kast SM, Gautschi O, Thomas RK, Sos ML.

Specific contributions:

- Viability screening of *RET*-rearranged cell lines against RET inhibitors AD80, vandetanib and cabozantinib as well as other TKIs
- Western blot analysis of *RET*-rearranged cell lines against RET inhibitors AD80, vandetanib and cabozantinib
- Viability screening of multiple lung adenocarcinoma cell lines against RET inhibitors AD80, vandetanib, cabozantinib as well as other TKIs
- Manuscript writing and editing

## CANCER

## Drugging the catalytically inactive state of RET kinase in RET-rearranged tumors

Dennis Plenker,<sup>1,2\*</sup> Maximilian Riedel,<sup>1,2\*</sup> Johannes Brägelmann,<sup>1,2</sup> Marcel A. Dammert,<sup>1,2</sup> Rakhee Chauhan,<sup>3</sup> Phillip P. Knowles,<sup>3</sup> Carina Lorenz,<sup>1,2</sup> Marina Keul,<sup>4</sup> Mike Bührmann,<sup>4</sup> Oliver Pagel,<sup>5</sup> Verena Tischler,<sup>2</sup> Andreas H. Scheel,<sup>6</sup> Daniel Schütte,<sup>2</sup> Yanrui Song,<sup>7</sup> Justina Stark,<sup>4</sup> Florian Mrugalla,<sup>4</sup> Yannic Alber,<sup>4</sup> André Richters,<sup>4</sup> Julian Engel,<sup>4</sup> Frauke Leenders,<sup>8</sup> Johannes M. Heuckmann,<sup>8</sup> Jürgen Wolf,<sup>9</sup> Joachim Diebold,<sup>10</sup> Georg Pall,<sup>11</sup> Martin Peifer,<sup>2</sup> Maarten Aerts,<sup>12,13</sup> Kris Gevaert,<sup>12,13</sup> René P. Zahedi,<sup>5</sup> Reinhard Buettner,<sup>6</sup> Kevan M. Shokat,<sup>14</sup> Neil Q. McDonald,<sup>3,15</sup> Stefan M. Kast,<sup>4</sup> Oliver Gautschi,<sup>10†</sup> Roman K. Thomas,<sup>2,9,16†</sup> Martin L. Sos<sup>1,2†‡</sup>

Oncogenic fusion events have been identified in a broad range of tumors. Among them, *RET* rearrangements represent distinct and potentially druggable targets that are recurrently found in lung adenocarcinomas. We provide further evidence that current anti-RET drugs may not be potent enough to induce durable responses in such tumors. We report that potent inhibitors, such as AD80 or ponatinib, that stably bind in the DFG-out conformation of RET may overcome these limitations and selectively kill *RET*-rearranged tumors. Using chemical genomics in conjunction with phosphoproteomic analyses in *RET*-rearranged cells, we identify the CCDC6-RET<sup>T788N</sup> mutation and drug-induced mitogen-activated protein kinase pathway reactivation as possible mechanisms by which tumors may escape the activity of RET inhibitors. Our data provide mechanistic insight into the druggability of RET kinase fusions that may be of help for the development of effective therapies targeting such tumors.

## INTRODUCTION

Targeted inhibition of oncogenic driver mutations with small molecules is a cornerstone of precision cancer medicine. *RET* rearrangements have been identified in a broad range of tumors, including 1 to 2% of lung adenocarcinomas, and their discovery sparked the hope for an effective treatment option in these patients (1–3). However, when compared to other oncogenic “driver” alterations, such as rearranged anaplastic lymphoma kinase (ALK), rearranged *RET* seems to be a difficult target, and to date, no drug has been successfully established for the treatment of these tumors (4–6). Recent clinical data suggest that overall response rates in patients treated with currently available *RET*-targeted drugs are rather limited and range between 18 and 53% (7–10). Improved selection of patients based on deep sequencing of individual tumors may

help increase these response rates, but still progression-free survival seems to be very limited (7, 8, 10, 11). These observations are particularly surprising from a chemical point of view because a broad spectrum of kinase inhibitors is known to bind to RET and to inhibit its kinase activity in vitro (6, 12). On the basis of these observations, we sought to characterize rearranged RET in independent cancer models to identify potent RET inhibitors with high selectivity and optimal biochemical profile to target *RET*-rearranged tumors.

## RESULTS

Kinase inhibitor AD80 shows extraordinary activity in *RET*-rearranged cancer models

Because clinical experience with *RET*-targeted drugs in lung cancer patients is rather disappointing, we sought to test a series of clinically and preclinically available drugs with anti-RET activity in Ba/F3 cells engineered to express either *KIF5B-RET* or *CCDC6-RET* (1, 2, 12, 13). In these experiments, AD80 and ponatinib exhibited 100- to 1000-fold higher cytotoxicity compared to all other tested drugs in *RET*-dependent, but not interleukin-3-supplemented, Ba/F3 cells (Fig. 1A and fig. S1, A and B). In line with these results, AD80, but not cabozantinib or vandetanib, prevented the phosphorylation of RET as well as of extracellular signal-regulated kinase (ERK), AKT, and S6K at low nanomolar concentrations in kinesin family member 5B (*KIF5B*)-*RET*-expressing Ba/F3 cells (Fig. 1B and table S1). These data are in line with our own retrospective analysis where out of four patients with *RET*-rearranged tumors, we observed only one partial response in a patient receiving vandetanib (P2) as first-line treatment (fig. S1, C to E, and table S2, A and B) (9). Sequencing of rebiopsy samples did not reveal candidate drug resistance mutations, suggesting that the target had been insufficiently inhibited (table S2C).

To validate the efficacy of AD80 and ponatinib in an alternative model, we induced *KIF5B-RET* rearrangements (*KIF5B* exon 15; *RET* exon 12) in NIH-3T3 cells using clustered regularly interspaced short

<sup>1</sup>Molecular Pathology, Institute of Pathology, Center of Integrated Oncology, University Hospital Cologne, 50937 Cologne, Germany. <sup>2</sup>Department of Translational Genomics, Center of Integrated Oncology Cologne-Bonn, Medical Faculty, University of Cologne, 50931 Cologne, Germany. <sup>3</sup>Structural Biology Laboratory, Francis Crick Institute, 44 Lincoln's Inn Fields, London WC2A 3LY, UK. <sup>4</sup>Faculty of Chemistry and Chemical Biology, TU Dortmund University, 44227 Dortmund, Germany. <sup>5</sup>Leibniz-Institut für Analytische Wissenschaften–ISAS–e.V., Dortmund, Germany. <sup>6</sup>Institute of Pathology, Center of Integrated Oncology, University Hospital Cologne, 50937 Cologne, Germany. <sup>7</sup>Crown BioScience, Inc., 3375 Scott Blvd, Suite 108, Santa Clara, CA 95054, USA. <sup>8</sup>NEO New Oncology GmbH, 51105 Cologne, Germany. <sup>9</sup>Department of Internal Medicine, Center for Integrated Oncology Köln Bonn, University Hospital Cologne, Cologne, 50931 Cologne, Germany. <sup>10</sup>Cancer Center, Lucerne Cantonal Hospital, 6000 Lucerne, Switzerland. <sup>11</sup>Department of Internal Medicine 5, University Hospital Innsbruck, Haematology/Oncology, Anichstraße 35, 6020 Innsbruck, Austria. <sup>12</sup>VIB-UGent Center for Medical Biotechnology, VIB, B-9000 Ghent, Belgium. <sup>13</sup>Department of Biochemistry, Ghent University, B-9000 Ghent, Belgium. <sup>14</sup>Department of Cellular and Molecular Pharmacology, Howard Hughes Medical Institute, University of California, San Francisco, San Francisco, CA 94158, USA. <sup>15</sup>Institute of Structural and Molecular Biology, Department of Biological Sciences, Birkbeck College, Malet Street, London WC1E 7HX, UK. <sup>16</sup>German Cancer Consortium (DKTK), partner site Heidelberg, and German Cancer Research Center (DKFZ), Heidelberg, Germany.

\*These authors contributed equally to this work.

†These authors contributed equally to this work.

‡Corresponding author. Email: martin.sos@uni-koeln.de

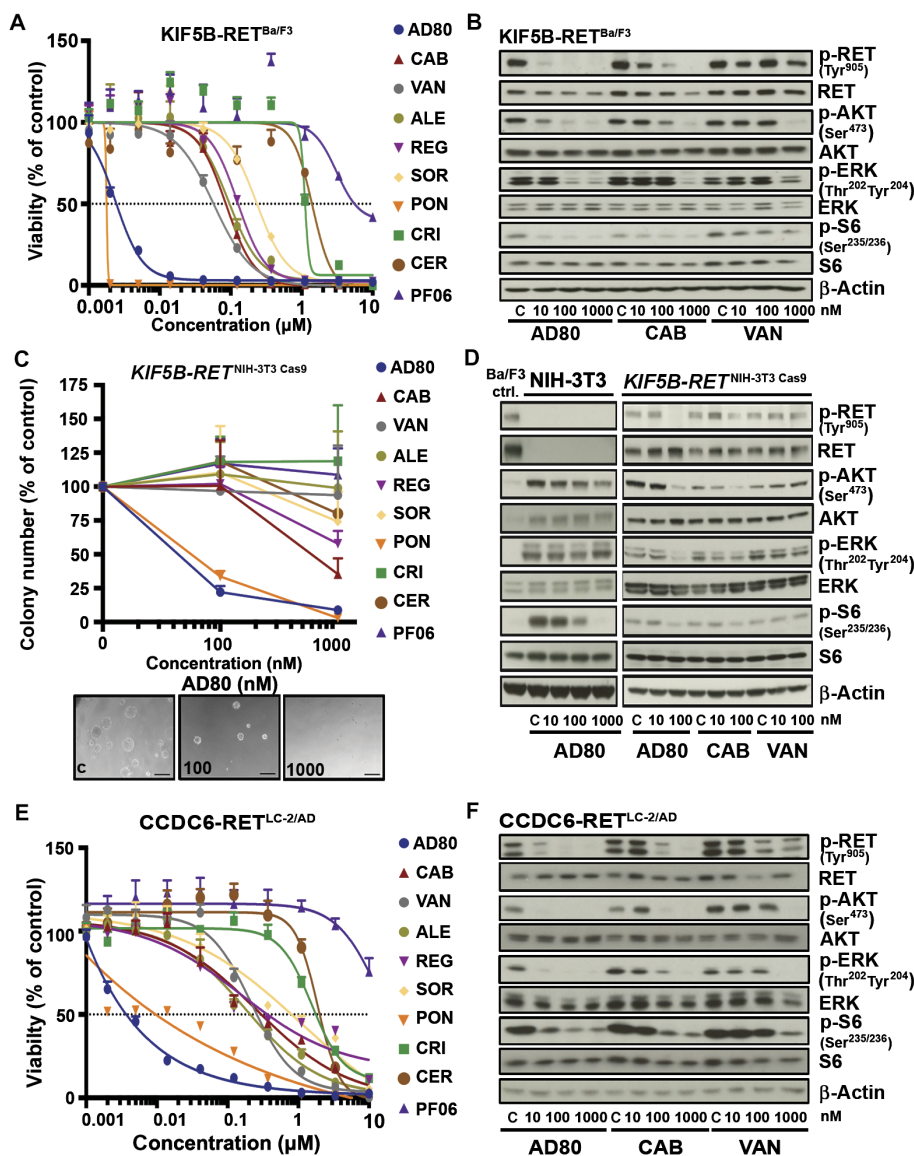


**Fig. 1. Cellular profiling of RET inhibitors identifies AD80 and ponatinib as potent compounds.** (A) Dose-response curves (72 hours) for AD80, cabozantinib (CAB), vandetanib (VAN), alectinib (ALE), regorafenib (REG), sorafenib (SOR), ponatinib (PON), crizotinib (CRI), ceritinib (CER), or PF06463922 (PF06) in KIF5B-RET-expressing Ba/F3 cells ( $n = 3$  technical replicates). (B) Immunoblotting results of KIF5B-RET-rearranged Ba/F3 cells after treatment (4 hours). C, control. (C) Relative mean colony number of NIH-3T3 cells engineered with KIF5B-RET fusion by CRISPR/Cas9 was assessed in soft agar assays after 7 days under treatment. Representative images of colonies under AD80 treatment are displayed in the lower panel. Scale bars, 100  $\mu\text{m}$  ( $n = 3$ ) (D) Immunoblotting of CRISPR/Cas9-engineered, KIF5B-RET-rearranged NIH-3T3 cells treated with AD80, cabozantinib, or vandetanib (4 hours). KIF5B-RET expressing Ba/F3 cells (Ba/F3 ctrl.) serve as control for RET signaling ( $n = 3$ ) (E) Dose-response curves (72 hours) for different inhibitors in LC-2/AD cells. (F) Immunoblotting was performed in LC-2/AD cells treated with AD80, cabozantinib, or vandetanib (4 hours).

palindromic repeats (CRISPR)/Cas9-mediated genome editing. We confirmed their anchorage-independent growth, increased proliferation rate, and high sensitivity to AD80 and ponatinib (Fig. 1C and fig. S2, A to C) (14). Again, treatment with AD80, but not cabozantinib or vandetanib, led to inhibition of phosphorylated RET (phospho-RET) and of downstream effectors of RET signaling at low nanomolar concentrations (Fig. 1D). AD80 led to dephosphorylation of S6 also in parental

NIH-3T3 cells and Ba/F3<sup>myr-AKT</sup> control cells, suggesting that S6 may represent an off-target at micromolar concentrations (Fig. 1D and fig. S2D) (13).

To further substantiate our results, we next tested our panel of RET inhibitors in the CCDC6-RET rearranged lung adenocarcinoma cell line LC-2/AD (15). We observed similar activity profiles with AD80 followed by ponatinib as the most potent inhibitors compared to all other tested drugs in terms of cytotoxicity at low nanomolar concentrations (Fig. 1E) and inhibition of phospho-RET and other downstream signaling molecules (Fig. 1F). Overall, our data suggest that in RET-rearranged cells, AD80 and ponatinib are 100- to 1000-fold more effective against RET and its downstream signaling than any other clinically tested anti-RET drug.

**AD80 and ponatinib effectively inhibit RET kinase in DFG-out conformation**

We benchmarked the genotype-specific activity of AD80 and ponatinib against well-described kinase inhibitors, such as erlotinib, BGI398, vandetanib, cabozantinib, regorafenib, alectinib, and ceritinib, in a panel of 18 cancer cell lines driven by known oncogenic lesions, such as mutant epidermal growth factor receptor (EGFR) or rearranged ALK, including two RET-rearranged cell lines (LC-2/AD and TPC-1) (fig. S3A) (6, 12, 16). Again, we identified AD80 and ponatinib as the most effective drugs and, through the calculation of median on-target versus off-target ratios, also as the most specific drugs in RET fusion-positive cells (fig. S3B and table S3).

To further characterize intracellular signaling induced by an RET inhibitor, such as AD80, we performed mass spectrometry-based phosphoproteomic analyses of LC-2/AD cells treated with 10 or 100 nM AD80. In AD80-treated cells, we observed a significant decrease of RET<sup>Y900</sup> phosphorylation with log<sub>2</sub>-fold changes of -1.07 ( $P = 0.009$ ; 10 nM AD80) and -2.11 ( $P = 0.0002$ ; 100 nM AD80), respectively (Fig. 2A). Among all phosphopeptides quantified under control, 10 nM, and 100 nM conditions ( $n = 11912$ ), the abundance of RET<sup>Y900</sup> was among the most decreased phosphopeptides (control versus 100 nM AD80;  $P = 0.00024$ ) and the most decreased receptor tyrosine kinases (fig. S3C). These results highlight that in these cells, RET is the primary target of AD80.

On the basis of these observations, we speculated that activation of RET-independent signaling pathways should largely abrogate the

Downloaded from <http://stm.sciencemag.org/> at UNIV UND STADTBIBLIOTHEK KOELN on April 14, 2021

cytotoxic effects of AD80. To this end, we supplemented LC-2/AD cells with exogenous receptor ligands and found that the activity of AD80 was significantly reduced ( $P \leq 0.05$ ) through the addition of EGF, hepatocyte growth factor, and neuregulin 1, indicating that RET is the primary cellular target in RET-rearranged LC-2/AD cells (fig. S4A).

To further characterize the high potency of AD80 and ponatinib against RET kinase fusions, we expressed and purified different truncated versions of the RET core kinase and juxtamembrane-kinase domain, as well as truncated forms of both coiled-coil domain containing 6 (CCDC6) ( $\Delta$ CCDC6-KD) and KIF5B ( $\Delta$ KIF5B-KD) kinase domain fusions (fig. S4, B and C) (17). We used these different RET fusion kinase domain constructs to determine the extent to which binding of a given compound has an effect on protein thermal stability, as measured by the melting temperature ( $T_m$ ). The difference in melting temperature with and without drug ( $\Delta T_m$ ) extrapolates the potency of the individual drugs against the respective constructs (17). To our surprise, we found that treatment with the type I inhibitors sunitinib or vandetanib resulted in a  $\Delta T_m$  of only 1° to 4°C, whereas the type II inhibitors sorafenib, ponatinib, or AD80 increased the  $\Delta T_m$  of up to 10° to 18°C (Fig. 2B and fig. S4, D to H). We observed the strongest effects in  $\Delta$ KIF5B-KD and  $\Delta$ CCDC6-KD constructs treated with AD80 and core KD with ponatinib (Fig. 2B, fig. S4D, and table S4). Such a shift for inhibitors that stabilize the catalytically inactive conformation of RET kinase, in which the DFG motif is flipped out (DFG-out) relative to its conformation in the active state (DFG-in), does not correlate with the differential in vitro kinase activity observed for sorafenib and other RET inhibitors (table S5) (6, 18).

To further characterize the relevance of a DFG-out conformation for the activity of RET inhibitors, we performed structural analyses. We used homology modeling based on a vascular EGFR (VEGFR) kinase [Protein Data Bank (PDB) code 2OH4 (19)] in the DFG-out complex similar to a previously published methodology (20), followed by extensive molecular dynamics (MD) simulation refinement. We observed that the root mean square deviation (RMSD) values remained largely stable over the time course of the MD simulation (RET<sup>wt</sup> and RET<sup>V804M</sup>), thus supporting our proposed model in which AD80 binds

in the DFG-out conformation of the kinase (fig. S5A). In this model, AD80 forms a hydrogen bond (H-bond) with the aspartate of the DFG motif that may be involved in the stabilization of the DFG-out conformation (Fig. 3A). A similar H-bond is also observed for cabozantinib, a known type II inhibitor, bound to RET<sup>wt</sup> (fig. S5B; see the Supplementary Materials and Methods for model generation). This finding corroborates the validity of our binding mode hypothesis, although the pose is biased by construction, being based on the refined RET<sup>wt</sup>/AD80 structure. Furthermore, we developed a binding pose model for AD57 (derivative of AD80) bound to RET<sup>wt</sup> (see below), which, upon superimposition, displays considerable similarity with the experimentally determined structure of AD57 bound to cSrc (PDB code 3EL8) in the DFG-out form, again validating our approach (figs. S4H and S5C). Next, we performed free energy MD simulations to transform AD80 into AD57. The calculations yielded a binding free energy difference of  $\Delta\Delta G^\circ = -0.21 \pm 0.17$  kcal mol<sup>-1</sup> at 25°C, which compares well with the values derived from median inhibitory concentration (IC<sub>50</sub>) in in vitro kinase measurements. These latter concentration-based measurements of binding affinity translate into an experimental estimate of the binding free energy difference of  $-0.41$  kcal mol<sup>-1</sup> with IC<sub>50</sub>(AD57) of 2 nM and IC<sub>50</sub>(AD80) of 4 nM (see the Supplementary Materials and Methods) (13). Using an integral equation approximation as an alternative computational approach, we obtained 0.1 kcal mol<sup>-1</sup>, also in close correspondence with both the MD and experimental results. Thus, these analyses further support the proposed DFG-out conformation as the preferred binding mode because such agreement between the experiment and the theory would not have been expected if the true and predicted binding modes were largely dissimilar.

Overall, our cellular screening, phosphoproteomic, biochemical, and structural data indicate that potent type II inhibitors, such as AD80 or ponatinib, have an optimal RET-specific profile that distinguishes them from currently available anti-RET drugs.

### Introduction of RET kinase gatekeeper mutation reveals differential activity of RET inhibitors

Secondary resistance mutations frequently target a conserved residue, termed gatekeeper, that controls access to a hydrophobic subpocket of

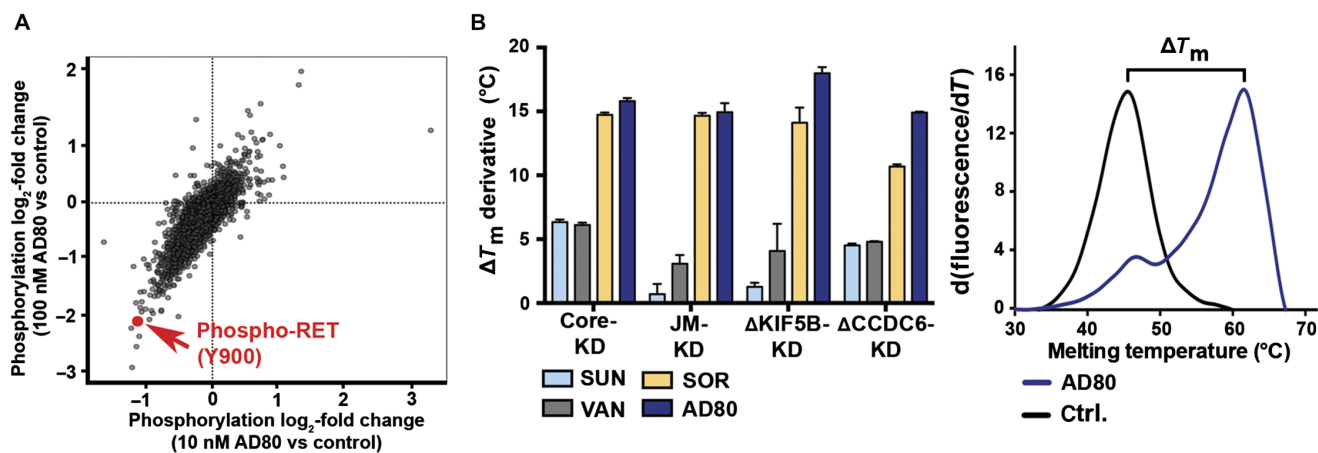


**Fig. 2. AD80 specifically targets RET and tightly binds to RET fusion kinase.** (A) Scatterplot of log<sub>2</sub>-fold phosphorylation change for LC-2/AD cells treated (4 hours) with either 10 or 100 nM AD80. Each dot represents a single phosphosite; phospho-RET (Y900) is highlighted in red. (B) Difference in melting temperatures after AD80, sorafenib (SOR), vandetanib (VAN), or sunitinib (SUN) addition ( $\Delta T_m$ ) and the respective SEM are shown for each construct. Thermal shift experiments were performed using independent preparations of each protein and were carried out in triplicates (left). Representative thermal melting curves for  $\Delta$ KIF5B-KD incubated with either AD80 (1  $\mu$ M) or the equivalent volume of dimethyl sulfoxide (DMSO) (ctrl.) are shown (right).

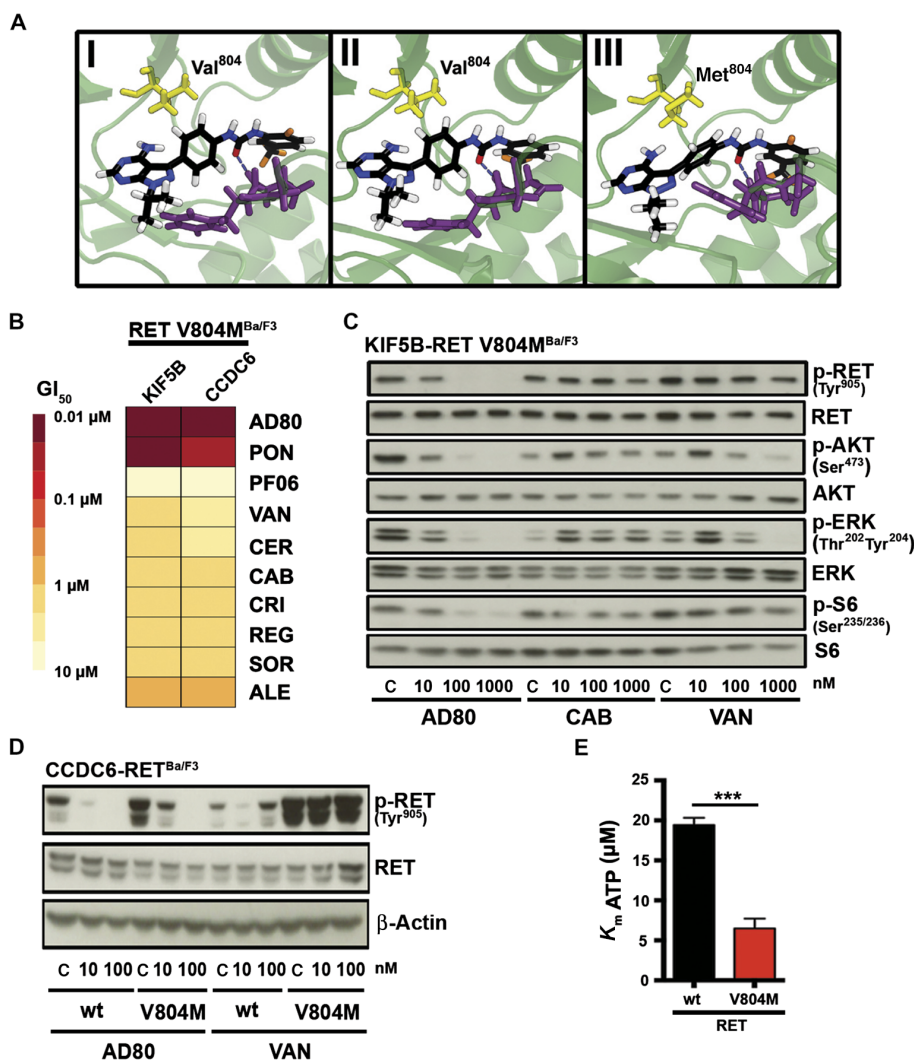


**Fig. 3. AD80 is active against gatekeeper mutant RET<sup>V804M</sup> cells.** (A) Optimized structures after extensive MD refinement followed by ALPB optimization. (i) RET<sup>wt</sup>/AD80 after 102 ns, (ii) RET<sup>wt</sup>/AD57 after 202 ns (92 ns from RET<sup>wt</sup>/AD80 simulation followed by 110 ns from TI-MD), and (iii) RET<sup>V804M</sup>/AD80 after 107 ns (side view). The DFG motif is shown in violet. Distances from the center of central phenyl to Val<sup>804</sup>-C(wt), Ile<sup>788</sup>-C(wt), and Met<sup>804</sup>-S(V804M) are 4.77, 3.90, and 4.29 Å, respectively. Dashed lines indicate the H-bond between the bound ligands and aspartate of the DFG motif. (B) Heat map of mean 50% growth inhibition (GI<sub>50</sub>) values ( $n \geq 3$ ) of Ba/F3 cells expressing CCDC6-RET<sup>V804M</sup> or KIF5B-RET<sup>V804M</sup> after 72 hours of treatment, as assessed for various inhibitors. (C) Immunoblotting of AD80-, cabozantinib-, or vandetanib-treated (4 hours) KIF5B-RET<sup>V804M</sup> Ba/F3 cells. (D) Immunoblotting of Ba/F3 cells expressing CCDC6-RET-RET<sup>wt</sup> or CCDC6-RET<sup>V804M</sup> under AD80 or vandetanib treatment (4 hours). wt, wild type. (E) Calculated Michaelis constant ( $K_m$ ) values of ATP binding to RET<sup>wt</sup> or RET<sup>V804M</sup> from three independent experiments. \*\*\* $P < 0.001$ ,  $n = 3$ .

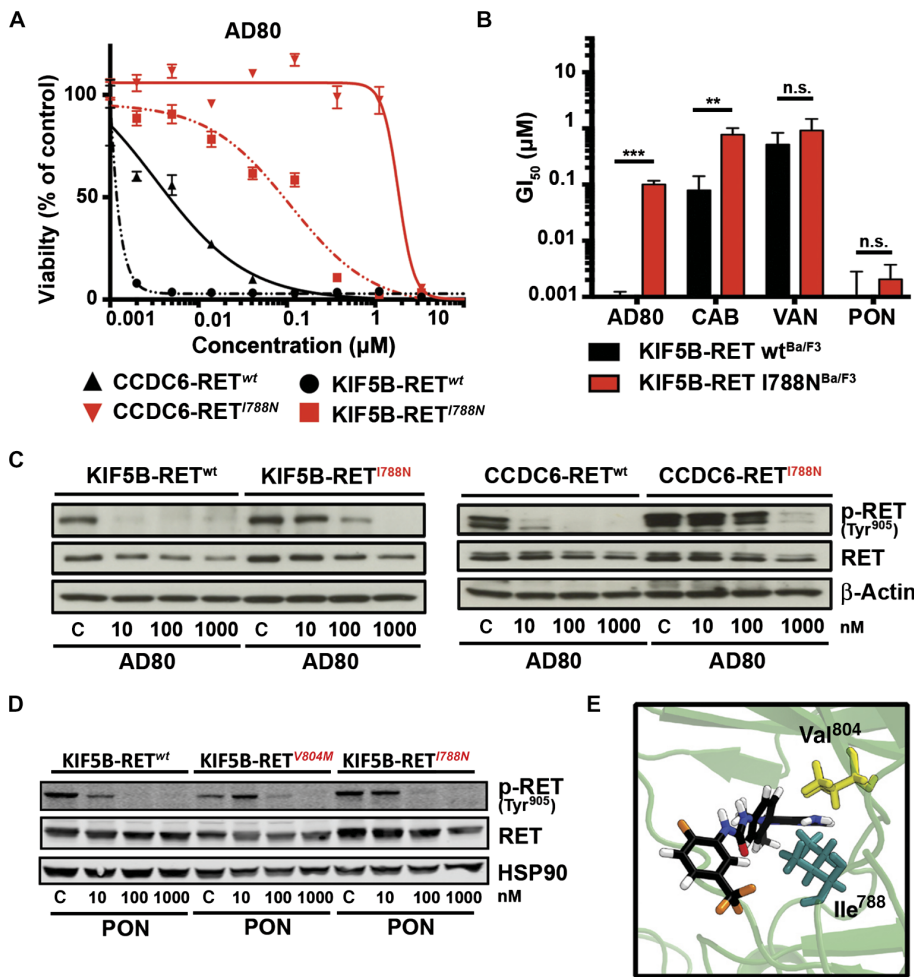
the kinase domain (21). To test the impact of the gatekeeper resistance mutations on RET inhibitors, we established Ba/F3 cells expressing KIF5B-RET<sup>V804M</sup> or CCDC6-RET<sup>V804M</sup> and tested them against a panel of different drugs. As expected, only ponatinib and AD80 showed high activity in these gatekeeper mutant cells (Fig. 3B) (22). Similar activity was observed when testing the AD80 derivatives AD57 and AD81 for their inhibitory potential on Ba/F3 cells expressing wild-type and V804M-mutated KIF5B-RET or CCDC6-RET (fig. S6A). This effect was also evident in the ability of AD80 to inhibit phosphorylation of RET as well as of ERK, AKT, and S6K in these cells (Fig. 3C and

table S1). Next, we used computational homology modeling coupled with MD refinement of AD80 in RET<sup>wt</sup> in comparison with RET<sup>V804M</sup>-mutant kinases. In line with our in vitro results, this analysis revealed high structural similarity and similar binding free energy estimates for both variants ( $-2.5 \text{ kcal mol}^{-1}$  for transforming RET<sup>wt</sup> to RET<sup>V804M</sup> bound to AD80 from the integral equation model) (see Fig. 3A and the Supplementary Materials and Methods).

In parallel, we noticed that independent of the individual treatment, RET phosphorylation tended to be higher in gatekeeper mutant cells when compared to wild-type RET (Fig. 3D). To further characterize these differences, we performed in vitro kinase assays and found that the introduction of the RET<sup>V804M</sup> mutation significantly ( $P < 0.001$ ) increases the affinity of the recombinant receptor for adenosine 5'-triphosphate (ATP) when compared to the recombinant wild-type receptor (Fig. 3E). Thus, similar to gatekeeper-induced effects on ATP affinity observed for EGFR<sup>T790M</sup> mutations, our data suggest that these effects may be of relevance for the activity of RET inhibitors in KIF5B-RET<sup>V804M</sup> and CCDC6-RET<sup>V804M</sup> cells (23).

#### Saturated mutagenesis screening identifies CCDC6-RET<sup>I788N</sup> drug resistance mutation

To identify RET kinase mutations that may be associated with resistance against targeted therapy, we performed accelerated mutagenesis of RET fusion plasmids (24, 25). We identified the CCDC6-RET<sup>I788N</sup> mutation by selection of an AD80-resistant cell population (table S6). To validate this finding, we engineered Ba/F3 cells expressing KIF5B-RET<sup>I788N</sup> or CCDC6-RET<sup>I788N</sup> and observed a robust shift in cytotoxicity in response to AD80 treatment (Fig. 4A), as well as the other RET inhibitors, cabozantinib and vandetanib, but not ponatinib (Fig. 4B and fig. S6B). Immunoblotting confirmed that the introduction of the KIF5B-RET<sup>I788N</sup> mutation had a minor effect on the efficacy of ponatinib but a major impact on AD80, as measured by phospho-RET analysis (Fig. 4, C and D). Computational binding mode analysis (Figs. 3A and 4E) suggests that both positions 804 and 788 are adjacent to the location of the central phenyl ring of AD80; characteristic distances between the phenyl center of mass and the nearest adjacent protein nonhydrogen sites to Val<sup>804</sup>-C(wt), Ile<sup>788</sup>-C(wt), Met<sup>804</sup>-S(V804M), and Ile<sup>788</sup>-C(V804M) are 4.77, 3.90, 4.29, and 4.61 Å, respectively. However, because V804M and I788N mutants responded differently to AD80, a clear conclusion about the molecular origin was



**Fig. 4. RET<sup>I788N</sup> mutations abrogate the activity of AD80 but not ponatinib.** (A) Dose-response curves for AD80 against Ba/F3 cells expressing KIF5B-RET<sup>wt</sup> (black) or KIF5B-RET<sup>I788N</sup> (red) and CCDC6-RET<sup>wt</sup> (black dashed line) or CCDC6-RET<sup>I788N</sup> (red dashed line) ( $n = 3$ ). (B) Bar graph of mean GI<sub>50</sub> values + SD (from  $n = 3$ ) for KIF5B-RET<sup>wt</sup> or KIF5B-RET<sup>I788N</sup> Ba/F3 cells treated (72 hours) with AD80, cabozantinib (CAB), vandetanib (VAN), or ponatinib (PON). \*\*\* $P < 0.001$ ; \*\* $P < 0.01$ ; n.s., not significant. (C) Immunoblot of Ba/F3 cells expressing KIF5B-RET<sup>wt</sup> or KIF5B-RET<sup>I788N</sup> and CCDC6-RET<sup>wt</sup> or CCDC6-RET<sup>I788N</sup> treated (4 hours) with AD80. (D) Immunoblot of KIF5B-RET<sup>wt</sup>, KIF5B-RET<sup>V804M</sup>, or KIF5B-RET<sup>I788N</sup> expressing Ba/F3 cells treated (4 hours) with ponatinib. HSP90 is used as loading control. (E) Optimized structure after extensive MD refinement followed by ALPB optimization. RET<sup>wt</sup>/AD80 after 102 ns (side view). Distance from the center of central phenyl to Ile<sup>788</sup>-C(V804M) is 4.61 Å.

not possible based on structural analysis alone, requiring further investigations. Thus, our data uncovered a resistance mutation RET<sup>I788N</sup> that may arise in RET-rearranged tumors under RET inhibitor treatment and that retains sensitivity against ponatinib.

**Feedback-induced activation of MAPK signaling modulates activity of RET inhibitors**

Beyond the acquisition of secondary mutations, drug treatment of cancer cells may also release feedback loops that override the activity of targeted cancer treatment (26, 27). To systematically characterize these effects, we analyzed altered gene expression by RNA-sequencing (RNA-seq) of LC-2/AD cells under AD80 treatment and performed gene set enrichment analysis (GSEA) (28). Our analyses revealed that treatment with AD80 results in up-regulation of genes that are typi-

cally repressed by active KRAS (KRAS down; adjusted  $P < 0.0001$ ). On the contrary, genes that are activated by KRAS were down-regulated (KRAS up; adjusted  $P = 0.003$ ) (Fig. 5A). Accordingly, the list of significantly down-regulated genes contained *DUSP6* (adjusted  $P < 1 \times 10^{-250}$ ), *SPRY4* (adjusted  $P = 5.75 \times 10^{-89}$ ), *DUSP5* (adjusted  $P = 2.52 \times 10^{-38}$ ), and other genes that buffer mitogen-activated protein kinase (MAPK) pathway (Fig. 5B) (29). This transcriptional deregulation of MAPK signaling was accompanied by residual phospho-ERK staining in immunoblotting analyses of RET-rearranged LC-2/AD cells after 24 hours of inhibitor treatment (fig. S6C). Using a Group-based Prediction System (GPS 2.12) to identify kinase-specific phosphosites that are perturbed in AD80-treated LC-2/AD cells assessed in our mass spectrometry-based analysis, we identified a marked enrichment of phosphosites known from different families of noncanonical MAPK kinases (MEKs), such as MAPK8 (66 phosphosites), MAPK13 (21 phosphosites), or MAPK12 (15 phosphosites) (Fig. 5C).

We next tested the relevance of Ras-MAPK pathway reactivation in RET-rearranged cells treated with AD80 alone or a combination of AD80 and the MEK inhibitor trametinib. In TPC-1 cells with limited vulnerability to RET inhibition, we observed a pronounced phospho-ERK signal in cells after inhibition with AD80 when compared to LC-2/AD cells (fig. S6D). The combination of AD80 and trametinib fully abrogated MAPK signaling and depleted the outgrowth of resistant cells in clonogenic assays and enhanced the reduction of viability (Fig. 5D and fig. S6, E and F).

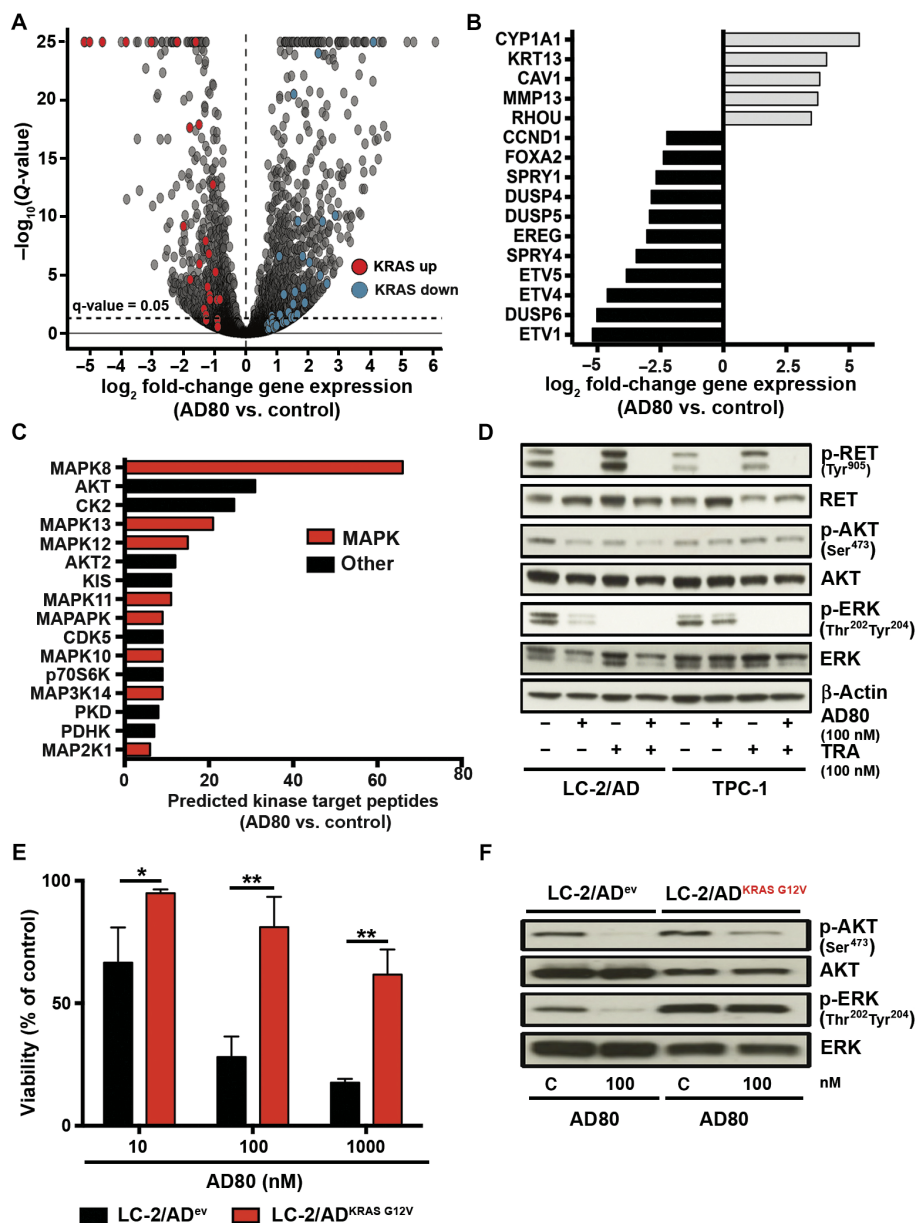
To formally test the relevance of MAPK pathway activation in the context of resistance to RET-targeted therapies in RET-rearranged cells, we stably transduced LC-2/AD cells with lentiviral KRAS<sup>G12V</sup>. Introduction of the oncogenic KRAS allele into LC-2/AD cells largely eliminated the activity of AD80, as measured in viability assays and by staining of phospho-ERK (Fig. 5, E and F). Overall, our data suggest that drug-induced transcriptional and posttranslational reactivation of Ras-MAPK signaling may modulate the activity of RET-targeted inhibitors in RET-rearranged cells.

**AD80 potently shrinks RET-rearranged tumors in patient-derived xenografts**

To compare the in vivo efficacy of AD80 head-to-head with other RET inhibitors, we engrafted NIH-3T3 cells driven by CRISPR/Cas9-induced KIF5B-RET rearrangements into NSG (nonobese

Downloaded from <http://stm.sciencemag.org/> at UNIV UND STADTBIBLIOTHEK KOELN on April 14, 2021

**Fig. 5. MAPK pathway activation may be involved in the development of resistance against RET inhibition.** (A) RNA-seq results of LC-2/AD cells treated (48 hours) with 100 nM AD80. Genes contained within the core enrichments of GSEA against the hallmark gene sets with genes up-regulated (KRAS up) or down-regulated (KRAS down) by active KRAS are highlighted by red and blue, respectively. The dashed line represents false discovery rate-adjusted Q value = 0.05. (B) Relevant genes from the top 50 genes with the strongest significant changes in RNA-seq after AD80 treatment (100 nM; 48 hours). (C) Predicted number of down-regulated phosphorylation sites for each kinase. All kinases with greater than or equal to six down-regulated phosphorylation sites are shown in hierarchical order. Kinases associated with MAPK pathway signaling are highlighted in red. (D) In immunoblotting assays, RET signaling was monitored in LC-2/AD and TPC-1 cells treated (48 hours) with AD80 (0.1  $\mu$ M), trametinib (TRA) (0.1  $\mu$ M), or a combination of both inhibitors. (E) LC-2/AD<sup>ev</sup> or LC-2/AD<sup>KRAS G12V</sup> cells were treated (72 hours) with AD80. Results are shown as means + SD ( $n = 3$ ). \*\*\* $P < 0.001$ ; \*\* $P < 0.01$ ; \* $P < 0.05$ . (F) Immunoblotting of LC-2/AD<sup>ev</sup> or LC-2/AD<sup>KRAS G12V</sup> cells under AD80 treatment (100 nM; 4 hours).



diabetic/severe combined immunodeficient gamma) mice. After the development of tumors, mice were treated with either vehicle or 12.5 to 25 mg/kg of AD80, cabozantinib, or vandetanib, and tumors were explanted 4 hours later (30, 31). We observed a pronounced reduction in phosphorylation of RET as well as AKT and ERK in tumors treated with AD80 (25 mg/kg) but not in tumors treated with cabozantinib or vandetanib (Fig. 6A). Encouraged by these results, we next treated a cohort ( $n = 16$ ) of patient-derived xenograft (PDX) mice engrafted with tumor tissue from a *CCDC6-RET*-rearranged colorectal cancer (CRC) patient with either vehicle or AD80 (25 mg/kg). Treatment with AD80 induced significant ( $P < 0.001$ ) tumor shrinkage in *CCDC6-RET* PDX<sup>wt</sup> (Fig. 6, B and C, and fig. S7A) (32). In line with our in vitro data for cells harboring *RET* gatekeeper mutations, tumor shrinkage ( $P < 0.01$ ) was robust but less pronounced when we treated PDX mice ( $n = 16$ ) engrafted with CRC tissue that had developed a *CCDC6-RET*<sup>V804M</sup> gatekeeper mutation under ponatinib treatment (Fig. 6, B and D, and fig. S7B) (33). Furthermore, we observed a robust reduction of cellular proliferation (*CCDC6-RET*<sup>wt</sup>,  $P < 0.001$ ; *CCDC6-RET*<sup>V804M</sup>,  $P < 0.05$ ), as measured by KI-67 staining

in *CCDC6-RET*<sup>wt</sup> and *CCDC6-RET*<sup>V804M</sup> tumors (Fig. 6, E and F). AD80 treatment did not cause body weight loss in either PDX model over the course of the study (fig. S7, C and D). Together, our data indicate that AD80 is a highly potent RET inhibitor with a favorable pharmacokinetic profile in clinically relevant *RET* fusion-driven tumor models.

**DISCUSSION**

Our chemical-genomic and chemical-proteomic analyses revealed three interesting findings with major implications for the development of effective therapies against *RET*-rearranged tumors: (i) *RET*-rearranged tumors show exquisite vulnerability to a subset of type II inhibitors that target the DFG-out conformation of RET kinase,

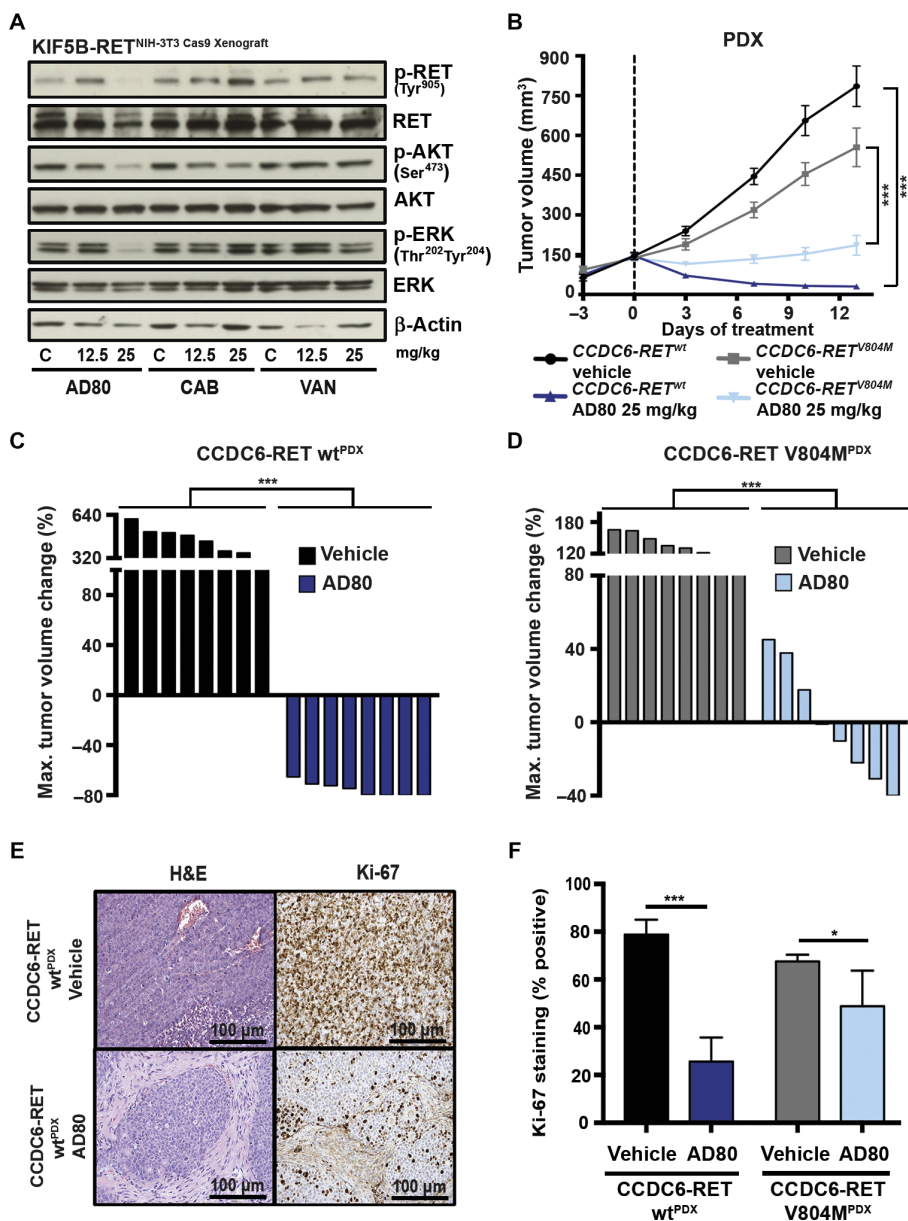


**Fig. 6. AD80 treatment effectively shrinks RET-rearranged tumors in PDX models.** (A) Immunoblotting of tumor tissue from CRISPR/Cas9-induced NIH-3T3<sup>KIF5B-RET</sup> xenografts was performed. Mice were treated (4 hours) with vehicle control or 12.5 or 25 mg/kg AD80, CAB, or VAN and were sacrificed. (B) Median tumor volume was assessed using consecutive measurements of PDX tumors driven by *CCDC6-RET*<sup>wt</sup> or *CCDC6-RET*<sup>V804M</sup> rearrangements under treatment with either AD80 (25 mg/kg; 14 days) or vehicle control (14 days). Treatment started at day 0. (C) Waterfall plot for each *CCDC6-RET*<sup>wt</sup> fusion-positive PDX depicting best response (14 days) under AD80 or vehicle control treatment. *\*\*\*P* < 0.001. (D) Waterfall plot for each *CCDC6-RET*<sup>V804M</sup>-positive PDX depicting best response (7 days) under AD80 or vehicle control treatment. *\*\*\*P* < 0.001. (E) Representative immunohistochemistry (IHC) staining for hematoxylin and eosin (H&E) and Ki-67 of AD80- or vehicle control-treated *CCDC6-RET*<sup>wt</sup> PDX. Scale bars, 100 μm. (F) Quantification of Ki-67 IHC staining. *\*\*\*P* < 0.001; *\*P* < 0.05.

(ii) compound specificity and compound activity can be faithfully determined in complementary *in vitro* and *in vivo* models of rearranged RET, and (iii) resistance mechanisms against targeted inhibition of RET may involve *RET*<sup>I788N</sup> mutations and the reactivation of MAPK signaling.

for effective targeted drugs against RET, our results provide a strong rationale for optimization of current therapeutic strategies and development of RET inhibitors for the effective treatment of RET-rearranged cancers.

The repurposing of crizotinib for the targeted treatment of *ALK*-rearranged tumors enabled a fast-track introduction of precision cancer medicine for this group of cancer patients and raised hopes that this approach may be a blueprint for the targeted treatment of other driver oncogenes, such as RET (34). Although initial clinical response rates were promising in selected patients, a median progression-free survival of less than 6 months and response rates of only about 18% in retrospective studies indicated that RET may be a difficult drug target after all (7, 9, 10, 35).

Our systematic characterization of anti-RET drugs revealed distinct activity and specificity profiles for the type II kinase inhibitors AD80 and ponatinib in independent *in vitro* and *in vivo* models across different lineages of RET-rearranged cancer. This finding is noteworthy because the biochemical profiling of these compounds and structurally related compounds would have suggested a broad spectrum of kinase targets (13, 36, 37). Our data also suggest that an inhibitory profile, including a stable binding in the DFG-out conformation of RET together with a potent *in vitro* kinase activity, may predict efficacy against RET-rearranged cancer cells. At the same time, our study is limited through the lack of insight into drug residence time or structural kinetics that may also contribute to the overall activity of type II inhibitors such as sorafenib and other RET inhibitors (20, 38).

Notably, we identified a *CCDC6-RET*<sup>I788N</sup> resistance mutation that renders a number of tested RET inhibitors ineffective while retaining vulnerability to ponatinib. These findings resemble the experience with *ALK*-rearranged tumors, where the availability of potent inhibitors allows a mutant-specific selection of inhibitors to overcome drug resistance (39). In addition, our results suggest that the reactivation of intracellular networks, including MAPK signaling, may contribute to drug tolerance and, over time, may modulate the efficacy of RET kinase inhibitors in RET-rearranged tumors. Given the evident clinical need

**MATERIALS AND METHODS****Study design**

The goal of our study was to systematically profile a series of kinase inhibitors to identify features that predict high activity against *RET*-rearranged tumors. In particular, we characterized the role of inhibitor binding to *RET* kinase. Furthermore, we performed chemical genomic analyses and transcriptional profiling to identify mechanisms of resistance against *RET* inhibitors in *RET*-rearranged cancer cells.

The selection of cell lines was based on availability of *RET*-rearranged cellular models. We used the *RET*-rearranged lung adenocarcinoma cell line LC2/AD and the *KIF5B-RET* and *CCDC6-RET* viral transduced Ba/F3 pro B cell line to benchmark the differential activity of different *RET* inhibitors. We specifically focused on the characterization of AD80 and ponatinib as the most active drugs. To further profile the intracellular effects of AD80, we used phosphoproteomics to demonstrate that phospho-*RET* is among the most decreased detected peptides. Because it was not possible for us to obtain crystal structures of AD80 in a complex with *RET*, we used homology-based modeling of the AD80:*RET* complex to further substantiate our hypothesis of AD80 binding the DFG-out conformation of *RET*. To identify resistance mutations against AD80 in *CCDC6-RET*, we performed saturated mutagenesis screening and found a I788N mutation but no mutations at the gatekeeper position V804 of *RET*. Finally, we used murine PDX models driven by *CCDC6-RET*<sup>wt</sup> or *CCDC6-RET*<sup>V804M</sup> showing potent in vivo efficacy of AD80. All experiments were performed at least three times. Screenings were performed in triplicates within each experiment. IHC analyses of PDX tumors were randomly selected and reviewed in a blinded fashion. More details for each individual experiment are indicated in Materials and Methods as well as in the main text and figure legends.

**CRISPR/Cas9**

CRISPR technology was used via a pLenti vector containing Cas9-IRES-blasticidine and two U6 promoters for expression of individual single-guide RNAs (sgRNAs) [sgRNA1 (intron 15 murine *KIF5B*), GGCACCAAACACTTCACCCC; sgRNA2 (intron 11 murine *RET*), GGGTGTAGCGAAGTGTGCAT] (14). Twenty-four hours after transfection, the medium was changed to medium supplemented with blasticidin (10 µg/ml) (Life Technologies) for 4 days.

**Immunoblot analyses**

Immunoblot analyses were performed as previously described (40). The individual antibodies are specified in the Supplementary Materials and Methods. Detection of proteins was performed via horseradish peroxidase or via near-infrared fluorescent antibodies using a LI-COR Odyssey CLx imaging system.

**Phosphoproteomic analyses**

LC-2/AD cells were treated with 0, 10, or 100 nM AD80, lysed, proteolytically digested with trypsin, and labeled with an isobaric mass tag (TMT10plex, Thermo Fisher Scientific). Peptides for global proteome analysis were fractionated by high-pH reversed-phase chromatography. Phosphopeptides were enriched via TiO<sub>2</sub> beads and fractionated using hydrophilic interaction chromatography (41). Fractions were analyzed by nano-liquid chromatography–tandem mass spectrometry on a Q Exactive HF mass spectrometer (Thermo Fisher Scientific), and data were analyzed using the Proteome Discoverer 1.4 software (Thermo Fisher Scientific). A detailed description can be found in the Supplementary Materials and Methods.

**Protein thermal shift assay**

Different variants of *RET* kinase domain were designed and ordered from GeneArt (Life Technologies). *RET* variants were expressed in SF21 cells and harvested 72 hours after transfection. Subsequently, proteins were purified and phosphorylated. To determine the protein thermal shift, protein variants were incubated with DMSO or 1 µM compound. SYPRO Orange dye (Life Technologies) was added to each drug-treated sample, and thermal shift was measured in a 7500 Fast Real-Time PCR machine (Applied Biosystems) in a temperature range of 25° to 90°C. Subsequent analysis was performed using Protein Thermal Shift Software v1.2 (Applied Biosystems). A detailed description can be found in the Supplementary Materials and Methods.

**Computational binding mode modeling**

Briefly, VEGFR was taken as a template for modeling and filling of sequence gaps, representing the relevant part of the wild-type *RET* protein. All ligand-bound models were created by superpositioning, followed by extensive MD simulations and energy minimization to relax the structures (*RET*<sup>wt</sup>/AD80, *RET*<sup>V804M</sup>/AD80, and *RET*<sup>wt</sup>/cabozantinib). For comparison with experimentally determined IC<sub>50</sub> ratios, the binding free energy difference between *RET*<sup>wt</sup>/AD80 and *RET*<sup>wt</sup>/AD57 was further estimated by MD simulations and integral equation calculations (42). The latter approach was also used for approximate determination of the impact of the V804M mutation on the binding affinity of AD80. A detailed description can be found in the Supplementary Materials and Methods.

**ATP-binding constant determination**

ATP *K<sub>m</sub>* determination for *RET*<sup>wt</sup> and *RET*<sup>V804M</sup> mutant was performed using the HTRF KinEASE TK assay (Cisbio) according to the manufacturer's instructions. To determine ATP *K<sub>m</sub>*, wild type and V804M mutant were incubated with different ATP concentrations (300 µM to 1.7 nM) for 20 min (*RET*<sup>wt</sup>) or 15 min (*RET*<sup>V804M</sup>). Phosphorylation of the substrate peptide was determined by Förster resonance energy transfer between europium cryptate and XL665. ATP *K<sub>m</sub>* (app) was calculated using a Michaelis-Menten plot.

**Patient-derived xenografts**

Tumor fragments from stock mice (BALB/c nude) inoculated with *CCDC6-RET* fusion–positive patient-derived tumor tissues (provided by Crown Bioscience Inc.) were harvested and used for propagation into BALB/c nude mice (32). Mice were randomly allocated into vehicle (5% DMSO and 40% PEG400 in saline)– and AD80 (25 mg/kg)–treated groups (oral gavage) when the average tumor volume reached 100 to 200 mm<sup>3</sup>. Tumor volume was measured twice weekly in two dimensions using a caliper, and the volume is expressed in cubic millimeters [TV = 0.5(*a* × *b*<sup>2</sup>), where *a* and *b* represent long and short diameter, respectively].

**Immunohistochemistry**

IHC was performed on Leica BOND automated staining systems using Ki-67 and Mib-1 (Dako) antibodies according to the manufacturer's instructions. Ki-67 labeling index was determined by manually counting 100 tumor cells in the area of the highest proliferation.

**Statistical analysis**

All statistical analyses were performed using Microsoft Excel 2011 or GraphPad Prism 6.0h for Mac or R (www.r-project.org/). *P* values were assessed using Student's *t* test, unless specified otherwise. Significance is marked with \**P* ≤ 0.05, \*\**P* ≤ 0.01, or \*\*\**P* ≤ 0.001.

## SUPPLEMENTARY MATERIALS

www.sciencetranslationalmedicine.org/cgi/content/full/9/394/eaah6144/DC1

## Materials and Methods

Fig. S1. Selective inhibition of signaling induced by rearranged RET and clinical activity in vivo.

Fig. S2. Induction of *KIF5B-RET* rearrangements in NIH-3T3 cells via CRISPR/Cas9 and S6 kinase as an off-target of AD80.

Fig. S3. Characterization of the activity profile of AD80.

Fig. S4. Delineation of the cellular targets of AD80 using ligand screens and thermal shift experiments.

Fig. S5. RMSD of RET and AD80 or cabozantinib over time and ALPB-optimized structures.

Fig. S6. Inhibitory potential of AD80 derivatives and resistance mechanisms against RET inhibition.

Fig. S7. Validation of PDX via fluorescent in situ hybridization (FISH) and in vivo effects induced by treatment with AD80.

Table S1. IC<sub>50</sub> values of AD80, cabozantinib, and vandetanib for phospho-RET in Ba/F3 cells expressing wild type or V804M *KIF5B-RET*.

Table S2. Rates of clinical response to currently available anti-RET drugs and clinical information of patients used in retrospective analysis.

Table S3. GI<sub>50</sub> values of the panel of patient-derived cell lines.

Table S4. Tabulated derivative melting temperatures (*T<sub>m</sub>*) and differences in melting temperature ( $\Delta T_m$ ) values.

Table S5. In vitro kinase assay of RET<sup>WT</sup>, RET<sup>V804M</sup>, and RET<sup>V804L</sup> mutants with different inhibitors.

Table S6. Experimental setup for saturated mutagenesis screening.

References (43–66)

## REFERENCES AND NOTES

- D. Lipson, M. Capelletti, R. Yelensky, G. Otto, A. Parker, M. Jarosz, J. A. Curran, S. Balasubramanian, T. Bloom, K. W. Brennan, A. Donahue, S. R. Downing, G. M. Frampton, L. Garcia, F. Juhn, K. C. Mitchell, E. White, J. White, Z. Zwirko, T. Peretz, H. Nechushtan, L. Soussan-Gutman, J. Kim, H. Sasaki, H. R. Kim, S.-i. Park, D. Ercan, C. E. Sheehan, J. S. Ross, M. T. Cronin, P. A. Jänne, P. J. Stephens, Identification of new *ALK* and *RET* gene fusions from colorectal and lung cancer biopsies. *Nat. Med.* **18**, 382–384 (2012).
- K. Takeuchi, M. Soda, Y. Togashi, R. Suzuki, S. Sakata, S. Hatano, R. Asaka, W. Hamanaka, H. Ninomiya, H. Uehara, Y. Lim Choi, Y. Satoh, S. Okumura, K. Nakagawa, H. Mano, Y. Ishikawa, *RET*, *ROS1* and *ALK* fusions in lung cancer. *Nat. Med.* **18**, 378–381 (2012).
- T. Kohno, H. Ichikawa, Y. Totoki, K. Yasuda, M. Hiramoto, T. Nammo, H. Sakamoto, K. Tsuta, K. Furuta, Y. Shimada, R. Iwakawa, H. Ogiwara, T. Oike, M. Enari, A. J. Schetter, H. Okayama, A. Haugen, V. Skaug, S. Chiku, I. Yamanaka, Y. Arai, S.-i. Watanabe, I. Sekine, S. Ogawa, C. C. Harris, H. Tsuda, T. Yoshida, J. Yokota, T. Shibata, *KIF5B-RET* fusions in lung adenocarcinoma. *Nat. Med.* **18**, 375–377 (2012).
- T. Kodama, T. Tsukaguchi, Y. Satoh, M. Yoshida, Y. Watanabe, O. Kondoh, H. Sakamoto, Alectinib shows potent antitumor activity against *RET*-rearranged non-small cell lung cancer. *Mol. Cancer Ther.* **13**, 2910–2918 (2014).
- R. Kurzrock, S. I. Sherman, D. W. Ball, A. A. Forastiere, R. B. Cohen, R. Mehra, D. G. Pfister, E. E. W. Cohen, L. Janisch, F. Nauling, D. S. Hong, C. S. Ng, L. Ye, R. F. Gagel, J. Frye, T. Müller, M. J. Ratain, R. Salgia, Activity of XL184 (Cabozantinib), an oral tyrosine kinase inhibitor, in patients with medullary thyroid cancer. *J. Clin. Oncol.* **29**, 2660–2666 (2011).
- M. G. Borrello, E. Airdini, L. D. Locati, A. Greco, L. Licitra, M. A. Pierotti, *RET* inhibition: Implications in cancer therapy. *Expert Opin. Ther. Targets* **17**, 403–419 (2013).
- A. Drilon, L. Wang, A. Hasanovic, Y. Suehara, D. Lipson, P. Stephens, J. Ross, V. Miller, M. Ginsberg, M. F. Zakowski, M. G. Kris, M. Ladanyi, N. Rizvi, Response to Cabozantinib in patients with *RET* fusion-positive lung adenocarcinomas. *Cancer Discov.* **3**, 630–635 (2013).
- G. S. Falchook, N. G. Ordóñez, C. C. Bastida, P. J. Stephens, V. A. Miller, L. Gaido, T. Jackson, D. D. Karp, Effect of the *RET* inhibitor vandetanib in a patient with *RET* fusion-positive metastatic non-small-cell lung cancer. *J. Clin. Oncol.* **34**, e141–e144 (2016).
- O. Gautschi, J. Milia, T. Filleron, J. Wolf, D. P. Carbone, D. Owen, R. Camidge, V. Narayanan, R. C. Doebele, B. Besse, J. Remon-Masip, P. A. Jänne, M. M. Awad, N. Peled, C.-C. Byoung, D. D. Karp, M. Van Den Heuvel, H. A. Wakelee, J. W. Neal, T. S. K. Mok, J. C. H. Yang, S.-H. I. Ou, G. Pall, P. Froesch, G. Zalcman, D. R. Gandara, J. W. Riess, V. Velcheti, K. Zeidler, J. Diebold, M. Früh, S. Michels, I. Monnet, S. Papat, R. Rosell, N. Karachaliou, S. I. Rothschild, J.-Y. Shih, A. Warth, T. Muley, F. Cabillic, J. Mazières, A. Drilon, Targeting *RET* in patients with *RET*-rearranged lung cancers: Results from the global, multicenter *RET* registry. *J. Clin. Oncol.* **35**, 1403–1410 (2017).
- K. Yoh, T. Seto, M. Satouchi, M. Nishio, N. Yamamoto, H. Murakami, N. Nogami, S. Matsumoto, T. Kohno, K. Tsuta, K. Tsuchihara, G. Ishii, S. Nomura, A. Sato, A. Ohtsu, Y. Ohe, K. Goto, Vandetanib in patients with previously treated *RET*-rearranged advanced non-small-cell lung cancer (LURET): An open-label, multicentre phase 2 trial. *Lancet Respir. Med.* **5**, 42–50 (2017).
- T. Cascone, K. R. Hess, S. Piha-Paul, D. S. Hong, I. M. Subbahl, T. Bhatt, A. Lui, S. Fu, A. Naing, F. Janku, D. D. Karp, F. Meric-Bernstam, J. V. Heymach, V. Subbahl, Safety, toxicity and activity of multi-kinase inhibitor vandetanib in combination with everolimus in advanced solid tumors, paper presented at the 2016 ASCO Annual Meeting (2016).
- M. Song, Progress in discovery of *KIF5B-RET* kinase inhibitors for the treatment of non-small-cell lung cancer. *J. Med. Chem.* **58**, 3672–3681 (2015).
- A. C. Dar, T. K. Das, K. M. Shokat, R. L. Cagan, Chemical genetic discovery of targets and anti-targets for cancer polypharmacology. *Nature* **486**, 80–84 (2012).
- P. S. Choi, M. Meyerson, Targeted genomic rearrangements using CRISPR/Cas technology. *Nat. Commun.* **5**, 3728 (2014).
- M. Suzuki, H. Makinoshima, S. Matsumoto, A. Suzuki, S. Mimaki, K. Matsushima, K. Yoh, K. Goto, Y. Suzuki, G. Ishii, A. Ochiai, K. Tsuta, T. Shibata, T. Kohno, H. Esumi, K. Tsuchihara, Identification of a lung adenocarcinoma cell line with *CCDC6-RET* fusion gene and the effect of *RET* inhibitors in vitro and in vivo. *Cancer Sci.* **104**, 896–903 (2013).
- M. L. Sos, K. Michel, T. Zander, J. Weiss, P. Frommolt, M. Peifer, D. Li, R. Ullrich, M. Koker, F. Fischer, T. Shimamura, D. Rauh, C. Mermel, S. Fischer, I. Stückerath, S. Heynck, R. Beroukhim, W. Lin, W. Winckler, K. Shah, T. LaFramboise, W. F. Moriarty, M. Hanna, L. Tolosi, J. Rahnenführer, R. Verhaak, D. Chiang, G. Getz, M. Hellmich, J. Wolf, L. Girard, M. Peyton, B. A. Weir, T.-H. Chen, H. Greulich, J. Barretina, G. I. Shapiro, L. A. Garraway, A. F. Gazdar, J. D. Minna, M. Meyerson, K.-K. Wong, R. K. Thomas, Predicting drug susceptibility of non-small cell lung cancers based on genetic lesions. *J. Clin. Invest.* **119**, 1727–1740 (2009).
- P. P. Knowles, J. Murray-Rust, S. Kjær, R. P. Scott, S. Hanrahan, M. Santoro, C. F. Ibáñez, N. Q. McDonald, Structure and chemical inhibition of the *RET* tyrosine kinase domain. *J. Biol. Chem.* **281**, 33577–33587 (2006).
- S. Müller, A. Chaikvad, N. S. Gray, S. Knapp, The ins and outs of selective kinase inhibitor development. *Nat. Chem. Biol.* **11**, 818–821 (2015).
- M. Hasegawa, N. Nishigaki, Y. Washio, K. Kano, P. A. Harris, H. Sato, I. Mori, R. I. West, M. Shibahara, H. Toyoda, L. Wang, R. T. Nolte, J. M. Veal, M. Cheung, Discovery of novel benzimidazoles as potent inhibitors of TIE-2 and VEGFR-2 tyrosine kinase receptors. *J. Med. Chem.* **50**, 4453–4470 (2007).
- B. Frett, F. Carlomagno, M. L. Moccia, A. Brescia, G. Federico, V. De Falco, B. Admire, Z. Chen, W. Qi, M. Santoro, H.-y. Li, Fragment-based discovery of a dual pan-*RET*/*VEGFR2* kinase inhibitor optimized for single-agent polypharmacology. *Angew. Chem. Int. Ed.* **54**, 8717–8721 (2015).
- F. Carlomagno, T. Guida, S. Anaganti, G. Vecchio, A. Fusco, A. J. Ryan, M. Billaud, M. Santoro, Disease associated mutations at valine 804 in the *RET* receptor tyrosine kinase confer resistance to selective kinase inhibitors. *Oncogene* **23**, 6056–6063 (2004).
- L. Mologni, S. Redaelli, A. Morandi, I. Plaza-Menacho, C. Gambacorti-Passerini, Ponatinib is a potent inhibitor of wild-type and drug-resistant gatekeeper mutant *RET* kinase. *Mol. Cell. Endocrinol.* **377**, 1–6 (2013).
- C.-H. Yun, K. E. Mengwasser, A. V. Toms, M. S. Woo, H. Greulich, K.-K. Wong, M. Meyerson, M. J. Eck, The T790M mutation in *EGFR* kinase causes drug resistance by increasing the affinity for ATP. *Proc. Natl. Acad. Sci. U.S.A.* **105**, 2070–2075 (2008).
- M. Azam, R. R. Latek, G. Q. Daley, Mechanisms of autoinhibition and STI-571/Imatinib resistance revealed by mutagenesis of *BCR-ABL*. *Cell* **112**, 831–843 (2003).
- J. M. Heuckmann, M. Hölzel, M. L. Sos, S. Heynck, H. Balke-Want, M. Koker, M. Peifer, J. Weiss, C. M. Lovly, C. Grütter, D. Rauh, W. Pao, R. K. Thomas, *ALK* mutations conferring differential resistance to structurally diverse *ALK* inhibitors. *Clin. Cancer Res.* **17**, 7394–7401 (2011).
- M. L. Sos, R. S. Levin, J. D. Gordan, J. A. Oses-Prieto, J. T. Webber, M. Salt, B. Hann, A. L. Burlingame, F. McCormick, S. Bandyopadhyay, K. M. Shokat, Oncogene mimicry as a mechanism of primary resistance to *BRAF* inhibitors. *Cell Rep.* **8**, 1037–1048 (2014).
- S. Chandralapaty, Negative feedback and adaptive resistance to the targeted therapy of cancer. *Cancer Discov.* **2**, 311–319 (2012).
- A. Subramanian, P. Tamayo, V. K. Mootha, S. Mukherjee, B. L. Ebert, M. A. Gillette, A. Paulovich, S. L. Pomeroy, T. R. Golub, E. S. Lander, J. P. Mesirov, Gene set enrichment analysis: A knowledge-based approach for interpreting genome-wide expression profiles. *Proc. Natl. Acad. Sci. U.S.A.* **102**, 15545–15550 (2005).
- C. A. Pratilas, B. S. Taylor, Q. Ye, A. Viale, C. Sander, D. B. Solit, N. Rosen, <sup>V600E</sup>*EBF1A* is associated with disabled feedback inhibition of *RAF*–*MEK* signaling and elevated transcriptional output of the pathway. *Proc. Natl. Acad. Sci. U.S.A.* **106**, 4519–4524 (2009).
- R. de Boer, Y. Humblet, J. Wolf, L. Nogová, K. Ruffert, T. Milenkova, R. Smith, A. Godwood, J. Vansteenkiste, An open-label study of vandetanib with pemtredex in patients with previously treated non-small-cell lung cancer. *Ann. Oncol.* **20**, 486–491 (2009).
- F. Bentzien, M. Zuzow, N. Heald, G. Gibson, Y. Shi, L. Goon, P. Yu, S. Engst, W. Zhang, D. Huang, L. Zhao, V. Vysotskaia, F. Chu, R. Bautista, B. Cancilla, P. Lamb, A. H. Joly, F. M. Yakes, In vitro and in vivo activity of cabozantinib (XL184), an inhibitor of *RET*, *MET*, and *VEGFR2*, in a model of medullary thyroid cancer. *Thyroid* **23**, 1569–1577 (2013).
- J. M. Gozgit, T.-H. Chen, T. Clackson, V. M. Rivera, *RET* fusions identified in colorectal cancer PDX models are sensitive to the potent *RET* inhibitor ponatinib. *Cancer Res.* **74**, 2726 (2014).

33. M. Yang, J. Cai, S. Guo, J.-P. Wery, H. Q. Li, Rapid conversion to resistance, of a colon PDX with ret-fusion, by ponatinib treatment could potentially be attributed to the introduction of the gate keeper mutation V804M. *Cancer Res.* **75**, 3581 (2015).
34. B. J. Solomon, T. Mok, D.-W. Kim, Y.-L. Wu, K. Nakagawa, T. Mekhail, E. Felip, F. Cappuzzo, J. Paolini, T. Usari, S. Iyer, A. Reisman, K. D. Wilner, J. Tursi, F. Blackhall, First-line crizotinib versus chemotherapy in ALK-positive lung cancer. *N. Engl. J. Med.* **371**, 2167–2177 (2014).
35. O. Gautschi, T. Zander, F. A. Keller, K. Strobel, A. Hirschmann, S. Aebi, J. Diebold, A patient with lung adenocarcinoma and RET fusion treated with vandetanib. *J. Thorac. Oncol.* **8**, e43–e44 (2013).
36. A. C. Dar, M. S. Lopez, K. M. Shokat, Small molecule recognition of c-Src via the imatinib-binding conformation. *Chem. Biol.* **15**, 1015–1022 (2008).
37. T. O'Hare, W. C. Shakespeare, X. Zhu, C. A. Eide, V. M. Rivera, F. Wang, L. T. Adrian, T. Zhou, W.-S. Huang, Q. Xu, C. A. Metcalf III, J. W. Tyner, M. M. Loriaux, A. S. Corbin, S. Wardwell, Y. Ning, J. A. Keats, Y. Wang, R. Sundaramoorthi, M. Thomas, D. Zhou, J. Snodgrass, L. Commodore, T. K. Sawyer, D. C. Dalgarno, M. W. N. Deininger, B. J. Druker, T. Clackson, AP24534, a pan-BCR-ABL inhibitor for chronic myeloid leukemia, potently inhibits the T3151 mutant and overcomes mutation-based resistance. *Cancer Cell* **16**, 401–412 (2009).
38. F. Carlomagno, S. Anaganti, T. Guida, G. Salvatore, G. Troncone, S. M. Wilhelm, M. Santoro, BAY 43-9006 inhibition of oncogenic RET mutants. *J. Natl. Cancer Inst.* **98**, 326–334 (2006).
39. J. F. Gainor, L. Dardaie, S. Yoda, L. Friboulet, I. Leshchiner, R. Katayama, I. Dagogo-Jack, S. Gadgeel, K. Schultz, M. Singh, E. Chin, M. Parks, D. Lee, R. H. DiCecca, E. Lockerman, T. Huynh, J. Logan, L. L. Ritterhouse, L. P. Le, A. Muniappan, S. Digumarthy, C. Channick, C. Keyes, G. Getz, D. Dias-Santagata, R. S. Heist, J. Lennerz, L. V. Sequist, C. H. Benes, A. J. Iafrate, M. Mino-Kenudson, J. A. Engelman, A. T. Shaw, Molecular mechanisms of resistance to first- and second-generation ALK inhibitors in ALK-rearranged lung cancer. *Cancer Discov.* **6**, 1118–1133 (2016).
40. L. Fernandez-Cuesta, D. Plenker, H. Osada, R. Sun, R. Menon, F. Leenders, S. Ortiz-Cuaran, M. Peifer, M. Bos, J. Daßler, F. Malchers, J. Schöttle, W. Vogel, I. Dahmen, M. Koker, R. T. Ullrich, G. M. Wright, P. A. Russell, Z. Wainer, B. Solomon, E. Brambilla, H. Nagy-Mignotte, D. Moro-Sibilot, C. G. Brambilla, S. Lantuejoul, J. Altmüller, C. Becker, P. Nürnberg, J. M. Heuckmann, E. Stoelben, I. Petersen, J. H. Clement, J. Sängler, L. A. Muscarella, A. la Torre, V. M. Fazio, I. Lahortiga, T. Perera, S. Ogata, M. Parade, D. Brehmer, M. Vingron, L. C. Heukamp, R. Buettner, T. Zander, J. Wolf, S. Perner, S. Ansén, S. A. Haas, Y. Yatabe, R. K. Thomas, *CD74-NRG1* fusions in lung adenocarcinoma. *Cancer Discov.* **4**, 415–422 (2014).
41. C. Dickhut, S. Radau, R. P. Zahedi, Fast, efficient, and quality-controlled phosphopeptide enrichment from minute sample amounts using titanium dioxide. *Methods Mol. Biol.* **1156**, 417–430 (2014).
42. J. Heil, S. M. Kast, 3D RISM theory with fast reciprocal-space electrostatics. *J. Chem. Phys.* **142**, 114107 (2015).
43. J. R. Wiśniewski, A. Zougman, N. Nagaraj, M. Mann, Universal sample preparation method for proteome analysis. *Nat. Methods* **6**, 359–362 (2009).
44. L. Kollipara, R. P. Zahedi, Protein carbamylation: In vivo modification or in vitro artefact? *Proteomics* **13**, 941–944 (2013).
45. J. M. Burkhardt, C. Schumbrutski, S. Wortelkamp, A. Sickmann, R. P. Zahedi, Systematic and quantitative comparison of digest efficiency and specificity reveals the impact of trypsin quality on MS-based proteomics. *J. Proteomics* **75**, 1454–1462 (2012).
46. K. Engholm-Keller, P. Birck, J. Størling, F. Pociot, T. Mandrup-Poulsen, M. R. Larsen, TISH—A robust and sensitive global phosphoproteomics strategy employing a combination of TiO<sub>2</sub>, SIMAC, and HILIC. *J. Proteomics* **75**, 5749–5761 (2012).
47. T. Taus, T. Köcher, P. Pichler, C. Paschke, A. Schmidt, C. Henrich, K. Mechtler, Universal and confident phosphorylation site localization using phosphoRS. *J. Proteome Res.* **10**, 5354–5362 (2011).
48. M. Spivak, J. Weston, L. Bottou, L. Käll, W. S. Noble, Improvements to the percolator algorithm for peptide identification from shotgun proteomics data sets. *J. Proteome Res.* **8**, 3737–3745 (2009).
49. Y. Xue, J. Ren, X. Gao, C. Jin, L. Wen, X. Yao, GPS 2.0, a tool to predict kinase-specific phosphorylation sites in hierarchy. *Mol. Cell. Proteomics* **7**, 1598–1608 (2008).
50. MODELLER; <https://salilab.org/modeller/>.
51. G. Sigalov, A. Fenley, A. Onufriev, Analytical electrostatics for biomolecules: Beyond the generalized Born approximation. *J. Chem. Phys.* **124**, 124902 (2006).
52. Amber; <http://ambermd.org/>.
53. J. Engel, A. Richters, M. Getlik, S. Tomassi, M. Keul, M. Termathe, J. Lategahn, C. Becker, S. Mayer-Wrangowski, C. Grütter, N. Uhlenbrock, J. Krüll, N. Schaumann, S. Eppmann, P. Kibies, F. Hoffgaard, J. Heil, S. Menninger, S. Ortiz-Cuaran, J. M. Heuckmann, V. Tinnefeld, R. P. Zahedi, M. L. Sos, C. Schultz-Fademrecht, R. K. Thomas, S. M. Kast, D. Rauh, Targeting drug resistance in EGFR with covalent inhibitors: A structure-based design approach. *J. Med. Chem.* **58**, 6844–6863 (2015).
54. W. L. Jorgensen, J. Chandrasekhar, J. D. Madura, R. W. Impey, M. L. Klein, Comparison of simple potential functions for simulating liquid water. *J. Chem. Phys.* **79**, 926–935 (1983).
55. NAMM; [www.ks.uiuc.edu/Research/namm/](http://www.ks.uiuc.edu/Research/namm/).
56. D. Beglov, B. Roux, An integral equation to describe the solvation of polar molecules in liquid water. *J. Phys. Chem. B* **101**, 7821–7826 (1997).
57. A. Kovalenko, F. Hirata, Three-dimensional density profiles of water in contact with a solute of arbitrary shape: A RISM approach. *Chem. Phys. Lett.* **290**, 237–244 (1998).
58. F. Mrugalla, S. M. Kast, Designing molecular complexes using free-energy derivatives from liquid-state integral equation theory. *J. Phys.: Condens. Matter* **28**, 344004 (2016).
59. C. Trapnell, L. Pachter, S. L. Salzberg, TopHat: Discovering splice junctions with RNA-Seq. *Bioinformatics* **25**, 1105–1111 (2009).
60. M. Lawrence, W. Huber, H. Pagès, P. Aboyoun, M. Carlson, R. Gentleman, M. T. Morgan, V. J. Carey, A. Pric, Software for computing and annotating genomic ranges. *PLOS Comput. Biol.* **9**, e1003118 (2013).
61. M. I. Love, W. Huber, S. Anders, Moderated estimation of fold change and dispersion for RNA-seq data with DESeq2. *Genome Biol.* **15**, 550 (2014).
62. A. Liberzon, C. Birger, H. Thorvaldsdóttir, M. Ghandi, J. P. Mesirov, P. Tamayo, The Molecular Signatures Database (MSigDB) hallmark gene set collection. *Cell Syst.* **1**, 417–425 (2015).
63. V. K. Mootha, C. M. Lindgren, K.-F. Eriksson, A. Subramanian, S. Sihag, J. Lehár, P. Puigserver, E. Carlsson, M. Ridderstråle, E. Laurila, N. Houstis, M. J. Daly, N. Patterson, J. P. Mesirov, T. R. Golub, P. Tamayo, B. Spiegelman, E. S. Lander, J. N. Hirschhorn, D. Altshuler, L. C. Groop, PGC-1 $\alpha$ -responsive genes involved in oxidative phosphorylation are coordinately downregulated in human diabetes. *Nat. Genet.* **34**, 267–273 (2003).
64. M. W. Karaman, S. Herrgard, D. K. Treiber, P. Gallant, C. E. Atteridge, B. T. Campbell, K. W. Chan, P. Ciceri, M. I. Davis, P. T. Edeen, R. Fararoni, M. Floyd, J. P. Hunt, D. J. Lockhart, Z. V. Milanov, M. J. Morrison, G. Pallares, H. K. Patel, S. Pritchard, L. M. Wodicka, P. P. Zarrinkar, A quantitative analysis of kinase inhibitor selectivity. *Nat. Biotechnol.* **26**, 127–132 (2008).
65. M. I. Davis, J. P. Hunt, S. Herrgard, P. Ciceri, L. M. Wodicka, G. Pallares, M. Hocker, D. K. Treiber, P. P. Zarrinkar, Comprehensive analysis of kinase inhibitor selectivity. *Nat. Biotechnol.* **29**, 1046–1051 (2011).
66. A. E. Drilon, C. S. Sima, R. Somwar, R. Smith, M. S. Ginsberg, G. J. Riely, C. M. Rudin, M. Ladanyi, M. G. Kris, N. A. Rizvi, Phase II study of cabozantinib for patients with advanced RET-rearranged lung cancers, paper presented at 2015 ASCO Annual Meeting (2015).

**Acknowledgments:** We thank T. Zillinger from the University Hospital Bonn for sharing the Cas9 expression and the backbone of the pLenti-IRES-blasticidin vector system, F. Malchers and members of the Sos Lab and Thomas Lab for the technical support, A. Florin and U. Rommerscheidt-Fuß for supporting us with IHC staining, and P. Kibies and L. Eberlein as well as L. Goeminne and L. Clement for supporting the computational modeling. We thank W. Pao and N. von Bubnoff for the TPC-1 and Ba/F3 cell line. We thank AstraZeneca for supporting vandetanib for off-label use, SOBI for providing cabozantinib for compassionate use, and F. Aebersold and A. Hirschmann for the diagnostic work. We also thank A. Dar and R. Cagan for helpful discussions. **Funding:** This work was supported by the German federal state North Rhine Westphalia and by the European Union (European Regional Development Fund: Investing In Your Future) as part of the PerMed.NRW initiative (grant 005-1111-0025 to R.K.T., J.W., and R.B.) as well as the EFRE initiative (grant LS-1-1-030 to R.B., J.W., R.K.T., and M.L.S.) and by the German Ministry of Science and Education (BMBF) as part of the e:Med program [grant nos. 01ZX1303 (to M.P.), 01ZX1603 (to R.K.T., J.W., and R.B.), and 01ZX1406 (to M.P. and M.L.S.)], by the Deutsche Forschungsgemeinschaft [through TH1386/3-1 (to R.K.T. and M.L.S. and JA1381/5-1 (to S.M.K.)], and by the German Consortium for Translational Cancer Research (DKTK) Joint Funding program. V.T. is the recipient of a joint European Respiratory Society/European Molecular Biology Organization Long-Term Research fellowship no. LTRF 2014-2951. N.Q.M. acknowledges that this work was supported by the Francis Crick Institute, which receives its core funding from Cancer Research UK (FC001115), the UK Medical Research Council (FC001115), and the Wellcome Trust (FC001115); by the NCI/NIH (grant reference 5R01CA197178); and by the Association for Multiple Endocrine Neoplasia Disorders MTC Research Fund. The authors acknowledge financial support by the Ministerium für Innovation, Wissenschaft und Forschung des Landes Nordrhein-Westfalen, the Senatsverwaltung für Wirtschaft, Technologie und Forschung des Landes Berlin, and the Bundesministerium für Bildung und Forschung (to O.P. and R.P.Z.). **Author contributions:** D.P., M.R., J.B., M.A.D., C.L., and D.S. performed the cloning and cell culture experiments. V.T., A.H.S., and R.B. analyzed the IHC and FISH images. Y.S. was responsible for the PDX establishment and measurements. J.S., F.M., Y.A., and S.M.K. performed the computational modeling. O.P. and R.P.Z. performed the quantitative phosphoproteomics and data analysis. M.K., M.B., A.R., J.S., J.E., M.A., and K.G. performed the in vitro kinase experiments and analyses. R.C., P.P.K., and N.Q.M. purified the recombinant RET fusion proteins and performed the thermal shift analyses. J.D., G.P., and O.G. contributed to the clinical patient data. F.L. and J.M.H. were responsible for the next-generation sequencing of RET. J.B. and M.P. analyzed the RNA-seq data. K.M.S. provided the compounds. D.P., M.R., J.B., M.D., F.L., J.W., N.Q.M., K.M.S., R.K.T., and M.L.S. interpreted the data and performed the statistical analyses. D.P., M.R., S.M.K., R.K.T., O.G., and M.L.S. wrote the manuscript. **Competing interests:** R.K.T. is a founder and consultant of NEO New Oncology GmbH and received commercial research grants from AstraZeneca, EOS, and Merck KgaA and honoraria from AstraZeneca, Bayer, NEO New Oncology AG, Boehringer Ingelheim, Clovis Oncology, Daiichi-Sankyo, Eli Lilly, Johnson & Johnson, Merck KgaA, MSD, Puma, Roche, and

Sanofi. F.L. and J.M.H. are employees of NEO New Oncology GmbH. M.L.S. received commercial research grants from Novartis. K.M.S. and M.L.S. are both patent holders for the compound AD80. K.M.S. and M.L.S., together with A. C. Dar, T. K. Das, T. G. Bivona, and R. L. Cagan, are inventors on a patent application (applicants Mount Sinai School of Medicine and the Regents of the University of California; publication no. US 2014/0243357 A1) that covers the compounds AD80, AD57, and AD81 and the use thereof. All other authors declare that they have no competing interests. **Data and materials availability:** RNA-seq data were deposited at the European Genome-phenome Archive ([www.ebi.ac.uk/ega/](http://www.ebi.ac.uk/ega/); accession number EGAS00001002335). The mass spectrometry proteomics data have been deposited to the ProteomeXchange Consortium via the PRIDE (Proteomics Identifications) partner repository with the data set identifier PXD006006. The Shokat Lab provided AD80, AD81, and AD57; compounds will be made available upon request. The remaining compounds were purchased from LC Laboratories and Selleckchem.

Submitted 21 July 2016  
Resubmitted 3 February 2017  
Accepted 21 March 2017  
Published 14 June 2017  
10.1126/scitranslmed.aah6144

**Citation:** D. Plenker, M. Riedel, J. Brägelmann, M. A. Dammert, R. Chauhan, P. P. Knowles, C. Lorenz, M. Keul, M. Bührmann, O. Pagel, V. Tischler, A. H. Scheel, D. Schütte, Y. Song, J. Stark, F. Mrugalla, Y. Alber, A. Richters, J. Engel, F. Leenders, J. M. Heuckmann, J. Wolf, J. Diebold, G. Pall, M. Peifer, M. Aerts, K. Gevaert, R. P. Zahedi, R. Buettner, K. M. Shokat, N. Q. McDonald, S. M. Kast, O. Gautschi, R. K. Thomas, M. L. Sos, Drugging the catalytically inactive state of RET kinase in RET-rearranged tumors. *Sci. Transl. Med.* **9**, eaah6144 (2017).

## Drugging the catalytically inactive state of RET kinase in RET-rearranged tumors

Dennis Plenker, Maximilian Riedel, Johannes Brägelmann, Marcel A. Dammert, Rakhee Chauhan, Phillip P. Knowles, Carina Lorenz, Marina Keul, Mike Bührmann, Oliver Pagel, Verena Tischler, Andreas H. Scheel, Daniel Schütte, Yanrui Song, Justina Stark, Florian Mrugalla, Yannic Alber, André Richters, Julian Engel, Frauke Leenders, Johannes M. Heuckmann, Jürgen Wolf, Joachim Diebold, Georg Pall, Martin Peifer, Maarten Aerts, Kris Gevaert, René P. Zahedi, Reinhard Buettner, Kevan M. Shokat, Neil Q. McDonald, Stefan M. Kast, Oliver Gautschi, Roman K. Thomas and Martin L. Sos

*Sci Transl Med* 9, eaah6144.  
DOI: 10.1126/scitranslmed.aah6144

### RET-ting out lung tumors

Gene fusions and rearrangements serve as oncogenic drivers in a number of tumor types, and some of these can be targeted with existing drugs. *RET* rearrangements have been identified as drivers in some lung adenocarcinomas, but previous attempts to target *RET* have not been successful. Plenker *et al.* determined why the drugs previously proposed for inhibiting *RET* were not sufficiently potent and showed that successful inhibition of *RET* requires the ability to bind *RET* in its catalytically inactive conformation, known as the "DFG-out conformation," thus locking it in an inactive state. The authors also identified drugs that bind *RET* in the desired conformation and demonstrated their efficacy in patient-derived xenograft models.

ARTICLE TOOLS	<a href="http://stm.sciencemag.org/content/9/394/eaah6144">http://stm.sciencemag.org/content/9/394/eaah6144</a>
SUPPLEMENTARY MATERIALS	<a href="http://stm.sciencemag.org/content/suppl/2017/06/12/9.394.eaah6144.DC1">http://stm.sciencemag.org/content/suppl/2017/06/12/9.394.eaah6144.DC1</a>
RELATED CONTENT	<a href="http://stm.sciencemag.org/content/scitransmed/9/380/eaag0339.full">http://stm.sciencemag.org/content/scitransmed/9/380/eaag0339.full</a> <a href="http://stm.sciencemag.org/content/scitransmed/8/368/368ra172.full">http://stm.sciencemag.org/content/scitransmed/8/368/368ra172.full</a> <a href="http://stm.sciencemag.org/content/scitransmed/8/350/350ra104.full">http://stm.sciencemag.org/content/scitransmed/8/350/350ra104.full</a> <a href="http://stm.sciencemag.org/content/scitransmed/5/209/209ra153.full">http://stm.sciencemag.org/content/scitransmed/5/209/209ra153.full</a>
REFERENCES	This article cites 61 articles, 13 of which you can access for free <a href="http://stm.sciencemag.org/content/9/394/eaah6144#BIBL">http://stm.sciencemag.org/content/9/394/eaah6144#BIBL</a>
PERMISSIONS	<a href="http://www.sciencemag.org/help/reprints-and-permissions">http://www.sciencemag.org/help/reprints-and-permissions</a>

Use of this article is subject to the [Terms of Service](#)

*Science Translational Medicine* (ISSN 1946-6242) is published by the American Association for the Advancement of Science, 1200 New York Avenue NW, Washington, DC 20005. The title *Science Translational Medicine* is a registered trademark of AAAS.

Copyright © 2017 The Authors, some rights reserved; exclusive licensee American Association for the Advancement of Science. No claim to original U.S. Government Works.

## **MYC paralog-dependent apoptotic priming orchestrates a spectrum of vulnerabilities in small cell lung cancer**

**Dammert MA**, Brägelmann J, Olsen RR, Böhm S, Monhasery N, Whitney CP, Chalishazar MD, Tumbrink HL, Guthrie MR, Klein S, Ireland AS, Ryan J, Schmitt A, Marx A, Ozretić L, Castiglione R, Lorenz C, Jachimowicz RD, Wolf E, Thomas RK, Poirier JT, Büttner R, Sen Triparna, Byers LA, Reinhardt HC, Letai A, Oliver TG, Sos ML.

Specific contributions:

- Generation and validation of CRISPRa cell lines
- Viability screening, Western blot analysis of CRISPRa cell lines and human SCLC cell lines
- Bisulfite sequencing of human SCLC cell lines
- ChIP experiments of human SCLC lines
- shRNA knockdown experiments in CRISPRa cell lines
- Overexpression experiments in CRISPRa cell lines
- Crystal violet combination assays in CRISPRa cell lines
- Generation and analysis of chemoresistant CRISPRa cell lines
- Manuscript writing and editing

ARTICLE

<https://doi.org/10.1038/s41467-019-11371-x>

OPEN

# MYC paralog-dependent apoptotic priming orchestrates a spectrum of vulnerabilities in small cell lung cancer

Marcel A. Dammert<sup>1,2,3,14</sup>, Johannes Brägelmann<sup>1,2,3,4,14</sup>, Rachele R. Olsen<sup>5,14</sup>, Stefanie Böhm<sup>2,3,14</sup>, Niloufar Monhasery<sup>1,2,3</sup>, Christopher P. Whitney<sup>5</sup>, Milind D. Chalise<sup>5</sup>, Hannah L. Tumbrink<sup>1,2,3</sup>, Matthew R. Guthrie<sup>5</sup>, Sebastian Klein<sup>2,3,4,6</sup>, Abbie S. Ireland<sup>5</sup>, Jeremy Ryan<sup>7</sup>, Anna Schmitt<sup>8,9</sup>, Annika Marx<sup>1,2,3</sup>, Luka Ozretić<sup>10</sup>, Roberta Castiglione<sup>4,6</sup>, Carina Lorenz<sup>1,2,3</sup>, Ron D. Jachimowicz<sup>8,9</sup>, Elmar Wolf<sup>11</sup>, Roman K. Thomas<sup>2</sup>, John T. Poirier<sup>12</sup>, Reinhard Büttner<sup>6</sup>, Triparna Sen<sup>13</sup>, Lauren A. Byers<sup>13</sup>, H. Christian Reinhardt<sup>4,8,9</sup>, Anthony Letai<sup>7</sup>, Trudy G. Oliver<sup>5</sup> & Martin L. Sos<sup>1,2,3</sup>

MYC paralogs are frequently activated in small cell lung cancer (SCLC) but represent poor drug targets. Thus, a detailed mapping of MYC-paralog-specific vulnerabilities may help to develop effective therapies for SCLC patients. Using a unique cellular CRISPR activation model, we uncover that, in contrast to MYCN and MYCL, MYC represses *BCL2* transcription via interaction with MIZ1 and DNMT3a. The resulting lack of *BCL2* expression promotes sensitivity to cell cycle control inhibition and dependency on MCL1. Furthermore, MYC activation leads to heightened apoptotic priming, intrinsic genotoxic stress and susceptibility to DNA damage checkpoint inhibitors. Finally, combined AURK and CHK1 inhibition substantially prolongs the survival of mice bearing MYC-driven SCLC beyond that of combination chemotherapy. These analyses uncover MYC-paralog-specific regulation of the apoptotic machinery with implications for genotype-based selection of targeted therapeutics in SCLC patients.

<sup>1</sup>Molecular Pathology, Institute of Pathology, University Hospital of Cologne, 50937 Cologne, Germany. <sup>2</sup>Department of Translational Genomics, Center of Integrated Oncology Cologne-Bonn, Medical Faculty, University of Cologne, 50931 Cologne, Germany. <sup>3</sup>Center for Molecular Medicine Cologne, University of Cologne, 50931 Cologne, Germany. <sup>4</sup>Else Kröner Forschungskolleg Clonal Evolution in Cancer, University Hospital Cologne, 50931 Cologne, Germany. <sup>5</sup>Department of Oncological Sciences, Huntsman Cancer Institute, University of Utah, Salt Lake City, UT 84112, USA. <sup>6</sup>Institute of Pathology, University Hospital of Cologne, 50937 Cologne, Germany. <sup>7</sup>Dana-Farber Cancer Institute, Harvard Medical School, Boston, MA 02215, USA. <sup>8</sup>Department I of Internal Medicine, University Hospital of Cologne, 50931 Cologne, Germany. <sup>9</sup>Cologne Excellence Cluster on Cellular Stress Response in Aging-Associated Diseases, University of Cologne, 50931 Cologne, Germany. <sup>10</sup>Department of Cellular Pathology, Royal Free Hospital, London NW3 2QG, UK. <sup>11</sup>Theodor Boveri Institute, Biocenter, University of Würzburg, 97074 Würzburg, Germany. <sup>12</sup>Memorial Sloan Kettering Cancer Center, New York, NY 10065, USA. <sup>13</sup>Department of Thoracic and Head & Neck Medical Oncology, University of Texas, MD Anderson Cancer Center, Houston, TX 77030, USA. <sup>14</sup>These authors contributed equally: Marcel A. Dammert, Johannes Brägelmann, Rachele R. Olsen, Stefanie Böhm. Correspondence and requests for materials should be addressed to T.G.O. (email: [trudy.oliver@hci.utah.edu](mailto:trudy.oliver@hci.utah.edu)) or to M.L.S. (email: [martin.sos@uni-koeln.de](mailto:martin.sos@uni-koeln.de))

Small cell lung cancer (SCLC) is an aggressive neuroendocrine subtype of lung cancer with a 5-year survival rate of only 6% that lacks effective targeted therapies or predictive markers for patient stratification. Genomic amplification of one of the transcription factor paralogs *MYC*, *MYCN*, or *MYCL* occurs in approximately 20% of SCLC patients<sup>1,2</sup>. *MYC* paralog activation is important for tumorigenesis and tumor maintenance, which would make *MYC* an ideal target for therapeutic intervention<sup>3–5</sup>. While direct inhibition of *MYC* has not yet been achieved, *MYC* paralog activation in SCLC induces distinct sensitivity profiles to targeted agents such as Aurora Kinase (AURK) or DNA damage checkpoint inhibitors that are preferentially effective in *MYC*-activated cells<sup>6–9</sup>. At the same time, BH3 mimetics, including drugs directed against the anti-apoptotic factors *BCL2* and *MCL1*, represent an attractive class of inhibitors in SCLC but it remains unclear which molecular factors prime susceptibility to these targets<sup>10</sup>. How overexpression of the individual *MYC* paralogs shapes the spectrum of vulnerabilities in SCLC remains elusive.

We hypothesize that a mechanistic understanding of the phenotypic differences associated with activation of individual *MYC* paralogs may allow the discovery of molecularly defined drug targets in SCLC patients. Using CRISPR/dCas9-mediated *MYC* paralog activation, we uncover a link between *MYC* signaling and the regulation of the apoptotic machinery with direct implications for the selection of targeted drugs for SCLC patients.

## Results

***MYC* activation is associated with low *BCL2* expression.** We analyzed transcriptomes of 42 patient-derived SCLC cell lines and 81 SCLC patient samples<sup>1,6,11</sup> and found that overexpression of individual *MYC* paralogs is largely mutually exclusive in both datasets (Fig. 1a, b). At the same time, the impact of individual *MYC* paralogs on overall survival remains unclear due to the limited amount of available expression data in SCLC patient cohorts (Supplementary Fig. 1a)<sup>12</sup>. These observations prompted us to dissect the specific role of each *MYC* paralog in SCLC, with the CRISPR/dCas9 Synergistic Activation Mediator (SAM) CRISPR activation (CRISPRa) system<sup>13</sup> that allows efficient induction of endogenous gene expression. After single guide RNA (sgRNA) selection and validation in NIH3T3 and GEMM-derived (*Trp53/Rb1*-deficient mice, RP) mouse embryonic fibroblasts (MEFs), we activated *Myc*, *Mycn*, or *Mycl* in genomically profiled (whole-exome sequencing (WES)) cells derived from early stage SCLC (RP) tumors<sup>14</sup> (Supplementary Fig. 1b–d). We observed increased transcription of the individual *Myc* paralogs and elevated *MYC* and *MYCN* protein expression (Fig. 1c, d). Although the magnitude of upregulation differed among *Myc* paralogs (Fig. 1c and Supplementary Fig. 1b, c), canonical *MYC* target genes<sup>6</sup> were similarly upregulated and proliferation rates were similar between individual cells (Fig. 1c and Supplementary Fig. 1e). However, *Myc*- but not *Mycn*- or *Mycl*-activation induced sensitivity to the AURK inhibitor, alisertib (Fig. 1e), and other cell cycle checkpoint inhibitors (volasertib,  $p = 0.006$  mock vs. *Myc*; adavosertib,  $p = 0.05$  mock vs. *Myc*, two-tailed unpaired  $t$  test) similar to patient-derived SCLC cells<sup>6,7</sup> (Supplementary Fig. 1f).

We next determined differentially expressed genes in *MYC*-high ( $n = 22$ ) vs. *MYC*-low ( $n = 20$ ) human SCLC cell lines (Fig. 1a)<sup>6,7</sup> to investigate these *MYC*-specific vulnerabilities. Consistent with the *MYC*-associated variant SCLC phenotype, high *MYC* expression correlated with elevated *NEUROD1* (Fig. 1f)<sup>6</sup>. Intriguingly, anti-apoptotic factor *BCL2* was significantly downregulated in *MYC*-overexpressing cells while other *BCL2* family members were not differentially expressed (Fig. 1f and Supplementary Fig. 1g, h). In addition, we observed a modest

trend toward a negative correlation of *MYC* and *BCL2* in an independent cohort of SCLC patients<sup>15</sup> (Supplementary Fig. 1i) and significantly decreased *Bcl2* expression in *Myc*-high tumors of *Myc*-driven SCLC mice (RPM) compared to *Trp53/Rb1*-deficient SCLC mouse tumors with low *Myc* expression (Supplementary Fig. 1j)<sup>6</sup>. Furthermore, *BCL2* and *ASCL1* proteins were only expressed in *MYCN*- and *MYCL*-amplified cells (Fig. 1g and Supplementary Fig. 1k). We observed a similar anti-correlation of *MYC* and *BCL2* protein levels in immunohistochemical (IHC) stainings of human SCLC tumor specimens ( $n = 48$ ) (Fig. 1h and Supplementary Table 1). *Myc* activation also suppressed *Bcl2* expression in CRISPRa cells ( $p = 0.004$  mock vs. *Myc*, two-tailed unpaired  $t$  test) (Fig. 1i). This anti-correlation between *MYC* and *BCL2* appears to be an exception rather than the rule since we primarily found a positive correlation between *MYC* and *BCL2* expression in the pan-cancer CCLE cohort<sup>16,17</sup> (Supplementary Fig. 1l). Reintroduction of *BCL2* strongly reduced sensitivity toward alisertib in both *MYC*-amplified patient-derived cell lines (Fig. 1j, k) and *Myc*-activated CRISPRa cells (Fig. 1l, m). Conversely, co-treatment of *BCL2*-overexpressing *Myc*-activated CRISPRa cells with *BCL2*-specific inhibitor venetoclax restored the activity of alisertib (Fig. 1m). Of note, exogenous *BCL2* overexpression did not alter cell cycle progression or proliferation rates (Supplementary Fig. 1m, n). Thus *MYC* paralog expression is tightly linked with *BCL2* expression, which determines susceptibility to cell cycle checkpoint inhibitors.

***MYC* represses *BCL2* expression.** As reported previously<sup>10</sup>, *BCL2* expression only partially translated into *BCL2* inhibitor activity (Fig. 2a, b and Supplementary Fig. 2a–d). Patient-derived ( $n = 4$ ) and murine CRISPRa cell lines with *MYCN/Mycn* overexpression were sensitive to *BCL2* inhibitors navitoclax and ABT-737, whereas *MYC/Myc*-overexpressing cells were more resistant to *BCL2* inhibition (Fig. 2a, b and Supplementary Fig. 2a–d). Since the CRISPRa cells showed an adherent growth phenotype that is associated with basal activation of *Myc* in these cells<sup>6,18</sup>, we performed short hairpin RNA (shRNA)-mediated knockdown of the endogenous *Myc* in *Mycn*-activated CRISPRa cells (Fig. 2c and Supplementary Fig. 2e). *Myc* knockdown induced *Bcl2* expression (Fig. 2c) and increased sensitivity to *BCL2* inhibitors (Fig. 2d, e and Supplementary Fig. 2f, g). Since repression of *BCL2* correlates with high DNA methylation at the *BCL2* promoter<sup>19</sup>, we assayed DNA methylation levels of the CpG island within the *BCL2* promoter in human SCLC cell lines. *MYC*-amplified cell lines ( $n = 3$ ) displayed high DNA methylation levels at the *BCL2* promoter (Fig. 2f), whereas *MYCN*- or *MYCL*-amplified cells ( $n = 3$ ) exhibited significantly less DNA methylation in this region indicating active transcription (*MYC*-amplified vs. non-*MYC*-amplified  $p = 0.0001$ , two-tailed unpaired  $t$  test; Fig. 2g). Similarly, high *MYC* expression correlated with high levels of *BCL2* promoter methylation in published methylation data of SCLC cell lines ( $n = 65$ ) (Supplementary Fig. 2h)<sup>20</sup> and patient-derived xenograft SCLC models (Supplementary Fig. 2i, j)<sup>21</sup>. These observations implicate a functional link between high *MYC* expression, increased *BCL2* promoter methylation, and low *BCL2* expression.

*MYC* was shown to facilitate the establishment of DNA methylation at gene promoters by cooperating with MIZ1 and DNA methyltransferase 3a (DNMT3a)<sup>22</sup>. Using chromatin immunoprecipitation (ChIP) assays, we observed co-occupancy of *MYC*, MIZ1, and DNMT3a at the *BCL2* promoter (Fig. 2h) with *MYC* binding at the transcriptionally inactive *BCL2* promoter being as pronounced as at the active *ACTB* promoter. MIZ1 and DNMT3a were enriched only at the *BCL2* promoter in *MYC*-high cells (Fig. 2h). This suggests that *MYC/MIZ1/*

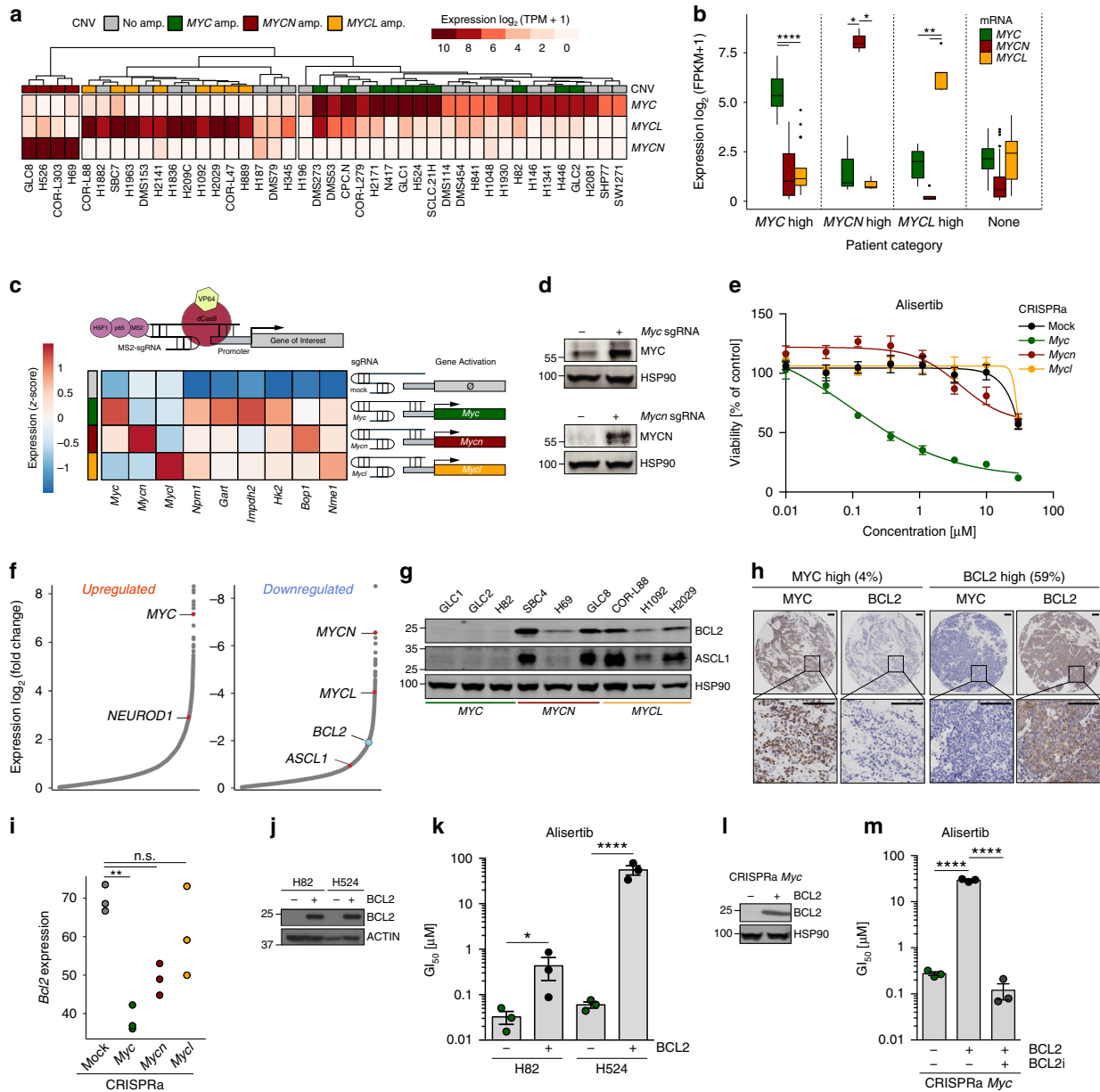


**Fig. 1** MYC activation is associated with low *BCL2* expression. **a** MYC paralog expression (TPM) and copy number variation (CNV) in human small cell lung cancer (SCLC) cell lines ( $n = 42$ ). **b** MYC paralog expression in SCLC patients. Center line (median), lower/upper box hinges (25th/75th percentile), whiskers extend to the most extreme value within  $1.5\times$  interquartile range (IQR) of the hinges. **c** CRISPRa system for transcriptional upregulation of *Myc* paralogs (top). Expression (z-scores) of *Myc* paralogs and *Myc* target genes in CRISPRa cells (bottom). **d** Western blot showing MYC and MYCN in *Myc*- and *Mycn*-activated CRISPRa cells compared to mock control. HSP90 was used as a loading control. **e** Viability screening of *Myc*-activated CRISPRa cells treated with alisertib for 96 h ( $n = 3$ ). **f** Differentially upregulated and downregulated genes (sorted by  $\log_2$  fold-change) in human SCLC cell lines ( $n = 42$ ) with high MYC ( $n = 22$ ) vs. low MYC ( $n = 20$ ) expression. **g** Western blot of ASCL1 and BCL2 in MYC paralog-amplified human SCLC cell lines ( $n = 9$ ). HSP90 was used as a loading control. **h** Immunohistochemical staining of MYC and BCL2 in tumors of SCLC patients with high MYC (left) or high BCL2 (right) expression (percentage of patients in the cohort ( $n = 49$ ) with high BCL2 or MYC levels is indicated). Scale bar = 100  $\mu\text{m}$ . **i** *Bcl2* expression (counts normalized to library size) in *Myc* paralog-activated CRISPRa cells. Benjamini–Hochberg-adjusted  $p$  values for *Myc* paralogs were obtained as contrasts of a global differential expression test. **j** Western blot showing BCL2 levels in MYC-amplified H82 and H524 cells  $\pm$  BCL2 overexpression. HSP90 was used as a loading control. **k**  $\text{GI}_{50}$  values of MYC-amplified H82 and H524 cells  $\pm$  BCL2 overexpression treated with alisertib for 72 h ( $n = 3$ ). **l** Western blot of BCL2 in *Myc*-activated CRISPRa cells  $\pm$  BCL2 overexpression. HSP90 was used as a loading control. **m**  $\text{GI}_{50}$  values of *Myc*-activated CRISPRa cells  $\pm$  BCL2 overexpression treated with alisertib alone or in combination with 500 nM venetoclax (BCL2i;  $n = 3$ ). Error bars indicate mean  $\pm$  SEM. Two-tailed unpaired  $t$  tests, \*\*\*\* $p < 0.0001$ , \*\* $p < 0.01$ , \* $p < 0.05$ . Source data are provided as a Source Data file

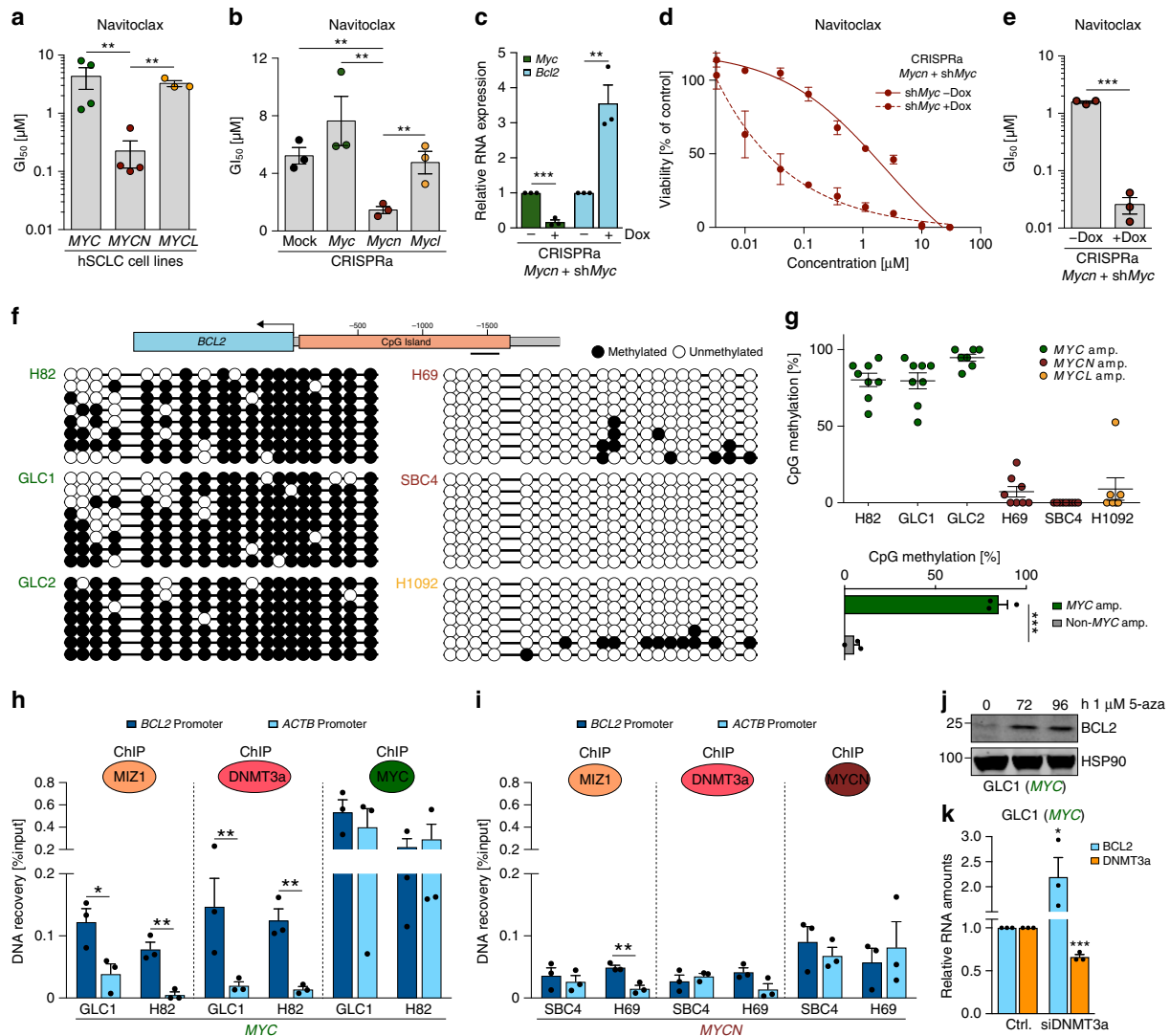


**Fig. 2** MYC represses *BCL2* expression. **a**  $GI_{50}$  values of MYC ( $n = 4$ ; GLC1, H82, H524, GLC2), MYCN ( $n = 4$ ; GLC8, H69, SBC4, COR-L303), and MYCL ( $n = 3$ ; H1092, H2029, SBC7) human small cell lung cancer (SCLC) cell lines treated with navitoclax for 96 h ( $n = 3$ ). **b**  $GI_{50}$  values of *Myc* paralog-activated CRISPRa cells treated with navitoclax for 96 h ( $n = 3$ ). **c** Relative mRNA levels (quantitative reverse transcription polymerase chain reaction (qRT-PCR)) of *Myc* and *Bcl2* in *Mycn*-activated CRISPRa cells with Tet-inducible *Myc* knockdown by shRNA at 72 h after doxycycline treatment ( $n = 3$ ). Data were normalized to 18S rRNA. **d** Viability screening of *Mycn*-activated CRISPRa cells after *Myc* knockdown treated with navitoclax for 96 h ( $n = 3$ ). **e**  $GI_{50}$  values of viability screening in **d** ( $n = 3$ ). **f** DNA methylation at the *BCL2* promoter (indicated region) measured by bisulfite sequencing. Lollipop diagram representing methylated (black) and unmethylated (white) CpGs in MYC (H82:  $n = 8$ , GLC1:  $n = 8$ , GLC2:  $n = 7$ ), MYCN (H69:  $n = 8$ , SBC4:  $n = 8$ ), and MYCL (H1092:  $n = 7$ ) amplified human SCLC cell lines. **g** Percentage of methylated CpG residues in MYC (H82, GLC1, GLC2), MYCN (H69, SBC4), and MYCL (H1092) amplified human SCLC cell lines (top). CpG methylation percentage (**f**) in SCLC cell lines ( $n = 6$ ) grouped by MYC amplification status (MYC-high  $n = 3$ , MYC-low  $n = 3$ ; bottom). **h, i** Occupancy at the *BCL2* promoter of MYC, MIZ1, and DNMT3a in MYC-amplified cells (GLC1, H82) (**h**) and of MYCN, MIZ1, and DNMT3a in MYCN-amplified cells (SBC4, H69) (**i**) measured by chromatin immunoprecipitation (ChIP) quantitative real-time PCR ( $n = 3$ ). ChIP signal is displayed as percentage of input. IgG (non-specific antibody control) signal was subtracted from ChIP signal of specific antibodies. **j** Western blot showing *BCL2* in MYC-amplified GLC1 cells treated with 1  $\mu$ M 5-azacytidine for the indicated times. HSP90 was used as loading control. **k** Relative mRNA expression (qRT-PCR) of *BCL2* and *DNMT3a* in MYC-amplified GLC1 cells treated with control small interfering RNA (siRNA) or *DNMT3a* siRNA ( $n = 3$ ). Data were normalized to 18S rRNA. Error bars indicate mean  $\pm$  SEM. Two-tailed unpaired *t* tests, \*\*\* $p < 0.001$ , \*\* $p < 0.01$ , \* $p < 0.05$ . Source data are provided as a Source Data file

DNMT3a may cooperatively mediate DNA methylation of the *BCL2* promoter (Fig. 2f). In contrast, in MYCN-amplified cells only low levels of MIZ1 and DNMT3a were bound to the *BCL2* promoter with no enrichment of DNMT3a compared to the *ACTB* promoter (Fig. 2i). Consistent with previous studies, only MYC but not MYCN or MYCL substantially interacted with

MIZ1 (Supplementary Fig. 2k), which is consistent with the model of MYC-specific *BCL2* repression<sup>23,24</sup>. Finally, both pharmacological inhibition of DNA methylation by 5-azacytidine in GLC1 cells as well as small interfering RNA (siRNA)-mediated DNMT3a knockdown in two MYC-amplified SCLC cell lines led to de-repression of *BCL2* (Fig. 2j, k

and Supplementary Fig. 2l). Thus DNMT3-mediated DNA methylation may play an important role in the MYC-induced repression of BCL2.

**MYC drives apoptotic priming and MCL1 dependency.** To assess the impact of differential BCL2 expression on the apoptotic machinery, we performed BH3 profiling<sup>25</sup> and observed that MYC-amplified SCLC cell lines ( $n=4$ ) were more primed for apoptosis induction (Fig. 3a) especially by MS1 peptide, which acts as an MCL1 antagonist (MYC-amplified vs. non-MYC-amplified  $p=0.01$ , two-tailed unpaired  $t$  test) (Fig. 3b). Consistently, MYC-amplified SCLC cell lines ( $n=4$ ) were more sensitive to MCL1 inhibitor S63845<sup>26</sup> compared to MYCN- ( $n=3$ ) and MYCL- ( $n=4$ ) amplified cell lines ( $p=0.003$  MYC vs. MYCN;  $p=0.001$  MYC vs. MYCL, two-tailed unpaired  $t$  test) (Fig. 3c, d and Supplementary Fig. 3a). Despite a lower activity against murine MCL1<sup>27</sup>, we observed an increased susceptibility to S63845 only in *Myc* but not in *Mycn*- or *Mycl*-activated CRISPRa cells (Fig. 3e). We also observed this MYC-induced sensitivity against MCL1 inhibition in clonogenic assays (Supplementary Fig. 3b). In line with previous reports, we observed a reduction of MCL1 protein stability upon AURK inhibition (Supplementary Fig. 3c)<sup>28</sup> potentially contributing to the high alisertib sensitivity of MYC-overexpressing cells.

BCL2 overexpression mitigated the effects of MCL1 inhibition (Fig. 3f, g), indicating the importance of MYC-induced BCL2 repression in defining MCL1 dependency and MYC-specific vulnerabilities in SCLC. Consistently, siRNA-mediated MCL1 knockdown reduced viability only in MYC-overexpressing cells (Fig. 3h, i) underlining the MYC-induced dependency on MCL1. Interestingly, MYC-amplified cells exhibited increased levels of the DNA-damage response (DDR) marker  $\gamma$ H2AX upon MCL1 knockdown and MCL1 inhibition (Fig. 3i; Supplementary Fig. 3d).

To determine the effects of BCL2 family inhibition in vivo, we evaluated the efficacy of BCL2 inhibitor venetoclax and MCL1 inhibitor S63845 in an *Myc*-driven SCLC mouse model (RPM)<sup>6</sup>. As expected, BCL2 inhibition had no beneficial effect on overall survival of RPM mice (Supplementary Fig. 3e). While single agent S63845 (25 or 40 mg/kg) and combined S63845/chemotherapy at 25 mg/kg of the MCL1 inhibitor had a modest effect on the survival of RPM mice, the 40 mg/kg S63845 and chemotherapy combination failed to improve survival of the mice beyond vehicle treatment (Supplementary Fig. 3e). While the trend for the higher efficacy of single agent MCL1 vs. BCL2 inhibition is consistent with our in vitro results, the limited affinity of S63845 for murine MCL1<sup>22,27</sup> may mask otherwise stronger effects in this murine GEMM. In addition, S63845/chemotherapy regimens induced pronounced weight loss indicating high toxicity for the

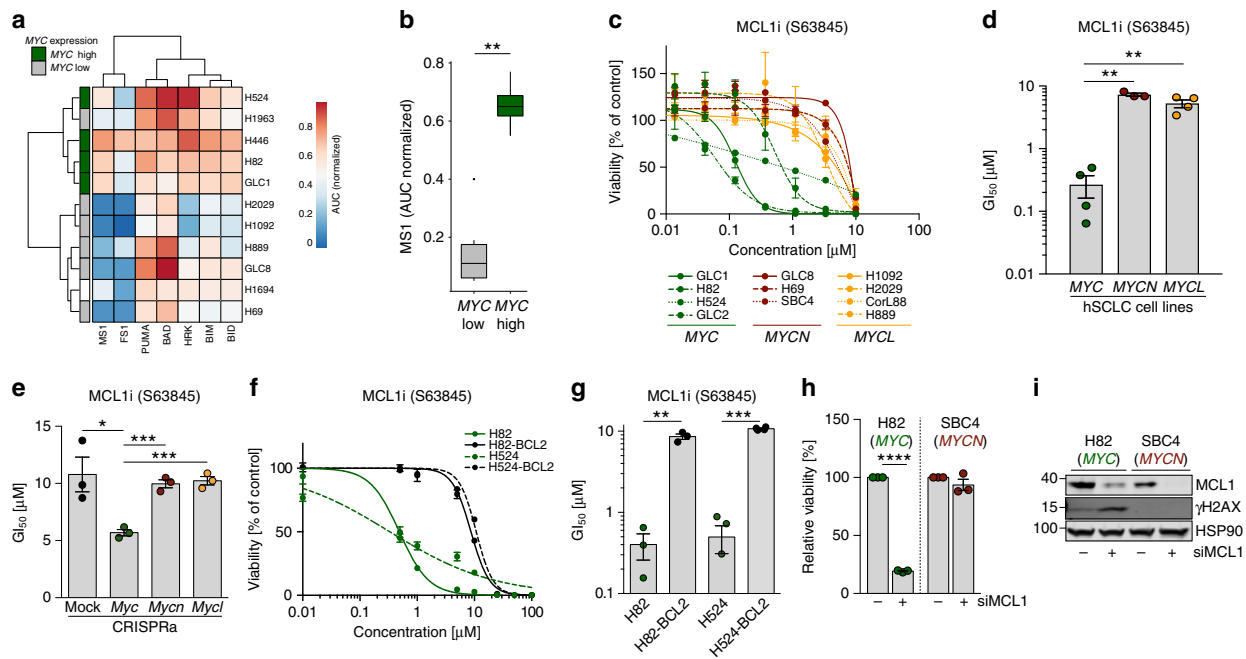


**Fig. 3** MYC drives apoptotic priming and MCL1 dependency. **a** Heatmap of BH3 profiling showing sensitivity of human small cell lung cancer (SCLC) cell lines against specific apoptosis-inducing peptides. MYC expression in the individual cell lines is annotated on the left. **b** Sensitivity of SCLC cell lines toward apoptosis induction by sensitizer peptide MS1 as marker for MCL1-dependent apoptosis. Cell lines are grouped into MYC low and high expression. Sensitivity is calculated as area under the curve. Center line (median), lower/upper box hinges (25th/75th percentile), whiskers extend to the most extreme value within 1.5 $\times$  interquartile range (IQR) of the hinges. **c** Cell viability screening of MYC ( $n=4$ ; GLC1, H82, H524, GLC2), MYCN ( $n=3$ ; GLC8, H69, SBC4), and MYCL ( $n=4$ ; H1092, H2029, CorL88, H889) amplified human SCLC cell lines treated with MCL1 inhibitor (S63845) for 72 h ( $n=3$ ). **d** GI<sub>50</sub> values SCLC cell lines treated with S63845. Cell lines are grouped according to their MYC status ( $n=3$ ). **e** GI<sub>50</sub> values of *Myc* paralog-activated CRISPRa cells treated with S63845. **f** Cell viability screening of MYC-amplified H82 and H524 cells  $\pm$  BCL2 overexpression treated with S63845 ( $n=3$ ). **g** GI<sub>50</sub> values of cell viability screening in **f** ( $n=3$ ). **h** Relative cell viability of H82 (MYC-amplified) and H69 (MYCN-amplified) human SCLC cell lines 48 h after transfection with non-targeted small interfering RNA (siRNA) or siRNA directed against MCL1 ( $n=3$ ). **i** Western blot showing MCL1 and  $\gamma$ H2AX levels in H82 (MYC-amplified) and H69 (MYCN-amplified) human SCLC cell lines 48 h after Ctrl. or MCL1 siRNA transfection. HSP90 was used as a loading control. Error bars indicate mean  $\pm$  SEM. Two-tailed unpaired  $t$  tests, \*\*\*\* $p < 0.0001$ , \*\*\* $p < 0.001$ , \*\* $p < 0.01$ , \* $p < 0.05$ . Source data are provided as a Source Data file

combination that prohibited a dose escalation for the MCL1 inhibitor (Supplementary Fig. 3f). Taken together, lack of BCL2 expression favors a potentially druggable MCL1 dependency in MYC-activated SCLC.

**MYC triggers a druggable DDR in vivo.** Next, we investigated the impact of cell cycle checkpoint inhibition on the induction of DDR and apoptosis. We observed that alisertib as well as volasertib treatment led to a rapid induction of  $\gamma$ H2AX and CC3 levels in human MYC-amplified and murine CRISPRa Myc-activated cells (Fig. 4a, b and Supplementary Fig. 4a, b). Using immunofluorescence, we observed increased steady-state levels of  $\gamma$ H2AX ( $p < 0.0001$ , one-way analysis of variance (ANOVA)) and DNA double-strand break (DSB) marker 53BP1 ( $p < 0.0001$ , one-way ANOVA) in Myc-activated murine SCLC cells suggesting DSB-mediated activation of the DDR in these cells (Fig. 4c, d). Basal DDR activation was also observed in MYC-overexpressing human SCLC cells (Supplementary Fig. 4c, d). Further elevation of DNA damage by chemotherapeutics (etoposide and cisplatin) or checkpoint kinase 1 (CHK1) inhibitors (prexasertib, PF-477736, MK-8776)<sup>6,9</sup> decreased viability preferentially in Myc-activated CRISPRa cells (Fig. 4e). Consistently, etoposide treatment of Myc-activated cells rapidly induced  $\gamma$ H2AX and CC3 levels (Supplementary Fig. 4e). Interestingly, BCL2 overexpression reduced  $\gamma$ H2AX levels after both etoposide and alisertib treatment of Myc-activated CRISPRa cells (Fig. 4f, g). We next combined AURK and CHK1 inhibition and observed synergistic activity at low nanomolar concentrations of alisertib and prexasertib in clonogenic and viability assays (Fig. 4h, i) with more pronounced synergy in Myc-activated cells (Supplementary Fig. 4f).

In SCLC patients who are routinely treated with first-line cisplatin/etoposide combination chemotherapy, emergence of chemo-resistance is rapid and frequent. To assess the efficacy of combined AURK/CHK1 inhibition in the setting of chemo-resistance, we generated chemo-resistant cell lines from Myc-activated CRISPRa cells (Supplementary Fig. 4g) and subjected these cells to combined AURK/CHK1 inhibition. We observed that chemo-resistance substantially increased resistance against combined AURK/CHK1 inhibition (Supplementary Fig. 4h) arguing for efficacy of this treatment strategy in the first-line setting but not upon chemo-resistance. Interestingly, chemo-resistant cells displayed increased AURK and CHK1 phosphorylation levels suggesting higher activity of both enzymes after chemo-resistance (Supplementary Fig. 4i).

We next sought to validate the efficacy of AURK/CHK1 inhibition in vivo in the Myc-driven RPM mouse model. Compared to vehicle treatment, CHK1 inhibitor treatment (prexasertib) prolonged survival of RPM mice similar to chemotherapy (cisplatin/etoposide) (Fig. 4j). The combination of prexasertib and AURK inhibitor (alisertib) further prolonged survival of RPM mice compared to chemotherapy (median survival 22.5 vs. 28 days;  $p = 0.005$ , Log-rank (Mantel-Cox) test; Fig. 4j). Furthermore, the combination of either prexasertib or alisertib with chemotherapy was slightly less effective (median survival 19 and 26 days) than the alisertib/prexasertib combination (Fig. 4j). Vehicle-treated mice exhibited rapid tumor growth while chemotherapy- or prexasertib-treated animals exhibited a modest delay in tumor growth followed by rapid relapse (Fig. 4k and Supplementary Fig. 4j). Of importance, mice treated with the combination of targeted therapy agents, alisertib and prexasertib, exhibited moderate weight loss compared to regimens in which targeted agents were combined with chemotherapy (Supplementary Fig. 4k). This suggests manageable toxicity of combined AURK/CHK1 inhibition and further strengthens our model in which

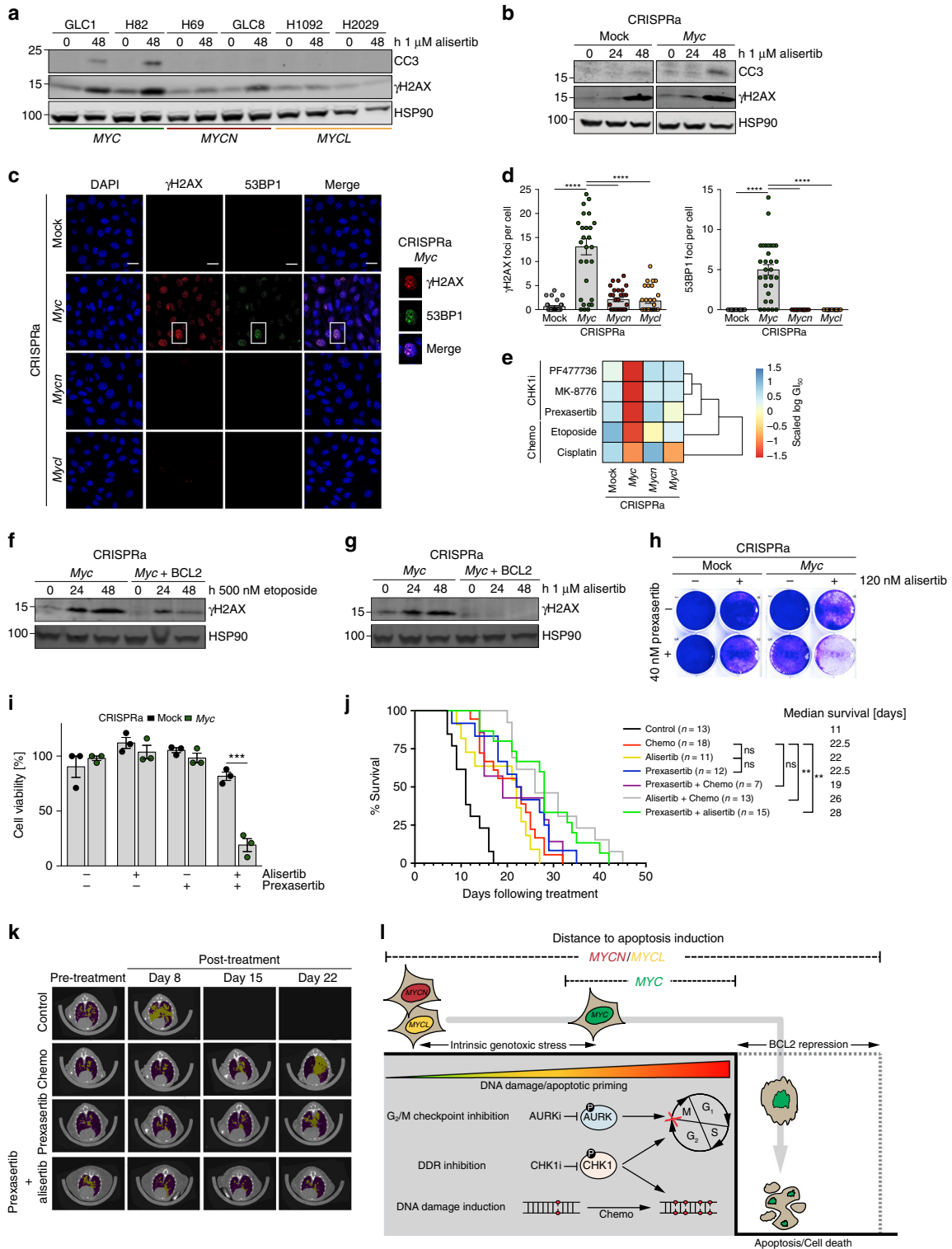
MYC-dependent tumors are more susceptible to perturbation of the cell cycle and DDR control pathways (Fig. 4i).

## Discussion

Here we investigated how MYC paralogs modulate drug dependencies in SCLC. We developed an isogenic CRISPRa-based model to study the endogenous activation of the different MYC paralogs in GEMM-derived SCLC cell lines. This cellular system allowed us to molecularly define and phenotypically characterize MYC-paralog-driven SCLC uncoupled from the divergent genetic background of patient-derived cell lines.

In summary, our data provide mechanistic insight into MYC-paralog-specific dependencies with direct implications for a personalized treatment against SCLC tumors. Our findings reveal a pivotal role for BCL2 as a major regulator of response to cell cycle and DNA damage checkpoint inhibitors. In SCLC cells, MYC activation represses BCL2 thereby limiting the pool of anti-apoptotic proteins. Indeed, we observed increased apoptotic priming and a strong MCL1 dependency in MYC-overexpressing cells, which are also vulnerable to direct and indirect DNA damage induction (Fig. 4l). Differential MYC protein levels do not alter MCL1 expression, so lack of BCL2 likely is the main driver of MYC-induced MCL1 dependency. Consistent with previous reports<sup>29</sup>, reintroduction of BCL2 mitigated DNA damage-induced cell death. The specific silencing of an anti-apoptotic protein such as BCL2 seems to be paradoxical since the benefit to MYC-activated cells is not obvious. A study by Ichim and colleagues described limited mitochondrial outer membrane permeabilization (MOMP), a phenomenon termed minority MOMP, as a trigger for cellular transformation and tumorigenesis<sup>30</sup>. In this scenario, limited caspase activity promotes DNA damage induction and genome instability. The steady-state  $\gamma$ H2AX levels in cells with high MYC strongly resemble such a limited MOMP baseline. Following this hypothesis, suppression of BCL2 may facilitate the induction of this phenotype. On the other hand, increased levels of  $\gamma$ H2AX may contribute to DNA damage accumulation in MYC-activated cells following chemotherapy and/or CHK1 inhibition. Furthermore, a disruption of the G2/M checkpoint via AURK inhibition, in the background of TP53/RB1-loss-induced defective G1/S checkpoint, may have the same cytotoxic effects. Failure to repair accumulated DNA lesions likely induces apoptosis followed by cell death (Fig. 4l).

We show that this MYC-specific vulnerability can be therapeutically exploited in vitro and in vivo by combined AURK/CHK1 inhibition. A translation of this regimen into a clinical setting might primarily be effective in a first-line setting since chemo-resistant cell lines were also resistant to combined AURK/CHK1 inhibition. The combination of two targeted therapy agents at tolerable doses might overcome the need for pan-toxic chemotherapy. Since the efficacy of combining targeted therapy with chemotherapy was also superior compared to chemotherapy alone, this strategy might prevent or delay the emergence of resistance. We observed less toxicity for combined AURK/CHK1 inhibition, which might overcome previously observed hematological toxicities for alisertib, especially in combination with chemotherapy<sup>31</sup>. Several clinical trials are already evaluating AURK (NCT03216343, NCT03092934, NCT02719691, NCT02134067, NCT01118611) and CHK1 (NCT02735980, NCT02797964, NCT02797977, NCT02873975) inhibitors either as single agents or in combination with chemotherapy in SCLC patients. A recently completed Phase II trial (NCT02038647) that investigated the effects of alisertib in combination with paclitaxel as second-line therapy for SCLC initially reported a significant increase in progression-free survival<sup>32</sup>. Interestingly, retrospective analysis of a subset of



patients revealed that the alisertib/paclitaxel combination preferentially improved survival of patients with high MYC protein expression<sup>33</sup>. This is in line with our data that suggest high MYC expression is predictive of response to AURK and/or CHK1 inhibition. Therefore, our data may facilitate the

selection of patients who particularly benefit from this treatment, reducing unnecessary toxicities. Thus our study bolsters the mechanistic understanding of the role of specific MYC paralogs for the fine-tuning of the apoptotic machinery and druggable dependencies in SCLC.

**Fig. 4** MYC triggers a druggable DNA-damage response (DDR) in vivo. **a, b** Western blot of cleaved caspase 3 (CC3) and  $\gamma$ H2AX in MYC-variant-amplified human small cell lung cancer (SCLC) cell lines ( $n = 6$ ) (**a**) or Myc-activated CRISPRa cells (**b**) treated with alisertib for the indicated times. HSP90 was used as a loading control. **c** Representative images of immunofluorescence (IF) experiments of Myc paralog-activated CRISPRa cells showing DAPI (DNA),  $\gamma$ H2AX (DDR activation), and 53BP1 (DNA double-strand breaks) staining (Scale bar: 20  $\mu$ m). **d** Quantification of **c** showing mean number of  $\gamma$ H2AX (top) and 53BP1 (bottom) foci per cell ( $n = 30$ ). Error bars indicate mean  $\pm$  SEM. One-way analysis of variance, \*\*\*\* $p < 0.0001$ . **e** Heatmap displaying sensitivity (scaled  $\log(GI_{50})$ ) of Myc paralog-activated CRISPRa cells treated with CHK1 inhibitors (MK8776, PF477736, prexasertib) or chemotherapeutics (etoposide, cisplatin) for 96 h ( $n = 3$ ). **f, g** Western blot of  $\gamma$ H2AX in Myc-activated CRISPRa cells  $\pm$  BCL2 overexpression treated with etoposide (**g**) and alisertib (**h**). HSP90 was used as a loading control. **h** Crystal violet assay of control and Myc-activated CRISPRa cells upon treatment with 120 nM alisertib, 40 nM prexasertib, and combined treatment for 96 h. **i** Viability of mock control and Myc-activated CRISPRa cells upon treatment with 120 nM alisertib, 40 nM prexasertib, and combined treatment for 96 h ( $n = 3$ ). Error bars indicate mean  $\pm$  SEM. Two-tailed unpaired  $t$  tests, \*\*\* $p < 0.001$ . **j** Survival analysis of RPM mice bearing MYC-driven SCLC treated with vehicle control (phosphate-buffered saline (PBS),  $n = 13$ ), chemotherapy (cisplatin/etoposide,  $n = 18$ ), Aurora Kinase (AURK) inhibitor alisertib ( $n = 11$ ), checkpoint kinase 1 (CHK1) inhibitor prexasertib ( $n = 12$ ), prexasertib+chemotherapy ( $n = 7$ ), alisertib+chemotherapy ( $n = 13$ ), and prexasertib+alisertib ( $n = 15$ ). Log-rank (Mantel-Cox) test, \*\* $p < 0.009$ . **k** Representative micro-computed tomographic images of RPM mice pre-treatment and after treatment with vehicle control (PBS), chemotherapy (cisplatin/etoposide), CHK1 inhibitor prexasertib, and prexasertib combined with AURK inhibitor alisertib. Tumors are colored in yellow, air space in purple. **l** Model of MYC paralog-dependent apoptotic priming and vulnerabilities in SCLC. Source data are provided as a Source Data file

## Methods

**Cell culture.** Human SCLC cell lines were obtained from ATCC and verified by STR profiling at the University of Utah DNA sequencing core facility or at the Institute for Forensic Medicine of the University Hospital of Cologne. GLC1, GLC2, H82, H524, GLC8, SBC4, H69, COR-L303, SBC7, COR-L88, MEF, and Myc-activated CRISPRa cells were cultured in RPM; H1092, H2029, and H889 were cultured in HITES; NIH3T3 and HEK293T cells were cultured in DMEM. All media were supplemented with 10% fetal bovine serum, 1% Penicillin/Streptomycin, and 1% L-glutamine. All cells were grown at 37 °C in a humidified atmosphere with 5% CO<sub>2</sub>.

**Reagents.** For cell culture studies, drugs were dissolved in dimethyl sulfoxide (DMSO) to a final stock concentration of 10 mM except for prexasertib (4.5 mM). With the exception of prexasertib (MedChemExpress), all compounds were purchased from Selleckchem.

**CRISPR activation.** Briefly, sgRNA sequences (see Supplementary Table 2) targeting promoters of *Myc*, *Mycn*, and *Mycl* were obtained from the sgRNA design tool (<http://sam.genome-engineering.org/database/>). Cas9-Activators with SAM, accessed 12/2015 and cloned into lentiSAMv2. Lentiviral particles of lenti-MS2-p65-HSF1\_Hygro and lentiSAMv2 (containing *Myc* paralog sgRNAs) were produced in HEK293T cells co-transfected with pMD.2 and pCMVd.8.9 helper plasmids. Target cells were first transduced with lentiviral particles of lentiMS2-p65-HSF1\_Hygro followed by hygromycin selection (400  $\mu$ g/ml). Selected cells were then transduced with lentiviral particles of lentiSAMv2 followed by blasticidin selection (1.5  $\mu$ g/ml).

**Cell viability screening.** To assess cell viability, cells were plated in 96-well plates in triplicates and compounds were added at 8 decreasing compound concentrations 24 h after seeding. Seventy-two hours later, cell viability was measured via Cell Titer-Glo (CTG) assay (Promega) and was normalized to DMSO-treated controls. Half-maximal growth inhibitory (GI<sub>50</sub>) concentrations of cell viability were inferred by fitting sigmoidal dose–response curves using the Prism 8 software (GraphPad). Data are represented as mean  $\pm$  SEM and significance was calculated by unpaired Student's  $t$  tests.

**Cell proliferation kinetics.** In all,  $2 \times 10^4$  cells were plated in triplicate in one well of a 12-well plate. Cell number was determined daily for 4 consecutive days. Data are presented as mean  $\pm$  SEM.

**Whole-exome sequencing.** DNA from Myc-paralog-activated cells was extracted using the Genra Puregene Tissue Kit (Qiagen) according to the manufacturer's instructions. Library preparation for exome sequencing was performed with the SureSelectXT Library Prep Kit and the Target Enrichment Kit using the Mouse All Exon Capture ab (Agilent, USA) following the SureSelectXT Automated Target Enrichment Illumina PE Multiplexed Seq protocol. Sequencing was performed with a  $2 \times 76$  bp protocol on a HiSeq4000. Raw sequencing reads were aligned to the mouse reference genome mm10 using BWA-MEM, followed by trimming of overlapping read pairs, and removal of PCR duplicates and secondary alignments. For copy number (CN) analysis, Scust<sup>34</sup> is applied to estimate purity-corrected CNs by conditionally optimizing likelihoods of allelic imbalances and read ratios relative to available mouse normal data. All sequencing data will be released upon publication. Sequencing data are deposited at EBI Array Express, accession # E-MTAB-7412.

**Transcriptome data analysis.** Human SCLC RNA-seq cell line generated within this study and SCLC cell line raw data used previously<sup>6</sup> were aligned to the human reference genome Hg38 using STAR<sup>35</sup> followed by gene expression quantification as transcript per million (TPM) and counts using RSEM<sup>36</sup>. For differential gene expression, cell lines were grouped according to MYC expression into MYC-high ( $n = 22$ , COR.L279, CPC.N, DMS114, DMS273, DMS454, DMS53, GLC1, GLC2, H1048, H1341, H1930, H2171, H446, H524, H82, H841, NCL.H146, NCL.H2081, NCL.N417, SCLC.21 H, SHP77, SW1271) and MYC-low ( $n = 20$ , COR.L303, COR.L47, COR.L88, DMS153, DMS79, GLC8, H1836, H196, H1963, H2029, H209C, H2141, H526, H69, H889, NCL.H1092, NCL.H187, NCL.H1882, NCL.H345, SBC7). Differential gene expression between groups was calculated from count-level data using DESeq<sup>27</sup>. Resulting  $p$  values were adjusted using Benjamini–Hochberg correction. Annotation of MYC paralog amplification status in human SCLC cell lines was obtained from published genomic data<sup>7,20,38</sup>. 3' RNA-seq data was aligned to the mouse reference genome GRCm38 using STAR and quantified with RSEM prior to downstream analysis. Processed human primary SCLC tumor sample data were acquired from a published study<sup>1</sup>. Primary samples were classified as MYC family member high vs. low based on gene expression, where cut-offs were derived from Gaussian-mixture models. In brief, samples were grouped by fitting two normal distributions to log-transformed expression of the MYC family member. Cut-offs between high and low expression groups were derived using the respective fitted distributions. Publicly available RNAseq data for a cohort of 79 SCLC patients<sup>15</sup> was obtained from GEO (GSE60052) including normalized log<sub>2</sub>-transformed expression per gene. Patients were categorized in 15 bins based on MYC expression. Median expression levels of MYC and BCL2 per bin were calculated and correlated using Spearman correlation coefficient. To assess RNA expression of *Bcl2* in mouse tumor models, we used published expression data including RNAseq of RPM ( $n = 11$ ) and RPR2 ( $n = 4$ ) mouse models<sup>6</sup>, supplemented with gene expression array data for RP ( $n = 10$ ) and RPP130 ( $n = 3$ ) mouse tumors (GSE18534)<sup>39</sup>. Log<sub>2</sub>-transformed intensity values were averaged per gene if multiple probes were present. To account for potential effects of expression analysis method, log<sub>2</sub>-FPKM values and log<sub>2</sub>-intensity values were transformed to  $z$ -scores per sample followed by quantile normalization per gene across samples prior to jointed analysis. To assess correlation of MYC and BCL2 mRNA expression across various cancer entities, cell line RNAseq data generated by the CCLE was downloaded from [www.depmap.org](http://www.depmap.org) (Release 19Q1). To account for entity-specific baseline expression differences of MYC and BCL2, log<sub>2</sub>-transformed expression levels quantified as TPM were first scaled per gene within each of the 27 tumor entities before calculating Pearson correlation.

**Cell cycle analysis by flow cytometry.** A total of  $5 \times 10^5$  cells were seeded in 6-well plates and incubated overnight, before addition of 2 mM thymidine for 16 h (first block). After the first block, cells were washed twice with phosphate-buffered saline (PBS) and incubated in growth medium for 8 h before addition of 2 mM thymidine for 16 h (second block). Cells were washed twice with PBS and released. Every 2 h in a period of 12 h, cells were trypsinized, washed with PBS, fixed with 70% ethanol, and incubated for half an hour on ice. Fixed cells were stored at 4 °C for the cell cycle analysis. Ethanol-fixed cells were centrifuged for 5 min at 300  $\times$  g, washed twice with cold PBS, and centrifuged for 5 min at 300  $\times$  g. Cells were then incubated with 100 mg/ml DNase-free RNaseA in PBS for 30 min on ice. Next, cells were washed with PBS and incubated with 100 mg/ml propidium iodide (PI) for 30 min at room temperature (RT) in the dark. Finally, cells were analyzed in a flow cytometer (BD Biosciences). PI fluorescence was determined using FL-3 channel, 488 nm. Raw data were analyzed with the FlowJo software.

**MIZ1/MYC co-immunoprecipitation.** HEK293T cells were transfected with pcDNA-HA-HA-MYC, pcDNA-HA-MYCN or pcDNA-HA-HA-MYCL in

combination with pcDNA-MIZ1. Two days post-transfection, cells were harvested and subjected to MIZ1 IP using anti-MIZ1 antibody (sc-139685, Santa Cruz Biotechnology, 4 µg). Antibody–protein complexes were captured using 20 µl protein G sepharose beads (Santa Cruz Biotechnology). Immunoprecipitates were then analyzed by western blot.

**GDSC methylation data analysis.** Publicly available human SCLC cancer cell line data<sup>20</sup> including gene expression were obtained from <http://www.cancerrxgene.org/> (Genomics of Drug Sensitivity in Cancer Project) and corresponding Illumina 450k methylation beta values (GSE68379) were downloaded from [www.ncbi.nlm.nih.gov/geo](http://www.ncbi.nlm.nih.gov/geo) (NCBI Gene Expression Omnibus, both accessed 27 Dec 2017). SCLC cell lines were classified as MYC high vs. MYC low based on RMA normalized basal MYC expression levels as described above. For methylation analyses, CpGs were filtered using a detection *p* value <0.01 followed by removal of probes containing single-nucleotide polymorphisms, non-CpG probes, and cross-reactive probes<sup>40</sup>. Prior to further downstream analysis, beta values were normalized by peak-based correction<sup>41</sup>. Illumina 450k array annotation files were used to select probes in the BCL2 gene body and promoter region.

**Drug combination screening.** Cells were plated in a 6 × 6 matrix of wells of a 96-well plate and treated with alisertib and prexasertib in various independent concentration pairs (concentrations were fixed ranging from 40 nM to 3.3 µM for alisertib and from 10 nM to 1.1 µM for prexasertib) for 96 h followed by viability measurement using CTG assay. Results of three replicate experiments were pooled and synergy was calculated applying a Bliss independence model using the R package synergyfinder<sup>42</sup>.

**Cycloheximide shutoff experiments.** Cells were seeded and pre-treated with DMSO (control) or 1 µM alisertib for 24 h before addition of 100 µg/ml cycloheximide for 0, 1, 2, 3, and 4 h. Cell lysates were prepared and analyzed by western blot. Protein amounts of MCL1 were calculated by the Image Studio Software (LICOR Biosciences) and normalized to HSP90 amounts.

**shRNA knockdown experiments.** shRNA targeting *Myc* (TGTAAGCTCAGCCATAATTT) was cloned into a Tet-pLKO-puro vector and cotransfected with pMD2.G and pCMVd.8.9 helper plasmids into HEK 293T cells using TransIT-LT1 reagent (Mirus). Forty-eight hours post-transfection, replication-incompetent lentiviruses were collected from the supernatant for infection in the presence of 8 µg/ml polybrene. Twenty-four hours after infection, growth medium was changed and 3 µg/ml puromycin was added for selection. After 5 passages, *Myc* knockdown was induced by addition of doxycycline (500 ng/ml) and *Myc* knockdown confirmed by RT-qPCR and immunoblot. For compound screenings, doxycycline was added when cells were plated.

**siRNA knockdown experiments.** siRNA pools targeting *MCL1* (siMCL1#1 GGUUUGGCAUAUCUAAUAA, siMCL1#2 GAAAGGUGGCAUCAGGAAUG, siMCL1#3 GAUAUCUCUCGGUACCUU, siMCL1#4 CGAAGGAAGUAUCGAAUUU), or *DNMT3a* (siDNMT3A#1 GCAUUCAGGUGGACCGCUA, siDNMT3A#2 GCACUGAAAUGGAAAAGGGU, siDNMT3A#3 CUCAGGCGCCUCAGAGCUA, siDNMT3A#4 GGGACUUGGAGAAGCGGAGS) were purchased from Dharmacon and transfected at 20 nM final concentration into SCLC cell lines (H82, SBC4, GLC1, GLC2) using Dharmafect Transfection Reagent #2 (Dharmacon). Growth medium was changed after 12 h. Experiments assessing knockdown efficiency, cell viability, gene expression, and immunoblots to determine knockdown effects were performed 48 h post-transfection.

**Protein overexpression experiments.** Vectors pMSCV-PIG (puro-IRES-GFP) and pMSCV-PIG-BCL2 were cotransfected with pMD2 and pCMVd.8.9 helper plasmids into HEK 293T cells using TransIT-LT1 reagent (Mirus), respectively. Forty-eight hours post-transfection, replication-incompetent lentiviruses were collected from the supernatant for infection of *Myc* CRISPRa cells and H82 and H524 cells in the presence of 8 µg/ml polybrene. Twenty-four hours after infection, growth medium was changed and 3 µg/ml (*Myc* CRISPRa cells) or 1 µg/ml (H82/H524) puromycin was added for selection for the duration of 6 days (3 passages). After selection, cells were analyzed for protein expression.

**RNA isolation qRT-PCR.** Total RNA was isolated using the Qiazol reagent (Qiagen) according to the manufacturer's instructions. In all, 1.5 µg of total RNA was subjected to DNaseI (Sigma) digestion and reverse transcribed using SuperscriptIII (Thermo Fisher Scientific) with random hexamer primers. Quantitative real-time PCR (qPCR) was performed using 7900HT Real-Time PCR System (Applied Biosystems) and the Power SYBR Green PCR Master Mix (Thermo Fisher Scientific). The qPCR primers used to analyze mRNA levels are listed in Supplementary Table 2. Data were normalized to 18S rRNA levels and are presented as mean ± SEM and significance was calculated by unpaired Student's *t* tests.

**RNA sequencing.** Total RNA was isolated using the RNeasy Mini Prep Kit (Qiagen) according to the manufacturer's instructions with a 75-bp paired-end protocol on a HiSeq4000 (Illumina, USA). 3' UTR RNA sequencing libraries for murine CRISPRa cells were prepared using the QuantSeq 3' mRNA-Seq Library Kit (Lexogen, Austria) and sequenced with a 50-bp single-end protocol on an Illumina HiSeq4000 (Illumina, USA). Sequencing data are deposited at EBI Array Express, accession # E-MTAB-7411.

**Chromatin immunoprecipitation.** Cells were crosslinked in 1% formaldehyde, and chromatin was extracted and sonicated. Equal amounts of chromatin were incubated overnight with specific antibodies against MYC (clone 9E11, ab56, Abcam, 5 µg), MYCN (clone B8.4.B, sc-53993, Santa Cruz Biotechnology, 4 µg), DNMT3a (ab2850, Abcam, 4 µg), MIZ1 (clone 10E2, Elmar Wolf, Würzburg, 15 µl anti-serum), or unspecific mouse IgG (sc-2025, Santa Cruz Biotechnology, 4 µg). ChIP complexes were captured using protein G Dynabeads (Thermo Fisher Scientific), washed, eluted, and decrosslinked. DNA was purified using the ChIP DNA Clean & Concentrator Kit (Zymo Research) and analyzed by qRT-PCR using primers listed in Supplementary Table 2. ChIP signals of non-specific background (IgG) were subtracted from specific antibody ChIP signals. ChIP signals were calculated as percentage of input. Data are presented as mean ± SEM and significance was calculated by unpaired Student's *t* tests.

**BH3 profiling assay.** Cells were pelleted, washed in PBS, resuspended in MEB2 buffer, and  $1 \times 10^4$  to  $2 \times 10^4$  cells were added to each well of a 384 non-binding plate containing MEB2 + 20 µg/ml digitonin + sensitizer peptides at 2× the final concentration. Permeabilized cells were incubated for 1 h at RT in the presence of peptides, fixed by the addition of formaldehyde to 1% final concentration for 10 min at RT, and neutralized by the addition of N2 buffer (Tris/glycine) to terminate fixation. Cells were stained overnight by adding Alexa647–Cytochrome C (clone 6H2, B4, Biolegend) to 250 ng/ml final concentration and Hoechst 33342 to 1 µg/ml final concentration. Analysis was conducted on a BD Fortessa or BD Fortessa X20 with gating on DAPI+ singlets and normalization of the Cytochrome C mean fluorescent intensity values to the buffer alone and 25 µM alamethicin controls.

**Immunofluorescence.** Murine *Myc* paralog-activated cells were grown on glass coverslips and human SCLC cells were grown on Nunc™ Lab-Tek™ coated with Gelatine solution 0.1% in PBS (PAN Biotech). Cells were fixed with 4% paraformaldehyde at RT, permeabilized in PBS containing 0.25% Triton X-100, and blocked in PBS containing 0.2% Tween 20 and 3% bovine serum albumin. Cells were incubated overnight with primary antibodies to γH2AX (#05-636, Merck, 1:500), MCL-1 (sc-819, Santa Cruz Biotechnology, 1:100), or 53BP1 (MAB3802, Merck, 1:500). After washing, cells were incubated with secondary antibodies conjugated to Alexa Fluor-488 (A11029, Thermo Fisher Scientific, 1:1000) and Alexa Fluor-647 (A32733, Thermo Fisher Scientific, 1:1000) in combination with DAPI (4',6-diamidino-2-phenylindole; Sigma, 1:1000). Coverslips were mounted using Fluoromount-GTM (Thermo Fisher Scientific). Microscopy was performed using a Zeiss Meta 710 confocal microscope and images were analyzed by the ImageJ software.

**Bisulfite sequencing.** Cellular DNA was extracted using the Puregene Kit (Qiagen) according to the manufacturer's instructions. Five hundred nanograms of DNA were bisulfite converted using the EZ DNA Methylation-Gold Kit (Zymo Research) according to the manufacturer's instructions. Bisulfite-converted DNA was subjected to methylation-specific PCR using specific primers for the *BCL2* promoter listed in Supplementary Table 2. PCR product was resolved on a 2% agarose gel and purified using the Monarch DNA Gel Extraction Kit (New England BioLabs), cloned into pCR4-TOPO TA Vector (Thermo Fisher Scientific), transformed into XL10-Gold Ultracompetent Cells (Agilent Technologies), and plated onto ampicillin selection LB-agar plates. DNA of single colonies was extracted using the NucleoSpin Plasmid EasyPure Mini Kit (Macherey-Nagel) and submitted to Sanger sequencing using sequencing primers M13-for and M13-rev (see Supplementary Table 2). Obtained sequences were analyzed and DNA methylation plots were generated using the QUMA quantification tool for methylation analysis<sup>43</sup>.

**Crystal violet assay.** In all,  $2 \times 10^5$  cells were plated into one well of a 6-well plate and treated with DMSO (control), 40 nM prexasertib, 120 nM alisertib, and the combination of prexasertib and alisertib. Seventy-four hours after treatment, cells were fixed in 4% paraformaldehyde in PBS, stained with 0.1% crystal violet in PBS, and rinsed in PBS before image acquisition.

**Generation of chemo-resistant cells.** *Myc*-activated CRISPRa cells were subjected to prolonged etoposide treatment at increasing concentrations starting from 500 nM for several weeks. The resulting, proliferating cell line was maintained in growth medium containing 2 µM etoposide.

**Mouse drug treatments.** To initiate lung tumors Rb1<sup>fl/fl</sup>;p53<sup>fl/fl</sup>;Myc<sup>LSL/LSL</sup> (RPM) mice were infected by intratracheal injection with  $1 \times 10^8$  Ad-CGRP-Cre virus

(University of Iowa Virus Vector Core). Mice were imaged with a Quantum FX or GX2 microCT system (Perkin Elmer) and randomized into treatment groups upon detection of ~10% lung tumor burden. Treatment groups included PBS control ( $n = 15$ ), chemotherapy (cisplatin/etoposide,  $n = 18$ ), prexasertib ( $n = 12$ ), or prexasertib combined with alisertib ( $n = 15$ ). Prexasertib (10 mg/kg in Captisol) was administered via subcutaneous flank injection twice a day on a weekly schedule of 2 days on and 5 days off. Prexasertib was provided by Dr. Lauren Byers and manufactured by the Institute for Applied Chemical Science at MD Anderson, Houston, TX. Alisertib (Apexbio Technology; 20 mg/kg in 10%  $\beta$ -cyclodextrin) was administered via oral gavage twice a day on a weekly schedule of 5 days on and 2 days off. For weekly chemotherapy treatments, cisplatin (Sigma-Aldrich; 5 mg/kg in PBS) was administered on day 1 and etoposide (Sigma-Aldrich; 10 mg/kg in 70% PEG in water) was given on day 2 by intraperitoneal injection. To decrease toxicity, mice treated with prexasertib and chemotherapy received cisplatin on day 1, etoposide on day 2, and prexasertib on days 5 and 6 of each weekly cycle. After 4 cycles of cisplatin/etoposide chemotherapy, mice were treated weekly with etoposide only. MCL1 inhibitor S63845 (25 mg/kg or 40 mg/kg in 20%  $\beta$ -cyclodextrin with 25 mM HCl) was administered by tail vein injection. Mice were treated with MCL1i at 25 mg/kg twice/week or 40 mg/kg once/week, and both treatment doses were tested in combination with cisplatin/etoposide chemotherapy. Since neither the 25 mg/kg nor 40 mg/kg monotherapy significantly improved survival, these groups were combined for data analysis. Both tested doses of S63845 + chemotherapy induced significant weight loss and toxicity. ABT-199 (50 mg/kg in 60% Phosal50, 30% PEG400, 10% ethanol) was administered by oral gavage once per day on a weekly schedule of 5 days on/2 days off. Mice were imaged at the start of each treatment cycle and 4 days post cisplatin, and images were quantified using the Analyze 11.0 (AnalyzeDirect) software. Endpoints for survival studies included labored breathing, >20% weight loss, or signs of toxicity. Mice were sacrificed via CO<sub>2</sub> asphyxiation prior to necropsy. Survival curve analysis was performed with the GraphPad Prism software. These experiments were approved by the HCI Institutional Animal Care and Use Committee (IACUC), and mice were housed in a specific pathogen-free barrier facility.

**Micro-computed tomographic (microCT) imaging.** Mice were scanned for 34 s under isoflurane anesthesia using a small animal Quantum FX or GX2 microCT (PerkinElmer) at 45  $\mu$ m resolution, 90 kV, with 160 mA current. Images were acquired using the PerkinElmer Quantum FX software and processed with Analyze 11.0 (AnalyzeDirect). Scans were calibrated for Hounsfield Units (HU) by determining the mean value of “Bed” and “Air” for representative scans using the region of interest (ROI) tool. Those values were matched to their known HU (40 and -1000 HU, respectively) by the “Image Algebra” tool. A  $3 \times 3 \times 3$  Median Filter was applied to every image using the “Spatial Filters” window. Thresholds for “Air” vs. “Dense Tissue” were set using the ROI and histogram tools. For total tumor burden analyses, an object map was created using the previously established thresholds and manually adjusted using “Spline Edit”, “Draw”, “Trace”, and “Nudge Edit” tools. The object map was then morphed, i.e., made binary by using the threshold morphing tool. Then the map was dilated 3 times using  $5 \times 5 \times 5$  Jack-shaped structuring elements. Holes were filled on every two-dimensional orientation and the map was finally brought back to its original size with the “Erode” tool 3 times using  $5 \times 5 \times 5$  Jack-shaped structuring elements. The volumetric analyses were then performed in the ROI window using the pre-established thresholds and non-airspace was calculated using the formula:  $\text{Nonairspace} = 1 - (\text{VolAir}/\text{ROIVol})$ .

**Immunohistochemistry.** Tissues were fixed in formalin overnight, then transferred to 70% ethanol, and embedded in paraffin (ARUP histology core). Formalin-fixed paraffin-embedded sections (4 micron) were used for hematoxylin and eosin and IHC staining. Antigen retrieval was performed by boiling slides for 20 min in 0.01 M citrate buffer, pH 6.0. Slides were blocked for 15 min with 3% H<sub>2</sub>O<sub>2</sub>, followed by 5% goat serum in PBS containing 0.1% Tween-20 (PBST). Primary antibodies were incubated overnight at 4 °C and include the following: BCL2 (#M088701-2, clone 124, Agilent), MYC (ab32072, Abcam), NEUROD1 (ab205300, Abcam), and ASCL1 (#556604, BD Pharmingen). Slides were then incubated with horseradish peroxidase (HRP)-conjugated secondary antibody (Vector Laboratories, 1:200) and developed with DAB (Vector Laboratories). A Nikon Eclipse Ci microscope and DS-Fi3 camera were used for imaging.

**Immunoblot.** Cell lysates were prepared using RIPA buffer supplemented with protease inhibitors (cOmplete Mini Protease Inhibitor Cocktail, Roche). Protein concentration was determined by BCA assay (Pierce) and equal amounts of protein were separated on 4–20% Tris-glycine sodium dodecyl sulfate-polyacrylamide gel electrophoresis (SDS-PAGE) gels (Thermo Fisher Scientific) and transferred to PVDF-FL membrane (Millipore). Membranes were blocked in 3% cold-fish gelatin blocking buffer in TBS, incubated with primary antibodies, washed, and incubated with fluorescently labeled secondary antibodies prior to detection with Odyssey CLx imaging system (LI-COR Biosciences). Images were processed using the Image Studio Software (LI-COR Biosciences). Primary antibodies are: MYC (#9402, Cell Signaling Technology, 1:1000), MYCN (sc-53993, Santa Cruz Biotechnology, 1:1000), MYCL (AF4050, R&D Systems, 1:1000), BCL2 (#2872, Cell Signaling Technology, 1:1000),

BIM (#2933, Cell Signaling Technology, 1:1000), BAD (#610391, BD Biosciences, 1:1000), BCL-XL (#2764, Cell Signaling Technology, 1:1000), HA (#3724, Cell Signaling Technology, 1:1000), MIZ1 (clone 10E2, Elmar Wolf, Würzburg, 1:500), ASCL1 (#556604, BD Biosciences, 1:1000), MCL1 (sc-819, Santa Cruz Biotechnology, 1:1000),  $\gamma$ H2AX (#05-636, Merck, 1:1000), Cleaved Caspase 3 - CC3 (#9664, Cell Signaling Technology, 1:500), pAURKA/B/C (#2914, Cell Signaling Technology, 1:1000), pCHK1<sup>S345</sup> (#2341, Cell Signaling Technology, 1:1000), and HSP90 (ADI-SPA-835, Enzo Life Sciences, 1:5000). Secondary antibodies are: goat anti-rabbit 800CW (#926-32211, LI-COR Biosciences, 1:10,000), goat anti-mouse 800CW (#926-3220, LI-COR Biosciences, 1:10,000), anti-rat 680 (#925-68029, LI-COR Biosciences, 1:10,000), goat anti-rabbit 680LT (#926-68021, LI-COR Biosciences, 1:10,000), and goat anti-mouse 680LT (#926-68020, LI-COR Biosciences, 1:10,000). Alternatively, cells were lysed in RIPA buffer supplemented with Pierce Protease inhibitors and sodium orthovanadate. Protein concentrations were measured with the DC protein assay (Bio-Rad), and equal protein volumes were resolved on SDS-PAGE gels. Samples were transferred to 0.2  $\mu$ m PVDF (Bio-Rad). Membranes were blocked in 5% milk/PBS-T prior to overnight incubation in primary antibody. Membranes were then incubated in secondary anti-rabbit-HRP or anti-mouse-HRP antibody (Jackson ImmunoResearch, 1:4000). After washing, membranes were developed with WesternBright ECL HRP (Advantia) and imaged on Hyblot autoradiography film. Primary antibodies used include the following: BCL2 (#2872, Cell Signaling Technology, 1:2000); MCL1 (#94296, Cell Signaling Technology, 1:2000); HSP90 (#4877, Cell Signaling Technology, 1:2000); and ACTIN (#A2066, Sigma, 1:10,000). Uncropped blots are displayed in the Source Data file.

**Reporting summary.** Further information on research design is available in the Nature Research Reporting Summary linked to this article.

### Data availability

All data supporting the findings in this study are available from the corresponding author upon reasonable request. The primary data underlying the graphs are provided in the Source Data File. Previously published datasets used in this study are available at Gene Expression Omnibus through accession codes GSE60052 (expression data SCLC patients) and GSE68379 (methylation data) and at European Genome-phenome Archive through accession codes EGAS00001002115 and EGAS00001000334 (both RNAseq human SCLC cell lines). RNAseq and WES data generated in this study have been deposited at EBI Array Express with the accession codes E-MTAB-7410 (RNAseq NCI-H69, COR-L303), E-MTAB-7411 (RNAseq rp181 CRISPRa), and E-MTAB-7412 (WES rp181).

Received: 30 November 2018 Accepted: 10 July 2019

Published online: 02 August 2019

### References

- George, J. et al. Comprehensive genomic profiles of small cell lung cancer. *Nature* **524**, 47–53 (2015).
- Peifer, M. et al. Integrative genome analyses identify key somatic driver mutations of small-cell lung cancer. *Nat. Genet.* **44**, 1104–1110 (2012).
- Gustafson, W. C. et al. Drugging MYCN through an allosteric transition in aurora kinase A. *Cancer Cell* **26**, 414–427 (2014).
- Dauch, D. et al. A MYC-aurora kinase A protein complex represents an actionable drug target in p53-altered liver cancer. *Nat. Med.* **22**, 744–753 (2016).
- Beaulieu, M. E. et al. Intrinsic cell-penetrating activity propels omomyc from proof of concept to viable anti-myc therapy. *Sci. Transl. Med.* **11**, 1–14 (2019).
- Mollaoglu, G. et al. MYC drives progression of small cell lung cancer to a variant neuroendocrine subtype with vulnerability to aurora kinase inhibition. *Cancer Cell* **31**, 270–285 (2017).
- Sos, M. L. et al. A framework for identification of actionable cancer genome dependencies in small cell lung cancer. *Proc. Natl Acad. Sci. USA* **109**, 17034–17039 (2012).
- Cardnell, R. J. et al. Protein expression of TTF1 and cMYC define distinct molecular subgroups of small cell lung cancer with unique vulnerabilities to aurora kinase inhibition, DLL3 targeting, and other targeted therapies. *Oncotarget* **8**, 73419–73432 (2017).
- Sen, T. et al. CHK1 inhibition in small-cell lung cancer produces single-agent activity in biomarker-defined disease subsets and combination activity with cisplatin or olaparib. *Cancer Res.* **77**, 3870–3884 (2017).
- Faber, A. C. et al. Assessment of ABT-263 activity across a cancer cell line collection leads to a potent combination therapy for small-cell lung cancer. *Proc. Natl Acad. Sci. USA* **112**, E1288–E1296 (2015).
- Rudin, C. M. et al. Comprehensive genomic analysis identifies SOX2 as a frequently amplified gene in small-cell lung cancer. *Nat. Genet.* **44**, 1111–1116 (2012).
- Johnson, B. E. et al. Myc family oncogene amplification in tumor cell lines established from small cell lung cancer patients and its relationship to clinical status and course. *J. Clin. Invest.* **79**, 1629–1634 (1987).

13. Konermann, S. et al. Genome-scale transcriptional activation by an engineered CRISPR-Cas9 complex. *Nature* **517**, 583–8 (2014).
14. Meuwissen, R. et al. Induction of small cell lung cancer by somatic inactivation of both Trp53 and Rb1 in a conditional mouse model. *Cancer Cell* **4**, 181–189 (2003).
15. Jiang, L. et al. Genomic landscape survey identifies SRSF1 as a key oncogene in small cell lung cancer. *PLoS Genet.* **12**, 1–22 (2016).
16. Barretina, J. et al. The Cancer Cell Line Encyclopedia enables predictive modelling of anticancer drug sensitivity. *Nature* **483**, 603–607 (2012).
17. Stransky, N. et al. Pharmacogenomic agreement between two cancer cell line data sets. *Nature* **528**, 84–87 (2015).
18. Zhang, W. et al. Small cell lung cancer tumors and preclinical models display heterogeneity of neuroendocrine phenotypes. *Transl. Lung Cancer Res.* **7**, 32–49 (2018).
19. Lochmann, T. L. et al. Venetoclax is effective in small cell lung cancers with high BCL-2 expression. *Clin. Cancer Res.* **24**, 360–369 (2018).
20. Iorio, F. et al. A landscape of pharmacogenomic interactions in cancer. *Cell* **166**, 740–754 (2016).
21. Poirier, J. T. et al. DNA methylation in small cell lung cancer defines distinct disease subtypes and correlates with high expression of EZH2. *Oncogene* **34**, 5869–5878 (2015).
22. Brenner, C. et al. Myc represses transcription through recruitment of DNA methyltransferase corepressor. *EMBO J.* **24**, 336–346 (2005).
23. Vo, B. H. T. et al. The interaction of Myc with Miz1 defines medulloblastoma subgroup identity. *Cancer Cell* **29**, 5–16 (2016).
24. Patel, J. H. & McMahon, S. B. BCL2 is a downstream effector of MIZ-1 essential for blocking c-MYC-induced apoptosis. *J. Biol. Chem.* **282**, 5–13 (2007).
25. Deng, J. et al. BH3 profiling identifies three distinct classes of apoptotic blocks to predict response to ABT-737 and conventional chemotherapeutic agents. *Cancer Cell* **12**, 171–185 (2007).
26. Kotschy, A. et al. The MCL1 inhibitor S63845 is tolerable and effective in diverse cancer models. *Nature* **538**, 477–482 (2016).
27. Brennan, M. S. et al. Humanized Mcl-1 mice enable accurate pre-clinical evaluation of MCL-1 inhibitors destined for clinical use. *Blood* **129**, 846–854 (2018).
28. Harley, M. E., Allan, L. A., Sanderson, H. S. & Clarke, P. R. Phosphorylation of Mcl-1 by CDK1-cyclin B1 initiates its Cdc20-dependent destruction during mitotic arrest. *EMBO J.* **29**, 2407–2420 (2010).
29. Strasser, A., Harris, A. W., Jacks, T. & Cory, S. DNA damage can induce apoptosis in proliferating lymphoid cells via p53-independent mechanisms inhibitable by Bcl-2. *Cell* **79**, 329–339 (1994).
30. Ichim, G. et al. Limited mitochondrial permeabilization causes DNA damage and genomic instability in the absence of article limited mitochondrial permeabilization causes DNA damage and genomic instability in the absence of cell death. *Mol. Cell* **57**, 860–872 (2015).
31. Liewer, S. & Huddleston, A. Alisertib: a review of pharmacokinetics, efficacy and toxicity in patients with hematologic malignancies and solid tumors. *Expert Opin. Investig. Drugs* **27**, 105–112 (2018).
32. Owonikoko, T. et al. OA05.05 randomized phase 2 study: alisertib (MLN8237) or placebo + paclitaxel as second-line therapy for small-cell lung cancer (SCLC). *J. Thorac. Oncol.* **12**, S261–S262 (2017).
33. Owonikoko, T. K. et al. Randomized phase 2 study of investigational aurora A kinase (AAK) inhibitor alisertib (MLN8237) + paclitaxel (P) vs placebo + P as second line therapy for small-cell lung cancer (SCLC). *Ann. Oncol.* **27**, 493–6 (2016).
34. Cun, Y., Yang, T. P., Achter, V., Lang, U. & Peifer, M. Copy-number analysis and inference of subclonal populations in cancer genomes using ScIust. *Nat. Protoc.* **13**, 1488–1501 (2018).
35. Dobin, A. et al. STAR: ultrafast universal RNA-seq aligner. *Bioinformatics* **29**, 15–21 (2013).
36. Li, B. & Dewey, C. N. RSEM: accurate transcript quantification from RNA-Seq data with or without a reference genome. *BMC Bioinformatics* **12**, 323 (2011).
37. Love, M. L., Huber, W. & Anders, S. Moderated estimation of fold change and dispersion for RNA-seq data with DESeq2. *Genome Biol.* **15**, 550 (2014).
38. Ingarano, M. et al. Two-photon excitation improves multifocal structured illumination microscopy in thick scattering tissue. *Proc. Natl Acad. Sci. USA* **111**, 5254–5259 (2014).
39. Schaffer, B. E. et al. Loss of p130 accelerates tumor development in a mouse model for human small-cell lung carcinoma. *Cancer Res.* **70**, 3877–3883 (2010).
40. Tian, Y. et al. ChAMP: updated methylation analysis pipeline for Illumina BeadChips. *Bioinformatics* **33**, 3982–3984 (2017).
41. Dedeurwaerder, S. et al. Evaluation of the Infinium Methylation 450K technology. *Epigenomics* **3**, 771–784 (2011).
42. He, L. et al. Methods for high-throughput drug combination screening and synergy scoring. *Methods Mol. Biol.* **1711**, 351–398 (2018).
43. Kumaki, Y., Oda, M. & Okano, M. QUMA: quantification tool for methylation analysis. *Nucleic Acids Res.* **36**, 170–175 (2008).

## Acknowledgements

We thank Marek Franitz, Christian Becker, and Janine Altmüller (Cologne Center for Genomics, University of Cologne) for technical support and Katia Garbert, Christian Müller, and Graziella Bosco (University of Cologne) for assistance with data acquisition. We also thank members of the Oliver Laboratory for technical support, especially Ismail Can and Danny Soltero. T.G.O. was supported in part by the NIH NCI (R01CA187487 and R21CA216504), the American Lung Association (LCD-506758), and the Huntsman Cancer Institute from the NIH NCI (P30CA042014). This work was furthermore supported by the Deutsche Forschungsgemeinschaft (CRC1399 to R.B., R.K.T., H.C.R., M.L.S.; KFO-286/RP2, RE 2246/2-1, RE 2246/7-1 to H.C.R. and TH1386/3-1 to R.K.T., M.L.S.), the Bundesministerium für Bildung und Forschung (eMed 01ZX1603A to H.C.R., R.B., R.K.T. and 01ZX1406 to M.L.S.), the German federal state North Rhine Westphalia (NRW) as part of the EFRE initiative (EFRE-0800397 to H.C.R., R.B., R.K.T. and M.L.S.), the Else Kröner-Fresenius Stiftung (EKFS-2014-A06 and 2016\_Kolleg.19 to H.C.R., R.C., R.D.J., S.K. and Memorial Grant 2018\_EKMS.35 to J.B.), the Köln Fortune program (to A.M.), and the Deutsche Krebshilfe (70113041 to H.C.R., 70112888 to M.L.S. and 70113129 to C.L.). Additional funding was provided by the Deutsche Krebshilfe as part of the Oncology Centers of Excellence funding program (to R.B.) and as part of the Small Cell Lung Cancer Genome Sequencing Consortium (109679 to R.K.T., R.B.).

## Author contributions

M.A.D., J.B., R.R.O., S.B., N.M., C.P.W., M.D.C., H.L.T., M.R.G., S.K., A.S.I., A.M., J.R., L.O., R.C., C.L., T.S. and J.T.P. performed experiments and analyzed and visualized the data; M.A.D., J.B., R.R.O., S.B., T.S., L.A.B., A.L., J.T.P., T.G.O. and M.L.S. conceived experimental design; A.S., R.D.J., E.W., R.K.T., H.C.R. and R.B., provided resources; M.A.D., J.B., S.B., T.G.O. and M.L.S. wrote the manuscript; T.G.O. and M.L.S. conceived the study, acquired funding, and supervised the project.

## Additional information

**Supplementary Information** accompanies this paper at <https://doi.org/10.1038/s41467-019-11371-x>.

**Competing interests:** M.L.S. and R.K.T. are founders and shareholders of PearlRiver Bio. M.L.S. received a commercial research grant from Novartis. R.K.T. is a founder of NEO New Oncology GmbH, now part of Siemens Healthcare, and received consulting and lecture fees from Merck, Roche, Lilly, Boehringer Ingelheim, Astra-Zeneca, Daiichi-Sankyo, MSD, NEO New Oncology, Puma, and Clovis. H.C.R. received consulting and lecture fees from Abbvie, Astra-Zeneca, Vertex, and Merck and received research funding from Gilead Pharmaceuticals; R.B. is an employee of Targos Molecular Pathology. The other authors declare no competing interests.

**Reprints and permission** information is available online at <http://npg.nature.com/reprintsandpermissions/>

**Peer review information:** *Nature Communications* thanks the anonymous reviewers for their contribution to the peer review of this work.

**Publisher's note:** Springer Nature remains neutral with regard to jurisdictional claims in published maps and institutional affiliations.



**Open Access** This article is licensed under a Creative Commons Attribution 4.0 International License, which permits use, sharing, adaptation, distribution and reproduction in any medium or format, as long as you give appropriate credit to the original author(s) and the source, provide a link to the Creative Commons license, and indicate if changes were made. The images or other third party material in this article are included in the article's Creative Commons license, unless indicated otherwise in a credit line to the material. If material is not included in the article's Creative Commons license and your intended use is not permitted by statutory regulation or exceeds the permitted use, you will need to obtain permission directly from the copyright holder. To view a copy of this license, visit <http://creativecommons.org/licenses/by/4.0/>.

© The Author(s) 2019

## **Systematic kinase inhibitor profiling identifies CDK9 as a synthetic lethal target in NUT midline carcinoma**

Brägelmann J, **Dammert MA\***, Dietlein F, Heuckmann JM, Choidas A, Böhm S, Richters A, Basu D, Tischler V, Lorenz C, Habenberger P, Fang Z, Ortiz-Cuaran S, Leenders F, Eickhoff J, Koch U, Getlik M, Termathe M, Sallouh M, Greff Z, Varga Z, Balke-Want H, French CA, Peifer M, Reinhardt HC, Örfi L, Kéri G, Ansén S, Heukamp LC, Büttner R, Rauh D, Klebl BM, Thomas RK, Sos ML.

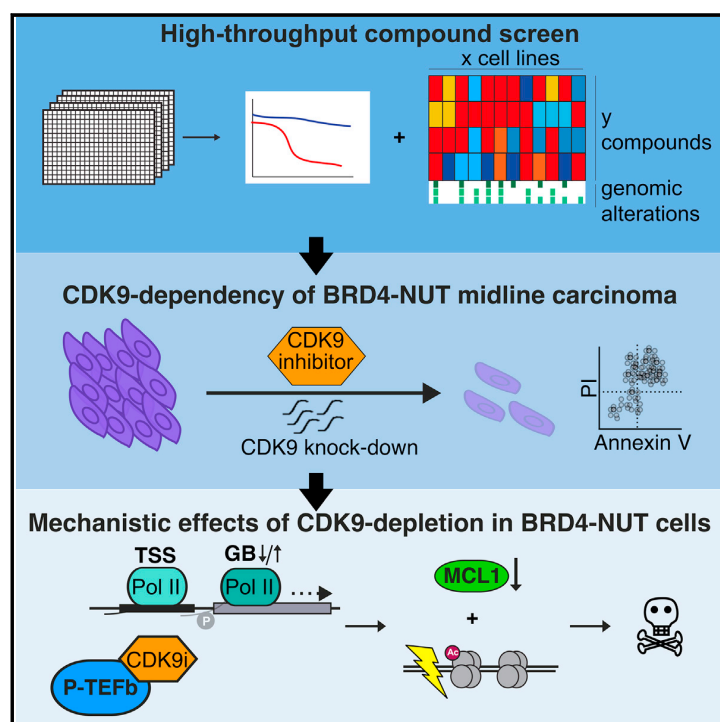
\* co-first author

Specific contributions:

- Viability screening of NUT carcinoma cells
- Western blot analysis of NUT carcinoma cells
- shRNA knockdown experiments in NUT carcinoma cells
- RT-qPCR experiments in NUT carcinoma cells
- ChIP experiments in NUT carcinoma cells
- Manuscript writing and editing

# Systematic Kinase Inhibitor Profiling Identifies CDK9 as a Synthetic Lethal Target in NUT Midline Carcinoma

## Graphical Abstract



## Authors

Johannes Brägelmann,  
Marcel A. Dammert, Felix Dietlein, ...,  
Bert M. Klebl, Roman K. Thomas,  
Martin L. Sos

## Correspondence

roman.thomas@uni-koeln.de (R.K.T.),  
martin.sos@uni-koeln.de (M.L.S.)

## In Brief

By screening 1,505 compounds against 78 cancer cell lines, Brägelmann et al. identify a specific sensitivity of *BRD4-NUT*-rearranged NUT midline carcinoma (NMC) cells to CDK9 inhibition. CDK9 inhibition affects transcriptional elongation, de-regulates MYC signaling, and induces apoptosis by suppressing anti-apoptotic MCL1. CDK9 may thus be a promising target in NMC.

## Highlights

- Screening 1,505 compounds against 78 cancer cell lines reveals distinct vulnerabilities
- NUT midline carcinoma cells are specifically sensitive to CDK9 inhibition (CDK9i)
- CDK9i perturbs MYC signaling, represses MCL1, and induces apoptosis in NMC cells
- CDK9 may represent a promising therapeutic target in NUT midline carcinoma



Brägelmann et al., 2017, Cell Reports 20, 2833–2845  
September 19, 2017 © 2017 The Authors.  
<http://dx.doi.org/10.1016/j.celrep.2017.08.082>

CellPress

# Systematic Kinase Inhibitor Profiling Identifies CDK9 as a Synthetic Lethal Target in NUT Midline Carcinoma

Johannes Brägelmann,<sup>1,2,13</sup> Marcel A. Dammert,<sup>1,2,13</sup> Felix Dietlein,<sup>3,13</sup> Johannes M. Heuckmann,<sup>4,13</sup> Axel Choidas,<sup>5,13</sup> Stefanie Böhm,<sup>1,2</sup> André Richters,<sup>5</sup> Debjit Basu,<sup>6</sup> Verena Tischler,<sup>2</sup> Carina Lorenz,<sup>1,2</sup> Peter Habenberger,<sup>5</sup> Zhizhou Fang,<sup>6</sup> Sandra Ortiz-Cuaran,<sup>2</sup> Frauke Leenders,<sup>2</sup> Jan Eickhoff,<sup>5</sup> Uwe Koch,<sup>5</sup> Matthäus Getlik,<sup>6</sup> Martin Termathe,<sup>6</sup> Muhammad Sallouh,<sup>6</sup> Zoltán Greff,<sup>7</sup> Zoltán Varga,<sup>7</sup> Hyatt Balke-Want,<sup>2,3</sup> Christopher A. French,<sup>8</sup> Martin Peifer,<sup>2</sup> H. Christian Reinhardt,<sup>3,12</sup> László Örfi,<sup>7,9</sup> György Kéri,<sup>7</sup> Sascha Ansén,<sup>3</sup> Lukas C. Heukamp,<sup>2,10</sup> Reinhard Büttner,<sup>10</sup> Daniel Rauh,<sup>6</sup> Bert M. Klebl,<sup>5</sup> Roman K. Thomas,<sup>2,10,11,\*</sup> and Martin L. Sos<sup>1,2,12,14,\*</sup>

<sup>1</sup>Molecular Pathology, Institute of Pathology, University of Cologne, Kerpener Str. 62, 50937 Cologne, Germany

<sup>2</sup>Department of Translational Genomics, Medical Faculty, University of Cologne, Weyertal 115b, 50931 Cologne, Germany

<sup>3</sup>Department I of Internal Medicine and Center for Integrated Oncology, University Hospital of Cologne, Kerpener Str. 62, 50937 Cologne, Germany

<sup>4</sup>NEO New Oncology GmbH, Gottfried-Hagen-Str. 20, 51105 Cologne, Germany

<sup>5</sup>Lead Discovery Center (LDC) GmbH, Otto-Hahn-Str. 15, 44227 Dortmund, Germany

<sup>6</sup>Faculty of Chemistry and Chemical Biology, TU Dortmund University, Otto-Hahn-Str. 4a, 44221 Dortmund, Germany

<sup>7</sup>Vichem Chemie Research Ltd., Herman Ottó u. 15, Budapest, Hungary

<sup>8</sup>Department of Pathology, Brigham and Women's Hospital, Harvard Medical School, Boston, MA 02115, USA

<sup>9</sup>Department of Pharmaceutical Chemistry, Semmelweis University, Hógyes E. U.9, Budapest, Hungary

<sup>10</sup>Institute of Pathology, Medical Faculty, University of Cologne, Kerpener Str. 62, 50937 Cologne, Germany

<sup>11</sup>German Cancer Research Center (DKFZ), German Cancer Consortium (DKTK), Heidelberg, Germany

<sup>12</sup>Center for Molecular Medicine Cologne, University of Cologne, 50931 Cologne, Germany

<sup>13</sup>These authors contributed equally

<sup>14</sup>Lead Contact

\*Correspondence: [roman.thomas@uni-koeln.de](mailto:roman.thomas@uni-koeln.de) (R.K.T.), [martin.sos@uni-koeln.de](mailto:martin.sos@uni-koeln.de) (M.L.S.)

<http://dx.doi.org/10.1016/j.celrep.2017.08.082>

## SUMMARY

Kinase inhibitors represent the backbone of targeted cancer therapy, yet only a limited number of oncogenic drivers are directly druggable. By interrogating the activity of 1,505 kinase inhibitors, we found that *BRD4-NUT*-rearranged NUT midline carcinoma (NMC) cells are specifically killed by CDK9 inhibition (CDK9i) and depend on CDK9 and Cyclin-T1 expression. We show that CDK9i leads to robust induction of apoptosis and of markers of DNA damage response in NMC cells. While both CDK9i and bromodomain inhibition over time result in reduced Myc protein expression, only bromodomain inhibition induces cell differentiation and a p21-induced cell-cycle arrest in these cells. Finally, RNA-seq and ChIP-based analyses reveal a *BRD4-NUT*-specific CDK9i-induced perturbation of transcriptional elongation. Thus, our data provide a mechanistic basis for the genotype-dependent vulnerability of NMC cells to CDK9i that may be of relevance for the development of targeted therapies for NMC patients.

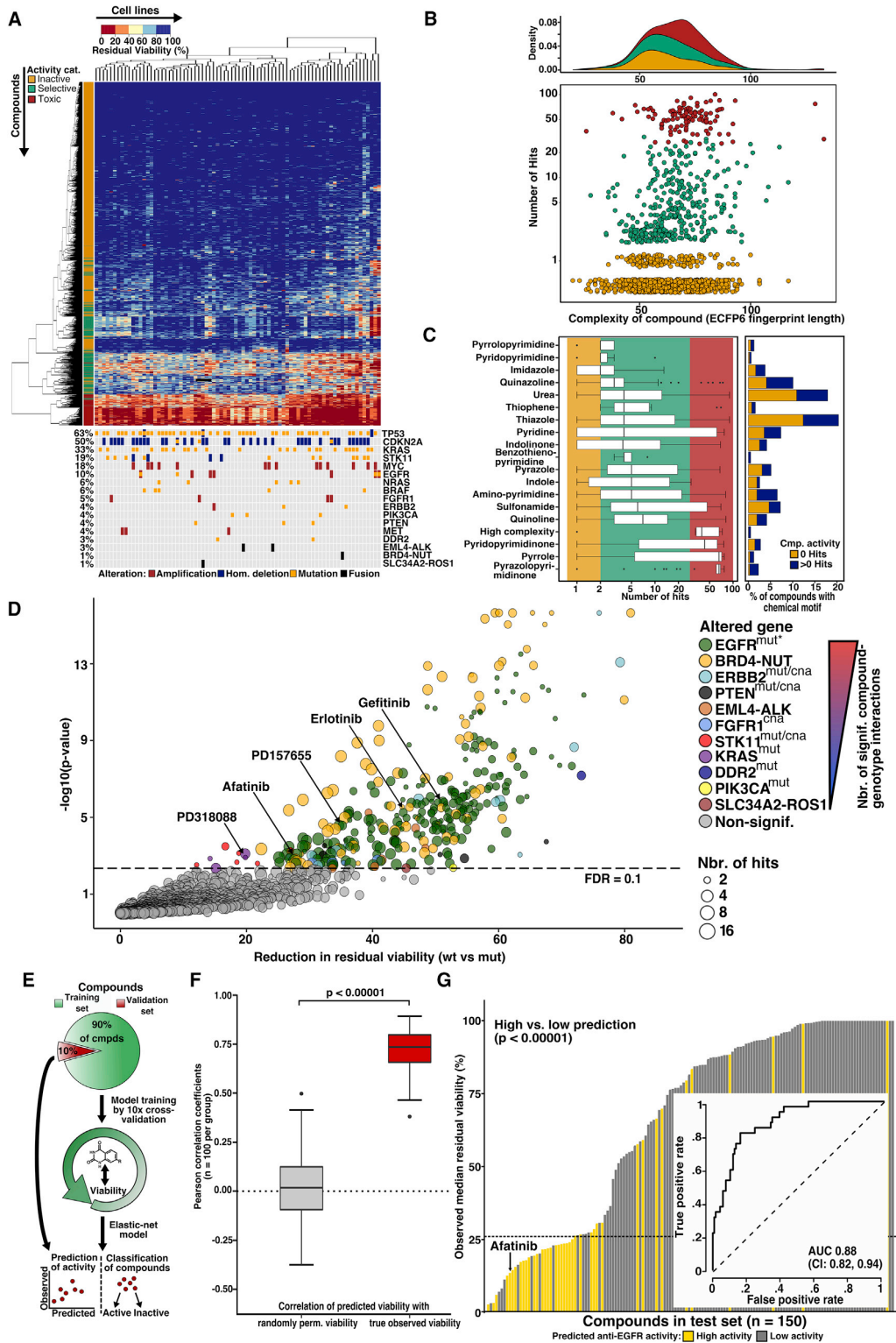
## INTRODUCTION

Systematic genomic profiling of tumors, combined with the development of targeted therapeutics, paved the way for a num-

ber of breakthroughs in the treatment of cancer patients (Büttner et al., 2013; Clinical Lung Cancer Genome Project (CLCGP) Network Genomic Medicine (NGM), 2013; Hyman et al., 2015; Kandoth et al., 2013). In genetically defined subgroups such as *EGFR*-mutant lung cancer the therapeutic exploitation of these alterations has already led to dramatic improvements in the clinical care of cancer patients (Flaherty et al., 2012; Rosell et al., 2012; Shaw et al., 2013; Van Cutsem et al., 2011). However, most oncogenic driver lesions are still considered to be undruggable.

Massively parallel interrogation of drug vulnerability across large panels of cancer cell lines has proved to be a valid tool for the identification and validation of genetically defined targets (Barretina et al., 2012; Garnett et al., 2012; Iorio et al., 2016; Martins et al., 2015; Seashore-Ludlow et al., 2015; Sos et al., 2009a, 2009b). Such screens can identify compounds that directly target driver alterations and offer the opportunity to discover additional vulnerabilities in non-mutated genes that only become essential in tumor-specific genetic backgrounds (Chan et al., 2011; Fece de la Cruz et al., 2015). Exploitation of such synthetic lethality has already provided alternative therapeutic approaches to selectively kill cancer cells while sparing normal tissue (McLornan et al., 2014). The cyclin-dependent kinases (CDKs) 1, 2, and 6 have been shown to gain relevance in several *MYC*-driven tumors and were thus proposed as context-specific synthetic lethal targets (Fece de la Cruz et al., 2015). Moreover, CDK9, which, together with Cyclin-T1, forms the positive transcription elongation factor b (P-TEFb) complex and induces transcriptional activation by hyperphosphorylating RNA polymerase





(legend on next page)

II (Pol II) (Lu et al., 2015; Morales and Giordano, 2016), was put forth as a potential therapeutic target in hepatocellular carcinoma (Huang et al., 2014), ovarian cancer (Lam et al., 2014), and hematological malignancies (Gregory et al., 2015; Walsby et al., 2014). As a consequence, several CDK inhibitors have entered clinical trials, but so far, a lack of specificity and resulting toxicity limits the clinical relevance of CDK inhibitors in cancer (Chen et al., 2014; Kumar et al., 2015; Morales and Giordano, 2016).

Here we evaluated the cellular activity of a library of 1,505 kinase inhibitors to systematically uncover genotype-specific vulnerabilities. Our data reveal that CDK9 inhibition specifically modulates transcriptional elongation and effectively impairs viability through induction of apoptosis and DNA damage response of NUT midline carcinoma (NMC) cells.

## RESULTS

### High-Throughput Cell Line Screening

In total, 1,505 chemical compounds with a spectrum of common kinase inhibitor motifs were screened against 78 cancer cell lines (Figures 1A–1C) (Barretina et al., 2012; Garnett et al., 2012; Sos et al., 2009b). Overall, 7.5% of all compound-cell line combinations were classified as candidate hits (Z score < -2, corresponding to a residual viability of <25.9% at 10  $\mu$ M) (Figure S1A). The high number of compounds that elicited only low or no cytotoxic effects across the cell lines is likely attributed to most compounds not having undergone previous target-based chemical or lead optimization (Figure 1A; Figure S1A). Based on the number of hits across cell lines ( $n_{\text{hits}}$ ), compounds showed a range of activity patterns ranging from lack of activity (65.2% of all compounds, termed inactive;  $n_{\text{hits}} < 2$ ) to broad and unselective toxicity (9.0%, termed toxic;  $n_{\text{hits}} > 30\%$  of cell lines) (Figure 1A).

To assess the impact of chemical complexity on compound activity, we calculated extended connectivity fingerprints (ECFP6) (Riniker and Landrum, 2013), whose lengths correspond to the number of distinct chemical features present in a given molecule. Neither biological selectivity nor compound potency depended on chemical complexity, as determined by the ECFP6-fingerprint length (Figure 1B). Inactive, selective, and toxic compounds were distributed at similar frequencies along the fingerprint lengths (Figure 1B, upper panel). However, analyses of compounds grouped by basic chemical scaffold (Hu

and Bajorath, 2013) indicated that the number of active compounds varied by core structures (Figure 1C). Specifically, compounds with selective patterns of activity were typically based on common scaffolds of established kinase inhibitors (e.g., amino-pyrimidines, imidazoles, indoles, pyrazoles, pyridines, quinazolines, and thiazoles) (Figure 1C, boxplot). By contrast, compounds based on a pyrazolopyrimidinone scaffold or those with a highly complex core structure (mainly staurosporine and derivatives thereof) were enriched in the group of primarily toxic activity (Figure 1C). Thus, within our dataset core, scaffolds are a major determinant of compound selectivity.

To discover genotype-specific effects of the selective compounds, cell lines were grouped according to the presence or absence of a given genomic alteration, and differences in the viability in those cell lines bearing such alteration and in those lacking it were tested by an ANOVA approach (Barretina et al., 2012; Garnett et al., 2012; Iorio et al., 2016; Sos et al., 2009b). Of all 6,664 possible compound-genotype combinations, 345 (hit rate = 5.2%) showed a significantly decreased viability in altered versus wild-type cell lines (false discovery rate [FDR]  $\leq$  0.1) with a significant enrichment of EGFR inhibitors scoring in EGFR-mutant cell lines (Figure 1D).

We hypothesized that based on the structural diversity of inhibitors with differential activity against EGFR, we might also be able to predict compound activity by chemical structure alone. To this end, we applied elastic net modeling for regression and classification of activity based on ECFP6 fingerprints using a training subset (90% of compounds), coupled with 10-fold cross-validation and subsequent testing on the remaining 10% of the compounds (Figure 1E) (Zou and Hastie, 2005). We first predicted median residual viability of EGFR-mutant cells as a continuous measure based on the fingerprints of compounds containing thiazoles ( $n = 398$ ) or quinazolines ( $n = 172$ ). Overall, a high degree of correlation between predicted and observed median viability was achieved for thiazoles (median Pearson  $r = 0.74$ ;  $p = 2.8 \times 10^{-33}$ ) (Figure 1F; Figure S1B) and quinazoline-based compounds (median Pearson  $r = 0.76$ ;  $p = 2.2 \times 10^{-47}$ ) (Figures S1C and S1D). Similarly, when performing binary predictions of compounds as having either high or low anti-EGFR activity in the complete compound set, irrespective of underlying scaffolds, compounds predicted to have high anti-EGFR activity exhibited significantly lower residual viabilities ( $p = 1.0 \times 10^{-8}$ ; area under the curve [AUC] 0.88) (Figure 1G). In an independent validation with data of the GlaxoSmithKline

### Figure 1. High-Throughput Cell Line Screening

- (A) Unsupervised hierarchical clustering of cell lines (columns,  $n = 78$ ) and compounds (rows,  $n = 1505$ ) based on residual viability (heatmap). Color bar (rows) represents classification of compounds based on the number of hits across cell lines. Bottom: annotation of known driver alterations and their frequency in the cell line panel.
- (B) Top: density plot of inactive, selective, and toxic compounds along the ECFP6-fingerprint length (color code as in A). Bottom: association of compound activity defined by the number of hits across cell lines, with chemical complexity assessed by the compounds' fingerprint lengths.
- (C) Bar graph: distribution of the most frequent scaffolds in the compound library. Boxplot: number of hits of active compounds grouped by chemical scaffold.
- (D) Volcano plot with viability reduction (x axis) and significance (y axis) of selective compounds ( $n = 392$ ) in genotypes annotated in (A) ( $n = 17$ ). (FDR, false discovery rate in the ANOVA model; \*H1975 was not included as EGFR<sup>mut</sup> due to its T790M resistance mutation.)
- (E) Schematic of the model building for elastic net models predicting percentage of viability or classifying compounds as active or inactive.
- (F) Correlation coefficients of predicted versus observed or randomly permuted residual viability in EGFR<sup>mut</sup> cell lines based on 100 elastic net models for thiazoles (two-sided Mann-Whitney test).
- (G) Classification of validation set compounds independent of underlying scaffold. Discriminatory capacity is indicated by the receiver operator analysis (ROC, inset; p value, Mann-Whitney test between compounds predicted to have high versus low activity against EGFR<sup>mut</sup> cell lines; CI, 95% confidence interval).

Protein Kinase Inhibitor Set (GSK PKIS) compounds, the elastic net model also reliably predicted high versus low activity against L858R-mutated EGFR ( $p = 1.9 \times 10^{-19}$ ; AUC 0.85; sensitivity 77.2%; specificity 81.9%) (Figure S1E).

Thus, our inhibitor screening data capture major genomic dependencies and our elastic net-based algorithm for the systematic deconvolution of genotype-chemotype relationships may be useful for the analysis of similar large-scale screening datasets.

### NMC Cells Are Sensitive to CDK9 Inhibition

The second most abundant genotype-chemotype interaction present in our dataset was identified for a *BRD4-NUT*-rearranged cell line (HCC2429) (Figure 1D) (Yan et al., 2011), which was among the cell lines with the highest degree of sensitivity toward several compounds (Figure S1F). *BRD4-NUT* fusions are a hallmark of NMC, a rare but highly aggressive tumor type associated with poor response to standard chemotherapy (French et al., 2003; Stathis et al., 2016). Among selective compounds with strong activity against HCC2429 cells, we identified LDC67, a known CDK9 inhibitor, as the most genotype-selective inhibitor (Figure 2A) (Albert et al., 2014). The 10 most active compounds shared structural features with LDC67 and known CDK inhibitors (Figure S2A) (Albert et al., 2014; Morales and Giordano, 2016; Rossi et al., 2005), suggesting that these chemotypes may be suited as a backbone for CDK inhibitors. To further validate our findings, we determined half-maximal growth inhibitory ( $GI_{50}$ ) values of LDC67 across 64 cell lines, including three NMC cell lines (HCC2429, 143100, and 690100), and found significantly ( $p = 1 \times 10^{-4}$ ) higher activity in all *BRD4-NUT*-rearranged cells compared to tumor cells lacking the rearrangement (Figure 2B; Figure S2B). We also observed a similar activity profile in the cases of the CDK inhibitor AT7519 ( $p = 5 \times 10^{-4}$ ) (Squires et al., 2009) and the bromodomain inhibitor JQ1 ( $p = 1.4 \times 10^{-7}$ ), which was previously shown to be active in NMC cells (Figures S2C and S2D) (Filippakopoulos et al., 2010). In line with these observations, CDK9 inhibition led to significantly reduced cell growth of *BRD4-NUT*-rearranged cells in clonogenic assays ( $p = 9 \times 10^{-7}$ ) (Figure 2C) and an induction of apoptosis at 24 hr ( $p = 0.001$ ) and 48 hr ( $p = 0.005$ ). Similarly, LDC67 treatment led to a significant increase in the sub-G1 fraction (control, 8.0%; LDC67, 57%;  $p = 0.047$ ) in *BRD4-NUT*-rearranged cells, but not in control cells (Figure S2E). We subsequently sought to determine potential mechanistic links between CDK9i and apoptosis induction. Because CDK9i has been described as conferring an apoptosis-primed state by repressing anti-apoptotic Mcl-1 (Gregory et al., 2015; Huang et al., 2014; Lemke et al., 2014), we analyzed Mcl-1 expression levels under LDC67 treatment as a function of time. Mcl-1 protein expression was almost abrogated in HCC2429 cells, but not in A549 (*KRAS<sup>mut</sup>*) cells (Figure 2E). In addition to interfering with global transcription and altering the balance of pro- and anti-apoptotic proteins, CDK9 was shown to be involved in the DNA damage response (Yu et al., 2010; Zhang et al., 2013). We therefore investigated the levels of  $\gamma$ H2AX and phospho-Chk2, surrogate markers of DNA damage (Yu et al., 2010), under LDC67 treatment. We observed strong upregulation of  $\gamma$ H2AX and phospho-Chk2 in HCC2429, while such induction was considerably lower in A549 cells (Figure 2E). In addition, we

were able to confirm a significant increase of  $\gamma$ H2AX-positive HCC2429 cells (24 hr) by fluorescence-activated cell sorting (FACS) analysis after co-staining for  $\gamma$ H2AX and cleaved caspase-3 (Figure 2F).

Overall, our data suggest that *BRD4-NUT*-rearranged NMC cells may be particularly vulnerable to CDK9 inhibition.

### *BRD4-NUT*-Driven Cells Display a Distinctive CDK9 Dependency

To test a specific dependency of NMC cells on CDK9 expression that may explain the observed phenotype in CDK9i-treated cells, we performed short hairpin RNA (shRNA)-mediated knockdown of both components of P-TEFb, CDK9, and Cyclin-T1 (Figures 3A and 3B). Similar to CDK9 inhibition, we observed a significant ( $p = 2 \times 10^{-4}$ ) reduction in cellular viability of NMC cells (HCC2429), but not of control cells (A549) (Figures 3A and 3B). We next tested the effects of LDC67 in NMC and control cells (A549 and HCC15) on phosphorylation of Pol II and observed a dose-dependent decrease of Ser2 phosphorylation, irrespective of the underlying genotype (Figure 3C). Previously, cellular efficacy of CDK9 inhibitors has been linked with changes in the complex formation of P-TEFb with its negative regulator HEXIM1 (Huang et al., 2014; Itzen et al., 2014; Lu et al., 2015; Morales and Giordano, 2016). To monitor such drug-induced effects, we performed immunoprecipitation assays of endogenous CDK9 in HCC2429 and A549 cells treated with LDC67. We observed a modest but reproducible reduction of HEXIM1-bound CDK9 in both cell lines (Figure 3D), with a more profound disruption of HEXIM1/CDK9 complexes in HCC2429 cells (72.6%) when compared to A549 cells (85.6%) after 4 hr LDC67 treatment (Figure 3D). We were able to validate this CDK9 inhibitor-induced effect when overexpressing FLAG-CDK9 in HCC2429 cells with a HEXIM1/FLAG-CDK9 ratio of 14.6% after LDC67 (4 hr) treatment (Figure S3A).

These data further highlight the relevance of CDK9 expression in NMC and suggest that the effects achieved by LDC67 may be attributable to direct inhibition of CDK9.

### CDK9-Specific Effects in NMC Cells

Previous reports have implicated *MYC* expression as a relevant downstream effector of *BRD4-NUT*-driven cells in the context of BRD4 inhibitor treatment (Grayson et al., 2014; Sos et al., 2009b). To test the relevance of *MYC* expression in *BRD4-NUT*-rearranged cells, we performed shRNA-mediated *MYC* knockdown and observed a significant ( $p = 8.1 \times 10^{-5}$ ) reduction of viability in HCC2429 cells that did not strongly differ ( $p = 0.1$ ) from that of A549 control cells (Figure S3B). When monitoring Myc protein levels during drug treatment, bromodomain inhibition with JQ1 led to a constant decrease of Myc protein expression as expected (Figures 4A and 4B; Figure S3C). To our surprise, we observed an initial moderate increase of Myc protein levels and a subsequent reduction after 48 to 72 hr of LDC67 treatment in HCC2429 *BRD4-NUT*-rearranged cells, but not in A549 control cells (Figures 4A and 4B; Figure S3C) (Lu et al., 2015). We observed a similar reduction of Myc protein levels, together with an increase in  $\gamma$ H2AX and depletion of Mcl-1 in the 143100 NMC cells but without the initial Myc increase, suggesting that the effect on Myc expression may be cell line specific (Figure S3D). The overlapping effects on Myc expression

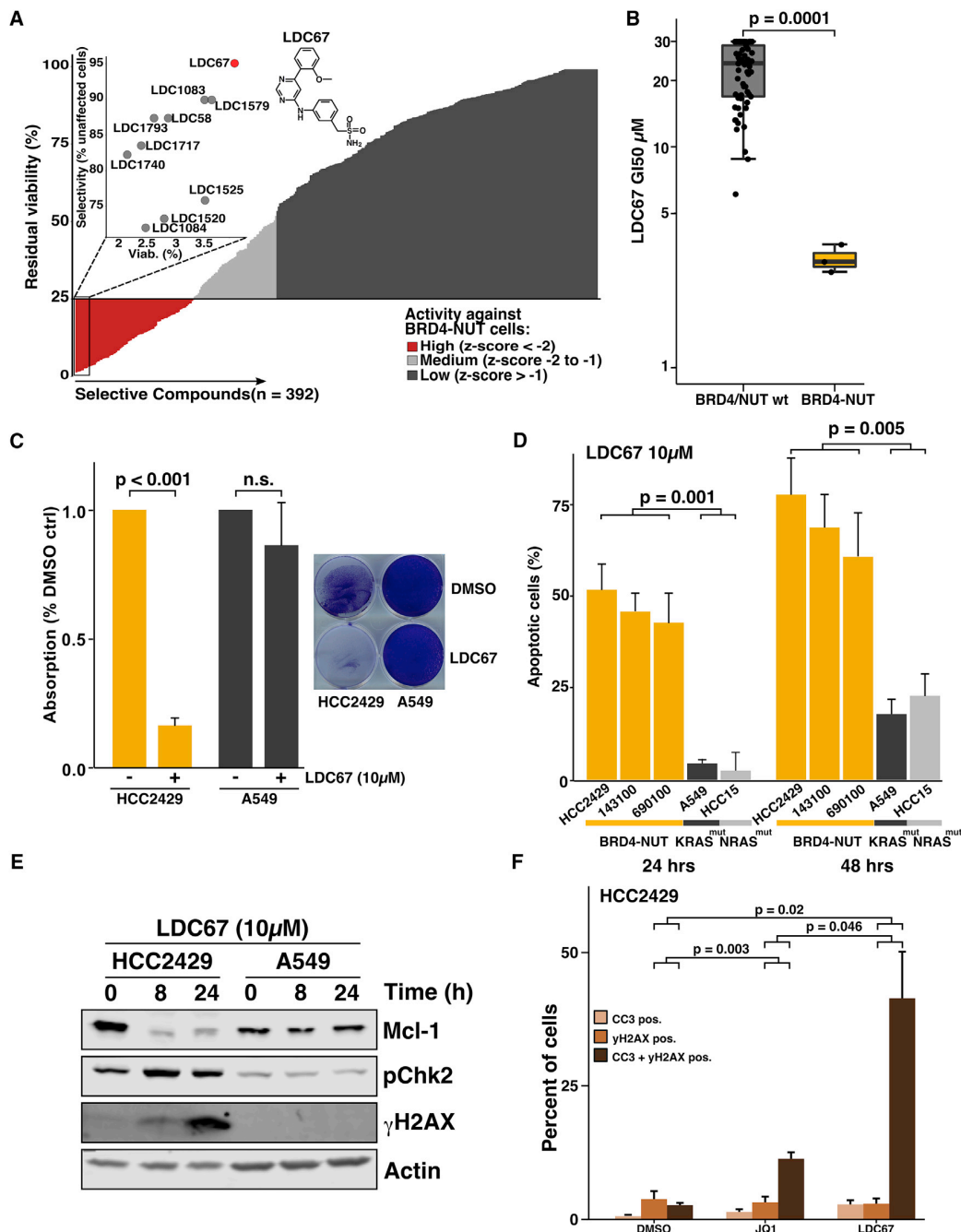


**Figure 2. CDK9 Inhibition Exhibits Distinct Effects on BRD4-NUT-Rearranged NMC Cells**

(A) Activity of selective compounds against BRD4-NUT-rearranged HCC2429 cells. To obtain the most genotype-selective inhibitor, the percentage of cell lines that were not impacted below the hit threshold was calculated for the ten most potent compounds (inset).

(B) GI<sub>50</sub> values from LDC67 dose-response curves (72 hr) across 64 cell lines.

(C) Clonogenic survival assays of HCC2429 and A549 of LDC67 treatment or DMSO control (mean ± SD; n = 3).

(D) Apoptosis measured by Annexin V flow cytometry in BRD4-NUT-rearranged and control cells following treatment with 10 μM LDC67 (mean ± SD; n = 3).

(E) Immunoblot of HCC2429 and A549 cells treated with LDC67 for the indicated periods.

(F) HCC2429 cells treated for 24 hr with 10 μM LDC67, 0.5 μM JQ1, or DMSO were co-stained for cleaved caspase-3 (CC3) and γH2AX and measured by flow cytometry (mean ± SEM; n = 3; p values calculated by two-tailed t tests).

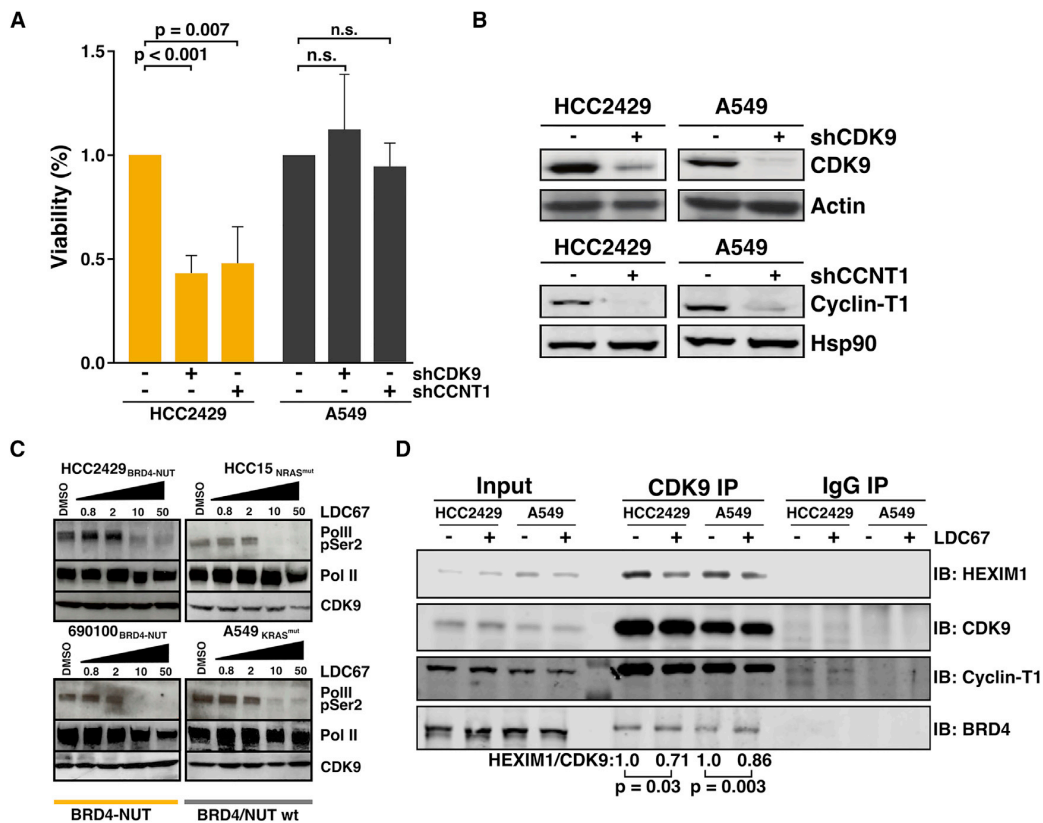


**Figure 3. Effects of CDK9 or Cyclin-T1 Perturbation in NMC Cells**

(A and B) shRNA-based gene knockdown of CDK9 or Cyclin-T1 was performed in HCC2429 and A549 cells and effects on viability (A) and protein levels (B) were assessed compared to controls (mean  $\pm$  SEM; n = 3).

(C) LDC67 on-target activity assessed by reduction of RNA polymerase II (Pol II) phosphorylation at Ser2 after 24 hr.

(D) Immunoprecipitations (IPs) of endogenous CDK9 show reduced HEXIM1/CDK9 complex abundance after 4 hr LDC67 treatment (n = 3; two-tailed t test). IgG was used as unspecific negative IP control.

induced by JQ1 and LDC67 may partly explain the additive effects observed for the combination of both compounds and partial cross-resistance of JQ1-persistent HCC2429 clones ( $GI_{50} = 11.62 \mu\text{M}$  JQ1P versus  $GI_{50} = 72 \text{ nM}$  parental) (Figures S3E–S3H).

We also observed that treatment with both inhibitors led to induction of cleaved caspase-3 within 24–48 hr (Figure 4A). Using a more quantitative approach, we noticed a significantly higher fraction of apoptotic cells under LDC67 compared to JQ1 treatment in flow cytometric analyses (LDC67 61% versus JQ1 31%;  $p = 0.02$ ) (Figure S3I). By contrast, only bromodomain inhibition, not CDK9 inhibition, led to a dramatic induction of the p53 target gene p21 and a block of S phase entry (Figures 4A–4E; Figure S3J). In parallel, in JQ1-treated, but not LDC67-treated, HCC2429 cells, we observed disassembly of hyperacetylated/p300-positive foci that may lead to restoration of p53 activity, as described in previous reports (Figures 4F and 4G) (Huang et al., 2014; Reynoird et al., 2010).

Thus, our data indicate that in contrast to bromodomain inhibition, CDK9 inhibition does not lead to a cell-cycle arrest and

that over time, both perturbations induce a similar reduction of Myc expression.

### CDK9 Inhibition Perturbs Defined Transcriptional Programs in NMC Cells

To further investigate the signaling patterns induced by CDK9 inhibition, we performed transcriptome profiling (RNA sequencing [RNA-seq]) in NMC cells. RNA-seq indicated that LDC67 treatment induces an initial increase (8 hr), followed by downregulation (48 hr) of transcripts involved in RNA binding and translation, of ribosomal subunits in gene set enrichment analyses (GSEAs) and included known surrogate markers of P-TEFb complex activity, such as *FOS* (Figures 5A–5C; Figure S4A; Tables S1 and S2) (Lu et al., 2015; Stathis et al., 2016; Yan et al., 2011). We were also able to confirm that LDC67 and JQ1 treatment was associated with a perturbation of cellular processes linked with Myc activity (Figure 5C; Tables S3 and S4). The changes induced by LDC67 were most prevalent in genes regulated by promoters with high affinity for Myc (Figure S4B) (Lorenzin et al., 2016; P.J. O'Dwyer et al.,

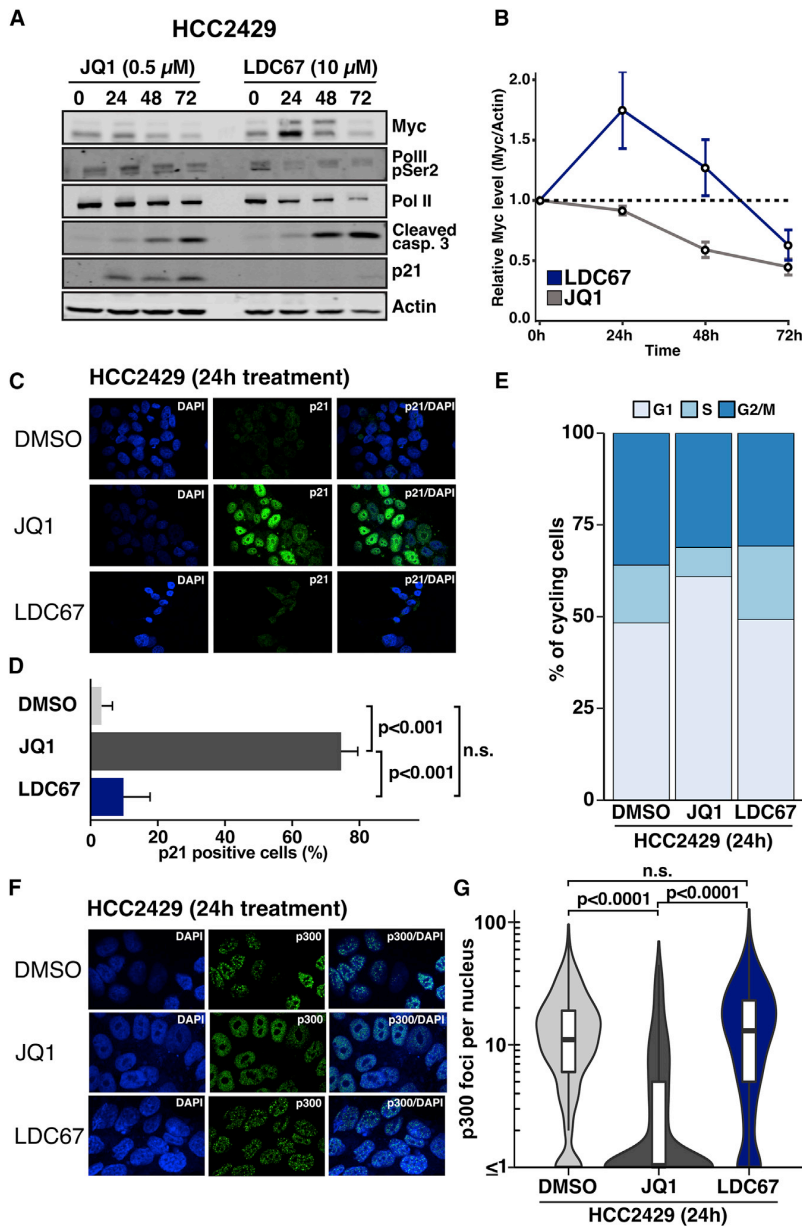


**Figure 4. Differential Effects of CDK9 and BRD4 Inhibition on NMC Cells**

(A and B) Effects of JQ1 and LDC67 treatment on protein levels in HCC2429 were assessed by immunoblotting (A) and Myc protein levels over time were quantified and normalized to actin (B) (mean  $\pm$  SEM; n = 5).

(C and D) Immunofluorescence of p21 protein expression in HCC2429 cells after 24 hr LDC67 (10  $\mu$ M) or JQ1 (500 nM) treatment (C). For quantification (D), in total, >100 cells were assessed per condition (bars represent the percentage of p21-positive cells  $\pm$  95% CI; p values were calculated by chi-square tests).

(E) Cell-cycle distribution of cycling cells assessed by flow cytometry of propidium iodide-stained HCC2429 cells after 24 hr treatment with 10  $\mu$ M LDC67 or 500 nM JQ1.

(F and G) Representative immunofluorescence (IF) images of HCC2429 cells stained for p300 foci after 24 hr DMSO, JQ1 (500 nM), or LDC67 (10  $\mu$ M) (F). Number of foci per nucleus was quantified in n = 3 experiments (G), with >250 cells per condition (two-tailed Wilcoxon tests).

To validate our RNA-seq results and to assess the impact of CDK9i on de novo transcription, we performed qRT-PCR of mature mRNA and of unspliced pre-mRNA for a set of upregulated genes (*FOS*, *JUNB*, and *MYC*) and downregulated genes (*FOXO6* and *KLHL23*) after LDC67 treatment. We chose 18S rRNA for qPCR normalization that remained stable under inhibitor treatment while RNA-seq normalizes expression relative to the complete transcriptome. Overall, the RNA-seq results validated well for mature and pre-mRNA (Figures 5B and 5E). Increased pre-mRNA levels of *FOS* and *JUNB* suggest that these genes are actively transcribed despite CDK9i. However, the strong decrease of *FOXO6* and *KLHL23* pre-mRNA indicates CDK9i-mediated elongation defects and abrogation of de novo transcription. *MYC* mRNA did not increase but instead stayed constant at 8 hr of LDC67 treatment,

followed by a delayed reduction at 48 hr (Figure 5B). The apparent difference to the RNA-seq results is most likely due to the aforementioned differences in normalization. Furthermore, *MYC* pre-mRNA levels were decreased after 8 and 48 hr of LDC67 treatment (Figure 5B). As expected, bromodomain inhibition with JQ1 led to a constant decrease of *MYC* pre-mRNA, mature mRNA, and protein expression (Figure 4A; Figures 5D and 5E). Depletion of CDK9 or Cyclin-T1 in these cells led to a similar reduction of premature and mature *MYC* mRNA corresponding to the respective knockdown efficacies (Figure 5F; Figure S4F).

2016, Cancer Res., abstract). As expected, the timing of the transcriptional changes and the individual gene sets in HCC2429 cells treated with the bromodomain inhibitor JQ1 strongly differed from those treated with the CDK9 inhibitor LDC67 (Figure 5C; Figures S4A–S4D). We also observed a robust enrichment of genes involved in cytoskeletal regulation in JQ1-treated cells and a reduction of cell-cycle gene sets (Figure 5C; Figure S4A; Tables S1 and S2), which may correspond to the morphological changes induced by JQ1 (Figure S4E) (Aleksyenko et al., 2015; Filippakopoulos et al., 2010; Grayson et al., 2014; Stathis et al., 2016).

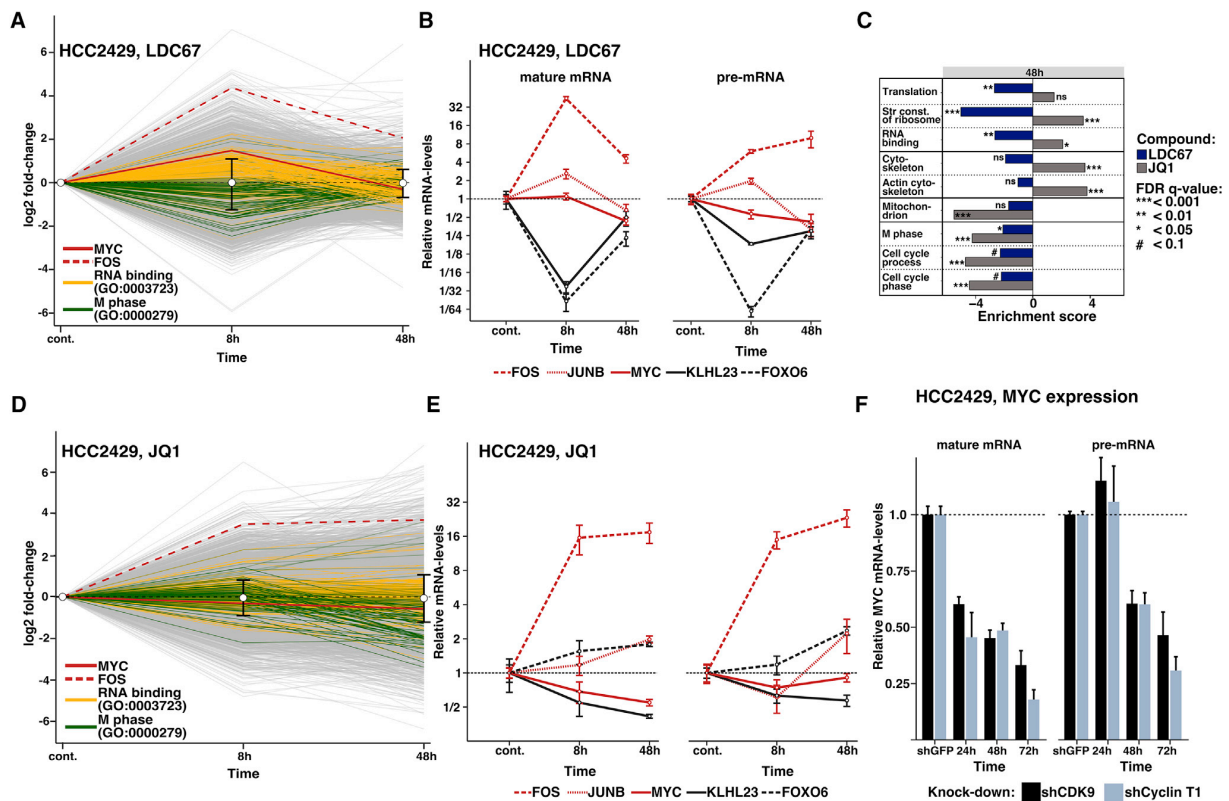


**Figure 5. Transcriptional Dynamics after CDK9 Inhibition in NMC Cells**

(A) Time course of RNA-seq log<sub>2</sub> fold changes for all genes (gray lines) between LDC67-treated and control (cont.) HCC2429 cells. Two gene ontology (GO) gene sets (yellow and green) and *MYC* and *FOS* (red) are indicated. Error bars represent median and 10% or 90% quantiles of all log<sub>2</sub> fold changes at respective time points.

(B) qRT-PCR (normalized to 18S rRNA) of selected genes following LDC67 (10 μM) or DMSO control (cont.) for mature mRNA (left) and for unspliced pre-mRNA (right) (mean ± SD; n = 3).

(C) GO terms enriched in gene set enrichment analysis (GSEA, C5) of RNA-seq data from HCC2429 treated (48 hr) with JQ1 (gray) or LDC67 (blue) compared to controls (x axis, normalized enrichment score; FDR-corrected q values < 0.1 are considered significant).

(D) Time course of RNA-seq log<sub>2</sub> fold changes for all genes (gray lines) between JQ1-treated and control (cont.) HCC2429 cells. Color codes as in (A).

(E) qRT-PCR (normalized to 18S rRNA) of selected genes following JQ1 (500 nM) treatment for mature mRNA (left) and for unspliced pre-mRNA (right) (mean ± SEM; n = 3).

(F) qRT-PCR time course of *MYC* mRNA normalized to 18S rRNA after CDK9 (black) or Cyclin-T1 (gray) knockdown compared to shGFP controls (mean ± SEM; n = 3).

Thus, CDK9 inhibition may lead to defined genotype-specific transcriptional changes but may also interfere with *MYC* mRNA stability and increase *MYC* translation rather than de novo transcription.

### CDK9 Inhibition Has a Major Effect on Transcriptional Elongation in NMC Cells

We next sought to directly evaluate the effect of CDK9 inhibition on the process of transcriptional elongation. To this end, we performed chromatin immunoprecipitation (ChIP) experiments after short-term CDK9 inhibition and measured Pol II occupancy for genes in which expression was increased (*MYC*, *FOS*, *JUNB*, and *SF3B4*) or did not increase (*FOXO6*, *KLHL23*, *BRG1*, and *NPM1*) relative to the global transcriptome

in RNA-seq analyses after short-term CDK9 inhibition (Figures 6A–6C; Figure S5). When assessing Pol II distribution with an antibody raised against the unphosphorylated C-terminal domain (CTD), Pol II occupancy in the gene body (GB) remained constant or was even increased in upregulated genes, while the GB signal was decreased in the other genes (Figures 6A–6C; Figure S5). The signal at the transcription start site (TSS) was more variable.

Overall, this translated into decreased pausing indices (PIs, or the ratio of TSS-bound Pol II to GB-bound Pol II) for the upregulated genes and constant or increased PI for the other genes (Figure 6D). These findings are compatible with higher transcription rates in the upregulated genes and correspond to significantly lower RNA expression of the genes with increased

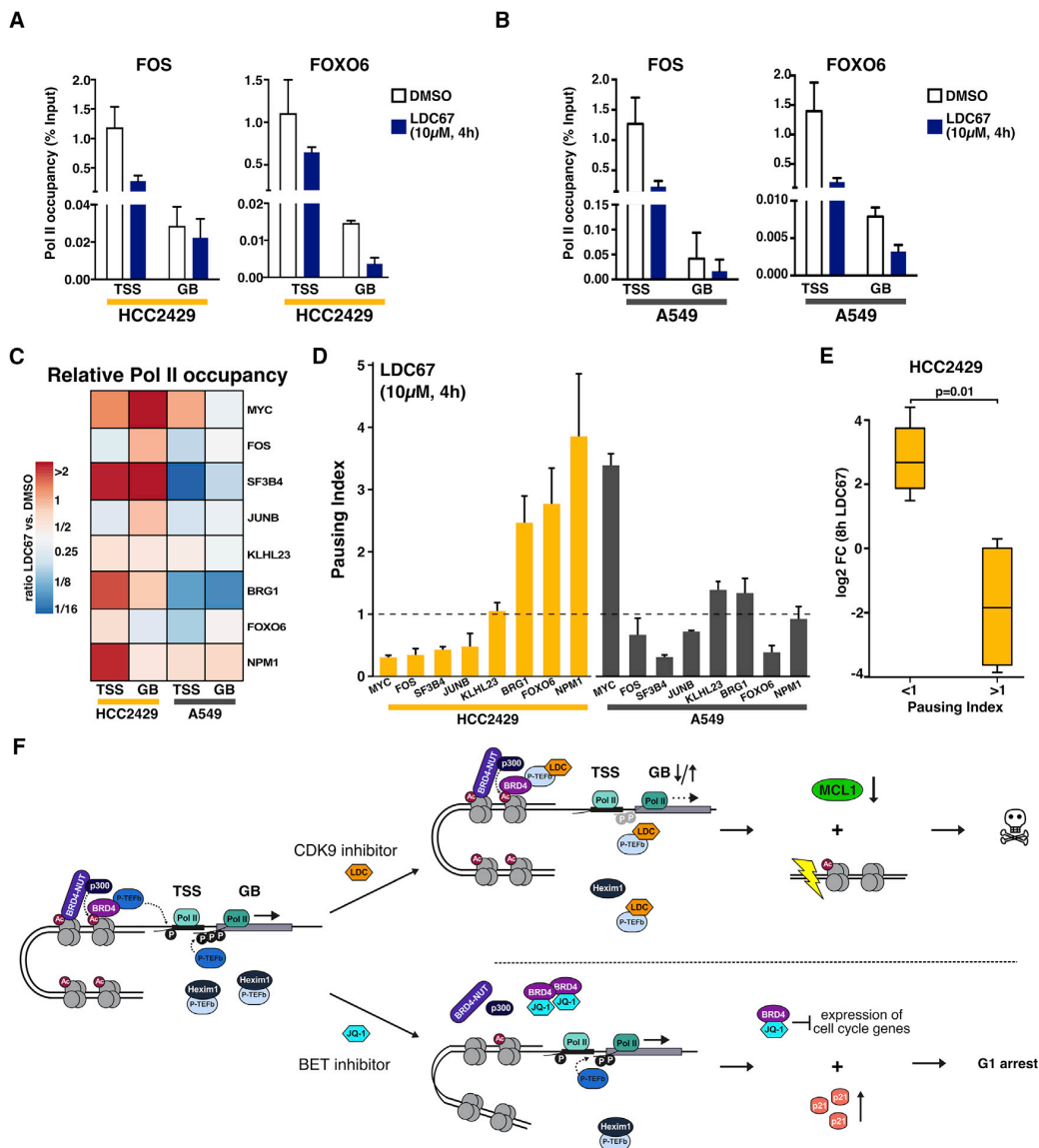


**Figure 6. Effects of CDK9 Inhibition on Pol II Occupancy**

(A and B) ChIP qPCR with an antibody raised against the unphosphorylated CTD assessing Pol II occupancy (displayed as a percentage of input DNA) at the transcription start site (TSS) and the gene body (GB) of *FOS* and *FOXO6* in HCC2429 (A) and A549 (B) after 4 hr LDC67 (10  $\mu$ M) treatment compared to DMSO controls (mean  $\pm$  SD, n = 3).

(C) Relative changes of unphosphorylated CTD Pol II signal at TSS and GB between LDC67 and control cells.

(D) Pausing index (Pol II at TSS to Pol II in GB) for the selected genes normalized to DMSO control (mean  $\pm$  SEM; n = 3).

(E) Log<sub>2</sub> fold changes in RNA-seq of HCC2429 cells treated with LDC67 (8 hr and 10  $\mu$ M) for the genes used for ChIP experiments. The p value between genes with high versus low PI was calculated by a Welch t test.

(F) Proposed model of the differential effects of CDK9 and JQ1 inhibition in NMC cells.

pausing ( $p = 0.01$  for  $PI > 1$  versus  $PI < 1$ ) (Figure 6E) (Huang et al., 2014; P.J. O'Dwyer et al., 2016, Cancer Res., abstract). By contrast, A549 cells showed reduced Pol II occupancy in all genes on the GB and at varying degrees at the TSS (Figures 6B and 6C; Figure S5).

To further investigate CDK9i-induced Pol II distribution, we performed ChIP analyses for Pol II p-Ser5 and Pol II p-Ser2, which indicate poised Pol II and elongating Pol II, respectively. As expected, the signal for p-Ser5 Pol II corresponded well to the total CTD-Pol II across the TSS and GB ( $r = 0.98$ ,

$p < 10^{-10}$ ). This substantiates the findings that LDC67 prevents Pol II pause release and productive elongation at *FOXO6* and *KLHL23*, thereby causing transcriptional repression of these genes (Figure S5). Surprisingly, we noticed a more pronounced decrease of the p-Ser2 Pol II signal following CDK9i at the TSS of *FOS* and *JUNB* than in the GB and higher p-Ser2 levels at the TSS, rather than a predominance of p-Ser2 Pol II signals in the GB (Figure S5). Even though this was unexpected, similar observations are known from other ChIP studies and may be due to the genes under study and the location of primers used in the qPCR (Nojima et al., 2015; Odawara et al., 2011; Stock et al., 2007; Zhang et al., 2016). However, the constant p-Ser2 levels in the gene bodies of *FOS* and *JUNB* following LDC67 treatment, as well as the increased pre-mRNA levels, indicate productive elongation and ongoing transcription during CDK9i. Although this might be due to incomplete block of P-TEFb activity or release of P-TEFb from its inhibitory complex after short-time inhibitor treatment (Lu et al., 2015), it may be speculated that this effect is potentially due to involvement of other CDKs (e.g., CDK12 and/or CDK13) that were shown to be capable of phosphorylating Ser2 of Pol II CTD (Bösken et al., 2014; Greifenberg et al., 2016).

Overall, differential effects were observed not only between HCC2429 and A549 but also among the genes investigated in HCC2429. Altogether, these data underline the distinctive role of CDK9 for transcriptional control in NMC cells, which may be linked with their specific vulnerability to CDK9 inhibition.

## DISCUSSION

Systematic screening of genetically annotated cancer cell lines has proved to be a suitable tool for the identification of genetic vulnerabilities and potential therapeutic targets (Barretina et al., 2012; Garnett et al., 2012; Iorio et al., 2016; Martins et al., 2015; Seashore-Ludlow et al., 2015; Sos et al., 2009b, 2009a). Our screening approach involving 1,505 kinase inhibitors coupled with a systematic deconvolution and prediction of genotype-chemotype relationships enabled a structure-based prediction of biological activity in silico and may thus be of value to focus future screening projects on the most promising candidate compounds.

To our surprise, one of the most striking genotype-specific vulnerabilities in our screen was the exquisite activity of LDC67, a known CDK9 inhibitor in NMC cells (Albert et al., 2014). Our chemical genomics approach uncovered a role of CDK9 as a non-oncogenic driver for tumorigenesis in *BRD4-NUT*-dependent cells mediated by regulation of transcription and Myc protein levels in NMC. CDK9 has also been identified as a key regulator of transcriptional regulation in *MYC*-overexpressing hepatocellular carcinoma (Huang et al., 2014). However, the evident CDK9i-induced differences on the level of Pol II-mediated transcriptional elongation observed in NMC and hepatocellular carcinoma indicate that these processes may be distinct for individual lineages.

NMC is a rare but highly aggressive tumor with a median survival of 6.7 months for which no approved therapies exist (Stathis et al., 2016). An initial report from a BET inhibitor phase I/II trial (GSK525762 and NCT01587703) described partial responses

in 2 of 10 NMC patients (P.J. O'Dwyer et al., 2016, Cancer Res., abstract), while another preliminary analysis reported a partial response in 3 of 4 NMC patients after BET inhibitor OTX015/MK-8628 with relapse within a few months (Stathis et al., 2016). Of 10 NMC cases treated with GSK525762, four patients responded with stable disease (P.J. O'Dwyer et al., 2016, Cancer Res., abstract). This is in line with the previous observations and our results, indicating that BRD4 inhibition leads to dissolution of hyperacetylated nuclear foci, release of p53 with induction of p21, cell-cycle arrest, and differentiation (Figures 4, 5C, 5D, and 6F; Figure S4E) (Alekseyenko et al., 2015; Grayson et al., 2014; Reynoird et al., 2010; Yan et al., 2011). By contrast, our data reveal that CDK9i may lead to robust Mcl-1 suppression, induction of DNA damage response and apoptosis in these cells (Figure 6F). For several genes, including *FOS*, transcription is increased following CDK9 inhibition. This has partly been attributed to CDK9i-induced release of P-TEFb from its inhibitory complex with HEXIM1 by a CDK9 inhibitor (Lu et al., 2015), an effect we also observed in NMC cells (Figure 3D and 6F; Figure S3A). We speculate that this phenomenon may be related to structural changes of P-TEFb induced by CDK9 inhibitor binding (Baumli et al., 2008). Although CDK9i-induced perturbation of *MYC* expression partially overlaps with the effects of bromodomain inhibition, it remains to be seen how much these effects contribute to the overall cellular phenotype observed for these types of inhibitors. Overall, our findings uncover major molecular differences between the mode of action of bromodomain and that of CDK9 inhibitors in NMC and suggest that CDK9 may be an attractive drug target in NMC patients.

In the past, clinical studies investigating spectrum CDK inhibitors such as dinaciclib or flavopiridol reported high rates of side effects and dose-limiting toxicities (Kumar et al., 2015; Morales and Giordano, 2016), but more selective compounds such as ribociclib (CDK4 and CDK6) demonstrated the feasibility of CDK inhibition even as first-line cancer treatment (Hortobagyi et al., 2016). For this reason, several CDK9 inhibitors with improved selectivity profiles were developed and hold promise for future development in clinical applications (Albert et al., 2014; Lam et al., 2014; Lu et al., 2015; Morales and Giordano, 2016). Our findings may therefore be of relevance for the future development of these drugs and the stratification of patients receiving these types of selective CDK9 inhibitors.

In conclusion, our study provides a framework for the deconvolution and prediction of genotype-chemotype relationships in a large-scale kinase inhibitor screen and identifies CDK9 as a druggable target in NMC. Our results also provide insight into CDK9 exerted control of transcriptional elongation and its genotype-specific effects in *BRD4-NUT*-rearranged tumors.

## EXPERIMENTAL PROCEDURES

### High-Throughput Screening

For high-throughput screening 78 genomically annotated patient-derived lung cancer cell lines were assayed against 1,505 small-molecular compounds predominantly consisting of compounds before lead or target-based optimization across a range of chemical scaffolds and a number of established reference kinase inhibitors. For screening, cell lines were treated at a single-dose concentration, which was determined during a preliminary screen. Residual viability was assessed after 72 hr by CellTiter-Glo (CTG, Promega). Chemical

information was captured by simplified molecular input line entry specification (SMILES) codes and by manual annotation of scaffolds (Figure S6). A number of compounds and cell lines were screened in duplicate to assess reproducibility. Moreover, external validity was assessed in a subset of compounds and cell lines by testing compound activity in dilution series to assess  $GI_{50}$  after 72 hr by CTG (Promega). Genotype-specific compound activity was assessed using an ANOVA approach similar to previous studies (Barretina et al., 2012; Garnett et al., 2012; Seashore-Ludlow et al., 2015), incorporating genotype and histological subtype in a random effects model. Activity predictions were done with elastic net regression models using ECFP6 fingerprints of the compounds as the predictor and residual viability or compound activity as the response. Models were trained on a subset of compounds with 10-fold cross-validation and were evaluated on the compounds not involved in model building and on an external validation dataset (Elkins et al., 2016).

#### Apoptosis, Proliferation, and Survival Assays

Apoptosis was measured by flow cytometry following Annexin V and propidium iodide staining on a FACS Gallios Flow Cytometer and the corresponding Kaluza analysis software (Beckman Coulter, USA). Cell-cycle analyses were performed by flow cytometry on methanol-fixed cells after propidium iodide staining. For FACS analysis of cleaved caspase-3 (CC3) and  $\gamma$ H2AX, cells were treated for indicated times, harvested by trypsinization, and fixed in 80% methanol. Fixed cells were permeabilized and blocked with PBS/1% BSA before they were incubated with primary antibodies at 4°C overnight. The following day, cells were washed, incubated with Alexa Fluor secondary antibodies (Thermo Scientific), and measured on a Gallios Flow Cytometer (Beckman Coulter, USA).

For clonogenic survival assays, cells were seeded in 6-well plates, treated for indicated times, fixed with 4% formaldehyde, and stained with crystal violet solution. For quantification, a 1% SDS solution was added to the wells for 30 min and absorption was measured at 590 nm in the supernatant.

#### Immunoblot, Immunoprecipitation, and Immunofluorescence Assays

Cellular signaling following LDC67 or JQ1 treatment was assessed by protein gel electrophoresis. Equal amounts of protein lysates were separated on 4%–20% Novex Tris-glycine gels (Invitrogen), transferred to polyvinylidene fluoride (PVDF) membrane, and incubated with indicated primary antibodies. Proteins were detected with the Odyssey CLx imaging system (LI-COR Biosciences). For immunoprecipitation, antibodies directed against endogenous CDK9 or transiently transfected FLAG-CDK9 were used for precipitation at 4°C overnight, followed by immunoblotting. FLAG-CDK9 plasmids were a gift of Prof. Qiang Zhou (University of California, Berkeley, USA) (Lu et al., 2015) and were transiently transfected before immunoprecipitation.

For immunofluorescence, cells were grown on coverslips and treated for 24 hr before fixation with 4% formaldehyde, followed by staining with the indicated primary antibodies at 4°C overnight. Samples were incubated with Alexa Fluor secondary antibodies (Thermo Scientific) for 2 hr and mounted with DAPI before imaging (Zeiss Meta 510 or Zeiss Meta 710).

#### shRNA Knockdowns

For knockdowns, respective shRNAs or shRNA against GFP (shGFP) were generated with pLKO.1-puro vectors. Replication-deficient lentiviruses were produced in HEK293T cells by co-transfection of pLKO.1-puro vectors and helper plasmids. Supernatant collected 48 hr after transfection of HEK293T cells was used to transfect HCC2429 and A549 cells. Knockdown efficiency and effects on cell viability were validated by immunoblotting and CTG (Promega) 4–6 days after transfection, as described previously (Sos et al., 2009a).

#### ChIP

For ChIP experiments, cells were cross-linked with formaldehyde before chromatin was extracted, sonicated, and incubated with primary antibodies (Pol II, pSer2-Pol II or pSer5-Pol II) or mouse immunoglobulin G (IgG) overnight. Antibody complexes were then captured with protein G beads, and DNA was eluted, decrosslinked, and purified. ChIP signals were calculated by qPCR (Table S5) relative to input levels after (IgG) background subtraction.

#### RNA Analysis

For RNA-seq and qPCR (Table S5) analyses, total RNA was isolated following LDC67 or JQ1 treatment. 3' RNA-seq libraries were prepared with the QuantSeq FWD 3' mRNA-Seq Kit (Lexogen, Austria), sequenced on an Illumina Hi-Seq 4000, and quantified after alignment to the human genome reference hg38. Data processing and statistical analyses were performed using Microsoft Excel (Microsoft, USA), GraphPad (Prism, USA), and R (R Development Core Team, 2011). Half-maximal growth inhibitory ( $GI_{50}$ ) concentrations of cell viability were inferred by fitting sigmoidal dose-response curves. Data are represented as mean  $\pm$  SEM, and significance was calculated by unpaired Student's *t* tests or Mann-Whitney tests unless indicated otherwise. The *p* values are always two-sided. For details, see Supplemental Information.

#### ACCESSION NUMBERS

The accession number for the RNA-seq data sets reported in this paper is European Genome-Phenome Archive: EGAS00001002588.

#### SUPPLEMENTAL INFORMATION

Supplemental Information includes Supplemental Experimental Procedures, six figures, and five tables and can be found with this article online at <http://dx.doi.org/10.1016/j.celrep.2017.08.082>.

#### AUTHOR CONTRIBUTIONS

J.B., M.A.D., F.D., J.M.H., A.C., S.B., C.L., V.T., A.R., D.B., Z.F., S.O.-C., M.G., M.T., M.S., and H.B.-W. performed experiments. A.C., J.E., U.K., F.D., Z.F., P.H., M.G., M.T., and M.S. performed drug screening. J.B., F.L., and M.P. analyzed RNA-seq data. C.A.F. provided NMC cell lines. Z.G., Z.V., L.Ö., G.K., and S.A. helped in experimental design and provided compounds and chemical structural information. J.B., M.A.D., S.B., A.C., Z.F., C.A.F., Z.V., L.Ö., G.K., H.C.R., S.A., L.C.H., R.B., D.R., B.M.K., R.K.T., and M.L.S. conceived experiments and wrote the manuscript. R.K.T. and M.L.S. conceived the study.

#### ACKNOWLEDGMENTS

We thank Prof. Oliver Gautschi (Cantonal Hospital Lucerne, Switzerland) for insightful discussions, Dr. Graziella Bosco (University of Cologne, Germany) for help with RNA-seq data processing, and Prof. Nicolaus Friedrich (University of Cologne, Germany) for immunohistological staining. We thank Prof. Qiang Zhou (University of California, Berkeley, USA) for providing FLAG-CDK9 constructs. B.M.K. dedicates this work to the memory of Dr. György Keri, CEO of Vichem and professor at the Semmelweis University, Budapest, Hungary. György recently lost his fight against cancer. He was a great scientist and a wonderful friend. We are also sad to announce that Z.G. passed away during the course of this project. With him we lost a productive researcher and much-valued colleague. This work was supported by the German federal state North Rhine Westphalia (NRW) as part of the FIT program (grant 314-4000-1209 to B.M.K. and LDC), by the European Union (European Regional Development Fund: Investing In Your Future) as part of the PerMed.NRW initiative (grant 005-1111-0025 to R.K.T., D.R., R.B., and LDC) and the EFRE initiative (grant EFFRE-0800397 to B.M.K., H.C.R., D.R., R.B., R.K.T., M.L.S., and LDC), by the German Ministry of Science and Education (BMBF) as part of the e:Med program (grants 01ZX1303 and 01ZX1603 to R.K.T., H.C.R., R.B., M.P., and D.R. and grant 01ZX1406 to M.L.S. and M.P.), by the German Consortium for Translational Cancer Research (DKTK) Joint Funding program (to R.K.T.), and by the BMBF as part of the NGFNplus program (grant 01GS08100 to R.K.T.). F.D. was supported by the Mildred-Scheel-Doktorandenprogramm of the Max-Planck Society (grant 110770 to F.D. and R.K.T.). V.T. is the recipient of a joint ERS/EMBO Long-Term Research Fellowship (LTRF 2014-2951) and a Swiss Cancer League postdoctoral research fellowship (BIL KFS-3402-02-2014). R.K.T. is a consultant of NEO New Oncology GmbH and received honoraria from AstraZeneca, Bayer, NEO New Oncology GmbH, Boehringer Ingelheim, Clovis Oncology, Daiichi-Sankyo, Eli Lilly,

Johnson & Johnson (J&J), Merck KGaA, MSD, Puma, Roche, and Sanofi. J.M.H. is a full-time employee and co-founder of NEO New Oncology GmbH. M.L.S. received a commercial research grant from Novartis. A.C., R.K.T., P.H., B.M.K., J.E., and J.M.H. hold the patent "CDK9 inhibitors in the treatment of midline carcinoma." R.B. has received honoraria for invited lectures and participation in SABs from Roche, Pfizer, Novartis, Boehringer-Ingelheim, Eli Lilly, Merck-Serono, and Qiagen. R.B. is a co-founder and serves as the chief scientific advisor of Targos Molecular Pathology Inc. (Kassel, Germany). D.R. reports consulting and lecture fees (Sanofi-Aventis, Astra-Zeneca, Novartis, Pfizer, Takeda, and Boehringer) and research support (MSD, Bayer Health Care, Merck-Serono, Bayer Crop Science, and J&J). H.C.R. received consulting and lecture fees (Merck, Celgene). A.C., P.H., J.E., U.K., and B.M.K. are employees of LDC, which has several commercial agreements in place with pharmaceutical companies.

Received: February 17, 2017  
Revised: June 27, 2017  
Accepted: August 24, 2017  
Published: September 19, 2017

## REFERENCES

- Albert, T.K., Rigault, C., Eickhoff, J., Baumgart, K., Antrecht, C., Klebl, B., Mittler, G., and Meisterernst, M. (2014). Characterization of molecular and cellular functions of the cyclin-dependent kinase CDK9 using a novel specific inhibitor. *Br. J. Pharmacol.* *171*, 55–68.
- Alekseyenko, A.A., Walsh, E.M., Wang, X., Grayson, A.R., Hsi, P.T., Kharchenko, P.V., Kuroda, M.I., and French, C.A. (2015). The oncogenic BRD4-NUT chromatin regulator drives aberrant transcription within large topological domains. *Genes Dev.* *29*, 1507–1523.
- Barretina, J., Caponigro, G., Stransky, N., Venkatesan, K., Margolin, A.A., Kim, S., Wilson, C.J., Lehár, J., Kryukov, G.V., Sonkin, D., et al. (2012). The Cancer Cell Line Encyclopedia enables predictive modelling of anticancer drug sensitivity. *Nature* *483*, 603–607.
- Baumli, S., Lolli, G., Lowe, E.D., Troiani, S., Rusconi, L., Bullock, A.N., Debreczeni, J.E., Knapp, S., and Johnson, L.N. (2008). The structure of P-TEFb (CDK9/cyclin T1), its complex with flavopiridol and regulation by phosphorylation. *EMBO J.* *27*, 1907–1918.
- Bösken, C.A., Farnung, L., Hintermair, C., Merzel Schachter, M., Vogel-Bachmayr, K., Blazek, D., Anand, K., Fisher, R.P., Eick, D., and Geyer, M. (2014). The structure and substrate specificity of human Cdk12/Cyclin K. *Nat. Commun.* *5*, 3505.
- Buettner, R., Wolf, J., and Thomas, R.K. (2013). Lessons learned from lung cancer genomics: the emerging concept of individualized diagnostics and treatment. *J. Clin. Oncol.* *31*, 1858–1865.
- Chan, D.A., Sutphin, P.D., Nguyen, P., Turcotte, S., Lai, E.W., Banh, A., Reynolds, G.E., Chi, J.-T., Wu, J., Solow-Cordero, D.E., et al. (2011). Targeting GLUT1 and the Warburg effect in renal cell carcinoma by chemical synthetic lethality. *Sci. Transl. Med.* *3*, 94ra70.
- Chen, E.X., Hotte, S., Hirte, H., Siu, L.L., Lyons, J., Squires, M., Lovell, S., Turner, S., McIntosh, L., and Seymour, L. (2014). A phase I study of cyclin-dependent kinase inhibitor, AT7519, in patients with advanced cancer: NCIC Clinical Trials Group IND 177. *Br. J. Cancer* *111*, 2262–2267.
- Clinical Lung Cancer Genome Project (CLCGP); Network Genomic Medicine (NGM) (2013). A genomics-based classification of human lung tumors. *Sci. Transl. Med.* *5*, 209ra153.
- Elkins, J.M., Fedele, V., Szklarz, M., Abdul Azeez, K.R., Salah, E., Mikolajczyk, J., Romanov, S., Sepetov, N., Huang, X.-P., Roth, B.L., et al. (2016). Comprehensive characterization of the published kinase inhibitor set. *Nat. Biotechnol.* *34*, 95–103.
- Fece de la Cruz, F., Gapp, B.V., and Nijman, S.M.B. (2015). Synthetic lethal vulnerabilities of cancer. *Annu. Rev. Pharmacol. Toxicol.* *55*, 513–531.
- Filippakopoulos, P., Qi, J., Picaud, S., Shen, Y., Smith, W.B., Fedorov, O., Morse, E.M., Keates, T., Hickman, T.T., Felletar, I., et al. (2010). Selective inhibition of BET bromodomains. *Nature* *468*, 1067–1073.
- Flaherty, K.T., Infante, J.R., Daud, A., Gonzalez, R., Kefford, R.F., Sosman, J., Hamid, O., Schuchter, L., Cebon, J., Ibrahim, N., et al. (2012). Combined BRAF and MEK inhibition in melanoma with BRAF V600 mutations. *N. Engl. J. Med.* *367*, 1694–1703.
- French, C.A., Miyoshi, I., Kubonishi, I., Grier, H.E., Perez-Atayde, A.R., and Fletcher, J.A. (2003). BRD4-NUT fusion oncogene: a novel mechanism in aggressive carcinoma. *Cancer Res.* *63*, 304–307.
- Garnett, M.J., Edelman, E.J., Heidorn, S.J., Greenman, C.D., Dastur, A., Lau, K.W., Greninger, P., Thompson, I.R., Luo, X., Soares, J., et al. (2012). Systematic identification of genomic markers of drug sensitivity in cancer cells. *Nature* *483*, 570–575.
- Grayson, A.R., Walsh, E.M., Cameron, M.J., Godec, J., Ashworth, T., Ambrose, J.M., Aserlind, A.B., Wang, H., Evan, G., Kluk, M.J., et al. (2014). MYC, a downstream target of BRD4-NUT, is necessary and sufficient for the blockade of differentiation in NUT midline carcinoma. *Oncogene* *33*, 1736–1742.
- Gregory, G.P., Hogg, S.J., Kats, L.M., Vidacs, E., Baker, A.J., Gilan, O., Lefebvre, M., Martin, B.P., Dawson, M.A., Johnstone, R.W., and Shortt, J. (2015). CDK9 inhibition by dinaciclib potentially suppresses Mcl-1 to induce durable apoptotic responses in aggressive MYC-driven B-cell lymphoma in vivo. *Leukemia* *29*, 1437–1441.
- Greifenberg, A.K., Hönig, D., Pilarova, K., Düster, R., Bartholomeeusen, K., Bösen, C.A., Anand, K., Blazek, D., and Geyer, M. (2016). Structural and functional analysis of the Cdk13/cyclin K complex. *Cell Rep.* *14*, 320–331.
- Hortobagyi, G.N., Stemmer, S.M., Burris, H.A., Yap, Y.-S., Sonke, G.S., Paluch-Shimon, S., Campono, M., Blackwell, K.L., André, F., Winer, E.P., et al. (2016). Ribociclib as first-line therapy for HR-positive, advanced breast cancer. *N. Engl. J. Med.* *375*, 1738–1748.
- Hu, Y., and Bajorath, J. (2013). Systematic identification of scaffolds representing compounds active against individual targets and single or multiple target families. *J. Chem. Inf. Model.* *53*, 312–326.
- Huang, C.-H., Lujambio, A., Zuber, J., Tschaharganeh, D.F., Doran, M.G., Evans, M.J., Kitzing, T., Zhu, N., de Stanchina, E., Sawyers, C.L., et al. (2014). CDK9-mediated transcription elongation is required for MYC addiction in hepatocellular carcinoma. *Genes Dev.* *28*, 1800–1814.
- Hyman, D.M., Puzanov, I., Subbiah, V., Faris, J.E., Chau, I., Blay, J.-Y., Wolf, J., Raje, N.S., Diamond, E.L., Hollebecque, A., et al. (2015). Vemurafenib in multiple nonmelanoma cancers with BRAF V600 mutations. *N. Engl. J. Med.* *373*, 726–736.
- Iorio, F., Knijnenburg, T.A., Vis, D.J., Bignell, G.R., Menden, M.P., Schubert, M., Aben, N., Gonçalves, E., Barthorpe, S., Lightfoot, H., et al. (2016). A landscape of pharmacogenomic interactions in cancer. *Cell* *166*, 740–754.
- Itzen, F., Greifenberg, A.K., Bösen, C.A., and Geyer, M. (2014). Brd4 activates P-TEFb for RNA polymerase II CTD phosphorylation. *Nucleic Acids Res.* *42*, 7577–7590.
- Kandath, C., McLellan, M.D., Vandin, F., Ye, K., Niu, B., Lu, C., Xie, M., Zhang, Q., McMichael, J.F., Wyczalkowski, M.A., et al. (2013). Mutational landscape and significance across 12 major cancer types. *Nature* *502*, 333–339.
- Kumar, S.K., LaPlant, B., Chng, W.J., Zonder, J., Callander, N., Fonseca, R., Fruth, B., Roy, V., Erlichman, C., and Stewart, A.K.; Mayo Phase 2 Consortium (2015). Dinaciclib, a novel CDK inhibitor, demonstrates encouraging single-agent activity in patients with relapsed multiple myeloma. *Blood* *125*, 443–448.
- Lam, F., Abbas, A.Y., Shao, H., Teo, T., Adams, J., Li, P., Bradshaw, T.D., Fischer, P.M., Walsby, E., Pepper, C., et al. (2014). Targeting RNA transcription and translation in ovarian cancer cells with pharmacological inhibitor CDKI-73. *Oncotarget* *5*, 7691–7704.
- Lemke, J., von Karstedt, S., Abd El Hay, M., Conti, A., Arce, F., Montinaro, A., Papenfuss, K., El-Bahrawy, M.A., and Walczak, H. (2014). Selective CDK9 inhibition overcomes TRAIL resistance by concomitant suppression of cFlip and Mcl-1. *Cell Death Differ.* *21*, 491–502.

- Lorenzin, F., Benary, U., Baluapuri, A., Walz, S., Jung, L.A., von Eyss, B., Kisker, C., Wolf, J., Eilers, M., and Wolf, E. (2016). Different promoter affinities account for specificity in MYC-dependent gene regulation. *eLife* 5, e15161.
- Lu, H., Xue, Y., Yu, G.K., Arias, C., Lin, J., Fong, S., Faure, M., Weisburd, B., Ji, X., Mercier, A., et al. (2015). Compensatory induction of MYC expression by sustained CDK9 inhibition via a BRD4-dependent mechanism. *eLife* 4, e06535.
- Martins, M.M., Zhou, A.Y., Corella, A., Horiuchi, D., Yau, C., Rakshandehroo, T., Gordan, J.D., Levin, R.S., Johnson, J., Jascur, J., et al. (2015). Linking tumor mutations to drug responses via a quantitative chemical-genetic interaction map. *Cancer Discov.* 5, 154–167.
- McLornan, D.P., List, A., and Mufti, G.J. (2014). Applying synthetic lethality for the selective targeting of cancer. *N. Engl. J. Med.* 371, 1725–1735.
- Morales, F., and Giordano, A. (2016). Overview of CDK9 as a target in cancer research. *Cell Cycle* 15, 519–527.
- Nojima, T., Gomes, T., Grosso, A.R.F., Kimura, H., Dye, M.J., Dhir, S., Carmo-Fonseca, M., and Proudfoot, N.J. (2015). Mammalian NET-seq reveals genome-wide nascent transcription coupled to RNA processing. *Cell* 161, 526–540.
- Odawara, J., Harada, A., Yoshimi, T., Maehara, K., Tachibana, T., Okada, S., Akashi, K., and Ohkawa, Y. (2011). The classification of mRNA expression levels by the phosphorylation state of RNAPII CTD based on a combined genome-wide approach. *BMC Genomics* 12, 516.
- R Development Core Team (2011). R: a language and environment for statistical computing (R Foundation for Statistical Computing).
- Reynold, N., Schwartz, B.E., Delvecchio, M., Sadoul, K., Meyers, D., Mukherjee, C., Caron, C., Kimura, H., Rousseaux, S., Cole, P.A., et al. (2010). Oncogenesis by sequestration of CBP/p300 in transcriptionally inactive hyperacetylated chromatin domains. *EMBO J.* 29, 2943–2952.
- Riniker, S., and Landrum, G.A. (2013). Open-source platform to benchmark fingerprints for ligand-based virtual screening. *J. Cheminform.* 5, 26.
- Rosell, R., Carcereny, E., Gervais, R., Vergnenegre, A., Massuti, B., Felip, E., Palmero, R., Garcia-Gomez, R., Pallares, C., Sanchez, J.M., et al.; Spanish Lung Cancer Group in collaboration with Groupe Français de Pneumo-Cancérologie and Associazione Italiana Oncologia Toracica (2012). Erlotinib versus standard chemotherapy as first-line treatment for European patients with advanced EGFR mutation-positive non-small-cell lung cancer (EURTAC): a multicentre, open-label, randomised phase 3 trial. *Lancet Oncol.* 13, 239–246.
- Rossi, K.A., Markwalder, J.A., Seitz, S.P., Chang, C.-H., Cox, S., Boisclair, M.D., Brizuela, L., Brenner, S.L., and Stouten, P.F.W. (2005). Understanding and modulating cyclin-dependent kinase inhibitor specificity: molecular modeling and biochemical evaluation of pyrazolopyrimidinones as CDK2/cyclin A and CDK4/cyclin D1 inhibitors. *J. Comput. Aided Mol. Des.* 19, 111–122.
- Seashore-Ludlow, B., Rees, M.G., Cheah, J.H., Cokol, M., Price, E.V., Coletti, M.E., Jones, V., Bodycombe, N.E., Soule, C.K., Gould, J., et al. (2015). Harnessing connectivity in a large-scale small-molecule sensitivity dataset. *Cancer Discov.* 5, 1210–1223.
- Shaw, A.T., Kim, D.-W., Nakagawa, K., Seto, T., Crinó, L., Ahn, M.-J., De Pas, T., Besse, B., Solomon, B.J., Blackhall, F., et al. (2013). Crizotinib versus chemotherapy in advanced ALK-positive lung cancer. *N. Engl. J. Med.* 368, 2385–2394.
- Sos, M.L., Fischer, S., Ullrich, R., Peifer, M., Heuckmann, J.M., Koker, M., Heynck, S., Stückerath, I., Weiss, J., Fischer, F., et al. (2009a). Identifying genotype-dependent efficacy of single and combined PI3K- and MAPK-pathway inhibition in cancer. *Proc. Natl. Acad. Sci. USA* 106, 18351–18356.
- Sos, M.L., Michel, K., Zander, T., Weiss, J., Frommolt, P., Peifer, M., Li, D., Ullrich, R., Koker, M., Fischer, F., et al. (2009b). Predicting drug susceptibility of non-small cell lung cancers based on genetic lesions. *J. Clin. Invest.* 119, 1727–1740.
- Squires, M.S., Feltell, R.E., Wallis, N.G., Lewis, E.J., Smith, D.M., Cross, D.M., Lyons, J.F., and Thompson, N.T. (2009). Biological characterization of AT7519, a small-molecule inhibitor of cyclin-dependent kinases, in human tumor cell lines. *Mol. Cancer Ther.* 8, 324–332.
- Stathis, A., Zucca, E., Bekradda, M., Gomez-Roca, C., Delord, J.P., de La Motte Rouge, T., Uro-Coste, E., de Braud, F., Pelosi, G., and French, C.A. (2016). Clinical response of carcinomas harboring the BRD4-NUT oncoprotein to the targeted bromodomain inhibitor OTX015/MK-8628. *Cancer Discov.* 6, 492–500.
- Stock, J.K., Giadrossi, S., Casanova, M., Brookes, E., Vidal, M., Koseki, H., Brockdorff, N., Fisher, A.G., and Pombo, A. (2007). Ring1-mediated ubiquitination of H2A restrains poised RNA polymerase II at bivalent genes in mouse ES cells. *Nat. Cell Biol.* 9, 1428–1435.
- Van Cutsem, E., Köhne, C.H., Láng, I., Folprecht, G., Nowacki, M.P., Cascinu, S., Shchepotin, I., Maurel, J., Cunningham, D., Tejpar, S., et al. (2011). Cetuximab plus irinotecan, fluorouracil, and leucovorin as first-line treatment for metastatic colorectal cancer: updated analysis of overall survival according to tumor KRAS and BRAF mutation status. *J. Clin. Oncol.* 29, 2011–2019.
- Walsby, E., Pratt, G., Shao, H., Abbas, A.Y., Fischer, P.M., Bradshaw, T.D., Brennan, P., Fegan, C., Wang, S., and Pepper, C. (2014). A novel Cdk9 inhibitor preferentially targets tumor cells and synergizes with fludarabine. *Oncotarget* 5, 375–385.
- Yan, J., Diaz, J., Jiao, J., Wang, R., and You, J. (2011). Perturbation of BRD4 protein function by BRD4-NUT protein abrogates cellular differentiation in NUT midline carcinoma. *J. Biol. Chem.* 286, 27663–27675.
- Yu, D.S., Zhao, R., Hsu, E.L., Cayer, J., Ye, F., Guo, Y., Shyr, Y., and Cortez, D. (2010). Cyclin-dependent kinase 9-cyclin K functions in the replication stress response. *EMBO Rep.* 11, 876–882.
- Zhang, H., Park, S.-H., Pantazides, B.G., Karpiuk, O., Warren, M.D., Hardy, C.W., Duong, D.M., Park, S.-J., Kim, H.S., Vassilopoulos, A., et al. (2013). SIRT2 directs the replication stress response through CDK9 deacetylation. *Proc. Natl. Acad. Sci. USA* 110, 13546–13551.
- Zhang, T., Kwiatkowski, N., Olson, C.M., Dixon-Clarke, S.E., Abraham, B.J., Greifenberg, A.K., Ficarro, S.B., Elkins, J.M., Liang, Y., Hannett, N.M., et al. (2016). Covalent targeting of remote cysteine residues to develop CDK12 and CDK13 inhibitors. *Nat. Chem. Biol.* 12, 876–884.
- Zou, H., and Hastie, T. (2005). Regularization and variable selection via the elastic net. *J.R. Stat. Soc.* 67, 301–320.

## Discussion

### Overcoming *EGFR*<sup>G724S</sup>-mediated osimertinib resistance through unique binding characteristics of second-generation EGFR inhibitors

Acquired resistance against 3<sup>rd</sup> generation EGFR inhibitor osimertinib is an emerging problem despite the substantial clinical effectiveness of osimertinib. The prevalent on-target resistance mutations after osimertinib treatment are EGFR C797S and G724S (Brown et al., 2019; Ercan et al., 2015; Fassunke et al., 2018). In the present study, two patients with acquired EGFR T790M gatekeeper mutations after treatment with first generation EGFR inhibitors exhibited loss of EGFR T790M but gained EGFR G724S during osimertinib treatment leading to progressive disease. EGFR T790M loss coinciding with EGFR G724S gain was also frequently observed in other patients that progressed in response to third generation EGFR inhibitors arguing for oncogenic driver capacity of EGFR G724S. On a molecular level, glycine substitution with serine in the G-rich loop of the EGFR tyrosine kinase domain increases structural flexibility and prevents binding of osimertinib and other third generation EGFR inhibitors. Remarkably, second generation inhibitors like afatinib and dacomitinib remain active against EGFR G724S, showing *in vitro* and *in vivo* efficacy. These results definitely warrant considerations to repurpose second-generation EGFR inhibitors in specific clinical settings such as acquired EGFR G724S despite their unfavorable toxicity profile that initially limited their clinical use in contrast to first- and third generation inhibitors. In addition, FDA-approved drugs like afatinib could be readily translated into the clinical setting. Although this proof-of-concept study and a case report demonstrating that combined osimertinib and afatinib treatment can evoke response and suppression of EGFR T790M and EGFR G724S sub-clones (Peled et al., 2017), it remains to be determined whether sequential or situational rotation or combinations of first, second, and third generation inhibitors depending on are translatable into clinical reality. This would require detailed, individually personalized treatment regimens and complicate derivation of general practice guidelines and/or clinical study design to show efficacy of such convoluted regimens. Another emerging aspect is the benefit of closely monitoring patients during the course of treatment and integrating molecular screening platforms that enable rapid identification of resistance mutations, which can then be therapeutically addressed. As exemplified by the effectiveness of afatinib against EGFR G742S in the present study, successful repurposing of older

inhibitor generations might be useful against resistance mutations against newer generation inhibitors. Other possible treatment strategies to target acquired resistance mutations against osimertinib, apart from designing new ATP-competitive inhibitors, could be allosteric EGFR inhibitors. Several studies demonstrated potent pre-clinical activity of allosteric inhibitors in osimertinib-resistant EGFR C797S models but must be investigated more comprehensively to evaluate their clinical potential (Jia et al., 2016; To et al., 2019). Another reason to continue the effort of TKI development against EGFR is that, to date, *EGFR*-mutant NSCLC displayed no clinically meaningful benefit from immune checkpoint inhibitors, despite their profound success in other entities (Hastings et al., 2019).

### **Drugging the catalytically inactive state of RET kinase in *RET*-rearranged tumors**

Comparable to *EGFR*-mutant NSCLC, clinical management of *RET*-rearranged NSCLC also tremendously improved with the clinical application of tyrosine kinase inhibitors. However, only recently in 2020, the first *RET*-specific inhibitors selpercatinib and pralsetinib were clinically approved for treatment of *RET*-rearranged NSCLC owing to the difficult-to-target characteristic of *RET* (Pall and Gautschi, 2021). Previously, multi-kinase inhibitors were used to treat *RET*-activated tumors with some success but due to limited *RET*-specific activity and inhibition of multiple other kinases resulting in substantial dose-limiting toxicity, considerably narrowing the therapeutic window (Gautschi et al., 2017). In our study, type II kinase inhibitors AD80 and ponatinib were identified to potently target KIF5B-*RET*- and CCDC6-*RET*-driven NSCLC. Importantly, type II kinase inhibitors bind to a hydrophobic pocket in the vicinity of the ATP-binding site of the kinase domain, which induces a DFG-out conformation of the conserved DFG motif in the activation loop of the kinase thereby trapping the target kinase in an inactive state (Kufareva and Abagyan, 2008). Remarkably, chemical properties of AD80 and ponatinib suggest binding to a broad range of kinases, however they displayed pronounced selectivity in viability assays preferentially against *RET*-rearranged NSCLC cell lines and retained activity against canonical *RET* gatekeeper mutation *RET* V804M. In contrast, clinically approved *RET* inhibitors cabozantinib and vandetanib are blocked by *RET* V804M. These proof-of-concept findings demonstrated that overcoming *RET* gatekeeper mutation is possible, even with multi-kinase inhibitors like AD80 and ponatinib. Nevertheless, recent *RET*-specific inhibitors undeniably represent the most promising approach for the treatment

of *RET*-rearranged NSCLC exemplified by their performance (Pall and Gautschi, 2021). However, repurposing of older generation inhibitors, just like second generation EGFR inhibitors in case of resistance against osimertinib might become more relevant with increasing number of acquired resistance mutations against newer generation inhibitors.

### **MYC paralog-dependent apoptotic priming orchestrates a spectrum of vulnerabilities in small cell lung cancer**

Despite this central role in tumorigenesis and tumor maintenance, MYC family members are yet undruggable targets. In SCLC, all three MYC paralogs, *MYC*, *MYCN*, and *MYCL* are frequently deregulated and are expressed mutually exclusive of one another. Therefore, SCLC is an ideal platform to study similarities and differences associated with each MYC paralog. Although, all three paralogs share functional and structural protein domains, they induce differential phenotypic and biological characteristics upon activation. As exemplified in SCLC, solely activation of *MYC* but not *MYCN* or *MYCL* in an otherwise identical genetic background led to differential drug sensitivity, gene expression patterns and epigenetic changes, confirming previous observations and allowing to pinpoint these alterations to MYC (Dammert et al., 2019; Mollaoglu et al., 2017; Sos et al., 2012). Active downregulation of *BCL2* exposes a MYC-specific MCL1-dependency in SCLC, which warrants follow-up *in vivo* studies once adequate MCL1 inhibitors are developed. However, MCL1 can also be targeted indirectly, e.g. by CDK9 inhibition reducing *MCL1* transcription and CDK9 inhibitors are widely available and could be evaluated in MYC-activated SCLC (Brägelmann et al., 2017b). Similarly, *MYCN* activation induced sensitivity to BH3-mimetics targeting BCL2 and BCL-xL but not MCL1 whereas high MYCL levels were associated with resistance to either of those compounds. Interestingly, the association of MYC and MIZ1, while MYCN and MYCL cannot bind MIZ1, marks the basis of *BCL2* repression by MYC/MIZ1-mediated DNMT3a recruitment and subsequent silencing of *BCL2*. Consequentially, comprehensive interactome studies of all three MYC paralogs could identify new candidates that differentially interact with particular MYC variants. Several studies have shown effectiveness of targeting the DNA damage response (DDR) machinery in SCLC *in vitro*, *in vivo*, and also in clinical settings (Dammert et al., 2019; Farago et al., 2019; Sen et al., 2017, 2019). However, the molecular basis leading to this sensitivity is not well understood. One possibility could be that SCLC

cells experience constant DNA damage from transcriptional and replicative stress fueled by oncogene activation, which activates CHK1 in order to slow down cell cycle progression and allow for DNA damage repair. Universal lack of p53 in SCLC prevents cell cycle arrest at the G1/S checkpoint and cells rely on CHK1 activity to activate the G2/M checkpoint. Failure to stall cell cycle at G2/M through CHK1 inhibition could force the cell to progress to mitosis with too high levels of DNA damage to properly divide leading to death in mitosis. MYC-activated SCLC display comparably higher DNA damage levels correlating with higher sensitivity to Aurora kinase inhibition, i.e. inhibition of mitotic progression. The observed synergy in combined CHK1 and AURK inhibition could therefore be too rapid entry into mitosis and then prolonging mitosis without proper DNA damage repair. Another important finding warranting further investigation is the MYC-induced elevated apoptotic priming that could be caused by lack of BCL2 leading to leaky, more easily permeabilizable mitochondria. This in turn could trigger some mitochondria to release cytochrome c even in non-insulted cells triggering sub-lethal caspase activity and DNA damage (Ichim et al., 2015). So, it is important to investigate the molecular underpinnings of DNA damage induction and whether it is actively contributing to transformation and aberrant growth or just a mere byproduct of high replication speed and transcriptional activity or whether DNA damage is required at all in the process of CHK1 inhibition. The current findings also evoke another important question of whether and how MYC paralogs and/or SCLC subtype-defining transcription factors shape phenotype and vulnerabilities of SCLC. Comprehensive studies are required to deconvolute whether MYC paralog-associated vulnerabilities are independent or dependent on the underlying SCLC subtype. So far, SCLC subtype-specific vulnerabilities have not been identified and it remains questionable whether the classification of SCLC into the proposed subtypes will entail any therapeutic consequence. Importantly, MYC-status of SCLC patients might be a better predictor for suitable therapy options demonstrated by increased clinical response of high *MYC*-expressing SCLC patients to an AURKA inhibitor / chemotherapy combination (Owonikoko et al., 2020).

### **Systematic kinase inhibitor profiling identifies CDK9 as a synthetic lethal target in NUT midline carcinoma**

Exemplified by the clinical failure of BET inhibitors in *BRD4-NUT* fusion carcinoma, druggability of transcription factors and chromatin modifiers remains challenging due

to the lack of structural features amenable for rational inhibitor design, the degenerated nature of binding sites leading to inhibition of multiple off-targets, or the pleiotropic role of these proteins in normal cellular processes apart from their oncogenic function. These disadvantages often lead to unspecific, toxicity-inducing adverse effects on organismal level resulting in dose reductions limiting clinical efficacy. Targeting BRD4-NUT-mediated, aberrant transcription through CDK9 inhibition circumvents the need to directly target BRD4-NUT and demonstrates the potential of synthetic lethal approaches in NUT carcinoma. CDK9 is a pan-essential gene for cells due to its function in cellular transcription ensuring productive transcriptional elongation and genetic knockout of CDK9 is associated with widespread lethality in cell lines (Anshabo et al., 2021). Therefore, like other pan-essential such as PLK1 or AURKA, CDK9 is not an ideal drug target and requires comprehensive pre-clinical effort to demonstrate the efficacy of CDK9 inhibition in a molecularly-defined context in contrast to pan-cytotoxic effects of CDK9 inhibition (Chang et al., 2021). To this end, the high throughput viability screening in our study strongly suggests preferential sensitivity to CDK9 inhibition is indeed associated with the molecular characteristics of NUT carcinoma. On top, CDK9-specificity of the inhibitor is especially important in this scenario to limit inhibition of other off-target CDKs that also have key functions in cellular processes like cell cycle progression. Another possible emerging target in NUT carcinoma might be MCL1, which was markedly downregulated upon CDK9 inhibition and proved to be an actionable target in MYC-activated SCLC. Interestingly, *MYC* is a prime target and substantially upregulated by BRD4-NUT (Grayson et al., 2014) and MYC-mediated, synthetic vulnerabilities, possibly MCL1 dependency, might overlap between SCLC and NUT carcinoma. However, more experimental evidence is needed to show targetability of MCL1 in NUT carcinoma. Recently, specific MCL1 inhibitors were developed and displayed encouraging pre-clinical results in hematological cancer models and are on the verge of clinical evaluation (Caenepeel et al., 2018) providing yet another tool to potentially exploit synthetic vulnerabilities in NUT carcinoma. Therefore, because of the pleiotropic deregulation of MYC in various cancers, strategies targeting MYC-associated vulnerabilities could potentially benefit cancer patients of multiple entities. On top, targeting increased MYC expression by dual HDAC / PI3K inhibition in NUT carcinoma displayed promising results *in vitro* (Sun et al., 2017) and is currently pursued in a clinical study (NCT02307240) again highlighting the relevance of activated MYC in NUT carcinoma.

## **Concluding remarks**

The introduction of molecularly guided, targeted therapy in lung cancer, especially in oncogene-driven NSCLC has substantially improved the prognosis for patients and enhanced quality of life under treatment in contrast to chemotherapy. The steadily increasing rate of approvals of specific small molecule inhibitors enlarges the fraction of NSCLC patients that potentially benefit from those drugs. However, the repertoire of inhibitors is finite and the challenge of acquired resistance against targeted kinase inhibitors remains. On- and off-target resistance mutations increase the complexity to devise rational treatment strategies. Drug combinations to address multiple oncogenic drivers at once are a promising approach but vast individual differences in tumors from case to case complicate design of clinical trials as well as embedding and application of such approaches in clinical practice. In sharp contrast to NSCLC, for a large number of lung cancer patients, particularly SCLC patients, no targeted therapy options are available. Despite extensive research efforts and encouraging pre-clinical studies with ensuing clinical trials, no targeted drugs have been approved for SCLC to date. Standard of care treatment with combination chemotherapy has only recently been complemented by addition of immune checkpoint inhibitors (ICIs) leading to marginally increased overall survival from 10 to 12-13 months compared to chemotherapy alone (Iams et al., 2020). So, treatment strategies that target tumor cells and boost immunotherapy efficacy might represent a worthwhile approach. In addition, improved molecular screening is needed to better identify patients that potentially benefit from targeted therapeutics and/or immunotherapy.

Another key aspect substantially complicating clinical management of NSCLC and SCLC is the high degree of intra-tumoral heterogeneity at time of diagnosis. The considerable level of heterogeneity at extensive stage disease increases the probability of therapy-resistant sub-clonal tumor populations already present within the tumor and facilitates the acquisition of drug-resistance mutations. Consequently, eradication of the dominant clonal tumor population by targeted therapy will not affect resistant sub-clones, which are then destined to grow out leading to tumor relapse. Therapeutic intervention at an earlier stage of tumor development might ameliorate this situation but requires better early detection methods. Liquid biopsy-based characterization of circulating tumor DNA (ctDNA) might be a suitable tool for early identification of actionable alterations. In conclusion, only concerted effort in better early detection, advancement of molecular understanding of the tumor to identify

tumor-specific vulnerabilities, the development of specific inhibitors targeting these vulnerabilities and rational design of clinical trials to provide these regimens to best-suited patients might enable the leap from mere management of lung cancer to actually curing lung cancer.

## References

- Alekseyenko, A.A., Walsh, E.M., Wang, X., Grayson, A.R., Hsi, P.T., Kharchenko, P. V., Kuroda, M.I., and French, C.A. (2015). The oncogenic BRD4-NUT chromatin regulator drives aberrant transcription within large topological domains. *Genes Dev.* *29*, 1507–1523.
- Anshabo, A.T., Milne, R., Wang, S., and Albrecht, H. (2021). CDK9: A Comprehensive Review of Its Biology, and Its Role as a Potential Target for Anti-Cancer Agents. *Front. Oncol.* *11*, 1–24.
- Blume-Jensen, P., and Hunter, T. (2001). Oncogenic kinase signalling. *Nature* *411*.
- Brägelmann, J., Böhm, S., Guthrie, M.R., Mollaoglu, G., Oliver, T.G., and Sos, M.L. (2017a). Family matters: How MYC family oncogenes impact small cell lung cancer. *Cell Cycle* *16*, 1489–1498.
- Brägelmann, J., Dammert, M.A., Dietlein, F., Heuckmann, J.M., Choidas, A., Böhm, S., Richters, A., Basu, D., Tischler, V., Lorenz, C., et al. (2017b). Systematic Kinase Inhibitor Profiling Identifies CDK9 as a Synthetic Lethal Target in NUT Midline Carcinoma. *Cell Rep.* *20*, 2833–2845.
- Brown, B.P., Zhang, Y.K., Westover, D., Yan, Y., Qiao, H., Huang, V., Du, Z., Smith, J.A., Ross, J.S., Miller, V.A., et al. (2019). On-target resistance to the mutant-selective EGFR inhibitor osimertinib can develop in an allele-specific manner dependent on the original EGFR-activating mutation. *Clin. Cancer Res.* *25*, 3341–3351.
- Caenepeel, S., Brown, S.P., Belmontes, B., Moody, G., Keegan, K.S., Chui, D., Whittington, D.A., Huang, X., Poppe, L., Cheng, A.C., et al. (2018). AMG 176, a Selective MCL1 Inhibitor, is Effective in Hematological Cancer Models Alone and in Combination with Established Therapies. *Cancer Discov.* CD-18-0387.
- Casaleto, J.B., and McClatchey, A.I. (2012). Spatial regulation of receptor tyrosine kinases in development and cancer. *Nat. Rev. Cancer* *12*, 387–400.
- Chang, L., Ruiz, P., Ito, T., and Sellers, W.R. (2021). Targeting pan-essential genes in cancer: Challenges and opportunities. *Cancer Cell* *39*, 466–479.

Ciampricotti, M., Karakousi, T., Richards, A.L., Quintanal-Villalonga, A., Karatza, A., Caeser, R., Costa, E.A., Allaj, V., Manoj, P., Spainhower, K.B., et al. (2021). Rlf-Mycl gene fusion drives tumorigenesis and metastasis in a mouse model of small cell lung cancer. *Cancer Discov.*

Collisson, E.A., Campbell, J.D., Brooks, A.N., Berger, A.H., Lee, W., Chmielecki, J., Beer, D.G., Cope, L., Creighton, C.J., Danilova, L., et al. (2014). Comprehensive molecular profiling of lung adenocarcinoma: The cancer genome atlas research network. *Nature* 511, 543–550.

Da Cunha Santos, G., Shepherd, F.A., and Tsao, M.S. (2011). EGFR Mutations and Lung Cancer. *Annu. Rev. Pathol. Mech. Dis* 6, 49–69.

Dammert, M.A., Brägelmann, J., Olsen, R.R., Böhm, S., Monhasery, N., Whitney, C.P., Chalishazar, M.D., Tumbink, H.L., Guthrie, M.R., Klein, S., et al. (2019). MYC paralog-dependent apoptotic priming orchestrates a spectrum of vulnerabilities in small cell lung cancer. *Nat. Commun.* 10.

Demedts, I.K., Vermaelen, K.Y., and Van Meerbeeck, J.P. (2010). Treatment of extensive-stage small cell lung carcinoma: Current status and future prospects. *Eur. Respir. J.* 35, 202–215.

Ercan, D., Choi, H.G., Yun, C.H., Capelletti, M., Xie, T., Eck, M.J., Gray, N.S., and Jänne, P.A. (2015). EGFR mutations and resistance to irreversible pyrimidine-based EGFR inhibitors. *Clin. Cancer Res.* 21, 3913–3923.

Farago, A.F., Yeap, B.Y., Stanzione, M., Hung, Y.P., Heist, R.S., Marcoux, J.P., Zhong, J., Rangachari, D., Barbie, D.A., Phat, S., et al. (2019). Combination olaparib and temozolomide in relapsed small-cell lung cancer. *Cancer Discov.* 9, 1372–1387.

Fassunke, J., Müller, F., Keul, M., Michels, S., Dammert, M.A., Schmitt, A., Plenker, D., Lategahn, J., Heydt, C., Brägelmann, J., et al. (2018). Overcoming EGFR G724S - mediated osimertinib resistance through unique binding characteristics of second-generation EGFR inhibitors. *Nat. Commun.* 9.

French, C.A. (2012). Pathogenesis of NUT midline carcinoma. *Annu. Rev. Pathol. Mech. Dis.* 7, 247–265.

French, C.A. (2018). NUT Carcinoma: Clinicopathologic features, pathogenesis, and treatment. *Pathol. Int.* 68, 583–595.

Gautschi, O., Milia, J., Filleron, T., Wolf, J., Carbone, D.P., Owen, D., Camidge, R., Narayanan, V., Doebele, R.C., Besse, B., et al. (2017). Targeting RET in patients with RET-rearranged lung cancers: Results from the global, multicenter RET registry. *J. Clin. Oncol.* 35, 1403–1410.

Gazdar, A.F., Bunn, P.A., and Minna, J.D. (2017). Small-cell lung cancer: what we know, what we need to know and the path forward. *Nat. Rev. Cancer.*

George, J., Lim, J.S., Jang, S.J., Cun, Y., Ozretić, L., Kong, G., Leenders, F., Lu, X., Fernández-Cuesta, L., Bosco, G., et al. (2015). Comprehensive genomic profiles of small cell lung cancer. *Nature* 524, 47–53.

Grayson, A.R., Walsh, E.M., Cameron, M.J., Godec, J., Ashworth, T., Ambrose, J.M., Aserlind, A.B., Wang, H., Evan, G.I., Kluk, M.J., et al. (2014). MYC, a downstream target of BRD-NUT, is necessary and sufficient for the blockade of differentiation in NUT midline carcinoma. *Oncogene* 33.

Gridelli, C., Rossi, A., Carbone, D.P., Guarize, J., Karachaliou, N., Mok, T., Petrella, F., Spaggiari, L., and Rosell, R. (2015). Non-small-cell lung cancer. *Nat. Rev. Dis. Prim.* 1, 15009.

Grunblatt, E., Wu, N., Zhang, H., Liu, X., Norton, J.P., Ohol, Y., Leger, P., Hiatt, J.B., Eastwood, E.C., Thomas, R., et al. (2020). MYCN drives chemoresistance in small cell lung cancer while USP7 inhibition can restore chemosensitivity. *Genes Dev.* 1–17.

Hastings, K., Yu, H.A., Wei, W., Sanchez-Vega, F., Deveaux, M., Choi, J., Rizvi, H., Lisberg, A., Truini, A., Lydon, C.A., et al. (2019). EGFR mutation subtypes and response to immune checkpoint blockade treatment in non-small-cell lung cancer. *Ann. Oncol.* 30, 1311–1320.

Herbst, R.S., Morgensztern, D., and Boshoff, C. (2018). The biology and management of non-small cell lung cancer. *Nature* 553.

Huang, Y.H., Klingbeil, O., He, X.Y., Wu, X.S., Arun, G., Lu, B., Somerville, T.D.D., Milazzo, J.P., Wilkinson, J.E., Demerdash, O.E., et al. (2018). POU2F3 is a master regulator of a tuft cell-like variant of small cell lung cancer. *Genes Dev.* 32, 915–928.

Iams, W.T., Porter, J., and Horn, L. (2020). Immunotherapeutic approaches for small-cell lung cancer. *Nat. Rev. Clin. Oncol.* 17.

Ichim, G., Lopez, J., Ahmed, S.U., Muthalagu, N., Giampazolias, E., Delgado, M.E., Haller, M., Riley, J.S., Mason, S.M., Athineos, D., et al. (2015). Limited Mitochondrial Permeabilization Causes DNA Damage and Genomic Instability in the Absence of Cell Death. *Mol. Cell* 57, 860–872.

Jia, Y., Yun, C.-H., Park, E., Ercan, D., Manuia, M., Juarez, J., Xu, C., Rhee, K., Chen, T., Zhang, H., et al. (2016). Overcoming EGFR(T790M) and EGFR(C797S) resistance with mutant-selective allosteric inhibitors. *Nature* 534, 129–132.

Jordan, E.J., Kim, H.R., Arcila, M.E., Barron, D., Chakravarty, D., Gao, J.J., Chang, M.T., Ni, A., Kundra, R., Jonsson, P., et al. (2017). Prospective comprehensive molecular characterization of lung adenocarcinomas for efficient patient matching to approved and emerging therapies. *Cancer Discov.* 7, 596–609.

Kim, D.W., Wu, N., Kim, Y.C., Cheng, P.F., Basom, R., Kim, D., Dunn, C.T., Lee, A.Y., Kim, K., Lee, C.S., et al. (2016). Genetic requirement for Mycl and efficacy of RNA Pol I inhibition in mouse models of small cell lung cancer. *Genes Dev.* 30, 1289–1299.

Kress, T.R., Sabò, A., and Amati, B. (2015). MYC: connecting selective transcriptional control to global RNA production. *Nat. Rev. Cancer* 15, 593–607.

Kufareva, I., and Abagyan, R. (2008). Type-II kinase inhibitor docking, screening, and profiling using modified structures of active kinase states. *J. Med. Chem.* 51, 7921–7932.

Lemmon, M.A., and Schlessinger, J. (2010). Cell signaling by receptor tyrosine kinases. *Cell* 141.

Mok, T.S., Wu, Y.-L., Thongprasert, S., Yang, C.-H., Chu, D.-T., Saijo, N., Sunpaweravong, P., Han, B., Margono, B., Ichinose, Y., et al. (2009). Gefitinib or Carboplatin–Paclitaxel in Pulmonary Adenocarcinoma. *N. Engl. J. Med.* 361.

Mollaoglu, G., Guthrie, M.R., Böhm, S., Brägelmann, J., Can, I., Ballieu, P.M., Marx, A., George, J., Heinen, C., Chalishazar, M.D., et al. (2017). MYC Drives Progression of Small Cell Lung Cancer to a Variant Neuroendocrine Subtype with Vulnerability to Aurora Kinase Inhibition. *Cancer Cell* 31, 270–285.

Owonikoko, T.K., Niu, H., Nackaerts, K., Csozsi, T., Ostoros, G., Mark, Z., Baik, C., Joy, A.A., Chouaid, C., Jaime, J.C., et al. (2020). Randomized Phase II Study of Paclitaxel plus Alistertib versus Paclitaxel plus Placebo as Second-Line Therapy for SCLC: Primary and Correlative Biomarker Analyses. In *Journal of Thoracic Oncology*, pp. 274–287.

Pall, G., and Gautschi, O. (2021). Advances in the treatment of RET-fusion-positive lung cancer. *Lung Cancer* 156.

Passaro, A., Jänne, P.A., Mok, T., and Peters, S. (2021). Overcoming therapy resistance in EGFR-mutant lung cancer. *Nat. Cancer* 2, 377–391.

Peifer, M., Fernández-Cuesta, L., Sos, M.L., George, J., Seidel, D., Kasper, L.H., Plenker, D., Leenders, F., Sun, R., Zander, T., et al. (2012). Integrative genome analyses identify key somatic driver mutations of small-cell lung cancer. *Nat. Genet.* 44, 1104–1110.

Peled, N., Roisman, L.C., Miron, B., Pfeffer, R., Lanman, R.B., Ilouze, M., Dvir, A., Soussan-Gutman, L., Barlesi, F., Tarcic, G., et al. (2017). Subclonal Therapy by Two EGFR TKIs Guided by Sequential Plasma Cell-free DNA in EGFR-Mutated Lung Cancer. *J. Thorac. Oncol.* 12, e81–e84.

Ramalingam, S.S., Vansteenkiste, J., Planchard, D., Cho, B.C., Gray, J.E., Ohe, Y., Zhou, C., Reungwetwattana, T., Cheng, Y., Chewaskulyong, B., et al. (2020). Overall Survival with Osimertinib in Untreated, EGFR-Mutated Advanced NSCLC. *N. Engl. J. Med.* 382, 41–50.

Rudin, C.M., Durinck, S., Stawiski, E.W., Poirier, J.T., Modrusan, Z., Shames, D.S., Bergbower, E.A., Guan, Y., Shin, J., Guillory, J., et al. (2012). Comprehensive genomic analysis identifies SOX2 as a frequently amplified gene in small-cell lung cancer. *Nat. Genet.* 44, 1111–1116.

Rudin, C.M., Poirier, J.T., Byers, L.A., Dive, C., Dowlati, A., George, J., Heymach, J. V., Johnson, J.E., Lehman, J.M., MacPherson, D., et al. (2019). Molecular subtypes of small cell lung cancer: a synthesis of human and mouse model data. *Nat. Rev. Cancer.*

Rudin, C.M., Brambilla, E., Faivre-Finn, C., and Sage, J. (2021). Small-cell lung cancer. *Nat. Rev. Dis. Prim.* 7.

Schabath, M.B., and Cote, M.L. (2019). Cancer progress and priorities: Lung cancer. *Cancer Epidemiol. Biomarkers Prev.* 28, 1563–1579.

Sen, T., Tong, P., Stewart, C.A., Cristea, S., Valliani, A., Shames, D.S., Redwood, A.B., Fan, Y.H., Li, L., Glisson, B.S., et al. (2017). CHK1 inhibition in small-cell lung cancer produces single-agent activity in biomarker-defined disease subsets and combination activity with cisplatin or olaparib. *Cancer Res.* 77, 3870–3884.

Sen, T., Rodriguez, B.L., Chen, L., Della Corte, C.M., Morikawa, N., Fujimoto, J., Cristea, S., Nguyen, T., Diao, L., Li, L., et al. (2019). Targeting DNA damage response promotes antitumor immunity through STING-mediated T-cell activation in small cell lung cancer. *Cancer Discov.* 9, 646–661.

Sequist, L. V., Yang, J.C.H., Yamamoto, N., O’Byrne, K., Hirsh, V., Mok, T., Geater, S.L., Orlov, S., Tsai, C.M., Boyer, M., et al. (2013). Phase III study of afatinib or cisplatin plus pemetrexed in patients with metastatic lung adenocarcinoma with EGFR mutations. *J. Clin. Oncol.* 31.

Skoulidis, F., and Heymach, J. V. (2019). Co-occurring genomic alterations in non-small-cell lung cancer biology and therapy. *Nat. Rev. Cancer* 19, 495–509.

Soria, J.-C., Ohe, Y., Vansteenkiste, J., Reungwetwattana, T., Chewaskulyong, B., Lee, K.H., Dechaphunkul, A., Imamura, F., Nogami, N., Kurata, T., et al. (2018). Osimertinib in Untreated EGFR -Mutated Advanced Non–Small-Cell Lung Cancer . *N. Engl. J. Med.* 378.

Sos, M.L., Dietlein, F., Peifer, M., Schöttle, J., Balke-Want, H., Müller, C., Koker, M., Richters, A., Heynck, S., Malchers, F., et al. (2012). A framework for identification of actionable cancer genome dependencies in small cell lung cancer. *Proc. Natl. Acad. Sci. U. S. A.* 109, 17034–17039.

Su, Z., Wang, Z., Ni, X., Duan, J., Gao, Y., Zhuo, M., Li, R., Zhao, J., Ma, Q., Bai, H., et al. (2019). Inferring the evolution and progression of small-cell lung cancer by single-cell sequencing of circulating tumor cells. *Clin. Cancer Res.* 25.

Subbiah, V., Yang, D., Velcheti, V., Drilon, A., and Meric-Bernstam, F. (2020). State-of-the-art strategies for targeting RET-dependent cancers. *J. Clin. Oncol.* 38, 1209–1221.

Sun, K., Atoyian, R., Borek, M.A., Dellarocca, S., Samson, M.E.S., Ma, A.W., Xu, G.X., Patterson, T., Tuck, D.P., Viner, J.L., et al. (2017). Dual HDAC and PI3K inhibitor CUDC-907 down regulates MYC and suppresses growth of MYC-dependent cancers. *Mol. Cancer Ther.* 16.

Sung, H., Ferlay, J., Siegel, R.L., Laversanne, M., Soerjomataram, I., Jemal, A., and Bray, F. (2021). Global Cancer Statistics 2020: GLOBOCAN Estimates of Incidence and Mortality Worldwide for 36 Cancers in 185 Countries. *CA. Cancer J. Clin.* *71*, 209–249.

Thein, K.Z., Velcheti, V., Mooers, B.H.M., Wu, J., and Subbiah, V. (2021). Precision therapy for RET-altered cancers with RET inhibitors. *Trends in Cancer* *xx*, 1–15.

Thng, D.K.H., Toh, T.B., and Chow, E.K.H. (2021). Capitalizing on Synthetic Lethality of MYC to Treat Cancer in the Digital Age. *Trends Pharmacol. Sci.* *42*, 166–182.

To, C., Jang, J., Chen, T., Park, E., Mushajiang, M., De Clercq, D.J.H., Xu, M., Wang, S., Cameron, M.D., Heppner, D.E., et al. (2019). Single and dual targeting of mutant egfr with an allosteric inhibitor. *Cancer Discov.* *9*, 926–943.

Travis, W.D., Brambilla, E., Nicholson, A.G., Yatabe, Y., Austin, J.H.M., Beasley, M.B., Chirieac, L.R., Dacic, S., Duhig, E., Flieder, D.B., et al. (2015). The 2015 World Health Organization Classification of Lung Tumors: Impact of Genetic, Clinical and Radiologic Advances since the 2004 Classification. *J. Thorac. Oncol.* *10*, 1243–1260.

Tumbrink, H.L., Heimsoeth, A., and Sos, M.L. (2021). The next tier of EGFR resistance mutations in lung cancer. *Oncogene* *40*.

Weinstein, I.B., and Joe, A. (2008). Oncogene addiction. *Cancer Res.* *68*.

Wolf, E., and Eilers, M. (2020). Targeting MYC Proteins for Tumor Therapy. *Annu. Rev. Cancer Biol.* *4*, 61–75.

Wooten, D.J., Groves, S.M., Tyson, D.R., Liu, Q., Lim, J.S., Albert, R., Lopez, C.F., Sage, J., and Quaranta, V. (2019). Systems-level network modeling of Small Cell Lung Cancer subtypes identifies master regulators and destabilizers. *PLoS Comput. Biol.* *15*, e1007343.

## Erklärung zur Dissertation

Hiermit versichere ich an Eides statt, dass ich die vorliegende Dissertation selbstständig und ohne die Benutzung anderer als der angegebenen Hilfsmittel und Literatur angefertigt habe. Alle Stellen, die wörtlich oder sinngemäß aus veröffentlichten und nicht veröffentlichten Werken dem Wortlaut oder dem Sinn nach entnommen wurden, sind als solche kenntlich gemacht. Ich versichere an Eides statt, dass diese Dissertation noch keiner anderen Fakultät oder Universität zur Prüfung vorgelegen hat; dass sie - abgesehen von unten angegebenen Teilpublikationen und eingebundenen Artikeln und Manuskripten - noch nicht veröffentlicht worden ist sowie, dass ich eine Veröffentlichung der Dissertation vor Abschluss der Promotion nicht ohne Genehmigung des Promotionsausschusses vornehmen werde. Die Bestimmungen dieser Ordnung sind mir bekannt. Darüber hinaus erkläre ich hiermit, dass ich die Ordnung zur Sicherung guter wissenschaftlicher Praxis und zum Umgang mit wissenschaftlichem Fehlverhalten der Universität zu Köln gelesen und sie bei der Durchführung der Dissertation zugrundeliegenden Arbeiten und der schriftlich verfassten Dissertation beachtet habe und verpflichte mich hiermit, die dort genannten Vorgaben bei allen wissenschaftlichen Tätigkeiten zu beachten und umzusetzen. Ich versichere, dass die eingereichte elektronische Fassung der eingereichten Druckfassung vollständig entspricht.

Teilpublikationen:

Fassunke, J., Müller, F., Keul, M., Michels, S., **Dammert, M.A.\***, Schmitt, A., Plenker, D., Lategahn, J., Heydt, C., Brägelmann, J., et al. (2018). Overcoming EGFR G724S - mediated osimertinib resistance through unique binding characteristics of second-generation EGFR inhibitors. *Nat. Commun.* 9.

Plenker, D., Riedel, M., Brägelmann, J., **Dammert, M.A.**, Chauhan, R., Knowles, P.P., Lorenz, C., Keul, M., Bührmann, M., Pagel, O., et al. (2017). Drugging the catalytically inactive state of RET kinase in RET-rearranged tumors. *Sci. Transl. Med.* 9, 1–12.

**Dammert, M.A.**, Brägelmann, J., Olsen, R.R., Böhm, S., Monhasery, N., Whitney, C.P., Chalisehar, M.D., Tumbrink, H.L., Guthrie, M.R., Klein, S., et al. (2019). MYC paralog-dependent apoptotic priming orchestrates a spectrum of vulnerabilities in small cell lung cancer. *Nat. Commun.* 10.

Brägelmann, J., **Dammert, M.A.\***, Dietlein, F., Heuckmann, J.M., Choidas, A., Böhm, S., Richters, A., Basu, D., Tischler, V., Lorenz, C., et al. (2017). Systematic Kinase Inhibitor Profiling Identifies CDK9 as a Synthetic Lethal Target in NUT Midline Carcinoma. *Cell Rep.* 20, 2833–2845.

\* co-first author

Datum, Name und Unterschrift